AN ASSESSMENT OF A GTEM CELL AS A TEST ENVIRONMENT USING MEASUREMENTS AND SIMULATIONS

XAVIER TOH IK NGU, BEng.

Thesis submitted to the University of Nottingham
for the degree of Doctor of Philosophy

JULY 2009

“Our Father, who art in heaven,
Hallowed be thy Name.
Thy kingdom come.
Thy will be done,
On earth as it is in heaven.
Give us this day our daily bread.
And forgive us our trespasses,
As we forgive those who trespass against us.
And lead us not into temptation,
But deliver us from evil.
For thine is the kingdom,
and the power,
and the glory,
for ever and ever.
Amen”

The Lord’s Prayer

Abstract

The Gigahertz Transverse Electromagnetic (GTEM) cell was developed about 20 years ago and the applications using GTEM cells for electromagnetic compatibility (EMC) measurements are continuously increasing. The research described in this Thesis proposes a new method for characterizing emissions from electrical appliances using a GTEM cell. The research adapts the method used in the Transverse Electromagnetic (TEM) cell where the measurements are done by using a two-port system which includes a phase measurement. This is a restriction in GTEM cells because only one port exists and normally only the magnitude reading can be performed. This requires the development and application of new techniques,

which allow the description of emitters in terms of equivalent electric and magnetic dipoles measured using a GTEM cell with phase measurement. A full field 3D Transmission Line Model (TLM) model of a GTEM cell is generated. Further simulations based on this model were performed to assess the behaviour of the emitters and when the GTEM cell is under actual working conditions. The model is also used to validate results obtained from measurements. The assumption that the dipole moments from a general emitter are in phase is also studied and evidence is presented to assess the validity of this assumption. The impact of the phase variations within an EUT towards the total radiated power estimated according to IEC 61000-4-20 is discussed and a technique to measure phase using a GTEM cell is introduced.

List of Publications

[1] Ngu X.T.I.; Nothofer A.; Thomas D.W.P.; and Christopoulos C*., "Time-Domain Modeling of a GTEM Cell Using Transmission-Line- Matrix"* UK National URSI Symposium, Abingdon, United Kingdom, July 2006.

[2] Ngu X.T.I.; Nothofer A.; Thomas D.W.P.; and Christopoulos C., *"The Impact of Phase in GTEM and TEM Emission Measurements"*, International Symposium on Electromagnetic Compatibility, EMC Europe, Barcelona, Spain, September 2006.

[3] Ngu X.T.I.; Nothofer A.; Thomas D.W.P.; and Christopoulos C., *"A Complete Model for Simulating Magnitude and Phase of Emissions from a DUT Placed Inside a GTEM Cell"*, IEEE Transactions on Electromagnetic Compatibility, EMC-49, p.285-293, May 2007.

[4] Ngu X.T.I.; Nothofer A.; Thomas D.W.P.; and Christopoulos C., *"A Complete Simulation of a Radiated Emission Test According to IEC 61000-4-20"*, Progress In Electromagnetics Research Symposium (PIERS) 22nd Proceedings, Prague, Czech Republic, p.34-38, August 2007.

[5] Ngu X.T.I.; Nothofer A.; Thomas D.W.P.; and Christopoulos C*., "The Impact of Phase Measurement toward the Total Radiated Power in A GTEM Cell"*, European Electromagnetics (EUROEM), Lausanne, Switzerland, July 2008

[6] Ngu X.T.I.; Nothofer A.; Thomas D.W.P.; and Christopoulos C., *"On the Performance of a Loaded GTEM Cell Using TLM Simulation"*, XXIX URSI General Assembly of the International Union of Radio Science, Chicago, Illinois, USA, August 2008

[7] Ngu X.T.I.; Nothofer A.; Thomas D.W.P.; and Christopoulos C., *"Effects of Phase Differences in GTEM Cell Measurements"*, International Symposium on Electromagnetic Compatibility, EMC Europe, Hamburg, Germany, September 2008

Acknowledgement

I would like to express my foremost gratitude to my Lord, Jesus Christ, who art in Heaven for all His limitless shower of blessings and love from the past, present and in the future. You are the inventor and I am just a founder.

I am deeply indebted to my three Supervisors, Professor Christos Christopoulos, Dr David W.P. Thomas and Dr Angela Nothofer, who patiently guided me through the journey of this study. Never will I be able to do it on my own without their astounding ideas and thoughts as well as encouragements. They have helped me not only in my study but also to be a better person. Professor Christos Christopoulos is the most humble man yet a man full of wisdom that I ever met in my life which still amazes me to this very day. Dr

David W.P. Thomas is always helpful and cheerful that, a helping hand is always there when I need it. And not to forget Dr Angela Nothofer who has been so generous providing me with countless stimulating ideas from her bountiful knowledge in the field of my study as well as morale support. It is one of the satisfactions in my life that I met these amazing people.

I also would like to thank my sponsor, University Technology Tun Hussein Onn Malaysia (UTHM) under the grant of Ministry of Education Malaysia for providing me with the financial support. The amount that was offered to me is unimaginable due to the currency conversion.

Dr John Paul who is the programmer of the regSolve has been so kind and helpful in answering trains of questions from me. I really appreciate his kindness. I have furthermore to thank the academic support staffs for their help with hardware and suggestions. The administrative staffs are equally honored and not forgotten too especially Mdm. Kathryn Sanderson whom is ever so helpful with my administrative tasks. To all my friends and colleagues, I thank you for being by my side when I needed you.

Last and never the least, I would like to thank my family; my father, mother, sister and brother for their support. Especially, I would like to give my very special thanks to my wife, Audrey whose patience, tolerance and love is beyond my comprehension.

May God look after you.

List of Contents

Chapter 3 - The GTEM Cell TLM Model

Chapter 4 - The Effect of Phase Differences

Chapter 5 - The Phase Measurement Method

Chapter 6 - Discussion and Conclusions

Appendix

List of Figures

List of Tables

Abbreviation Symbol and Mathematical Convention

EMC	Electromagnetic Compatibility
IEC	International Electrotechnical Commission
RF	Radio Frequency
EMI	Electromagnetic Interference
ESD	Electrostatic Discharge
NEMP	Nuclear Electromagnetic Pulse
LEMP	Lightning Electromagnetic Pulse
FCC	Federal Communication Commission
CEN	European Committee for Standardization
CENELEC	European Committee for Electrotechnical Standardization
ETSI	European Telecommunications Standards Institute
BSI	British Standards Institution
OATS	Open Area Test Site

FAR	Full Anechoic Room
SAR	Semi Anechoic Room
TEM	Transverse Electromagnetic
CISPR	Special International Committee on Radio Interference
RAM	Radio Absorber Material
EUT	Equipment under test (also known as DUT for device under test)
GTEM	Gigahertz Transverse Electromagnetic
RCCTLO	Rectangular Coaxial Cone Transmission Line with an Offset inner conductor
TLM	Transmission Line Model
HP	Hewlett Packard
FDTD	Finite Difference Time Domain
FEM	Finite Element Method
MoM	Method of Moments
TDR	Time domain Reflectometer
PCB	Printed circuit board
PNA	Power Network Analyser
SWR	Standing wave ratio
GUI	Graphic user interface
SMA	Sub-Miniature version A
BALUN	Balance to unbalance
LED	Light emitting diode
IR	Infrared
ADC	Analogue to digital converter
DAC	Digital to analogue converter
Ah	Ampere hour (or mili Ampere hour for mAh)
GPIB	General Purpose Interface Bus

x	Horizontal axis
y	Vertical axis
z	Longitudinal axis

x’	EUT horizontal axis
y’	EUT vertical axis
z’	EUT longitudinal axis
$\bar{z}$	Longitudinal unit vector
mm	Millimeter
cm	Centimeter
m	Meter
M	Mega
Hz	Hertz
Ω	Ohm
$\overline{E}$	The vector electric field
$\overline{H}$	The vector magnetic field
$\overline{E}_n$	Vector orthonormal electric function
$\overline{H}_n$	Vector orthonormal magnetic function
a_n , b_n	Expansion coefficient
$\overline{m_e}$	Electric dipole moment
$\overline{m_m}$	Magnetic dipole moment
J	Normalized filament current
$\bar{e}_o$	Normalized y electric field
P_s	Sum of power
P_d	Difference of power
k	Boltzmann constant
V	Voltage
tan	Tangent
E_n	Electric field with direction n (for n = x, y or z)
H_n	Magnetic field with direction n (for n = x, y or z)
V_{pp}	Voltage peak to peak
V_{ac}	Alternating current Voltage

V_{dc}	Direct current Voltage
dB	decibel
dBm	decibel above 1 mili-Watt
min	Minimum
mag	Magnitude
ϕ	Phase
s	Second (Time)
W	Watt
Z_c	Characteristic impedance
Z_i	Characteristic impedance along the transmission line
Z_l	Characteristic impedance of load
Z_s	Characteristic impedance of source
E_{max}	Maximum electric field
Gnd	Ground

Chapter 1

Background and Literature Review

1.0 Electromagnetic compatibility

Electromagnetic Compatibility or EMC is defined as *"The ability of an equipment or a system to function satisfactorily in its electromagnetic environment without introducing intolerable electromagnetic disturbance to anything in that environment"* according to the International Electrotechnical Commission (IEC) [1]. Paul stated in his book [2] that "A system is electromagnetically compatible with its environment if it satisfies three criteria:

1. It does not cause interference with other systems
2. It is not susceptible to emissions from other systems

3. It does not cause interference with itself”

EMC is divided into two categories which are the emission and the immunity (susceptibility). These two categories are then subdivided into radiated and conducted. Radiated emission is where a device unintentionally generates radio frequency (RF) waves which propagate in the surrounding free-space. In contrast, the radiated immunity is the condition where a presence of RF in the ambience is likely to affect the ability of a device to function normally. Conducted emission and immunity refer to the condition where EM energy is guided by wires e.g. mains wires. Examples are harmonics, voltage fluctuations and etc. Other sources of Electromagnetic Interference (EMI) include Electrostatic Discharge (ESD), Nuclear Electromagnetic Pulse (NEMP) and Lightning Electromagnetic Pulse (LEMP). Figure 1.1 summarizes the components of EMC.

There are many organizations in the world concerned with EMC regulations. The most important organization is the International Electrotechnical Commission (IEC). Others are the Federal Communication Commission (FCC) in United States; Comité Européen de Normalisation or European Committee for Standardization (CEN), Comité Européen de Normalisation Electrotechniques or European Committee for Electrotechnical Standardization (CENELEC) and European Telecommunications Standards Institute (ETSI) in Europe; and British Standards Institution (BSI) in Britain.

The EU directive 2004/108/CE (which replaced 89/336/EEC) [3] states

that in order for electronic devices to be marketed within the European Union, they have to obtain a CE mark by complying with EMC limits as stated in EMC standards. To achieve this, the manufacturers have to perform a series of radiated and conducted emission and immunity tests as well as other EMI tests.

The components of EMC are shown in Figure 1.1. Each of the components has its own specific testing methods. These testing methods are governed by standards that specify the procedures and rules of testing. In emission tests, these standards specify the limits for a range of equipment. In immunity tests, the EUT has to withstand a certain level of interference specified by the standards in order to pass the tests. Since the work in this Thesis concentrates on the radiated emission, only the radiated emission test methods will be discussed.

Radiated emission test are performed in a number of environments including the Open Area Test Site (OATS), Full or Semi Anechoic Room (FAR and SAR) and the Transverse Electromagnetic (TEM) waveguide. Testing in these environments is briefly discussed in the following sections.

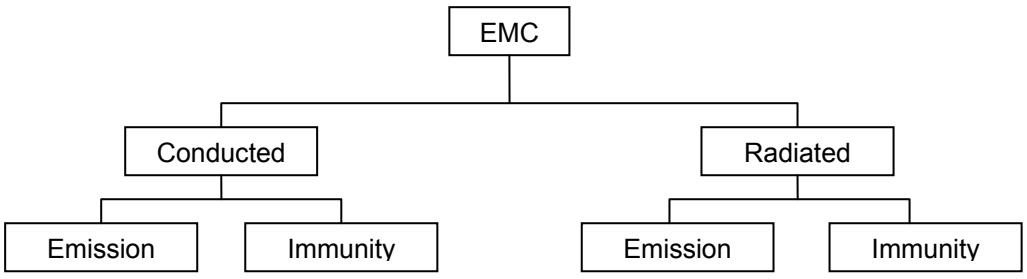

Figure 1.1 Components of EMC

1.1 The OATS for EMC radiated measurements

Early radiated emission tests were conducted in an open space where an antenna was used to measure the radiation coming from an EUT. The open space was carefully chosen so that there were no obstructing objects that could potentially result in reflections and were free from ambient electromagnetic noise. This setup marks the beginning of the OATS which is the standard environment for radiated emission measurements. The OATS test environment is the most important and its use is the earliest adopted in many emission standards. The OATS is still being reference by major standards such as the CISPR 22 [4] and the IEC61000-4-3 [5] to the present. The measurements made in other test environments can be accepted by correlating them with OATS.

According to [4], the locations of the EUT and the measuring antenna are the foci of an ellipse as shown in Figure 1.2. The major diameter of the ellipse is twice the distance *R* while the minor diameter of the ellipse is $\sqrt{3}R$ where *R* is the distance between the measuring antenna and the EUT. The standards specify an option for the distance between the measuring antenna and the EUT *R* to be either 3 m, 10 m or 30 m for far field measurements. The area encompassed by the ellipse must be free from any reflecting objects and shall be covered by a flat perfect conductor serving as a ground plane. A perfect conductor is practically not achievable but the use of copper or aluminium is considered ideal.

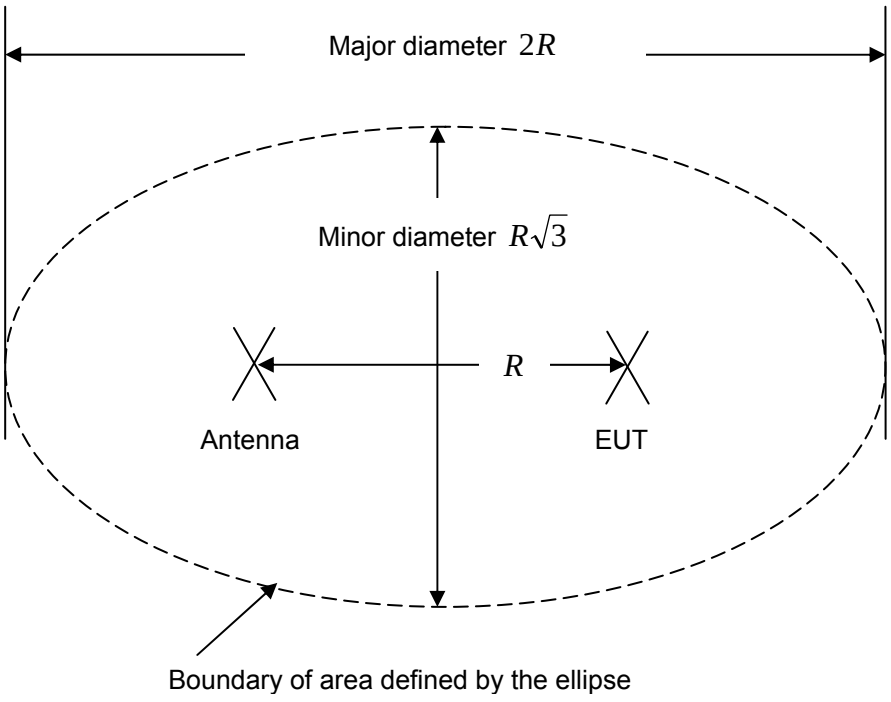

Figure 1.2 Open Area test Site configuration

To perform the radiated emission test using an OATS, the EUT is first placed 0.8 m above the ground plane on a turntable at one of the foci of the ellipse. The measuring antenna is placed on the other focus of the ellipse. The measuring antenna is in turn horizontally and vertically polarized and a maximum hold scan is performed using a spectrum analyser while the EUT is rotated 360^{o}. To avoid the nulls caused by the destructive combination of the direct and the reflected wave from by the ground, the antenna is scanned between the heights of one to four metres.

However, the emerging mobile phone, television and radio antenna towers cause problems to OATS. The ambient noise (e.g. from mobile phone antenna towers) can be high and may affect the measurement results

because radiations from these transmitters are often higher than the limits specified in the standards. To solve this problem, SAR was introduced. A SAR is a screened room acting as a Faraday cage to segregate ambient noise from the actual noise radiated by an EUT. The side and upper walls are lined with Radio Absorbing Material (RAM) to prevent reflections. The metallic floor acting as a ground plane remains exposed and the whole SAR setup is actually simulating an OATS setup with a difference that a low ambient noise open space is no longer required. A SAR offers the advantage of performing radiated emission tests according to OATS procedures without space consent but at a much higher construction cost.

As mentioned above, the procedure for OATS measurement requires an antenna height scan from one to four metre. Changing the location of an antenna relative to a ground plane introduces errors in EMC tests because the antenna factor of the measuring antenna changes. The impact of this can be minimized by introducing FAR where the ground plane of the SAR is also lined up with RAM to simulate a free space environment. With the reflections being absorbed by the RAM, the height scan is no longer being required and reduces the errors caused by the antenna factor. This also improves repeatability as the impact of changing ambient noise in an OATS is minimised. The high costs and space constraints of FAR and SAR are not affordable for many organizations and this calls for a smaller and cheaper alternative test environment. Such environment is the TEM cell developed to

overcome for the disadvantages of the FAR and SAR. The TEM cell is briefly discussed in the following sections.

1.2 TEM waveguide for EMC radiated measurements

A waveguide with a separate inner conductor is a transmission line system where a TEM wave can propagate. A TEM wave has an electric field component E_y and a magnetic component field H_x both transverses to the direction of propagation z (i.e. E_z and H_z = 0) as shown in Figure 1.3. The electric and magnetic components are always in phase and the TEM wave has a wave impedance of $\approx$ 377Ω. Another characteristic of a TEM wave is that it has no lower cut off frequency. Hence, a TEM wave can propagate from DC to certain frequencies depending on the size of the waveguides. There are various methods to generate TEM waves, and they can be guided along or propagate in a system where two conductors exist separated by a dielectric medium. These systems are such as two-wire transmission line, two parallel conducting planes, strip lines and coaxial cables.

The TEM cell was invented by Crawford [6] and it is a two-port rectangular coaxial transmission line. It consists of two symmetrically tapered sections and a parallel middle section. The parallel middle section is the location where the Equipment Under Test (EUT) is placed. A TEM cell is a closed coaxial structure and operates at frequencies where ideally only the

fundamental TEM mode exists. This is the main advantage of using a TEM cell for radiated emission tests because the emission from an EUT in far field is a form of TEM wave which will couple into the TEM mode inside a TEM cell. A typical TEM cell is shown in Figure 1.4.

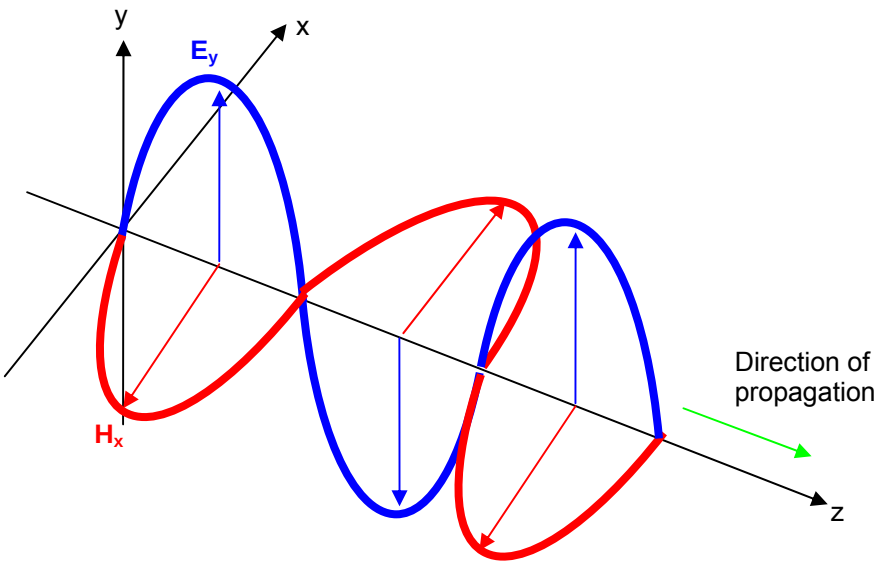

Figure 1.3 The TEM wave

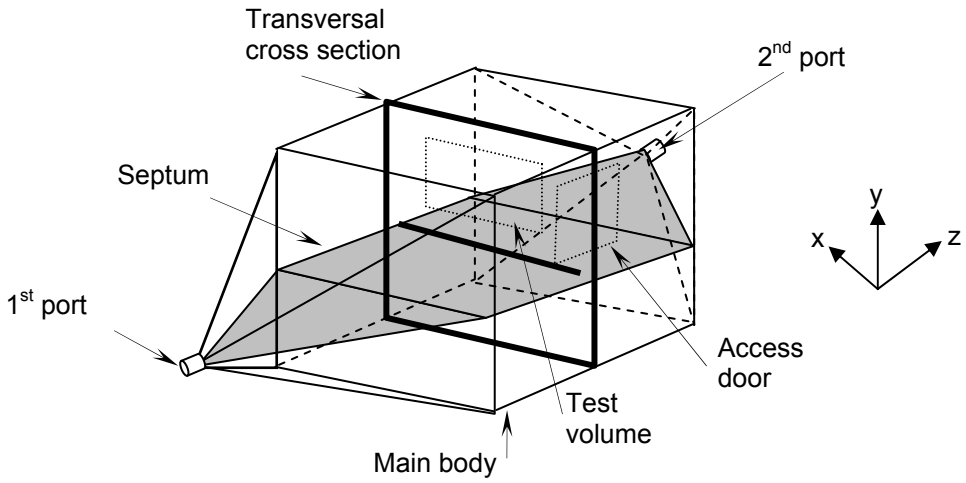

Figure 1.4 Major parts of a TEM cell

The polarization of the fundamental TEM mode is fixed with respect to the cell geometry. This feature is convenient for small dipole antenna calibrations where the antenna can be carefully aligned with the known electric field direction. Other advantages of a TEM cell are that the test environment is shielded from ambient RF noises. It is a cost effective pre-compliance test environment as compare to the FAR and SAR. The use of a TEM cell is limited by the highest frequency that the cell can operate. Above this frequency, higher order modes (other than the TEM mode) start to appear. The appearance of the higher order modes depends on the size of the TEM cell. The appearance of these higher order modes (shown in Figure 1.5) is also caused by the transition between the tapered region and the parallel middle section.

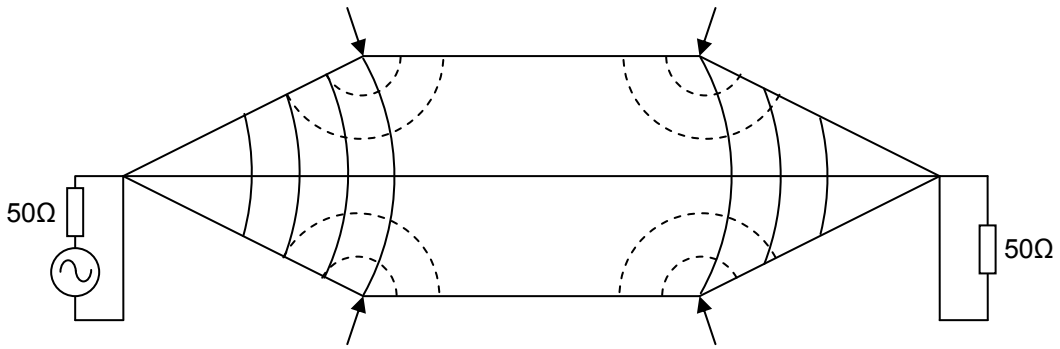

Figure 1.5 Propagation of waves in a TEM cell. Dotted lines show the appearance of the higher order modes and the arrows show the locations where higher order modes are excited

To improve on this design, a single port TEM cell was developed. The single port TEM cell, known as the Gigahertz Transverse Electromagnetic cell (GTEM), is an important addition into the world of EMC testing. The GTEM cell was introduced about two decades ago by Konigstein and Hansen [7]. Since then, many names have been given to the GTEM cell. Among them are tapered TEM, broadband TEM, rectangular coaxial cone line with an offset inner conductor (RCCTLO) and so on. All these names refer to the same GTEM cell. A typical GTEM cell is shown in Figure 1.6. A GTEM cell consists of five major parts. These are (1) the four sides of triangular shaped walls and the rectangular back wall, (2) the 50 Ω port, (3) pyramid shaped radio absorbing material (RAM), (4) internal triangular shaped septum and (5) 50 Ω resistive termination. The GTEM cell was not invented from scratch but rather as an improved version of the TEM cell. The creation of the GTEM cell is intended to extend the usable upper frequency limit beyond the value set by the existence of higher order modes in the traditional TEM cell. The GTEM cell is constructed so that it has only the flared section of the TEM cell thus eliminating the transition between the tapered region and the parallel plate of a TEM cell. This is shown in Figure 1.7.

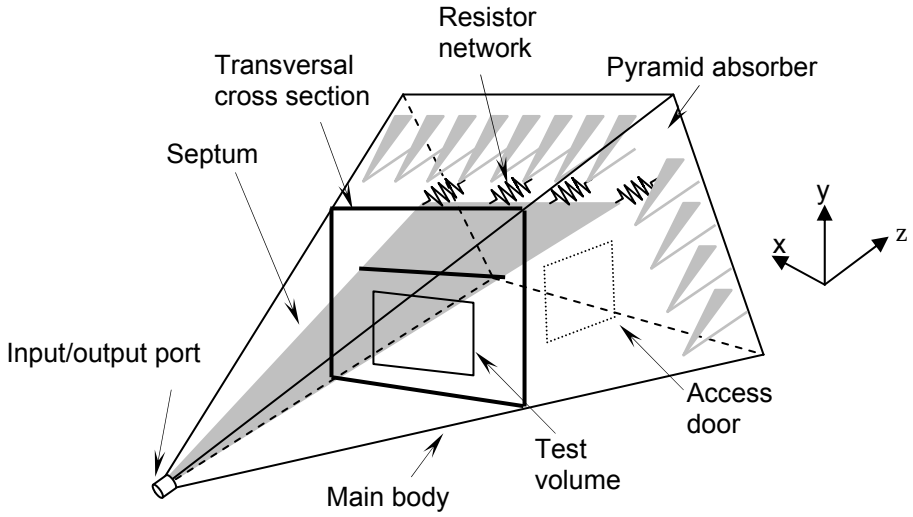

Figure 1.6 Major parts of a GTEM cell

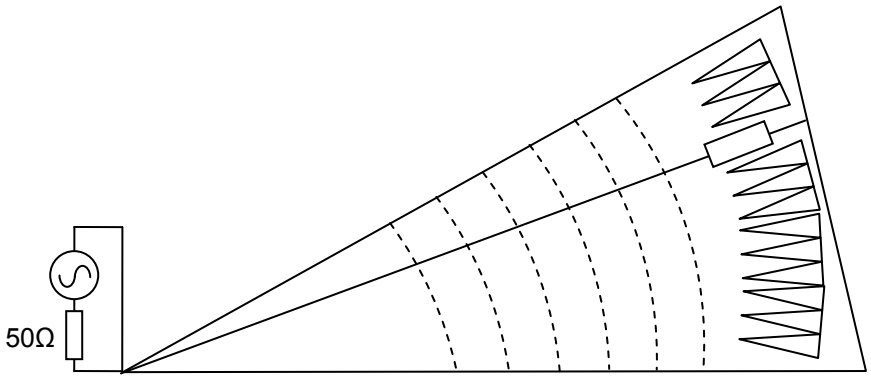

Figure 1.7 Dotted lines show propagation of wave in GTEM cell

To realise a single port cell, a termination is required to replace the second port of the TEM cell. The inner conductor or the septum is terminated by a number of resistors combining up to a total of 50 Ω functioning as a termination for the lower frequency components. Broadband pyramidal RAMs are also placed at this end section of the cell acting as termination for higher frequency components.

A GTEM cell model 5407 manufactured by ETS Lindgren [8] is shown in Figure 1.8. This GTEM cell will be the subject of the study in this Thesis. All experimental work was carried out in this cell and all simulation work was based on the physical dimensions of this cell. The physical and electrical characteristics of the GTEM 5407 are given in the following sections.

In this Thesis, both the experimental and simulation work were involved. Thus, in order to differentiate the terms used in the experiments and simulations and to prevent confusion, it is convenient to define the term 'GTEM *cell*' for the experimental work in the GTEM cell and the term 'GTEM *model*' for the simulation work. The following sections present some comparisons between the GTEM and TEM cells.

Figure 1.8 A GTEM 5407 Series

1.3 Comparison between TEM and GTEM cells

1.3.1 Physical comparison

A TEM cell is a waveguide with symmetric physical properties. It has two tapered regions from the two ports. A rectangular region then joins the two tapered regions forming the entire cell. Hence, the major parts of a TEM cell are the main rectangular body, the septum and the two ports.

In contrast to a TEM cell, a GTEM cell has an asymmetrical physical property. The two main physical differences between a GTEM cell and a TEM cell are that a GTEM cell has only one port and one tapered region. The second port that is available in a TEM cell is terminated electrically with a resistor network and RAM in a GTEM cell. This is further explained in the next section under electrical properties. The physical dimension of a GTEM 5407 is shown in Figure 1.9. These are also the sizes used in the GTEM model.

In a GTEM cell, the EUT is normally placed below the offset septum within the cross section of the GTEM cell. In contrast, the EUT can be placed either on top or below the centrally located septum in a TEM cell. The working volumes of both cells are defined as a third of the volume contained below the septum within the cross section of the cells.

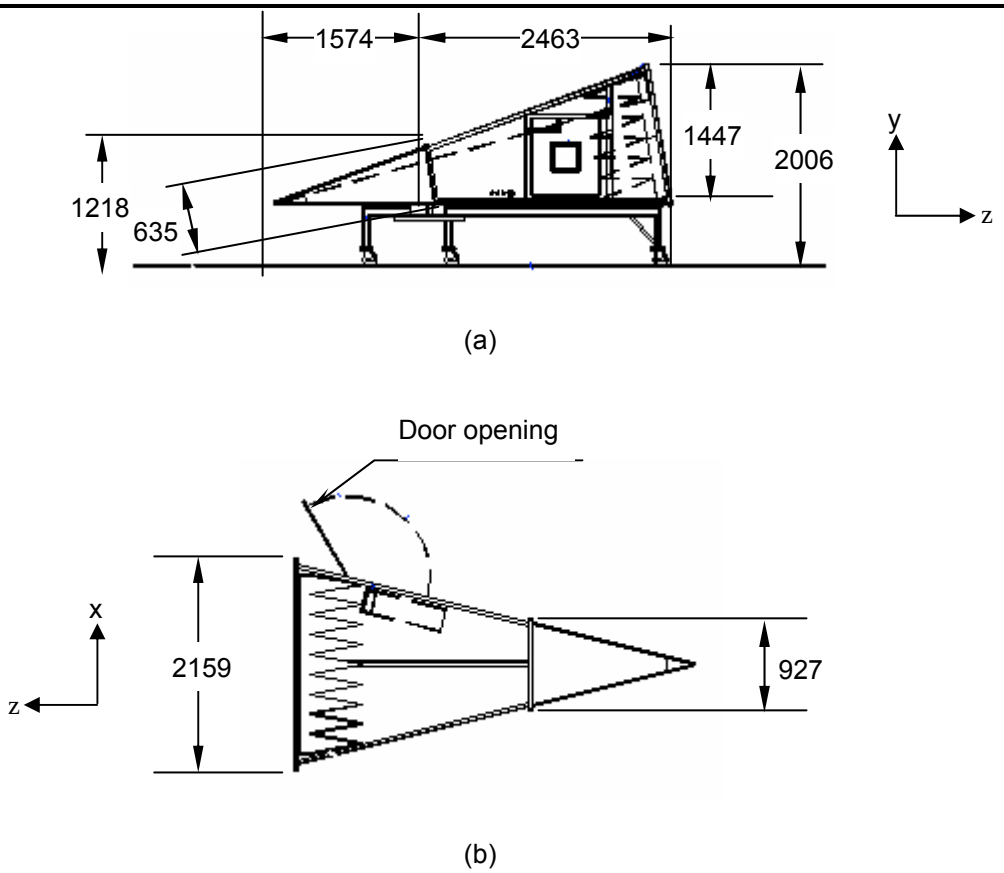

Figure 1.9 Physical dimensions of a GTEM 5407, (a) side view and (b) top view. Picture adapted from [8]. All dimensions are in mm.

1.3.2 Electrical comparison

TEM and GTEM cells are designed to produce a 50 Ω transmission line characteristic impedance. The ports have 50 Ω connectors which are linked to the body of the cells which also have 50 Ω characteristic impedance. The inner conductor or the septum is positioned relative to the upper and lower wall of a TEM cell as to achieve a 50 Ω characteristic impedance. In contrast to a TEM cell, a GTEM cell has a pyramidal structure with increasing cross

section away from the port. The septum position also produces a 50 Ω characteristic impedance but the asymmetry ensures that the EUT minimally disturbs this impedance. This is because there is no transition between the tapered region and the parallel region as in a TEM cell, where the higher order modes are excited. Icheln [9] in his Thesis describes how the characteristic impedance of a GTEM cell can be obtained numerically.

Since a GTEM cell has no second port, the electromagnetic field components that are transverse to the direction of propagation along the cell have to be terminated to prevent reflections. Higher frequency components are terminated using the RAM while lower frequency components are terminated through the 50 Ω resistive networks. The absence of the second port in a GTEM cell along with the asymmetric structure has brought advantages. It makes it possible to perform measurements at frequencies much higher than in a TEM cell (GHz in comparison to a few hundred MHz in a similar size TEM cell). This is because the usable upper frequency of a TEM cell is determined by the lowest cut off frequency of the first higher order mode which is affected by the cross section of the cell. According to Crawford [6], the TE_{10} cut off frequency $f_{c,10}$ is given by:

$$f_{c,10} = \frac{c}{2W} \tag{1.1}$$

where c is the speed of light and W is the width of the TEM cell.

1.4 Review of the measurement methods using the GTEM cell

A GTEM cell is mainly used for EMC testing. In recent years, a number of methods have been presented in an effort to improve the performance and accuracy of the measurements made using a GTEM cell. These are mostly to obtain better accuracy on the total radiated power from an EUT. These methods also include correlation to measurements performed in an OATS. A good summary on the measurement methods that are currently available was presented by Harrington [10]. A few of these methods are discussed in this Thesis.

The electric and magnetic dipole moments calculation is the main method that is used by most algorithms to obtain the total power radiated by an EUT. This method was first used in measurements in a TEM cell. Since a GTEM cell is similar to the TEM cell in terms of the electrical properties, the dipole moments method was then modified for the use in a GTEM cell.

There are many GTEM cell to OATS correlation algorithms to date. Each of the proposed correlation algorithms has its own requirements on the number of EUT orientations and the corresponding numerical calculations. The correlation algorithm introduced by Wilson [11] has 3, 6 or 9 EUT orientations depending on *a priori* knowledge of the EUT and also based on the existence of degeneracy in the initial measurement results. Higher number of EUT orientations (9 orientations) is required for EUTs that exhibit degeneracy in the initial measurements. Carbonini [12] introduced a

correlation algorithm that requires seven EUT orientations which involved rotating an EUT by ±45^{o} along the coordinate axes. Smaller rotation angles are better for some EUTs that are difficult to rotate and EUTs that have many connecting cables. Lee [13] introduced a method that requires 15 EUT orientations. This method considers the phase difference between dipole moments by extracting the phase information from the power measurements of the fifteen EUT orientations. All the correlation methods mentioned above measure the voltage at the GTEM cell port from each of the EUT orientations to calculate the free space total radiated power. The first step, that is to obtain the total radiated power in free space, is important because the accuracy of this value determines the accuracy of later correlation to OATS.

A method to determine the total power radiated by an EUT in free space using a TEM cell was introduced by Ma [14] . It is not a GTEM cell to OATS correlation algorithm but rather a method to obtain total power radiated by an EUT in free space that involves phase measurements. The phase measurement is related to the phase difference between the dipoles moments of an EUT. This method cannot be easily adopted for use in a GTEM cell because a GTEM cell has only one port. The method introduced by Wilson is currently in use in the IEC 61000-4-20 [15]. This will be further discussed in the following section. Some authors encountered problems with the methods mentioned above and have made some improvement to the correlation algorithms. Further details may be found in Heidemann and Garbe [16, 17] and Berger [18].

1.5 The technique used in the IEC 61000-4-20

The correlation method used in IEC 61000-4-20 [15] is of prime interest in this study because this method is standardized and governs the rules and methodology in GTEM cell measurement worldwide. Thus, its accuracy is crucially important. The GTEM cell to OATS correlation technique used in [15] is actually adapted from the method reported by Wilson in [11] and [19]. There are two methods stated in this standard; with and without correlation to the OATS. The earlier is the method by Wilson.

The method used here requires three EUT orientations. By rotating an EUT to three orthogonal orientations, three different measurements using a spectrum analyser are taken. Similar to [14], the standard adopts the dipole model where any radiation source of a finite size may be represented by an equivalent dipole. Using the three measured values, the total radiated power is then calculated. A normalized vertical electric field is involved in this calculation. Hence, a measured or calculated value of this normalized vertical electric field is required in the correlation calculations.

From the calculated value of the total radiated power, the correlation to the OATS method can then be obtained. An objective of this work is to investigate the accuracy of the first set of calculations, that is, the total radiated power calculation. This value needs to be accurate for the following OATS correlation to be accurate. However, in order to apply this method, two major assumptions have to be made. The first is to assume that an EUT is

electrically small; that is less than 0.1 times the wavelength. The second is to assume that the EUT's dipole moments are all in phase. Another assumption is that the gain of an EUT radiating elements would not exceed that of a dipole antenna. Osburn and Bronaugh [20] claim that the current GTEM cell to OATS correlation algorithms are not fit for EUTs that exhibit frequencies greater than one GHz and the assumption that the gain of an EUT radiating elements will not exceed that of a dipole antenna is not sound [21, 22].

In the following sections, the problems arising from making these assumptions in [15] are summarized. Also, the number of orientations required for the testing in a GTEM cell according to [15] is explained.

1.6 The assumption of negligible phase difference between dipole moments

Most of the previous work on calculating total radiated power from an EUT does not take account of phase, but is based only on the magnitude of the power emitted. Authors such as [11] have introduced some measurement methods that do not require the phase. This is based on the assumption that the dipole moments are all in phase if: (1) The EUT is electrically small in comparison to the wavelength and (2) There is only one single dominant radiating source. By making these assumptions, the measurements are made easier because the mathematical algorithm is much simpler, the number of

EUT orientations during measurements is reduced and most importantly, measurements can be done simply using a GTEM cell.

It is found in this Thesis that, both assumptions do not hold fully in many of today's applications. The first assumption is difficult to justify in present day electrical appliances where an EUT is electrically large due to the use of frequencies beyond the GHz region. The second assumption may be true in some circumstances. However, the information on the number of radiators inside an EUT is not easily available.

It is very difficult to meet the assumption requirements mentioned above in current EMC tests. A *priori* knowledge has to be available to determine if an EUT is suitable to be tested using a GTEM cell. In addition, knowledge of the number of radiators is also difficult or almost impossible to obtain. It is found that the omission of phase in the GTEM cell measurement affects measurement accuracy.

1.7 The number of EUT orientations

Of all the methods mentioned in Section 1.5, the three-orientation method is implemented in the IEC 61000-4-20. This is because the correlation algorithm performs well for frequencies less than one GHz and it has the least orientation count which eases the whole process of EMC testing in a GTEM cell. However, this method is not without some shortcomings.

Figure 1.10 shows a simple EUT consisting of a cube with six possible orientations. The measurement orientations become an issue when only three out of the six orientations are used in measurements. The measured EUT orientations are shown by the bold arrows in Figure 1.10. In this case, the emissions from the other orientations (orientations that are not selected) are missed. A missed radiation scan can arise due to the positioning of an unintentional antenna such as a printed circuit board. An unintentional radiator may have multiple radiation lobes which may not couple efficiently to the GTEM cell. This causes a problem because not all directions of the EUT are measured and consequently, the total radiated power is assessed inaccurately. To make the situation worse, time varying radiation or intermittent radiation due to the specific functions of the equipment introduces another ambiguity.

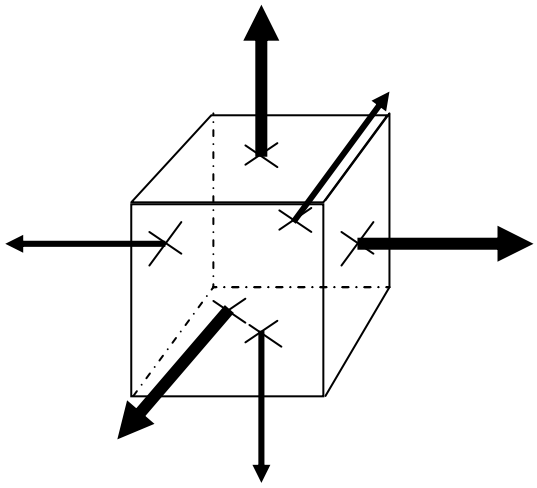

Figure 1.10 An EUT with selected measurement orientations are shown in bold arrows. Not chosen orientations are shown in thin arrows

1.8 The representation of EUT by dipole moments

This section presents a brief introduction on the representation of radiation from an EUT by equivalent dipole moments. There are many different representations of dipole moments models and each has its own number of required EUT orientations. The method according to [14] involves phase measurement and it is particularly useful for later work on the phase measurements presented in the Thesis. The following equations summarize the electric and magnetic dipole moments separation method in a TEM cell measurement based on NBS Technical Note 1059 [14]. This method will be modified and be used later for GTEM cell phase measurements.

A: Separation between electric and magnetic dipole moment

The two ports of the TEM cell are termed as first and second ports. The vector electric field appearing at the first port is:

$$\overline{E}^{(+)} = \sum_n a_n \overline{E}_n^{(+)} \tag{1.1}$$

where $\overline{E}_n^{(+)}$ is the *n*th electric mode propagating from the first port and a_n is the mode amplitude. The vector electric field appearing at the second port is:

$$\overline{E}^{(-)} = \sum_n b_n \overline{E}_n^{(-)} \tag{1.2}$$

where $\overline{E}_n^{(-)}$ is the *n*th electric mode propagating from the second port and b_n is the mode amplitude. The vector magnetic field appearing at the first port is:

$$\overline{H}^{(+)} = \sum_n a_n \overline{H}_n^{(+)} \tag{1.3}$$

where $\overline{H}_n^{(+)}$ is the *n*th magnetic mode propagating from the first port and a_n is the mode amplitude. The vector magnetic field appearing at the second port is:

$$\overline{H}^{(-)} = \sum_n b_n \overline{H}_n^{(-)} \tag{1.4}$$

where $\overline{H}_n^{(-)}$ is the *n*th magnetic mode propagating from the second port and b_n is the mode amplitude. When the source is a short infinitesimally thin current filament with an electric dipole moment $\overline{m_e}$, then

$$a_o = b_o = -\frac{1}{2}\overline{m}_e \cdot \overline{e}_{oy} \tag{1.5}$$

where

$$\overline{m_e} = J\,\overline{d\ell} \tag{1.6}$$

J = normalized filament current

$\overline{d\ell}$ = directed length vector of the short dipole

$\overline{e_{oy}}$ = normalized y component of the electric field

When the source is a small current loop with a magnetic dipole moment $\overline{m_m}$, then:

$$a_o = -b_o = -\frac{1}{2} j k \left(\overline{m}_m \times \bar{z}\right) \cdot \bar{e}_{oy} \tag{1.7}$$

where

$$\overline{m_m} = J' \overline{ds} \tag{1.8}$$

J' = normalized loop current

$\overline{ds}$ = vector loop area

$\overline{e_{oy}}$ = normalized y component of the electric field

The e_{oy} is the normalized y component of the electric field of the TEM mode at a particular test location. The term 'normalized' here refers to the electric field generated per 1 W input power. Combining both small electric and magnetic dipoles, the principle of superposition gives,

$$a_o = -\frac{1}{2}\left(\overline{m}_e + j k \overline{M}\right) \cdot \bar{e}_{oy} \tag{1.9}$$

and

$$b_o = -\frac{1}{2}\left(\overline{m}_e - j k \overline{M}\right) \cdot \bar{e}_{oy} \tag{1.10}$$

where

$$\overline{M} = \overline{m}_m \times \bar{z} \tag{1.11}$$

The sum power is:

$$P_s = \left| a_o + b_o \right|^2 = \left| \overline{m}_e \cdot \bar{e}_{oy} \right|^2 \tag{1.12}$$

The difference power is:

$$P_d = \left| a_o - b_o \right|^2 = k^2 \left| \overline{M} \cdot \bar{e}_{oy} \right|^2 \quad (1.13)$$

The sum of power (P_s) depends only on the electric dipole moment while the difference of power (P_d) depends only on the magnetic dipole moment. These equations do not apply directly to the single port GTEM cell.

B: The purpose of power sum and difference

The expansion coefficients a_o and b_o, for the TEM mode, n = 0 are given by Equation (1.9) and (1.10). From Equation (1.12) and (1.13), $\overline{m}_m$ and $\overline{m}_e$ can be distinguished by taking the power sum from six EUT positions (P_{s1} to P_{s6}) and the power difference (P_{d1} to P_{d6}) according to [14]. The following relation can be used to determine the electric and magnetic dipole.

$$\begin{pmatrix} m_{ex}^2 \\ m_{ey}^2 \\ m_{ex}^2 \end{pmatrix} = [C][P_s] / 2\left(p^2 + q^2\right) \quad (1.14)$$

$$\begin{pmatrix} m_{mx}^2 \\ m_{my}^2 \\ m_{mx}^2 \end{pmatrix} = [C][P_d] / 2k^2\left(p^2 + q^2\right) \quad (1.15)$$

where

$$[C] = \begin{pmatrix} 1 & 1 & -1 & -1 & 1 & 1 \\ 1 & 1 & 1 & 1 & -1 & -1 \\ -1 & -1 & 1 & 1 & 1 & 1 \end{pmatrix} \tag{1.16}$$

$$[P_s] = \begin{pmatrix} P_{s1} \\ P_{s2} \\ P_{s3} \\ P_{s4} \\ P_{s5} \\ P_{s6} \end{pmatrix} \tag{1.17}$$

$$[P_d] = \begin{pmatrix} P_{d2} \\ P_{d1} \\ P_{d4} \\ P_{d3} \\ P_{d6} \\ P_{d5} \end{pmatrix} \tag{1.18}$$

To distinguish between the electric and magnetic dipole moments, equations (1.19) and (1.20) are used.

$$\begin{pmatrix} m_{ex}\, m_{ey} \cos(\psi_{ex} - \psi_{ey}) \\ m_{ey}\, m_{ez} \cos(\psi_{ey} - \psi_{ez}) \\ m_{ez}\, m_{ex} \cos(\psi_{ez} - \psi_{ex}) \end{pmatrix} = [D][P_s] / 2(q^2 - p^2) \tag{1.19}$$

$$\begin{pmatrix} m_{mx}\, m_{my} \cos(\psi_{mx} - \psi_{my}) \\ m_{my}\, m_{mz} \cos(\psi_{my} - \psi_{mz}) \\ m_{mz}\, m_{mx} \cos(\psi_{mz} - \psi_{mx}) \end{pmatrix} = [D][P_d] / 2k^2(q^2 - p^2) \tag{1.20}$$

where

$$[D] = \begin{pmatrix} 1 & -1 & f & f & -f & -f \\ -f & -f & 1 & -1 & f & f \\ f & -1f & -f & -f & 1 & -1 \end{pmatrix} \tag{1.21}$$

$$f = \frac{2pq}{(P^2 + q^2)} \tag{1.22}$$

ψ_e and ψ_m are phases that correspond to the electric dipole and magnetic dipole moments respectively.

Once the sum and difference of powers are calculated, the components of electric and magnetic dipole moments can then be calculated. With this information, further calculations can be done to calculate the electric and magnetic dipole moments for an EUT that consists of both electric and magnetic sources.

1.9 Phase and its measurement in a GTEM cell

Two important issues were investigated in this Thesis. These issues are (1) the assumption of no phase difference and (2) the phase measurement in a GTEM cell. From Section 1.6, it is known that an assumption that there is no phase difference between dipole moments is made for GTEM cell measurement. This assumption is because there is no significant phase difference if an EUT is electrically small and has only one dominant single radiator. An initial hypothesis is to assume that some phase difference between dipole moments still exists even for a EUT that meets the criteria mentioned above. Further and thorough investigations related to the phase assumption are presented in Chapter 4.

If there is a possibility to obtain phase information by measurement using a GTEM cell, the algorithm in [14] can be used to calculate total

radiated power. The GTEM cell has only one port and it is generally assumed to be impossible to perform a phase measurement. However, by investigating the similarity of a GTEM cell with a TEM cell, a solution to this difficulty can be found. Though, the GTEM and TEM cells do not look exactly the same physically, they do share some electrical similarities. The idea of the method is to reproduce the second port measurement by rotating the EUT by 180^o in the y axis. By taking the two separate measurement readings (0^o and 180^o), it is hoped that the phase information can be obtained. To make this method realizable, a new experimental setup in the GTEM cell is required.

A spectrum analyser can be used to measure power or voltage readings from a GTEM cell. However, a spectrum analyser is not able to perform more sophisticated measurements such as the phase measurement as it can only perform magnitude readings. The spectrum analyser was replaced with a vector network analyser (VNA) as this instrument can perform phase and magnitude measurements simultaneously. A measurement configuration has to be designed to obtain phase information. Once these requirements are met, then the measurement method according to [14] can be performed using the GTEM cell. This will be outlined in Chapter 5 under 'The Phase Measurement Method'.

1.10 The Transmission Line Model (TLM)

TLM is the primary method used in the simulations discussed in this Thesis. This simulation technique method is fully described in [23]. Recent developments have been led by The George Green Institute for Electromagnetics Research (GGIEMR) headed by Professor Christopoulos. This method is then incorporated into codes by Paul [24] forming a solver called ‘regSolve’.

In recent years, various numerical methods have been used to model the GTEM cell in an effort to know more about its electrical characteristics such as the field distributions and characteristic impedance. By studying the behaviour of a GTEM cell numerically, one can better understand the experimental results obtained from a GTEM cell. Numerical models that use Finite Difference Time Domain (FDTD), Finite Element Method (FEM) and Method of Moments (MoM) have been successfully applied to GTEM studies [25-31]. In this thesis, the TLM method will be used to model the GTEM cell. The reason is because the TLM code is readily available at the of this work. The GTEM cell was carefully modelled so that it can represent the actual GTEM cell geometry with acceptable accuracy.

In the following section, preliminary simulation and experimental work was done to support the hypothesis of this work that is to investigate the validity of the assumption of no phase difference between dipole moments of an EUT.

1.11 A TEM cell simulation to verify the hypothesis

In order to assess the impact of phase, TEM cell simulations using TLM were performed. The TEM model was excited by placing a dipole antenna and a magnetic loop in the centre of the cell. These antennas were excited with 200 MHz sinusoids at 1 V. Two simulated voltage outputs were taken at the first and second ports of the cell respectively. These are the voltages induced between the septum and the body of the cell. The phases of the voltages obtained at the first and second ports were compared. Any phase differences would be obvious from these results. The phase differences for all three orientations were then compared to observe any phase change between orientations. The purpose of this simulation is to examine the phase difference between each of the electric dipole moments and between each of the magnetic dipole moments.

In Figure 1.11, a dipole antenna that was aligned vertically results in a same phase voltage output at the two ends as expected since the field is propagating uniformly towards both ends. This position results in the best coupling since the dominant electric field from the dipole was aligned parallel to the vertical y electric field in the TEM model. There is no phase difference observed in this orientation (shown in Figure 1.12) because the dipole appears symmetrical to both the ports of the TEM model. To explain this in a circuit analogy, a dipole is seen as a voltage source *V* connected in parallel

with two resistors Z_A and Z_B shown in Figure 1.13. Thus, the voltages across the resistors, V_{ZA} and V_{ZB} are equal.

A horizontally aligned antenna shown in Figure 1.14 resulted in negligible voltages (Figure 1.15). This is as expected because this position gives the worst coupling position of dipole electric field relative to the vertical y fundamental mode electric field in the TEM model. The phase difference cannot be observed in this orientation since the simulated signal is very low.

In Figure 1.16, the dipole was aligned to the longitudinal direction of the TEM model. In this orientation, the voltage readings at the ends are about 180^o out of phase as shown in Figure 1.17. The circuit analogy shown in Figure 1.18 shows the phase of the voltage across the resistor V_{ZA} differs by 180^o with respect to the voltage across the resistor V_{ZB}. The coupling at this position is small but not as small as for the horizontal position.

In Figure 1.19, a magnetic loop was orientated where the direction normal to the area of the loop was facing the openings of the TEM model. A zero phase difference was observed between the voltage readings of the first and second ports. Similar to the explanation for the dipole in the first orientation, there was no phase difference observed in this orientation (shown in Figure 1.20) because the magnetic loop appears symmetrical to both the ports of the TEM model. In addition, significant voltages obtained from this orientation in the TEM model suggests that the magnetic loop has other field components such as the vertical electric field (behaving like a dipole) that would couple to the TEM even though the dominant magnetic field was not

aligned to the horizontal magnetic field of the TEM model. The horizontal magnetic field of the TEM model is the direction of the magnetic component of the TEM mode thus it is the direction where the magnetic field couples efficiently in TEM model.

In Figure 1.21, the magnetic loop was orientated where the direction normal to the area of the loop was facing the top or bottom of the TEM model. In this orientation, the dominant magnetic field from the loop is directed to the vertical axis thus it would not couple efficiently into the TEM model. The existence of other field components such as the electric field as suggested in the previous paragraph does not couple easily in this orientation thus resulting in noise at the ports of the TEM model shown in Figure 1.22.

In Figure 1.23, the magnetic loop was orientated where the direction normal to the area of the loop was facing the horizontal direction of the TEM model. The direction of the dominant magnetic field from the loop is now in the same direction as the horizontal axis of the TEM model thus it would couple efficiently into the TEM model resulting in the highest voltage (shown in Figure 1.24) obtained from all three orientations.

The phase difference behaviour in Figure 1.20 and 1.24 can be explained using a circuit analogy by representing the magnetic loop by an equivalent current source, *C*. The orientation of the magnetic loop as shown in Figure 1.19 is represented in a circuit shown in Figure 1.25 where the current source is parallel to the two load resistors. The current source was positioned this way to represent the direction of the dominant magnetic field generated

by the loop. These load resistors will experience equal magnitude and phase from the current source thus explaining the same phase behaviour.

In Figure 1.23, the orientation of the magnetic loop is represented by a current source positioned in series with the two load resistors as shown in Figure 1.26. The load resistors are experiencing an 180^{o} phase shift relative to each other due to the polarity of the current source.

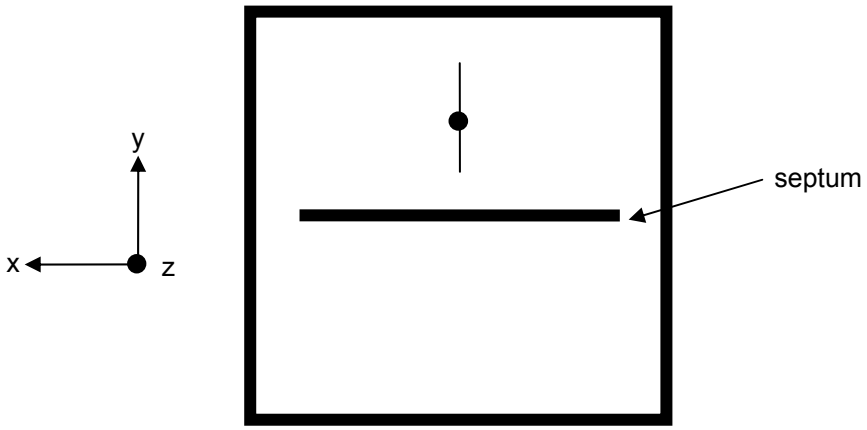

Figure 1.11 Electric dipole 1st orientation (View from the xy plane)

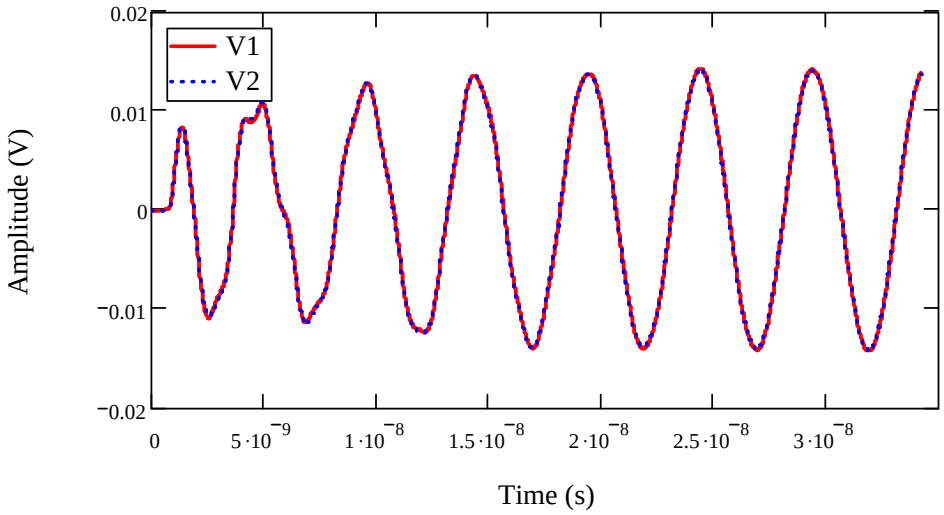

Figure 1.12 V1 and V2 are voltages (V) reading at both ends respect to time (s) for Electric dipole 1st orientation

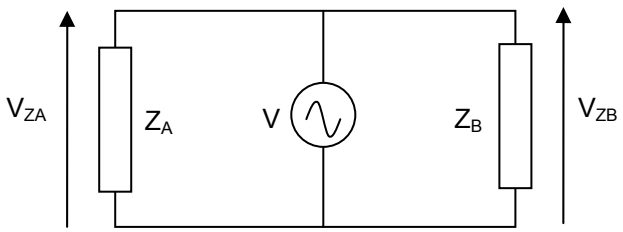

Figure 1.13 Circuit analogy explaining the zero phase shift in V_A and V_B in electric dipole 1st orientation

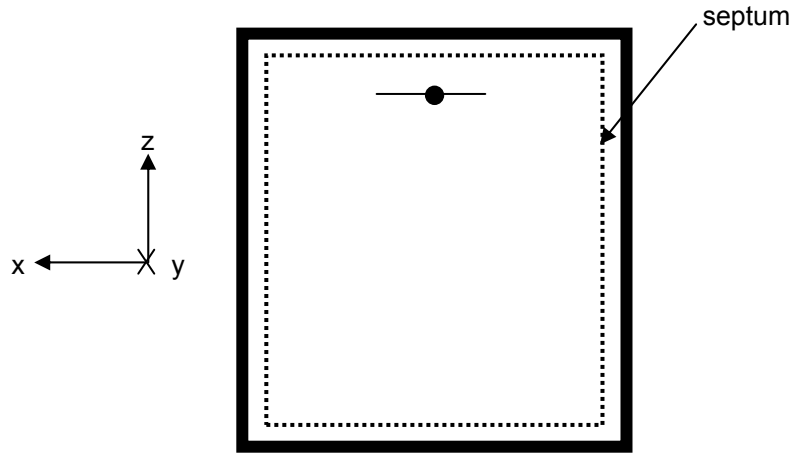

Figure 1.14 Electric dipole 2nd orientation (View from the xz plane or from the top)

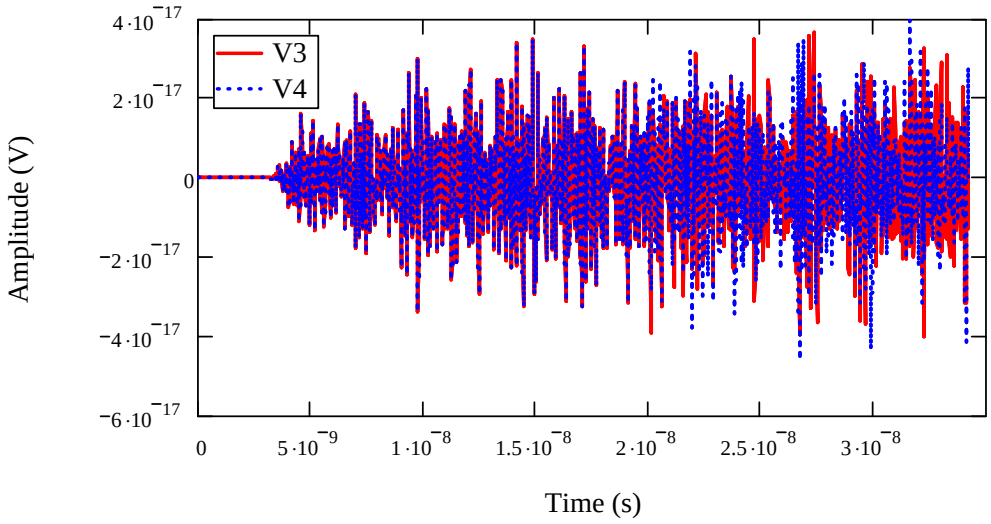

Figure 1.15 V3 and V4 are voltages (V) reading at both ends respect to time (s) for Electric dipole 2nd orientation

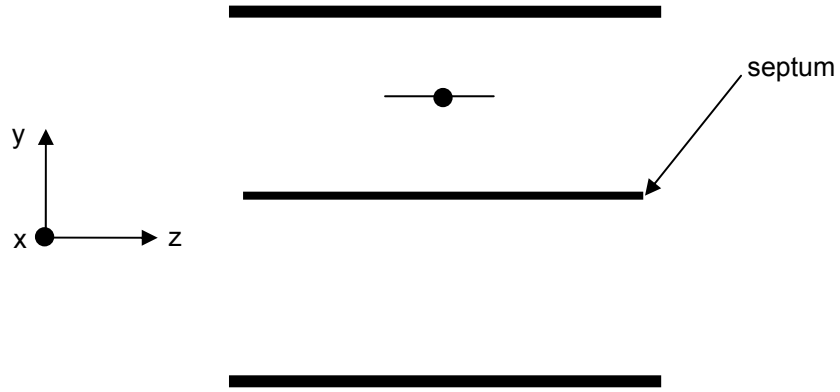

Figure 1.16 Electric dipole 3rd orientation (View from the yz plane)

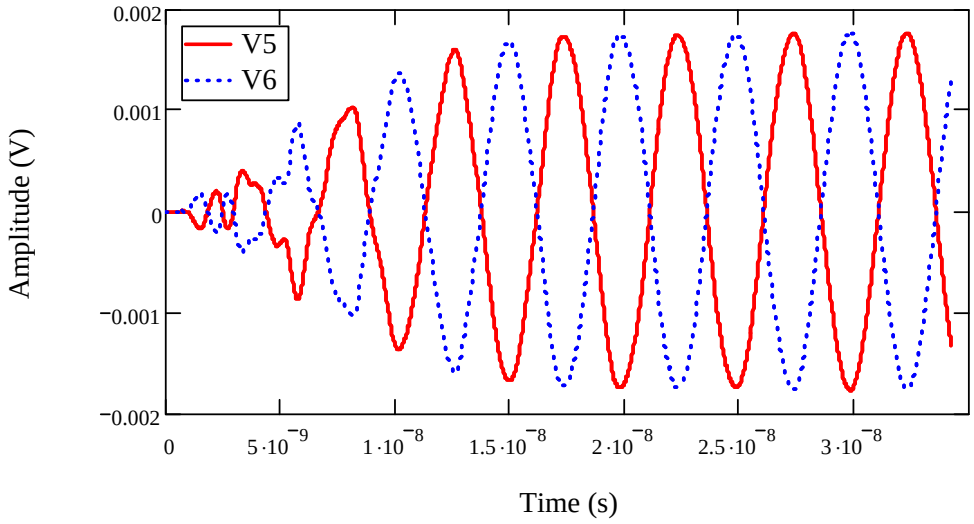

Figure 1.17 V5 and V6 are voltages (V) reading at both ends respect to time (s) for electric dipole 3rd orientation

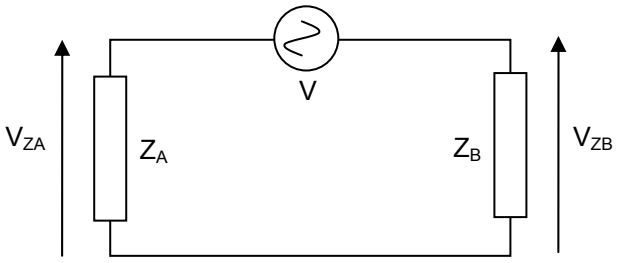

Figure 1.18 Circuit analogy explaining the 180° phase shift in V_A and V_B in electric dipole 3rd orientation

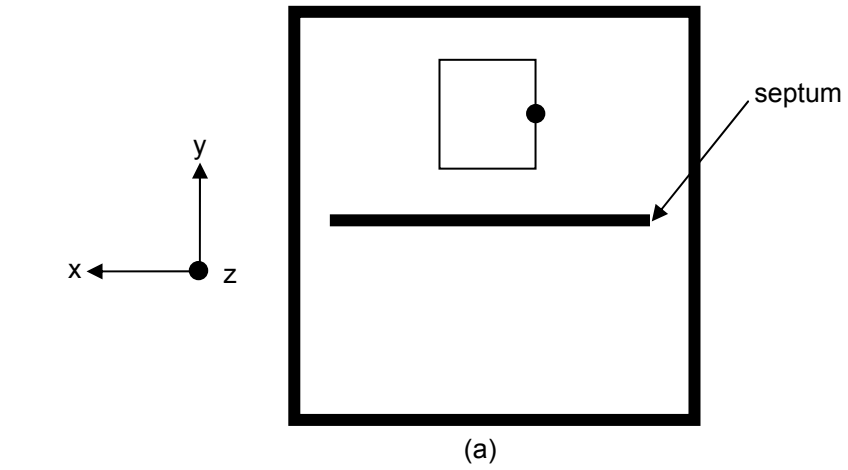

(a)

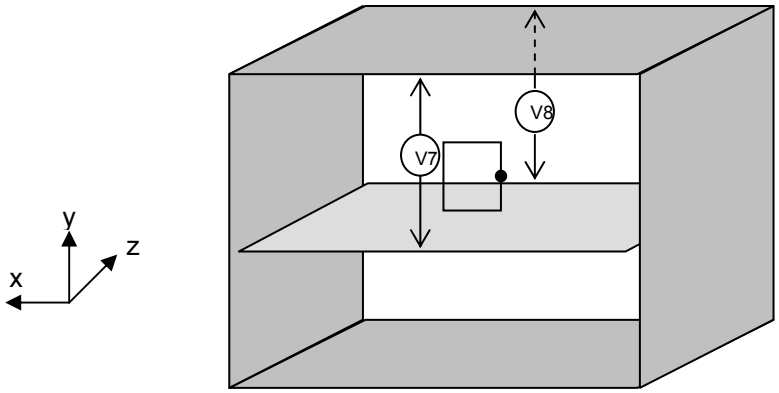

(b)

Figure 1.19 Magnetic loop 1st orientation looking in (a) the xy plane and (b) 3D view

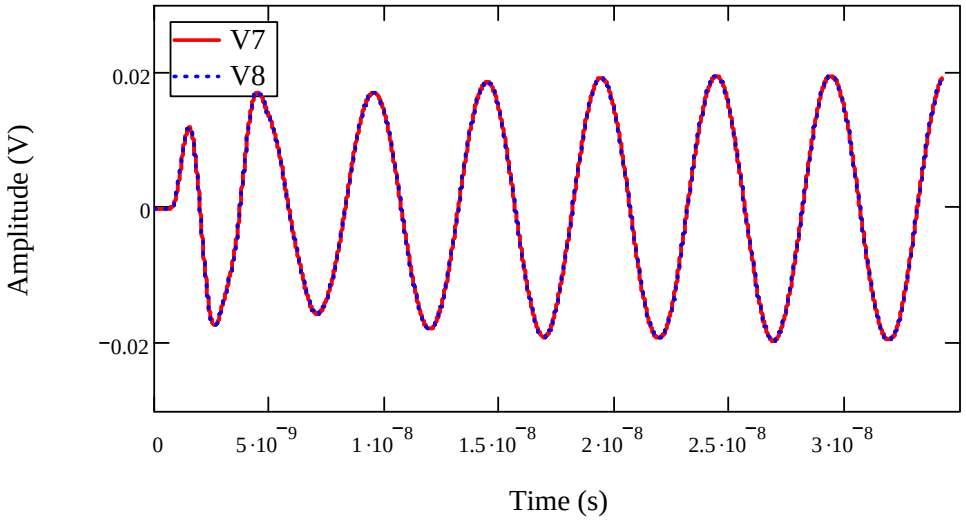

Figure 1.20 V7 and V8 are voltages (V) reading at both ends respect to time (s) for Magnetic loop 1st orientation

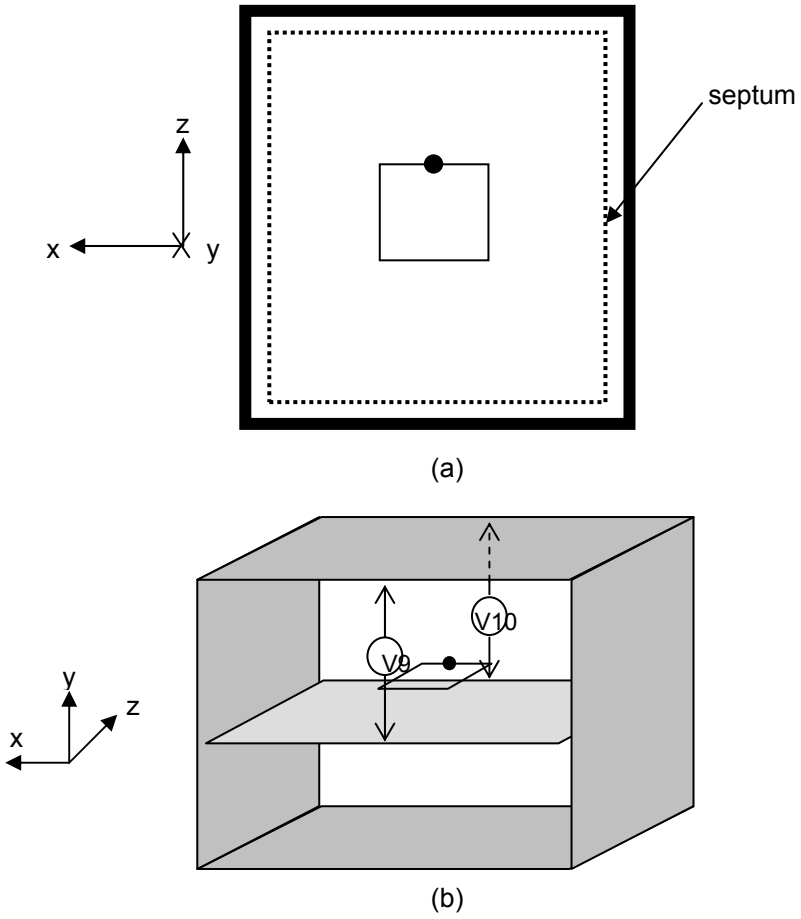

Figure 1.21 Magnetic loop 2nd orientation looking in (a) the xz plane and (b) 3D view

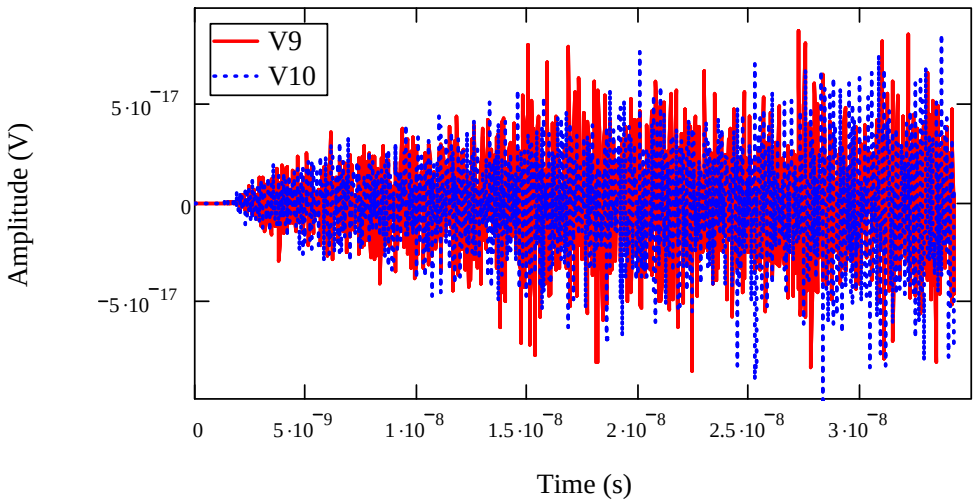

Figure 1.22 V9 and V10 are voltages (V) reading at both ends respect to time (s) for Magnetic loop 2nd orientation

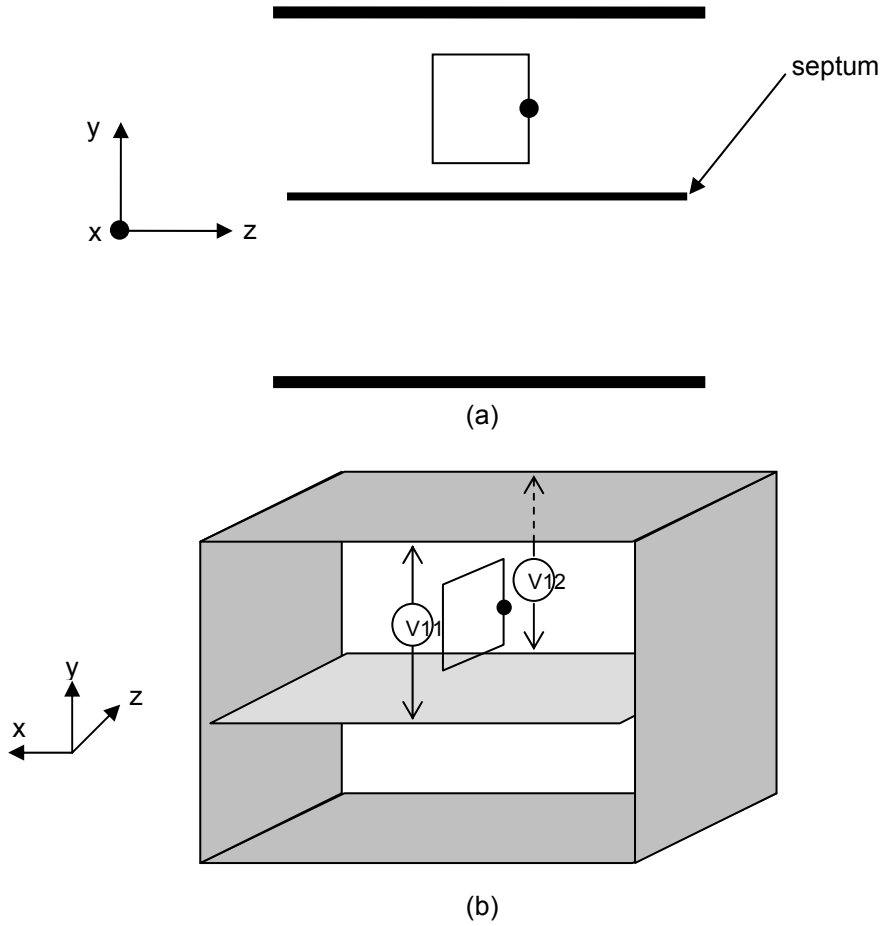

Figure 1.23 Magnetic loop 3rd orientation looking in (a) the yz plane and (b) 3D view

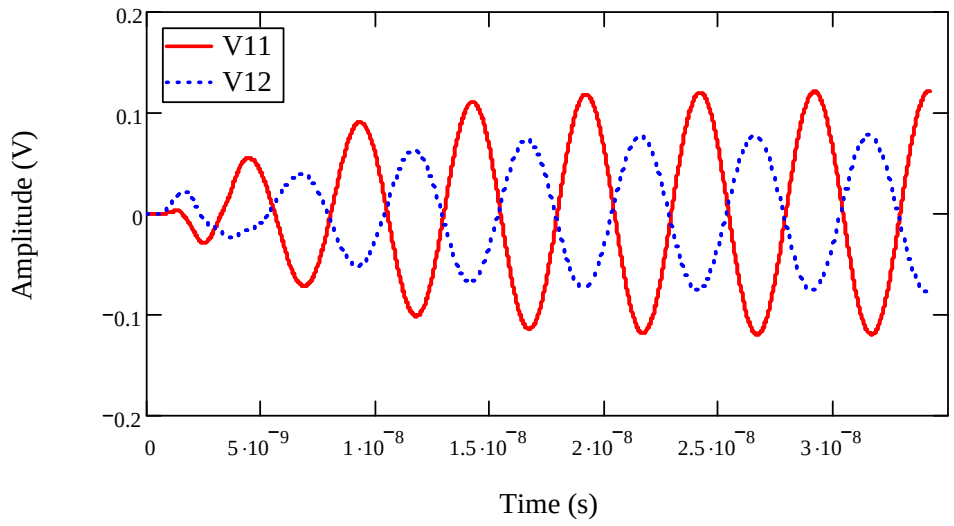

Figure 1.24 V11 and V12 are voltages (V) reading at both ends respect to time (s) for Magnetic loop 3rd orientation

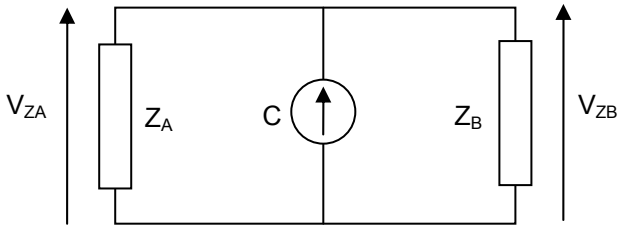

Figure 1.25 Circuit analogy explaining the zero phase shift in V_A and V_B for magnetic loop 1st orientation

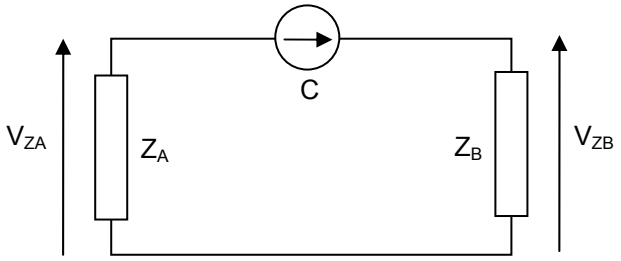

Figure 1.26 Circuit analogy explaining the 180^o phase shift in V_A and V_B in electric dipole 3rd orientation

1.12 Experimental measurements to verify the hypothesis

A simple dipole antenna was placed into a GTEM cell to represent an EUT. The dipole antenna was excited at its resonant frequency of 670 MHz. The phase differences between the signal that was fed into the EUT and the signal received from the GTEM cell port were compared for each orientation as opposed to comparing the phase between the two ends as in the TEM simulations.

The dipole was rotated in the three orthogonal orientations shown in Figure 1.27 and the phases were measured at the GTEM cell output port at each orientation. Figure 1.28 shows the phase differences for the three measured signals at the three different orientations. It is shown that the phase differences of all three orientations do not match each other. Line A intercept 670 MHz at -13^{o} shows a 13^{o} out of phase from the reference signal and same applies to line B and line C. The signals received in orientations A and B differ in phase by 34^{o} (47^{o}-13^{o}).

The differences in the phases in all three orientations are significant judging from the fact that the EUT is a single electric dipole antenna. These results together with the simulation results presented in Section 1.11 suggest that phase differences are significant and the assumption does not hold even for a simple electric dipole radiator. This conclusion supports the study to obtain phase information about an EUT from measurements performed using a GTEM cell. In the next section, a procedure to obtain the phase information

about an EUT from a GTEM cell using a modified method from [14] is explained.

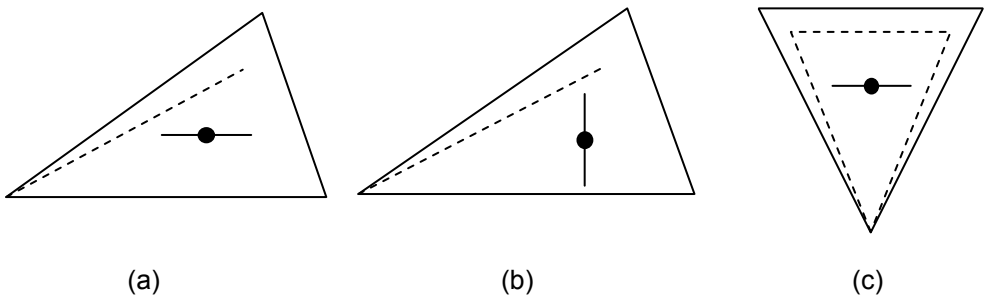

Figure 1.27 Electric dipole at (a) 1st, (b) 2nd and (c) 3rd orientation

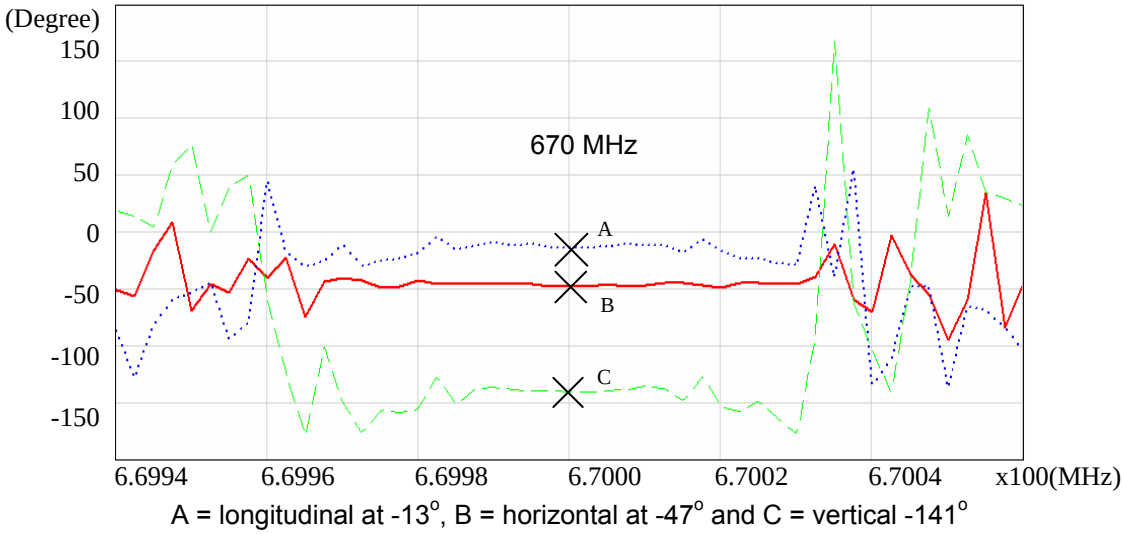

Figure 1.28 The measured phases at three different orientations of dipole antenna in the GTEM cell

1.13 The required number of orientations

To use the dipole expansion algorithm, an EUT has to be placed in certain orientations in a GTEM cell to get the phase information. The number of orientations considered in this Thesis is based on [14]. According to [14], an EUT is first arbitrary orientated. A rotation of 45^o around the z axis is required for the first phase and power measurement and then a 90^o rotation thereafter for the second phase and power measurement. While this is good for a TEM cell, it is not the same case for a GTEM cell since a second port is not available in a GTEM cell. Since a GTEM cell has similar electric properties, the second port measurement can be performed by rotating the EUT by 180^o inside the usable volume. This will result in an additional six orientations. This adds up to 12 sets of data for one EUT measurement in a GTEM cell. Figures 1.29-1.30 show the six orientations (at 0^o) of the EUT inside a GTEM cell. The basic six orientations (at 0^o) will have to be further rotated by 180^o to obtain another six EUT orientations (not shown).

In Figure 1.29, the first orientation is shown in (a). For the first measurement, the EUT has to be rotated by 45^o around the z axis shown in (b) and then another 90^o around the z axis shown in (c) for the second measurement. The same applies to the second and third orientation in Figure 1.30 – 1.31. As mentioned, an additional rotation of 180^o, which is not shown in these figures, has to be added. This is further described in detail in Chapter 5.

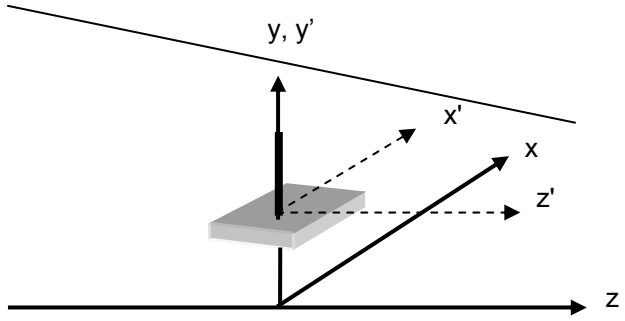

(a)

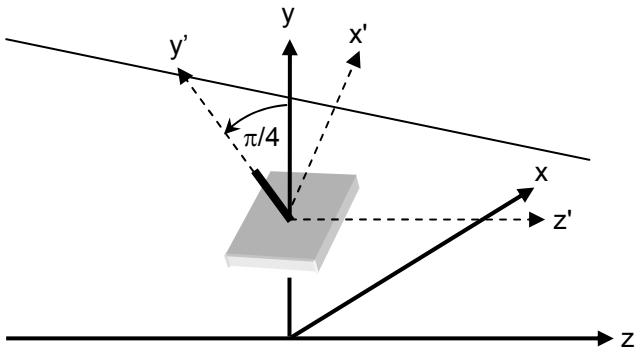

(b)

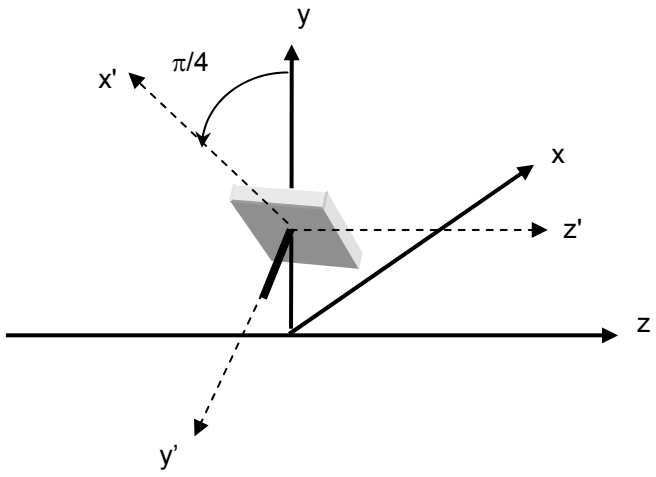

(c)

Figure 1.29 (a) The first orthogonal position, (b) first orientation after 45^{o} rotation and (c) second orientation after additional 90^{o} rotation

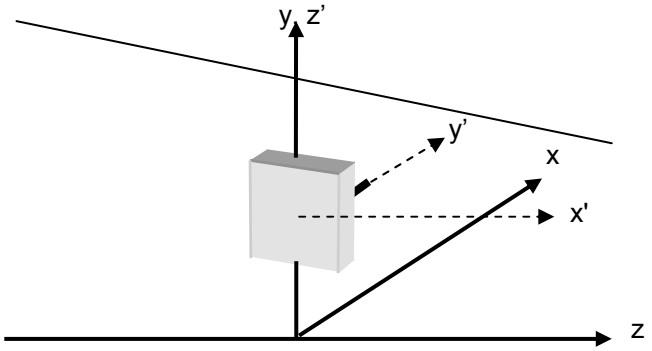

(a)

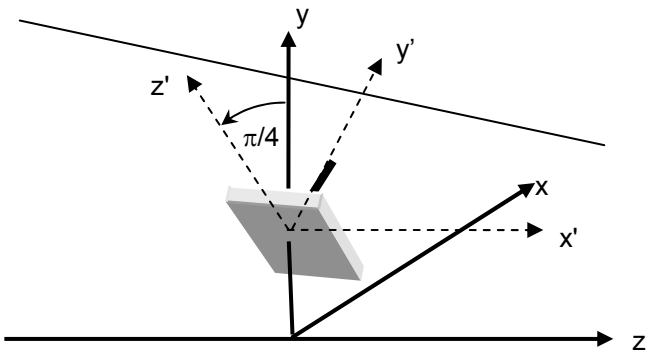

(b)

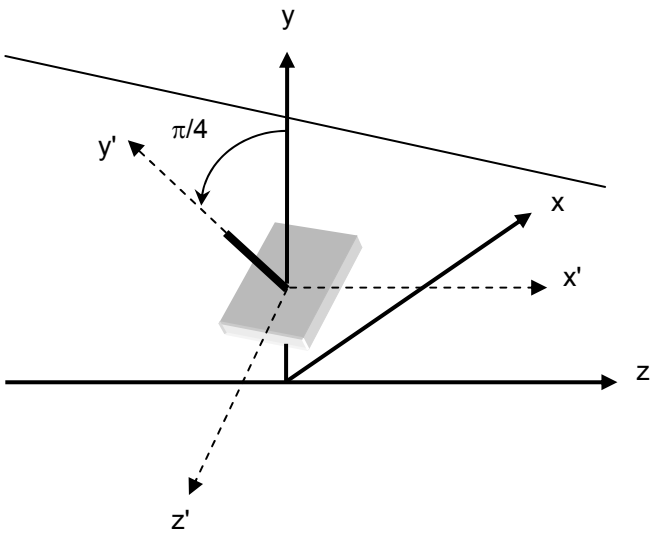

(c)

Figure 1.30 (a) The second orthogonal position, (b) third orientation after 45^{o} rotation and (c) fourth orientation after additional 90^{o} rotation

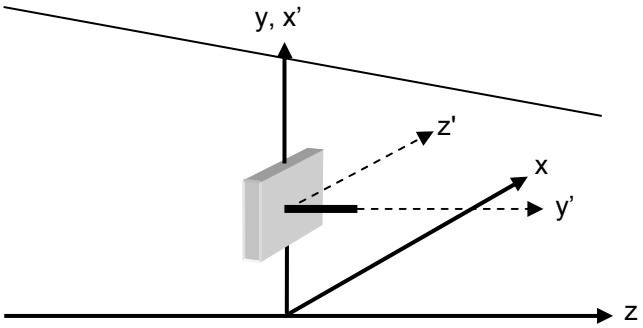

(a)

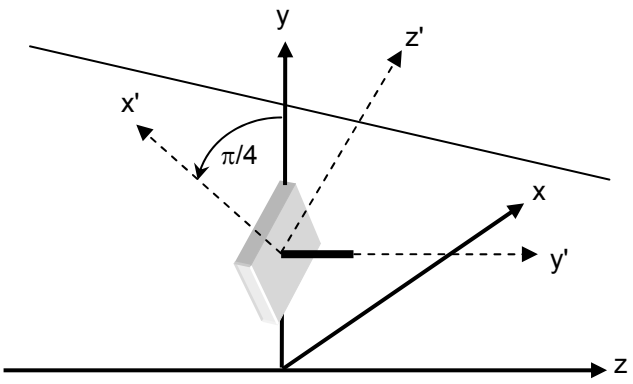

(b)

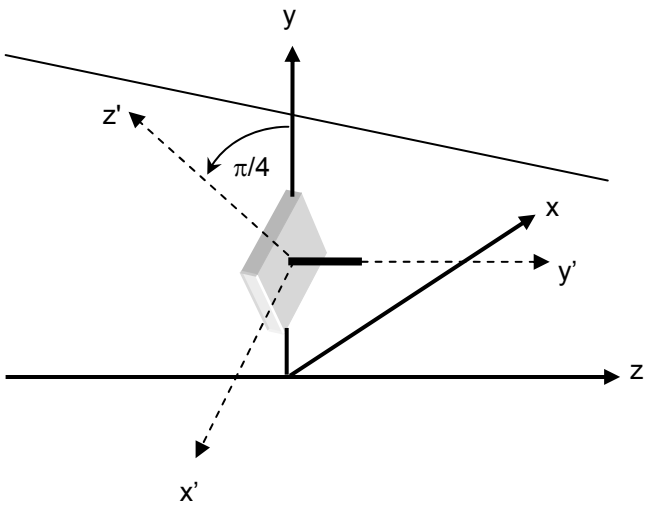

(c)

Figure 1.31 (a) The third orthogonal position, (b) fifth orientation after 45^{o} rotation and (c) sixth orientation after additional 90^{o} rotation

1.14 Thesis overview

The assumption of a single phase for all EUT's dipole moments was investigated in this chapter in both simulations and experiments. All EUTs that were used in the Thesis are described in Chapter 2 to ensure that they are suitable. Knowledge on these EUTs helps in describing later results. Chapter 3 describes a complete model for simulating magnitude and phase of emissions from an EUT placed inside a GTEM cell. The similarities between a GTEM cell and a TEM cell are then investigated in terms of their electrical properties. The impact of phase on measurements using a GTEM cell was investigated and is presented in Chapter 4. In Chapter 5, an experimental method to measure the phase differences of the dipole moments of an EUT in a GTEM cell was developed.

The Thesis concludes that (1) the assumption of no phase difference between dipole moments of an EUT does not hold even for a simple radiator, (2) the GTEM and TEM cells have similar electrical properties even though they are not similar physically, (3) a good TLM model can be achieved by the addition of realistic RAM and a proper design structure to form a 50 Ω characteristic impedance complete with thorough model verification to ensure its validity, (4) phase measurement can be performed in a GTEM cell even though only one port is available, (5) the phase difference between the dipole moments of an EUT has an impact on the power magnitude measured at the port of a GTEM cell and the inclusion of the phase difference between the

dipole moments of an EUT decreases the error in the total radiated power calculation

1.15 References

1. IEC(161), *"International Electrotechnical Commission Electropedia",* Chapter 161-01-07: Electromagnetic compatibility / Basic concepts, January 2007.

2. Paul C.R., *"Introduction to Electromagnetic Compatibility"*. Second Edition, 2006: John Wiley & Sons.

3. 2004/108/EC D., *"On the approximation of the laws of the Member States relating to electromagnetic compatibility and repealing Directive 89/336/EEC",* Official Journal of the European Union, 15 December 2004, p. L 390/24.

4. CISPR22, *" Information technology equipment - Radio disturbance characteristics - Limits and methods of measurements",* Third Edition 1997-11.

5. 61000-4-3, *"Electromagnetic Compatibility (EMC) – Part 4-3: Testing and measurement techniques. Radiated, Radio-Frequency, Electromagnetic Field Immunity Test",* International Electrotechnical Commission, Geneva, Switzerland, 2003.

6. Crawford M.L., *"Generation of Standard EM Fields Using TEM Transmission Cells",* Electromagnetic Compatibility, IEEE Transactions on, 1974, EMC-16(4), p. 189-195.

7. Konigstein D. and Hansen D. *"A new family of TEM-cells with enlarged bandwidth and optimized working volume",* 7th International Zurich Symposium on Electromagnetic Compatibility, Zurich, Switzerland, 1987, p. 127-132.

8. ETS-Lindgren, *"Gigahertz Transverse Electromagnetic cell (GTEM) Model 5400 Series "*, 2005, Cedar Park, TX.

9. Icheln C., *"The construction and application of a GTEM cell"*, Master Thesis, Faculty of Electrical Engineering, 1995, Technical University of Hamburg-Harburg.

10. Harrington T.E. *"Catalog of TEM waveguide radiated emissions correlation methods",* IEEE International Symposium on Electromagnetic Compatibility, Minneapolis, Minnesota, August 19-23, 2002, p. 486-491.

11. Wilson P., *"On correlating TEM cell and OATS emission measurements",* IEEE Transactions on Electromagnetic Compatibility, 1995, 37(1), p. 1-16.

12. Carbonini L. *"A new procedure for evaluating radiated emissions from wideband TEM cell measurements",* International conference Electromagnetic Advanced Applications, Torino, 1995, p. 133-136.

13. Ae-Kyoung L. *"An algorithm for an advanced GTEM to ground plane correlation of radiated emission test",* IEEE International Symposium on Electromagnetic Compatibility, Santa Clara, California, August 19-23, 1996, p. 58-62.

14. Ma M.T. and Koepke G., *"A method to quantify the radiation characteristics of an unknown interference source",* NBS Tech. Note 1059, Oct. 1982.

15. 61000-4-20, *"Electromagnetic Compatibility (EMC) – Part 4: Testing and measurement techniques. Section 20: Emission and immunity testing in transverse electromagnetic (TEM) waveguides",* International Electrotechnical Commission, Geneva, Switzerland, 2003.

16. Heidemann M. and Garbe H. *"Improvement of GTEM to OATS correlation",* IEEE International Symposium on Electromagnetic Compatibility, Washington, D.C., August 21-25, 2000, p. 909-914.

17. Clay S. *"Improving the correlation between OATS, RF anechoic room and GTEM radiated emissions measurements for directional radiators at frequencies between approximately 150 MHz and 10 GHz",* IEEE International Symposium on Electromagnetic Compatibility, Denver, Colorado USA, August 24-28, 1998, p. 1119-1124.

18. Berger H.S. *"Radiated emissions test correlation between G-TEM, SAC and OATS facilities using digital phones",* IEEE International Symposium on Electromagnetic Compatibility, Dallas, August 9-13, 1993, p. 295-299.

19. Wilson P.F. *"On simulating OATS near-field emission measurements via GTEM cell measurements",* IEEE International Symposium on Electromagnetic Compatibility, Dallas, August 9-13, 1993, p. 53-57.

20. Osburn J.D.M. and Bronaugh E.L. *"GHz TEM (GTEM) cell to open area test site (OATS) correlation algorithm verification issues above 1 GHz",* EMC/ESD International Conference, Denver, Colorado USA, 1993, p. 356-360.

21. Osburn J.D.M. and Bronaugh E.L., *"A measurement and calculation procedure to remove the 'gain no greater than a dipole' restriction in the GTEM-OATS correlation algorithm",* EMC 94 -Barcelona 4th International Symposium Exhibition Technical Normative on Electromagnetic Compatibility, Barcelona, Spain, 1994.

22. Thelberg M.J., Bronaugh E.L. and Osburn J.D.M. *"GTEM to OATS radiated emissions correlation from 1-5 GHz",* IEEE International Symposium on Electromagnetic Compatibility, Chicago USA, August 22-26, 1994, p. 387, 390, 389, 388, 391, 392 (pages printed out of sequence).

23. Christopoulos C., *"The Transmission-Line Modeling Method: TLM"*, 1995, New Jersey IEEE Press.

24. Paul J., Christopoulos C. and Thomas D.W.P., *"A 3-D Time Domain TLM Electromagnetic Field Solver: regSolve"*, 2000, Nottingham: University of Nottingham.

25. Ishigami S., Harima K. and Yamanaka Y. *"Estimation of E-field distribution in a loaded GTEM cell",* IEEE International Symposium on Electromagnetic Compatibility, Montreal, Canada, August 13-17, 2001, p. 129-134.

26. De Leo R., Rozzi T., Svara C. and Zappelli L., *"Rigorous analysis of the GTEM cell",* IEEE Transactions on Microwave Theory and Techniques, 1991, 39(3), p. 488-500.

27. Harrington T.E. *"GTEM fields FDTD modeling",* IEEE International Symposium on Electromagnetic Compatibility, Austin, Texas USA, August 18-22, 1997, p. 614-619.

28. Harrington T.E., Zhong C. and Foegelle M.D. *"GTEM radiated emissions correlation testing and FDTD modeling",* IEEE International Symposium on Electromagnetic Compatibility, Seattle, Washington D.C USA, August 2-6, 1999, p. 770-775.

29. Hansen D., Ristau D., Radasky W.A. and Smith K.S. *"Sources of problems in the GTEM field structure and recommended solutions",* International Symposium on Electromagnetic Compatibility, Santa Clara, California USA, August 19-23, 1996, p. 48-51.

30. Hansen D., Ristau D., Spaeth T., Radasky W.A., and Smith K.S. *"Expansions on the GTEM field structure problem",* IEEE International Symposium on Electromagnetic Compatibility, Atlanta, USA, August 14-18, 1995, p. 538-542.

31. De Leo R. and Schiavoni A., *"FDTD evaluation of scattering by metallic objects in GTEM cells",* Science, Measurement and Technology, IEE Proceedings-, 1994, 141(4), p. 287-292.

Chapter 2

Equipment Under Test (EUT)

2.0 Introduction

Many practical EUTs were considered throughout the duration of this work. These EUTs are either an electric, or a magnetic radiator or a combination of both electric and magnetic radiators. Practical EUTs are very important because they show behaviour that represents real situations. Considering their importance, this chapter describes the construction of the EUTs used in the entire work of this Thesis. This is to ensure that suitable EUTs are used and that knowledge on the behaviour of the EUTs helps in later results interpretation.

2.1 A dipole antenna

The first EUT is a dipole antenna with only two copper wires acting as the dipole elements and these wires were soldered onto a SMA female connector feed. This antenna has the worst accuracy in the measurement environment because it is difficult to rotate the antenna to the required position. The cable that feeds this antenna adds more uncertainty to the results due to the emissions from the common-mode current and impedance mismatch. To obtain better positioning, the dipole antenna was housed in an octagonal structure made from cardboard as shown in Figure 2.1 (a). The antenna elements were attached to the octagonal structure to prevent them from moving or bending when the antenna was rotated. In addition, this housing helped to maintain the centre point of the antenna. The antenna is balanced by using a balance to unbalance (BALUN) transformer. This suppresses the emission of the cable by decreasing the common mode current. This also treats the 75 Ω to 50 Ω impedance mismatch.

The octagonal structure that housed the dipole elements can be used to position the EUT to the major x, y and z orientations effectively when used together with the XYZ rotator made by Nothofer [1] shown in Figure 2.2. This is because the octagonal structure has sides with an angle which match directly on to the XYZ rotator. Since a lot of EUT orientations are performed in this work, the EUT has to be able to rotate easily and accurately. In doing so

the cable that feeds the EUT will be displaced in each position. This displacement can cause repeatability problems.

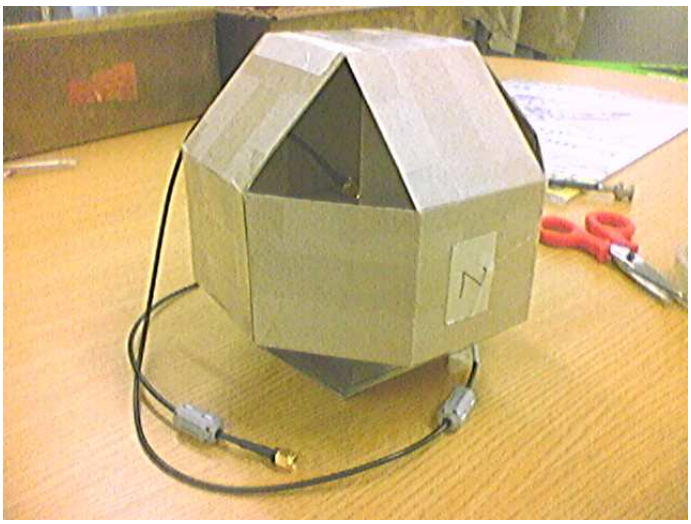

Figure 2.1 Antenna in octagonal object with ferrite clamped coaxial cable

Figure 2.2 The unique angled XYZ rotator

2.2 A dipole antenna with a static cable feed

The EUT in Section 2.1 has repeatability problems due to the undefined placement of the feeding coaxial cable inside the GTEM cell. To solve the problem, another version of dipole antenna was constructed. This antenna has a static cable feed in which the cable was static while the elements of the antenna were rotated as shown in Figure 2.3. This antenna has a rotating centre which feeds the signal to the elements. This antenna is effective if the size of its elements is much bigger compared to the size of the centre metallic feeder. The radiating signal from the metallic feeder will interfere significantly with the signal radiated from the elements in a way that the overall antenna will be more like a spherical antenna rather than a dipole antenna. In addition, this antenna structure suffers from common-mode emission from the cable feed due to the unbalance current. To suppress the common-mode currents, a BALUN and ferrite clamps along the length of the coaxial cable to the BALUN were used. Ferrite is useful in attenuating the common-mode current flowing on the shield of the external conductor of the coaxial cable as shown in Figure 2.4. The BALUN will treat the unbalance current as well as the mismatch between the dipole antenna and the 50 Ω coaxial. Instead of rotating the dipole antenna feeder, one can also create different dipole antenna orientation by screwing in the antenna elements at the available screw holes in other orientations. The finished product of the antenna is shown Figure 2.5.

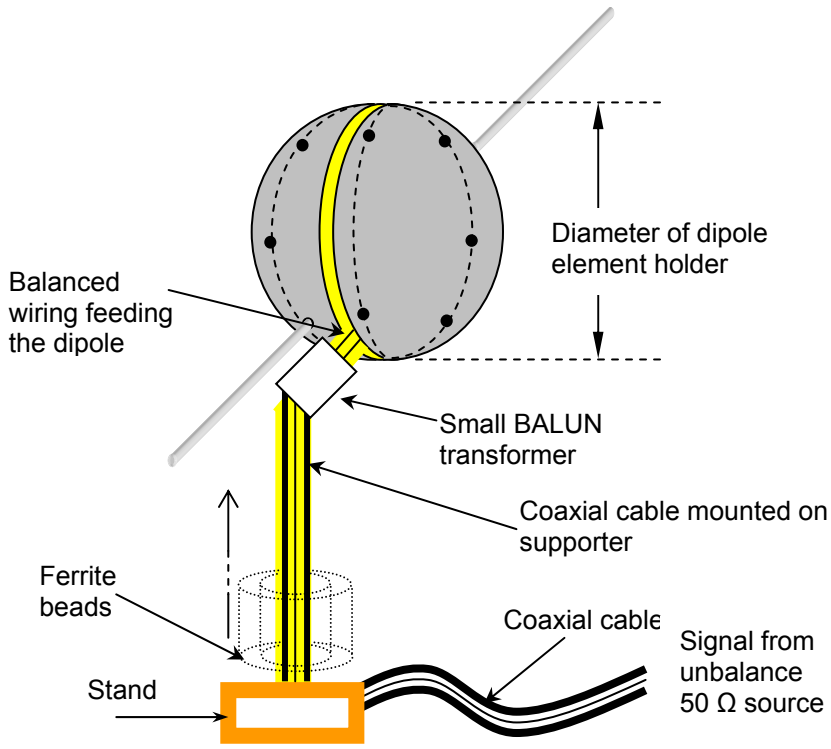

Figure 2.3 Antenna with static cable feed

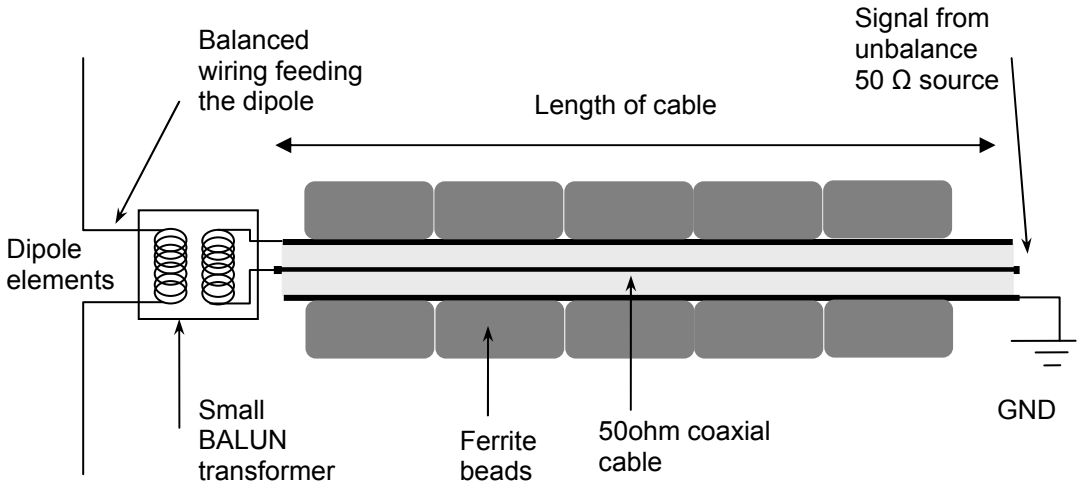

Figure 2.4 Schematic view of the of the static cable feed dipole antenna

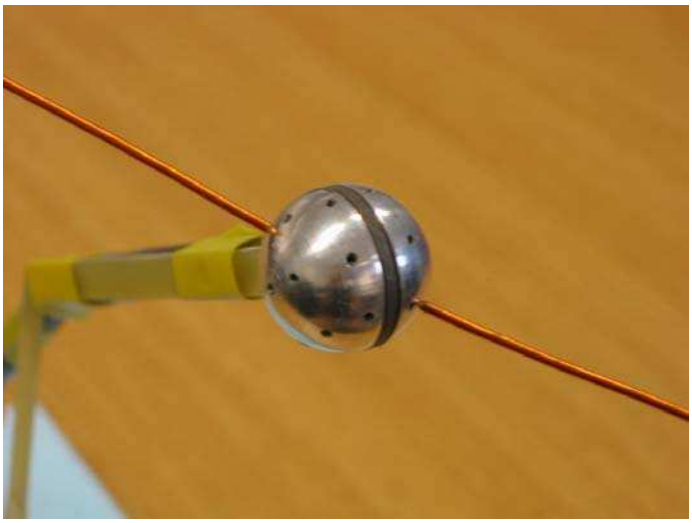

(a)

(b)

Figure 2.5 (a) The antenna element feeder with the ability to rotate in the middle and the antenna element screw holes and (b) Static feeder dipole antennas showing dipole elements in one orientation

2.3 Optical fibre Radio Frequency (RF) transmission system

In the GTEM cell phase measurements described later in this Thesis, the antennas mentioned in the previous sections are affected by the cables. The study of phase in a GTEM cell can be easily disturbed and this can invalidate the results of the study. A non-metallic cable feed to the antenna will be useful for this work. A radio frequency (RF) to fibre antenna interface was constructed to remove errors and ambiguities. This is a spherical dipole antenna operating using fibre optic channel to bring the required signal into the transmitting antenna housing. The studies and usage of the spherical dipole radiators have been reported in [2] and [3].

An optical driver (laser, light emitting diode (LED) or infrared (IR)) is directly fed from a signal generator where it modulates the optical light output according to the input signal. The modulated optical light is then transmitted by the fibre channel and a photodiode on the receiver side recovers the electric signal. The recovered signal is then amplified and applied to the spherical dipole antenna. The bandwidth of the operation is determined by the optical transceivers that are used such as laser, infrared or LED as shown in Table 2.1. To reduce the cost of making this prototype, the LED optical system was selected. However, this reduces the maximum usable frequency down to 200 MHz. The advantages of the LED system are: (1), it eliminates the use of expensive analogue to digital converter (ADC) and digital to analogue converter (DAC) pairs if a digital signal transmission is employed,

(2), it reduces components, system size and cost, and (3) it can be implemented easily.

Table 2.1

Comparison chart between types of transmitter and signal bandwidth

Operating frequency	Types of photodiode
1- 200 MHz	LED
100-200 MHz	Infrared
200 MHz - 2.5 GHz	Laser

The disadvantages of the fibre optic spherical antenna system are that the received signal depends on the optical transmission process i.e. fibre loss, critical bends and the radiation energy depends on the life of the battery. Care must be taken to make sure that battery conditions do not affect emission levels. The operational block diagram is shown in Figure 2.6 and the signal flow diagram is shown in Figure 2.7. Before the signal was fed into the external fibre optic transmitter, some signal power was coupled with a directional coupler. This would provide a reference signal as required for the phase measurements.

Figure 2.8 (a) shows the exterior appearance of the spherical dipole radiator when housed inside an octagonal structure made from foam that is transparent to electromagnetic wave. The sides of this structure have an angle such that when used together with the XYZ rotator, it can rotate the spherical antenna to different orthogonal orientations. The position of the spherical dipole antenna inside of the foam structure can be seen from

Figure 2.8 (b). The complex interior due to the limited space of the spherical dipole antenna is shown in Figure 2.9.

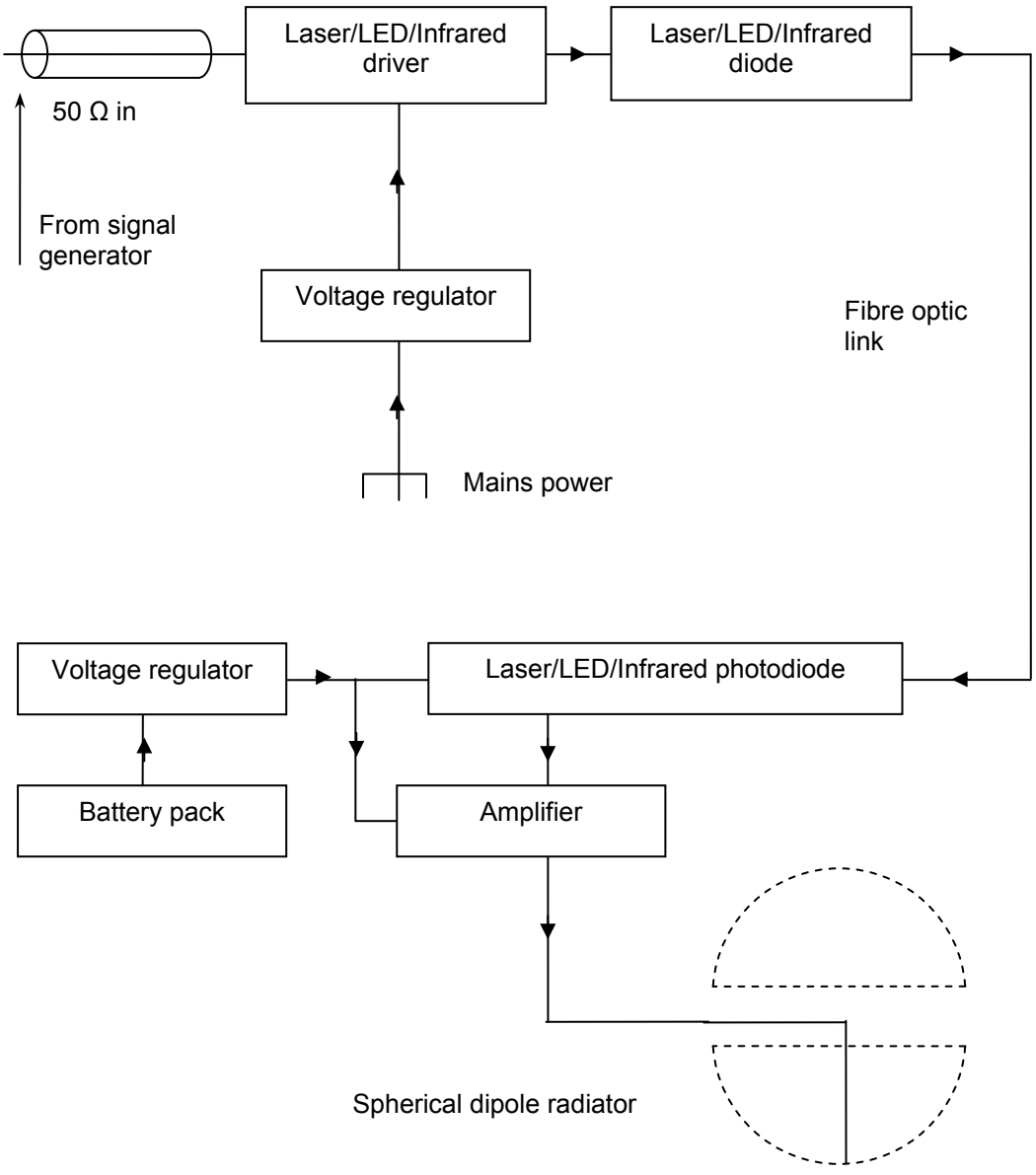

Figure 2.6 Block diagram showing the operation of the spherical dipole antenna

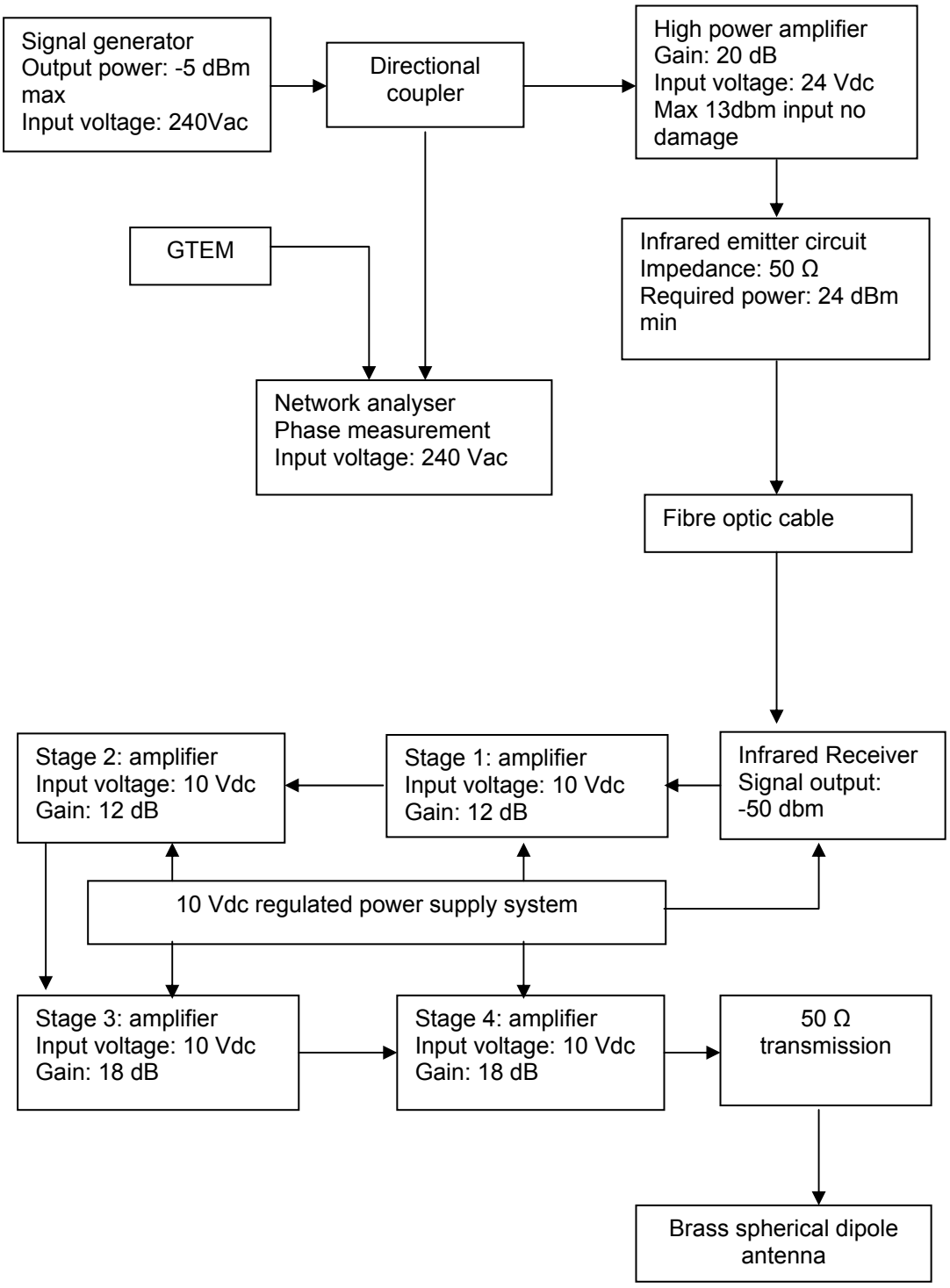

Figure 2.7 Signal flow diagrams for the spherical dipole antenna

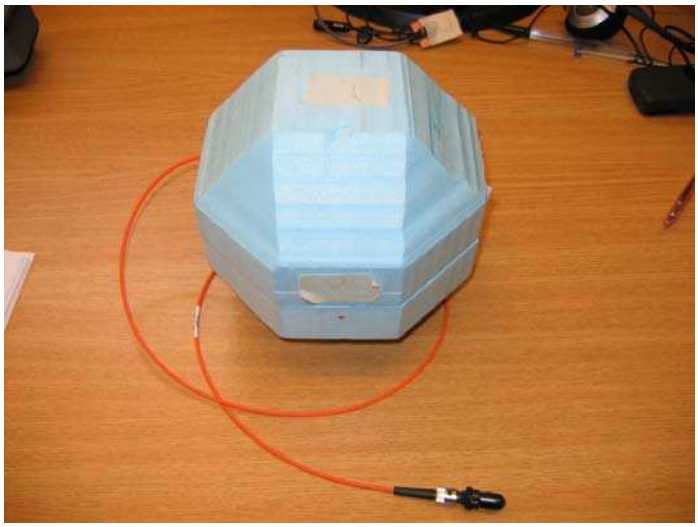

(a)

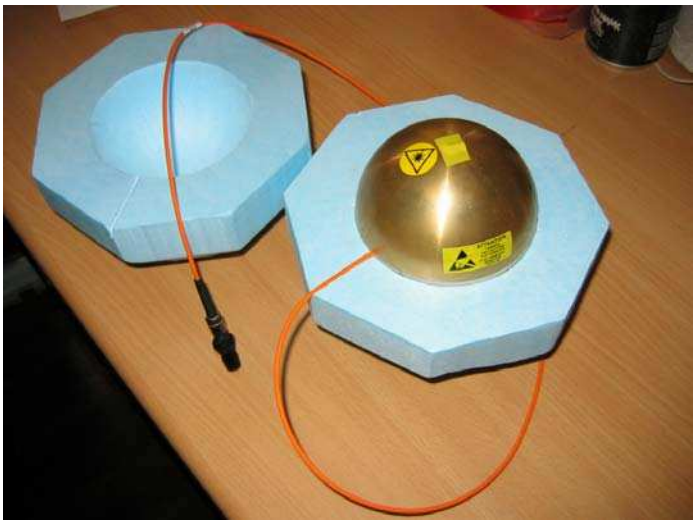

(b)

Figure 2.8 The finished spherical dipole radiator looking at the external appearance (a) housed inside an octagonal structure and (b) with half of the octagonal cube removed

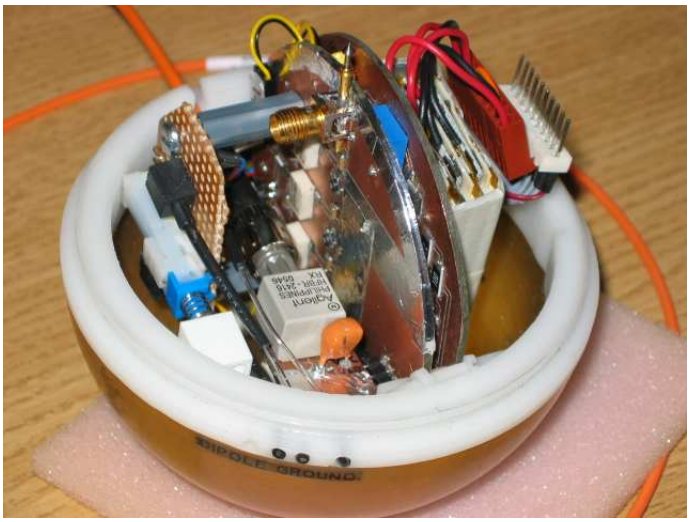

Figure 2.9 Interior look of the spherical dipole antenna with half the brass hemisphere removed

The design of the circuit has some major advantages in terms of the power supply management system because the parameter known to affect this system most is the power supply voltage. Thus, the power supply system for this antenna was given a thorough consideration. Many power supply systems use traditional lithium ion battery pack and normal voltage regulator. The first disadvantage of a lithium ion battery is the low charge capacity measured in Ampere hour (Ah) or mili Ampere hour (mAh) for smaller charge capacity battery. This requires the battery to be charged very often during a period of measurement. In such an arrangement, when operated with low end voltage regulators, the actual supplied voltage to the system by the voltage regulator tends to have the same voltage gradient as the battery voltage as shown in Figure 2.10 (a). In other words, as the battery voltage decreases exponentially over time, the supplied voltage to the circuit also behaves in the

same way. Thus, the output power of the amplifier that is affected by the supplied voltage varies. This will result in errors in the power magnitude emitted by the antenna.

The second disadvantage of the lithium ion battery system is the small voltage rating per cell. More batteries are required to be cascaded to obtain the required voltage for the system. This will increase the weight of the overall antenna system and creates other problems due to the limited space inside the spherical radiator. Other disadvantages are the inability of the lithium ion battery to hold its charge over a period of time and the memory effect of the battery in terms of charging. The design of the power supply system in this Thesis involved the use of a lithium polymer battery, a more advanced voltage regulator system and lastly a battery voltage monitoring circuit. The advantages of this design are described in the following paragraphs.

Firstly, the lithium polymer battery has a larger charge capacity and higher voltage per cell. The voltage is typically 3.7 V typical per cell and has 1800 mAh per cell. The higher voltage per cell reduces the number of batteries required to achieve the required voltage to run the antenna circuitry while the larger capacity per cell prolongs the available operating time. Secondly, the lithium polymer can retain its charge over a long period of time even when not in used. This means that no charging is required before use and even if charging is required, the battery can be charged at anytime since it has no memory effect, thus no damage is done to the battery.

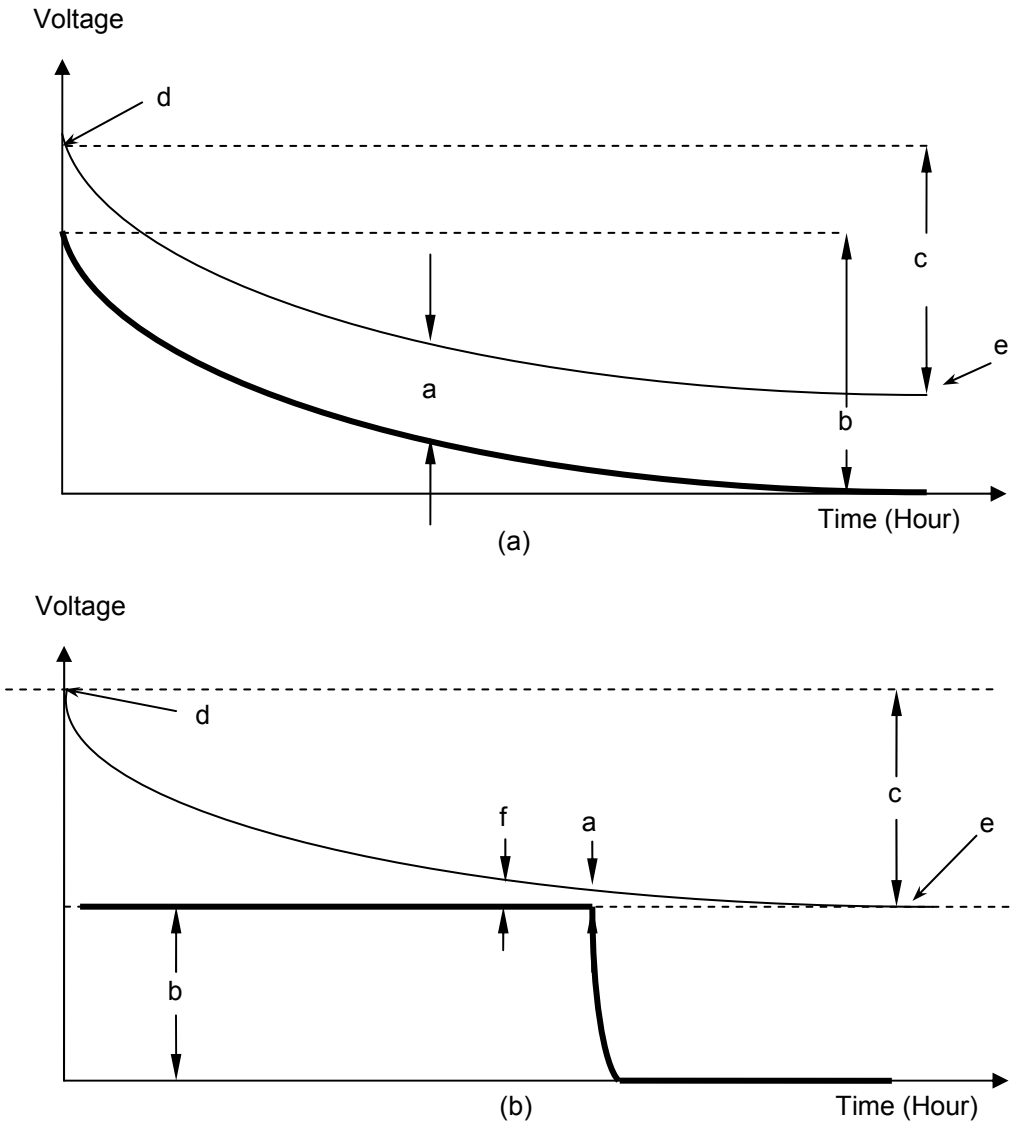

Figure 2.10 Comparison between the battery voltage and the supplied voltage by the voltage regulator in respect with time for (a) conventional power supply system and (b) the power supply system in this spherical dipole antenna. Bold line represents the supplied voltage into the antenna circuitry. Legends:

(a) Voltage dropped between at the voltage regulator; the working voltage for the voltage regulator to operate
(b) Gradient of supplied system voltage during battery discharge
(c) Gradient of battery voltage during battery discharge
(d) Fully charged battery voltage
(e) Low battery voltage
(f) Low Battery warning voltage

Unlike the traditional voltage regulator, the voltage regulator used in this Thesis has a feedback reference voltage. This feedback is used by the regulator to supply constant voltage to the antenna circuitry even when the voltage of the battery is decreasing over time as shown in Figure 2.10 (b). This design solves the variable supply voltage issue of the antenna amplifier. In addition, the power supply system included a battery voltage monitor system that will turn on the warning LEDs once the battery voltage is below a certain threshold. This is to inform the user that the battery needs charging and will cut off soon. Once the voltage of the battery has reached the voltage regulator minimum operating threshold voltage, the voltage regulator will cut off the supply to the antenna circuitry shutting down the system. No further measurements can be done at this state. In summary, the operation of this antenna amplifier has a constant gain with this system.

Before initial use, the fibre optic circuit was tested to obtain its insertion loss. The receiver circuit produced -14 dBm output at its port when a 0 dBm power was sent into the external transmitter circuit. It was concluded that the transmission system exhibited 14 dB insertion loss. A correction factor of +14 dB would be needed to compensate this loss.

Next, the extent of the effects of attaching cables to this EUT was observed. The EUT (spherical dipole antenna) was then loaded into the GTEM cell and the power is measured from the output port of the GTEM cell for all 12 orientations according to the standard. First, measurements were taken from the EUT fed via a shielded coaxial cable. Second, measurements

were taken from the EUT fed by a fibre optic transmission system. These results were then compared with a simulation performed according to the same experimental setup and the results are shown in Figure 2.11. The difference between all three methods has now become apparent. The experimental measurement that used the fibre optic system shows a better agreement with the simulation results apart from some orientations where a major difference was observed. In the simulation result, the values of the measured powers in orientations 3, 6, 9 and 12 are very low because the dipole antenna at these orientations was aligned in the cross field component which is the worst coupling orientation in the GTEM cell. The same happened to the measurement with the fibre optic system in the GTEM cell but the readings are limited by the ability of the spectrum analyser to display traces that passed well below the noise floor of the spectrum analyser.

It is shown that significant errors are introduced by cables even for a simple spherical dipole radiator. The identified parameters that affect the emission from cable such as (1) the arrangements of the cables, (2) relative positions of the cables in respect to the GTEM cell, (3) type of cable used e.g. coaxial, (4) signal carried by the cable and (5) length of the cable. The arrangement of the cables is how the cables are bundled in the GTEM cell. This is particular important for long cable EUTs. The arrangement of cables determines the mutual capacitive or inductive coupling of the cables thus affecting the emissions. The relative positions of the cables in respect to the GTEM cell are important since emissions from cables that coincide with the

strong coupling direction will result in more errors. A balanced cable has lower emission than an unbalanced cable such as the coaxial cable. Common-mode current may exist of the outer conductor of the coaxial cable and this resulted in emissions from the cables. In circumstances where coaxial cables must be used, emissions can be minimized by using ferrite clamps. This also leads to the type of signals that are carried on the cables. Non time-varying signals such as DC voltage tend not to radiate but the time-varying signals existing inside the EUTs may couple into this signal and thus lead to emission from the cables. Lastly, longer cables are prone to emission due to the larger radiating surfaces. Thus, connecting cables must be kept short or minimum to decrease the emission.

Some EUTs used in this Thesis involved using the coaxial cable as the feeding cable for the EUTs. Among the actions taken to minimize the emission from the cable are (1) to install ferrite clamp along the coaxial cables and (2) to install a BALUN between the EUT and the source. In addition, the lengths of the cables are kept short to minimize the radiation surface of the cables.

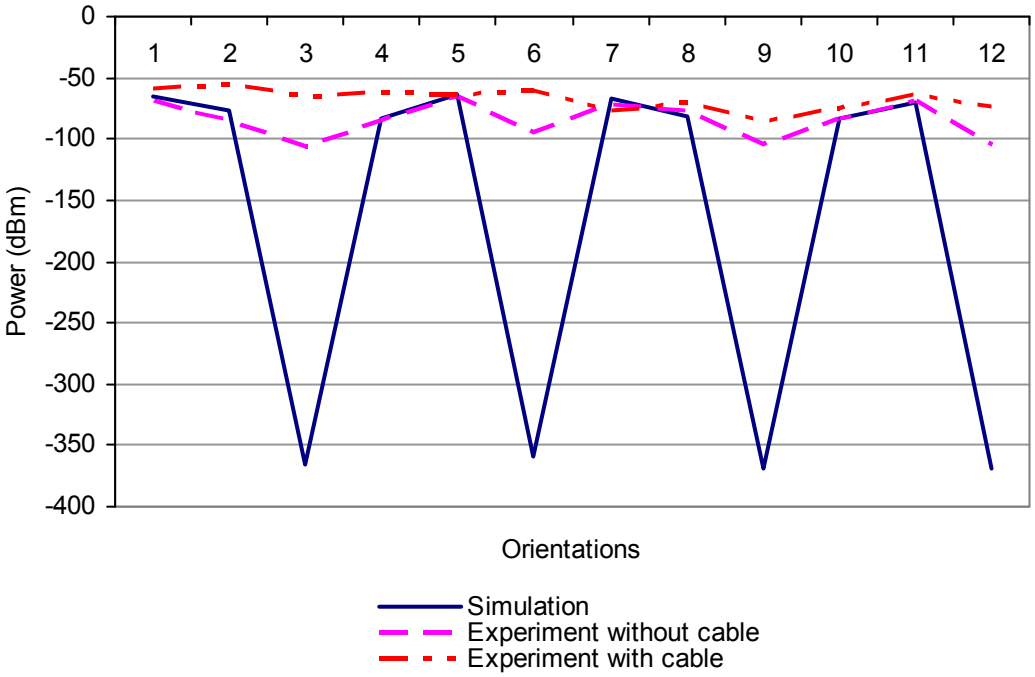

Figure 2.11 Comparison between simulation and experimental (cable and non-cable)

2.4 A metal box with a slot (magnetic loop)

A more practical EUT consisting of a metal box with a lid and aperture was constructed. This EUT was constructed using brass material. The dimension of the metal box is 29x29x11 cm. The lid opening enables the user to install any appropriate circuit inside the box for testing inside the GTEM cell. To prevent field leakage, the lid was tightly closed using conductive copper fingers. The aperture of the box is formed by a piece of brass plate held together to the box using screws and nuts. The aperture size of the box can be changed easily by exchanging this brass plate with different aperture

sizes. In this work, a signal source is used to excite the box at the middle of the aperture forming a current loop to act as a magnetic radiator. A signal is fed externally via the fibre optic link into an internal transceiver circuit in which the optical signal is transformed into an electrical signal. This voltage excites the box at a power and frequency set externally via a fibre optic transmitter. This fibre optic transceiver system is similar to the spherical antenna system mentioned in Section 2.3. The only difference is the circuit layout (shown in Figure 2.12) which is no longer constrained by the size of the spherical dipole. The recovered electrical signal is fed across the opening of the aperture of the metal box at its middle as shown in Figure 2.13. Similar to the antenna system mentioned in Section 2.3, the signal can be coupled to the network analyser with a directional coupler to provide a reference signal as required for the phase measurements. All the schematics and PCB footprints involved in the construction of the radio to fibre optic antenna system are shown in Appendix A.

The metal box with an aperture is one of the main EUTs used in this work. Thus, knowledge of its behaviour is important in interpreting results. Before further analysis was done, the electrical properties of the metal box were studied. The intention here is to examine the current flow characteristic as well as its magnetic field distribution around the metal box. It can be assumed that the box would have three major current paths, which are shown in Figure 2.14. The first and second current paths would be formed at the face of the box where the aperture was excited. The third current path is the

current that flows around the box. To obtain more accurate paths for these currents, a simulation using Concept II [4] was performed. Shown in Figure 2.15 are the directions of the surface currents and their respective magnitudes. It is obvious that the current intensity is strong at the excitation region of the box because it is where the source of the current starts and gradually decreases as the current flows further away from the excitation region dividing itself into different paths. These paths seen from Figure 2.15 support the earlier assumption in Figure 2.14.

Since this EUT is quite large in comparison to the usable volume in the GTEM cell, an evaluation on the electric field distributions when loaded and unloaded into a GTEM cell was performed numerically. This is to prevent 'overloading' the GTEM which could disturb the electric field inside the GTEM cell. The investigation also involved loading the GTEM with a grounded metal box. Electric or magnetic fields disturbance is expected when loading a GTEM cell. In this evaluation, the result shows a minimal field distribution disturbance, which is favourable in later work in the Thesis. Full detail of this investigation is available in Appendix B.

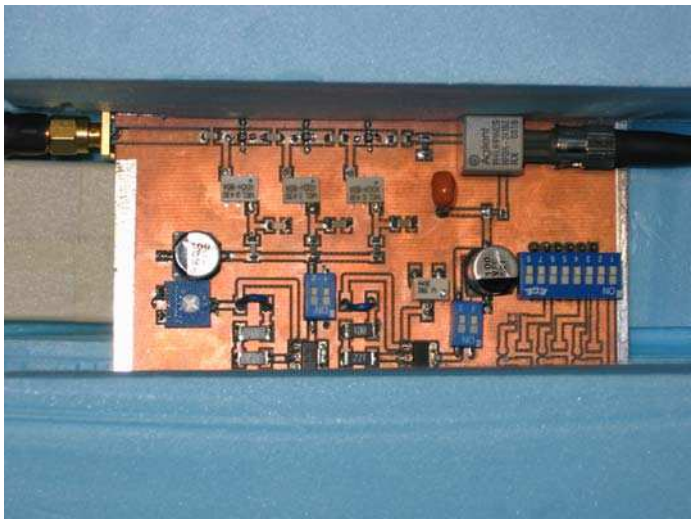

Figure 2.12 PCB layout for the fibre optic receiver when being housed inside the metal box

Figure 2.13 The connection from the receiver circuit to the middle of the aperture where the box is excited with a signal

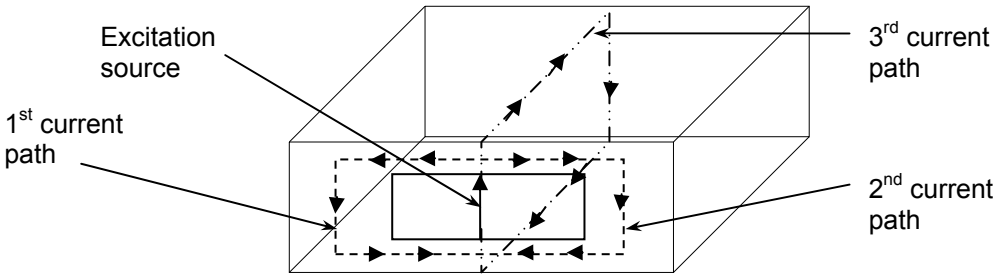

Figure 2.14 Three major current paths exist on the metal box surface

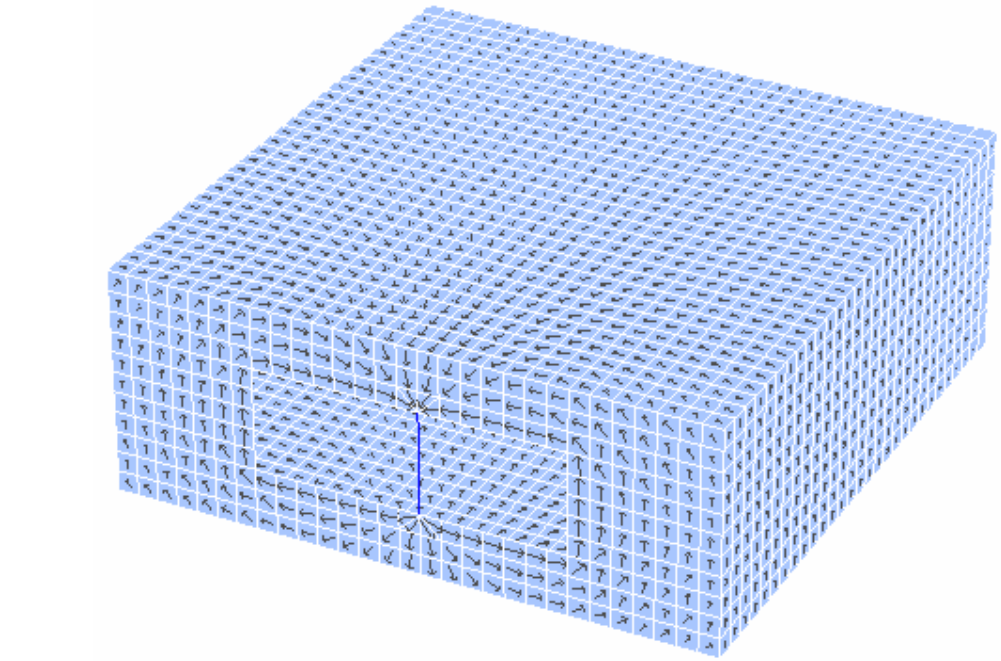

(a)

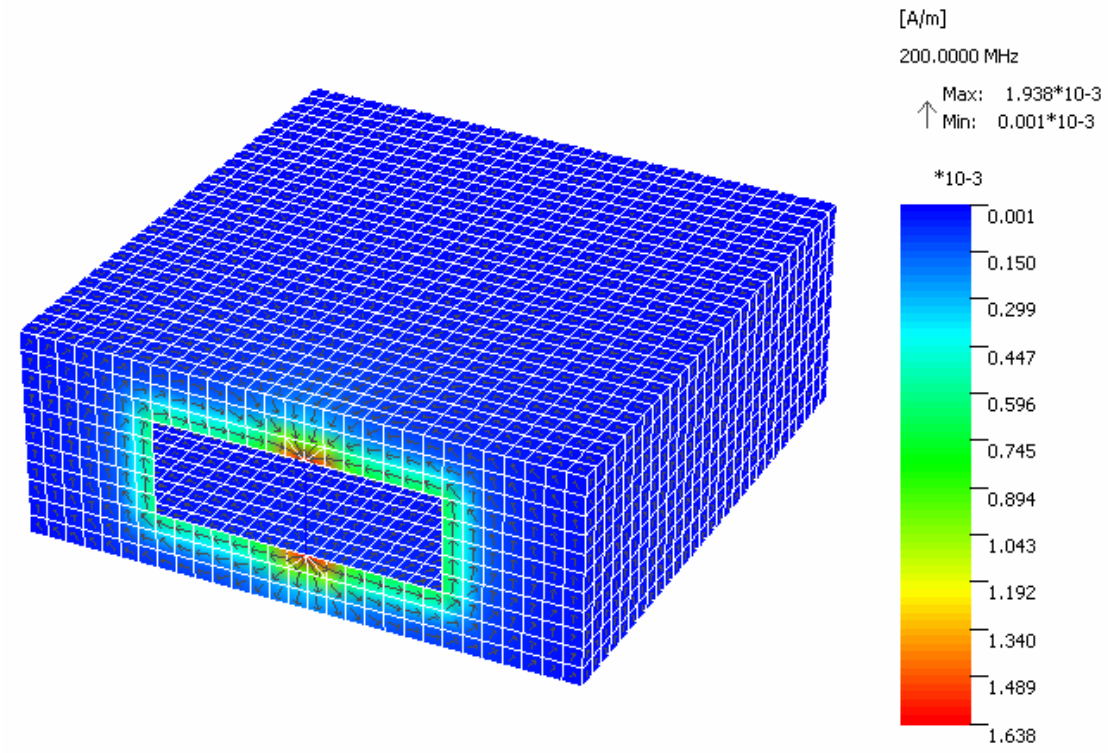

(b)

Figure 2.15 (a) The directions of the currents on the surface of the box and (b) their respective magnitudes relative to the magnetic field

2.5 A metal box with a monopole on top

This EUT consists of a monopole located on top of a metal box acting as the finite ground plane as shown in Figure 2.16. The size of this metal box is 29x29x11 cm. The monopole's length is chosen to be 19 cm so that the overall lengths of the physical size of the EUT in all x, y and z axis are about 30 cm for the convenience of specifying the simulation meshes. The monopole is located approximately at the centre on the top of the metal box.

Figure 2.16 A metal box with one monopole on top

2.6 A metal box with two monopoles on top

Another EUT configuration comprising of two parallel monopoles located on top of a metal box as the finite ground plane is shown in

Figure 2.17. The size of this metal box is identical to the metal box mentioned in Section 2.5. This EUT is particularly useful in the study of phase effects in GTEM cell measurements because both monopoles affect each other when the phase difference between the two supplied voltages is varied. This study is presented in Chapter 4. The monopoles are 19 cm in length and the locations of the monopoles are shown in Figure 2.18. Both monopoles are fed with signals via separate cables clamped with ferrites to minimize interference caused by the cables.

Figure 2.17 A metal box with two monopoles on top

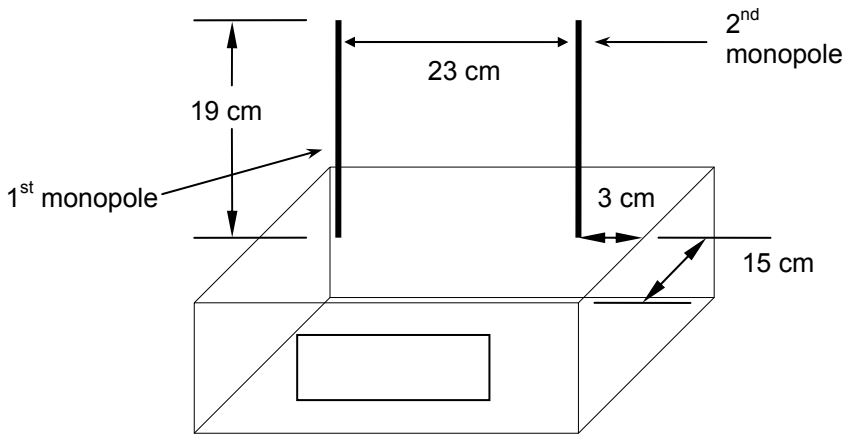

Figure 2.18 Locations of the two monopoles on top of the metal box

2.7 A metal box with a slot and a raised lid

A metal box with a slot and a raised lid is an EUT that has both electric and magnetic radiators. This EUT is shown in Figure 2.19. The aperture acts as a magnetic radiator, while the raised lid driven by a separate signal source serves as the electric radiator. The lid is raised 1 cm above the metal box and the aperture is 15x5 cm. Both excitation sources are independent and externally fed via coaxial cables. Ferrites were clamped along the length of the coaxial cables feeding the EUT to minimize interference caused by the cables. The purpose of this EUT is to examine the effect of phase in GTEM cell measurement when the phase of the electric or the magnetic radiator is altered. More about this study is explained in Chapter 4.

Figure 2.19 Electric and magnetic radiator in an single EUT

2.8 A metal box with slots on its two sides

A metal box with slots on its two sides consists of two apertures acting as two separate magnetic radiators located in different polarizations. One aperture is located on one side of the metal box while the other aperture is located on the top of the metal box. Both apertures are excited in the middle by independent sources via separate coaxial cables. Similarly, ferrites were clamped along the length of the coaxial cables feeding the EUT to minimize interference caused by the cables. Figure 2.20 shows the construction of the magnetic radiator. Both apertures are 8x8 cm in dimension.

Figure 2.20 EUT construction of two magnetic radiator apertures

2.9 A metal box with three orthogonal monopoles

A metal box with three orthogonal monopoles was implemented in simulation only and not in experiments. This is because the EUT consisting of three monopoles require three separate sources to drive them and this was not possible with the available equipment. At the time of this work, only two signal generators were available. Furthermore, connecting these monopoles using separate cables may distort the results. This EUT is shown in Figure 2.21. The main purpose of this design is to study the effect of phase difference on the total radiated power measured using a GTEM when the dipole moments are aligned orthogonal to each other's. This study is presented in Chapter 4.

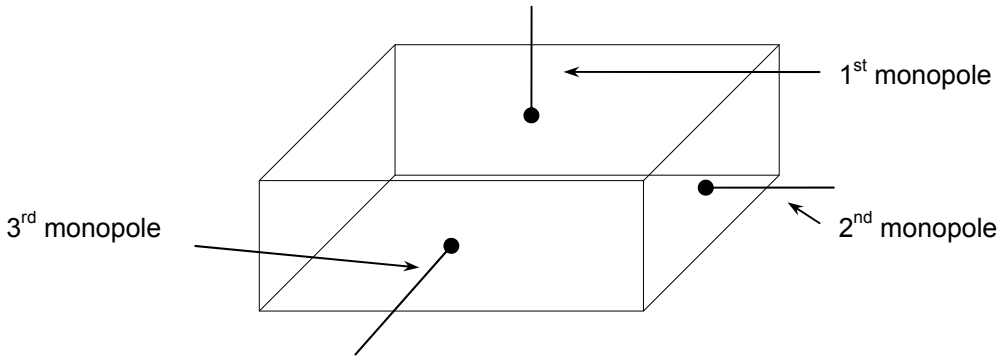

Figure 2.21 Orthogonal axis monopole EUT constructions

2.10 Conclusion

Various types of EUT have been introduced in this chapter. The EUTs range from a simple dipole radiator to more complex radiators such as the metal box with an aperture. The main purpose of this chapter is to describe all the EUTs that were involved in the study of the characteristic of the GTEM cell. This is important because by studying the behaviour of these EUTs, results obtained in both simulations and experimental can be interpreted and analyzed. In addition, the use of various types of EUTs shows that the work done in this Thesis is broad enough to encompass designs resembling practical EUTs. Thus, the results obtained from this study of the characteristic of the GTEM are more representative of practical situations.

2.11 References

1. Nothofer A., *"Emissionsmessungen in GTEM-Zellen"*, Diplomarbeit Thesis, Institut fur Grundlagen der Electroteknik und Messtechnik, June 1995, Universitat Hannover.

2. Dawson L. and Marvin A.C., *"Procedure for new draft of Defence Standard 59-41-calibrating screened room antenna combinations against OATS",* Electromagnetic Compatibility, IEEE Transactions on, 1999, 41(4), p. 368-374.

3. Consortium of DRA, NPL, York Univ., Nottingham Univ., *"Requirements for the origination of a draft emission calibration procedure"*, DRA, 1996, Ref. DERA/EL/EMCT/TR/96/7/2/6/1.0, available EMCT Sec., DRA Aquila, Bromley, Kent, BR1 2JB U.K.

4. Institute of Electromagnetic Theory, Technical University of Hamburg Harburg, "*The CONCEPT-II Code*", Last update: 13 Feb 2009, [Cited: 20 Dec 2009], Available: http://www.tet.tu-harburg.de/concept/index.en.html

Chapter 3

The GTEM TLM Model

3.0 Introduction

In this chapter, the work on creating a numerical model for the GTEM cell is described. This model is very important for the study of the GTEM cell characteristics because some characteristics are difficult to study experimentally but can be more easily understood using the numerical model. The TLM method was first developed by Johns and Beurle [1]. The TLM method described in [2] is used as the numerical method for the GTEM model. The simulation will be performed using a TLM solver software running on a UNIX platform which was previously developed by Paul [3] and is called

regSolve. In order to use this software, a text file with coordinates was generated to define the cells that resemble the required structure of interest, material type, etc. The reasons for choosing TLM as the numerical code are because TLM solver was readily available at the time of this work and has never been used on a large scale object such as the GTEM cell. Other numerical methods cannot easily include practical RAM details inside the GTEM model and normally employ numerical absorbing boundary condition to simulate the RAM [4]. Another critical part in the construction of the GTEM model is the accuracy with the angles of which the four walls are modelled and the angle which the septum makes relative to the upper and lower walls. This is important because these walls and the septum must produce the required characteristic impedance of 50 Ω. To help study possible variation of the 50 Ω impedance from the port to the termination of the GTEM model, a TEM model was first created. The details of the TEM model are explained in the following section.

3.1 Construction of TEM model

A TEM model was constructed before the more complex GTEM model was attempted so that the information gained from the TEM model about its characteristic impedance as a function of the side wall geometries can later

provide a useful insight into how the impedance of the GTEM model would behave as a function of the cross-sectional height to width ratio.

The TEM cell consists of four major parts. These are the (1) tapered ends, (2) the cuboid body, (3) the inner septum and (4) the two ports at each end. The tapered parts located at both ends of the structure were also shaped to provide 50 Ω impedance. To model the tapered region, meshes were stair-cased to form the required angle. A diagram of the TEM model is shown in Figure 3.1. The TEM model was modelled to be as far as possible similar to the TEM cell created by Crawford [5].

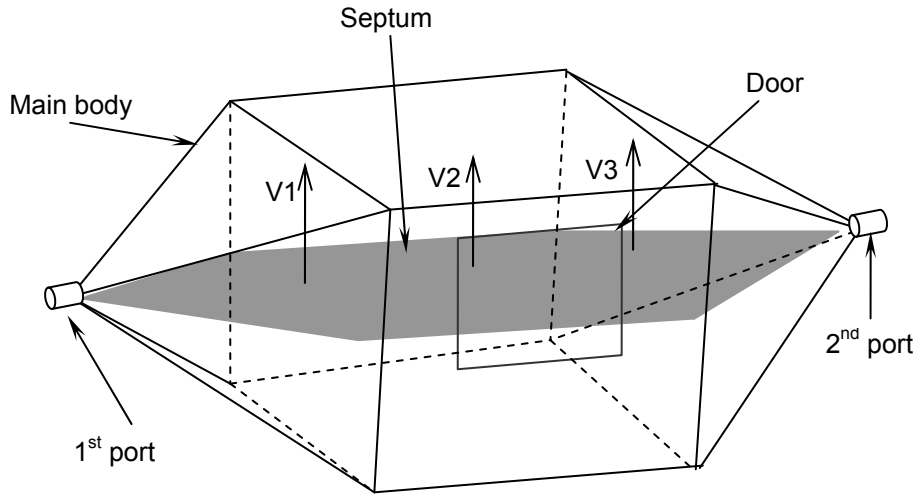

Figure 3.1 The different major parts of a typical TEM cell

3.2 Verification of 50 Ω TEM model

There are two ways of verifying the 50 Ω characteristic impedance of the TEM model. One is to use analytical formulae [6] to approximate the impedance from known geometries. The other is to simulate a 1 V single pulse excited at one of the ports of the TEM model and observe the pulse propagation along the transmission line. The result from the analytical approach is an approximation and gives results which do not necessarily represent the actual behaviour of this TEM model. The later method is preferred since it is directly linked to the modelled structure. A trapezoid pulse of 1 V was transmitted from the first port to the second port of the TEM model and the voltages and currents at locations shown in Figure 3.1 were simulated. These voltage pulses are shown in Figure 3.2. The pulses with a magnitude 0.5 V were obtained which indicate that the cell impedance was a near match to the source, load and the transmission line. This is based on a simple circuit analogy shown in Figure 3.3. The impedances at the particular locations along the transmission line are then calculated and are shown in Figure 3.2. The calculated impedances are close to 50 Ω.

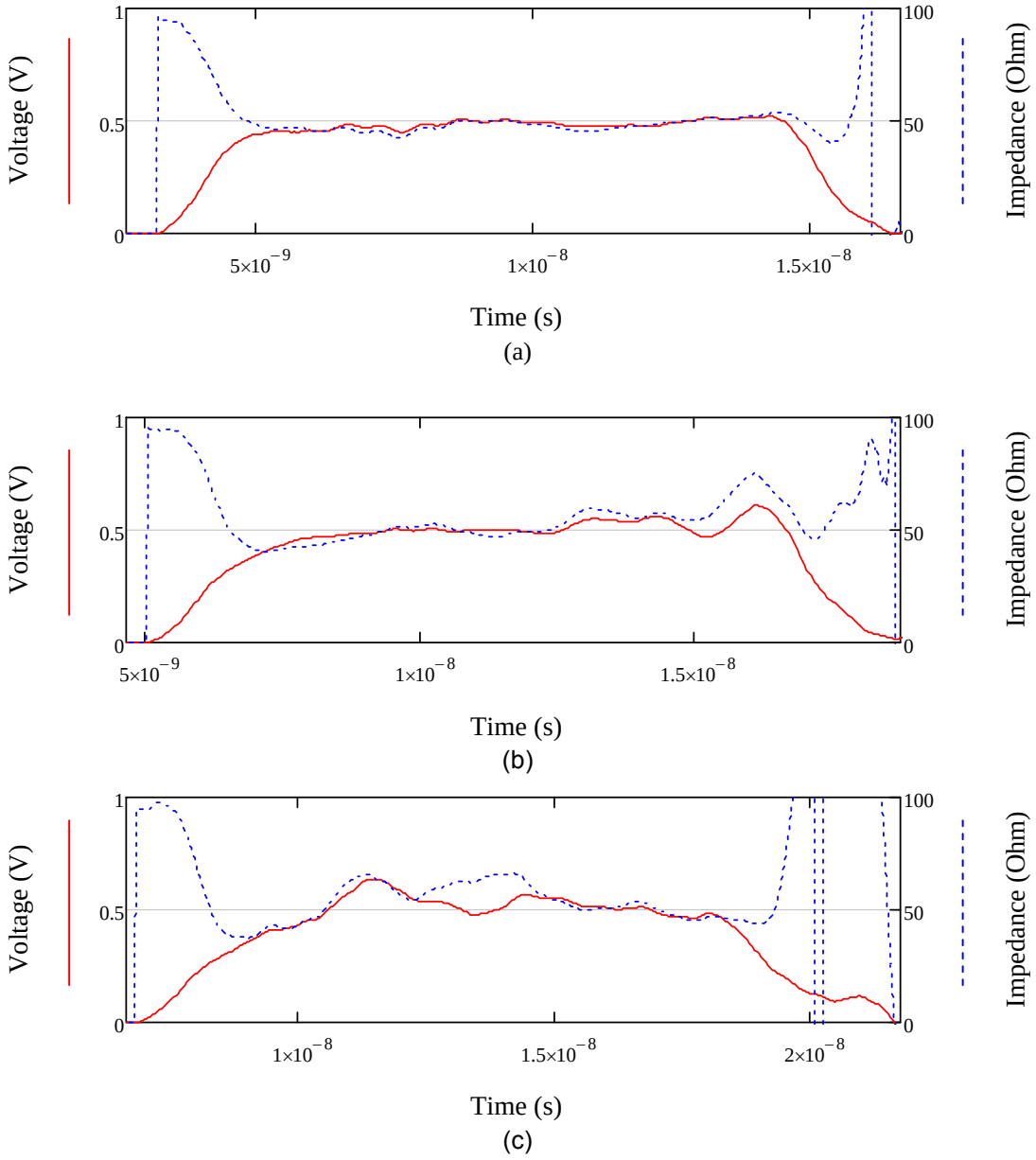

Figure 3.2 Impedance (broken line) and voltage (solid line) at the probe points at (a) V1, (b) V2 and (c) V3 according to Figure 3.1

In Figure 3.2, the shape of the obtained pulse shows some irregularities. First, this was due to errors associated with modelling angled objects using a Cartesian mesh. The stair-cased mesh cannot produce the exact angle required to form the two tapered regions of the TEM model. These approximated tapered regions produce characteristic impedance other than 50 Ω which leads to the distortion of the voltage pulse. Second, the fast rise-time and fall-time of the pulse contain high frequency components. These cannot be handled accurately by the model due to the limitation that the allowable wavelength of the highest frequency, which must be at least ten times bigger than the size of the mesh. Failure to meet this requirement results in numerical dispersion of the voltage pulse.

It was concluded that, successful 50 Ω impedance structure could be obtained if the cell is carefully constructed according to the correct height to width ratio. This information provides confidence in creating the GTEM model which has more complicated angled structures. The construction of the GTEM model is described in the following sections followed by validations to ensure its reliability and accuracy.

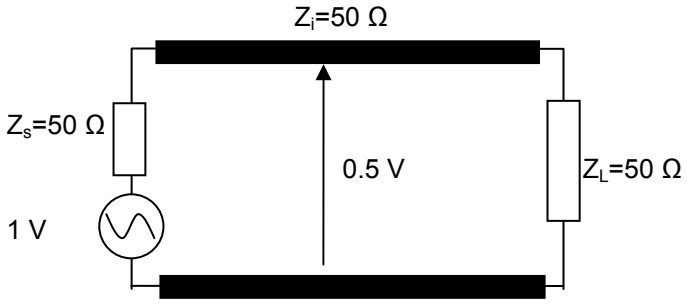

Figure 3.3 Circuit theory analogy of voltage along the transmission line of matched impedance. Z_i is the characteristic impedance of the line

3.3 Construction of the GTEM model

A GTEM model is an important tool in the work of this Thesis. It serves as a comparison tool to verify experimental works as well as a way to investigate the complex behaviour of the GTEM cell, particularly the effect of phase which is investigated in this Thesis. A GTEM model is far more complex compared to the TEM model as mentioned in the previous section due to the addition of several construction parts. The basic construction of a GTEM cell was explained in Chapter 1. The first stage in this modelling is to create the appropriate input file that represents the geometry of a GTEM cell. The simulation cells were arranged to be as close as possible to the actual GTEM cell geometry. The model is based on the GTEM cell manufactured by ETSI Lindgren [7]. This device is available in the GGIEMR laboratory and thus reasonable comparisons can be performed between the model and the actual cell. Each part of the GTEM model was created by defining the cells that form the required structures. The technique used here is similar to the technique used to build the TEM model. The GTEM model differs from the TEM model by the addition of the RAM material and the resistor network.

At the time of the model development, the TLM solver based on a Cartesian mesh was well developed and the reliability of using the Cartesian mesh had been proven. Since the GTEM cell is a structure that involves planes at different angles in its construction rather than right angle junctions, the effort to mimic these angles in the model as close as possible using the

square-block mesh was rather torturous. The model was created using 0.02 m discretization size. This setting caused a stair-case length of 20 mm for every step increase in the mesh which results in a coarse angle resolution. The GTEM cell is not geometrically symmetrical in terms of a transmission line from one end to the other end. This is the major difficulty in getting the model to behave as a 50 Ω transmission line.

The major dimensions of the GTEM cell given by the data sheet for model 5407 are shown in Figure 3.4 (a) and the geometries of the GTEM model are shown in Figure 3.4 (b). The values (in prime) in Figure 3.4 (b) are obtained from Figure 3.4 (a) using the Pythagoras theorem. The reasons for designing the GTEM model using Figure 3.4 (b) architecture are discussed below. Firstly, side A and side B were made similar, so that both have similar behaviour rather than as in Figure 3.4 (a) where side A would be stair-cased in the model and side B is flat. Secondly, the stair-casing effect at side C was avoided. Designing side C or the back wall of the GTEM cell is important since any model imperfections would cause unwanted reflections. Another advantage of this choice in the model is that the pyramidal RAM implementation has been made relative easy as the pyramidal sides are now symmetrical. All these are important key features that lead to a good model.

From Figure 3.4 (b), by dividing the length of side B (3973 mm) by the mesh size (20 mm), it is concluded that one side of the GTEM cell wall i.e. side B will need approximately 198 lines of code in cell definition. This was too time consuming for manual generation since a miss-calculation of one line of

the code would successively misplace other coordinates. This could lead to accumulated errors. In addition, the input text files showed no clear evidence should there be any problem due to the coordinate of the structure unless one decided to calculate and check all over again.

Based on this observation, a piece of software based on Visual Basic™ was created to aid the coding process. The Graphic User Interchange (GUI) is shown is Figure 3.5. Relevant information on the required structure of the GTEM model was programmed into the software. This software generates the four main walls of the GTEM model, septum, resistor network and the back wall from the sizes specified by users. The software could complete the whole task of coding quickly using a standard computer. This is very useful since a manual generation would take days and still generate errors due to the repetitive task. The creation of the GTEM TLM model input file generator software has offered reliable yet speedy creation of the GTEM model structure. The software is not entirely a GUI software, but simply a coordinate generator according to user inputs on the size of the GTEM cell. It is limited to a mesh size of 2000, 2000, 5000 (n_x, n_y, n_z). A massive mesh size structure is not advised since it will be impossible to simulate the structure in the UNIX cluster due to time and memory constraints. The output of the software is a text (.txt) file, which represents the GTEM cell structure (shown in Figure 3.6). This file can be copied and pasted into input (.in) file for regSolve. The total number of cells is in an excess of 20,000.

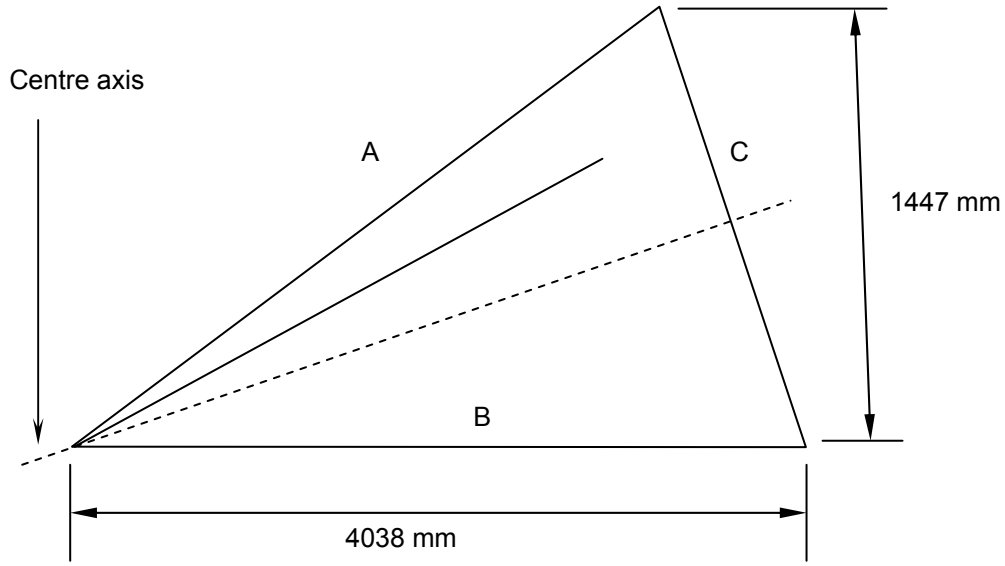

(a)

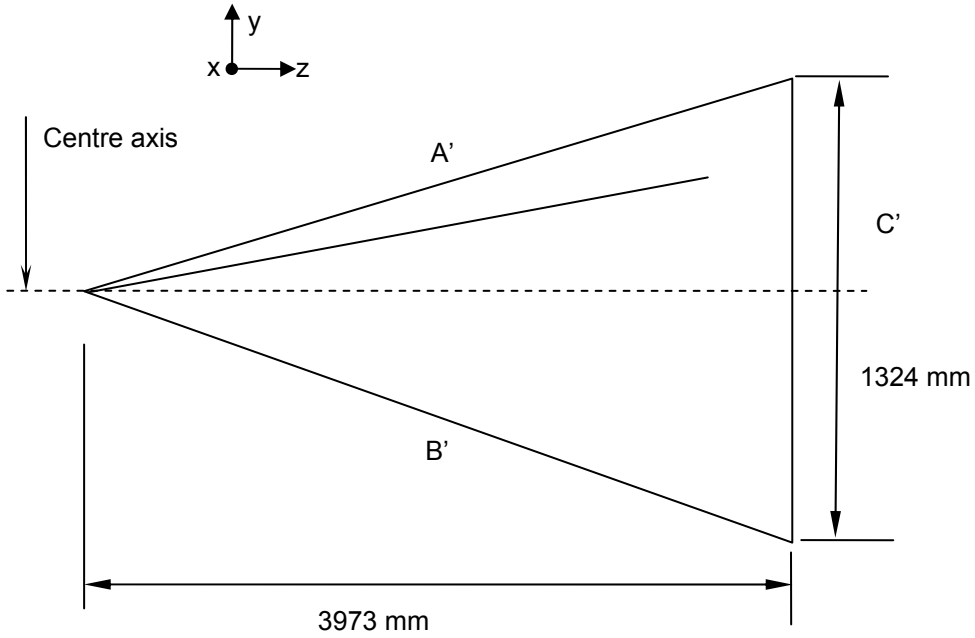

(b)

Figure 3.4 The GTEM cell geometries for (a) size 5407 and (b) the GTEM model

An important part of the GTEM model that contributes to the performance of the model is the pyramidal RAM model. Pyramidal RAM is used to provide a termination for higher frequencies to minimise reflections. Pyramidal RAM in the real GTEM 5407 has the dimensions shown in Figure 3.7. The pyramidal RAM model structure used in the GTEM model was a very close approximation to the real RAM found in the GTEM cell as regards to its size and tapered angle.

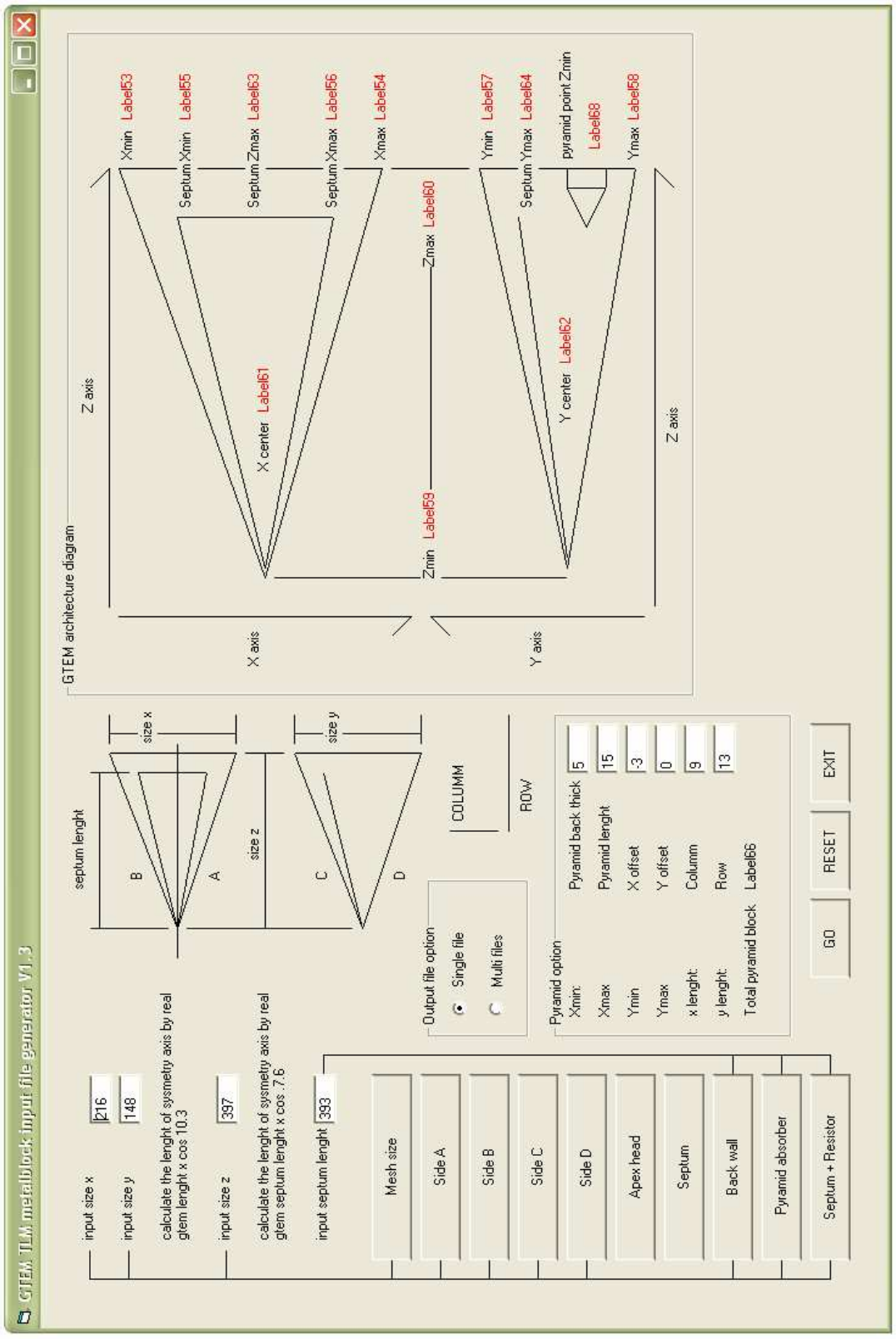

Figure 3.5 TLM solver input file generator software

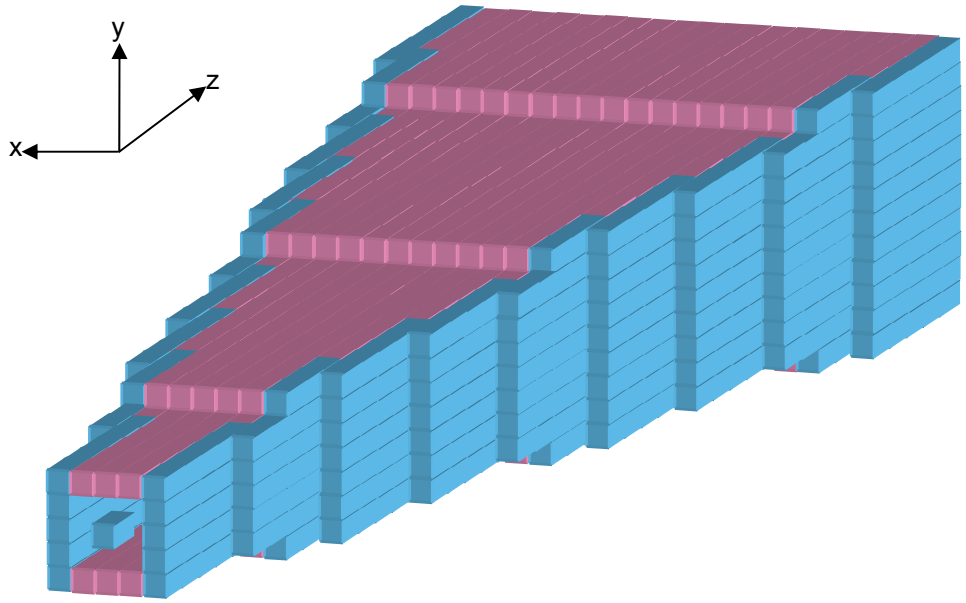

Figure 3.6 Structure of the GTEM model constructed using the cubic cells

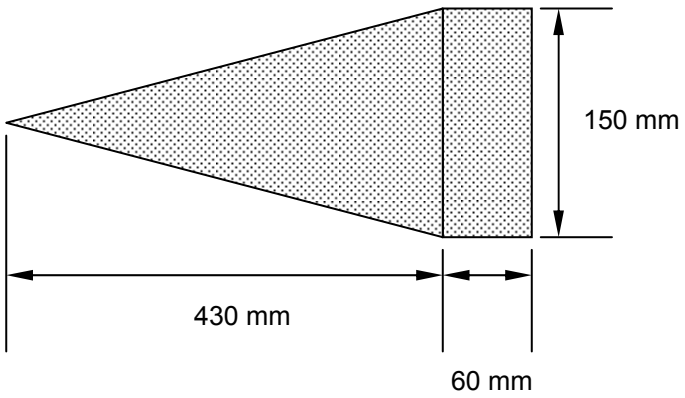

Figure 3.7 Size of the pyramid absorber in the GTEM cell 5407

The construction of the RAM is also through defining the required cells to form the shape of the pyramid. Each of the cells that define the whole pyramid has different material properties. The RAM used in the GTEM cell comprises of carbon loaded material and it has been found that its frequency dependent dielectric properties can be represented by multiple Debye relaxations [3]. The effective relative permittivity is given by:

$$\varepsilon_{r,eff}(s) = \varepsilon_{r\infty} + \frac{\sigma_e}{s\,\varepsilon_0} + \sum_{i=0}^{NP-1} \frac{\Delta\chi_{ei}}{1 + s\,\tau_{ei}} \tag{3.1}$$

where *NP* is the number of relaxations, $\Delta\chi_{ei}$ is the strength of the i^{th} relaxation and τ_{ei} is the time-constant of the i^{th} relaxation. Using a function called "multi-Debye-Dielectric" in the regSolve, each pyramid block is made to consist of multiple small cells with defined material properties. The airspace and pyramid material will differentiate themselves by different values of ε_r. The material properties used here are as in [8]. Figure 3.8 shows the arrangement of cells to represent the pyramidal shape. The coloured cells indicate different material properties (lossy material) compared to the white cells (free space).

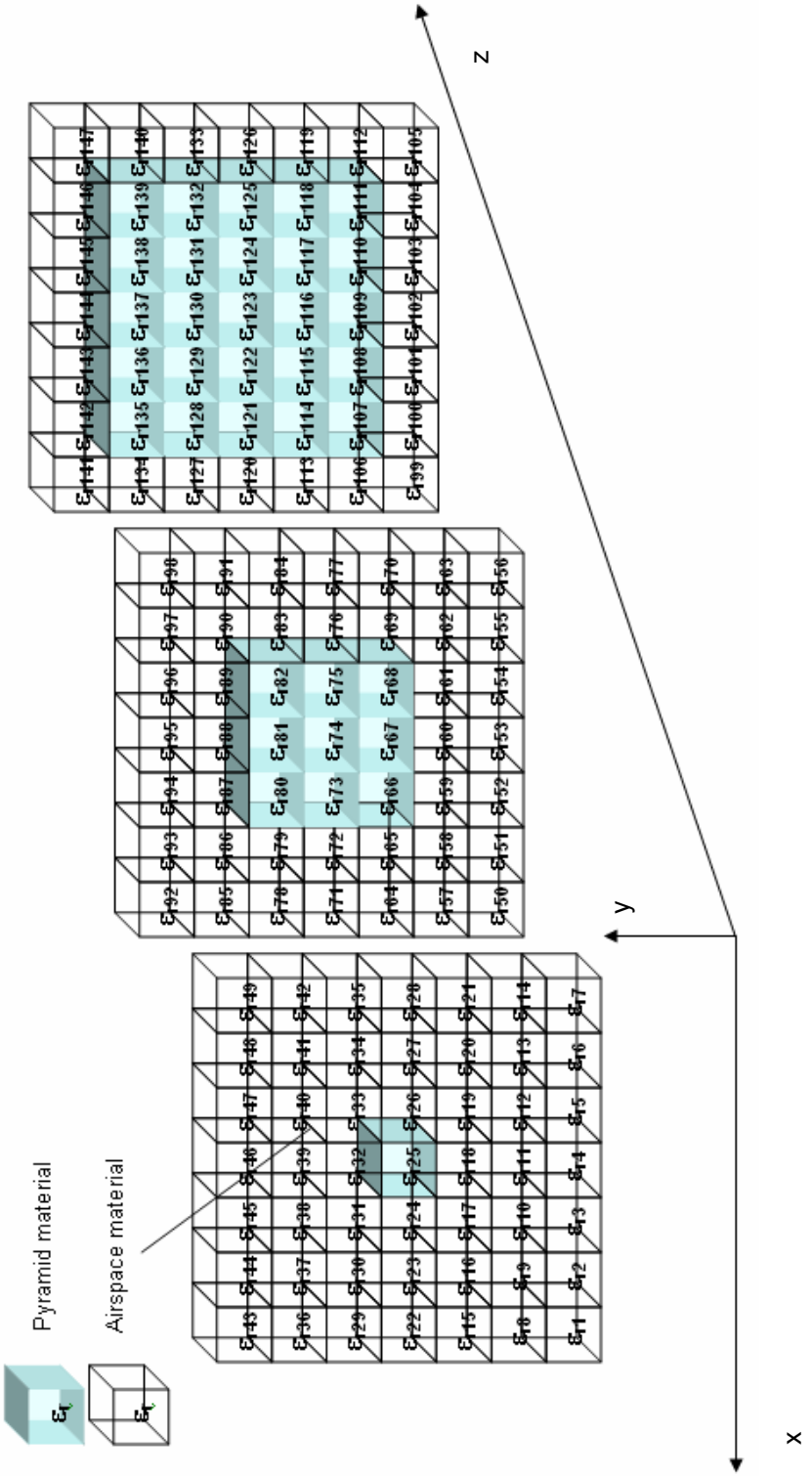

Figure 3.8 One pyramid block architecture

The resistor network installed at the end of the septum of a GTEM cell is of equal importance as the pyramid absorber. The resistor network serves as the termination for lower frequencies. The total resistance of the resistor network is designed to be 50 Ω to match the impedance of the GTEM cell. In the GTEM cell, the 50 Ω termination is implemented by a network of resistors as shown in Figure 3.9. The resistor distribution used in the model followed the same configuration as the real GTEM cell 5407. Once all the text files are combined into a single text file, it is then passed to the TLM solver for execution.

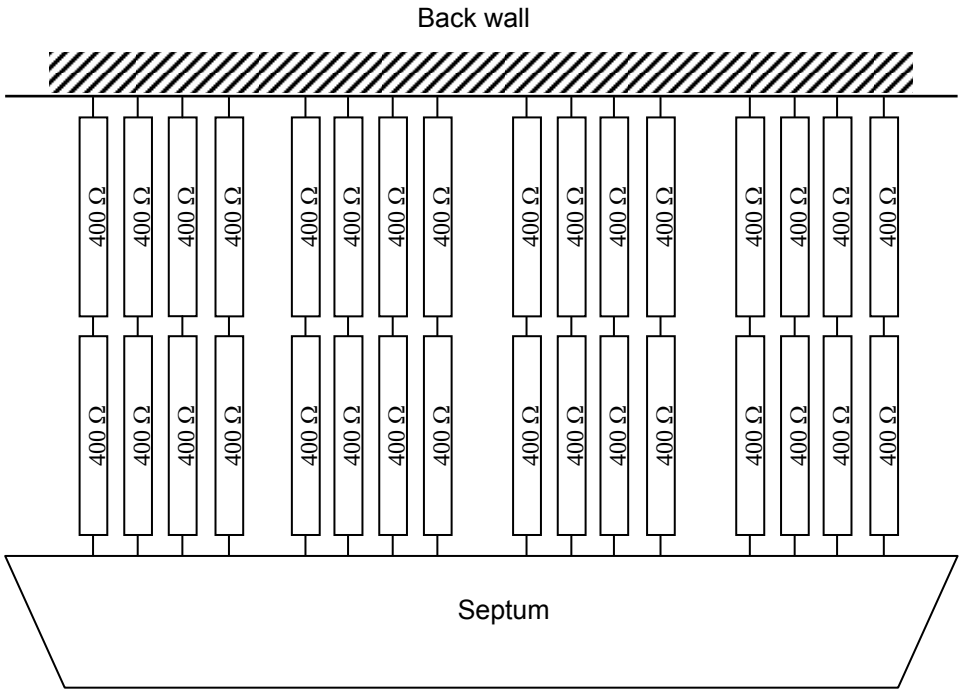

Figure 3.9 Resistor distributions in the GTEM cell termination

3.4 The differences between the GTEM model and the GTEM cell

Since the GTEM model is made of cubic cells, the model cannot mimic the exact geometry of the actual GTEM cell. The deviations between these two geometries are investigated in this section. The comparison performed in this section is important to ensure that the geometry of the model does not deviate significantly from the actual cell.

Figure 3.10 shows the actual geometry of a GTEM cell model 5407 according to the manufacturer datasheet while Figure 3.11 shows the resulting geometry of the GTEM model. A quick comparison shows how closely the geometry of the GTEM model resembles the physical GTEM cell itself including the pyramid model inside the GTEM model. The basic geometry of a pyramid absorber is shown in Figure 3.12. Table 3.1 lists all the geometrical differences between the GTEM cell and the model. The information presented in Table 3.1 shows that the stair-casing effect causes geometry deviations. These errors are investigated further in the following section.

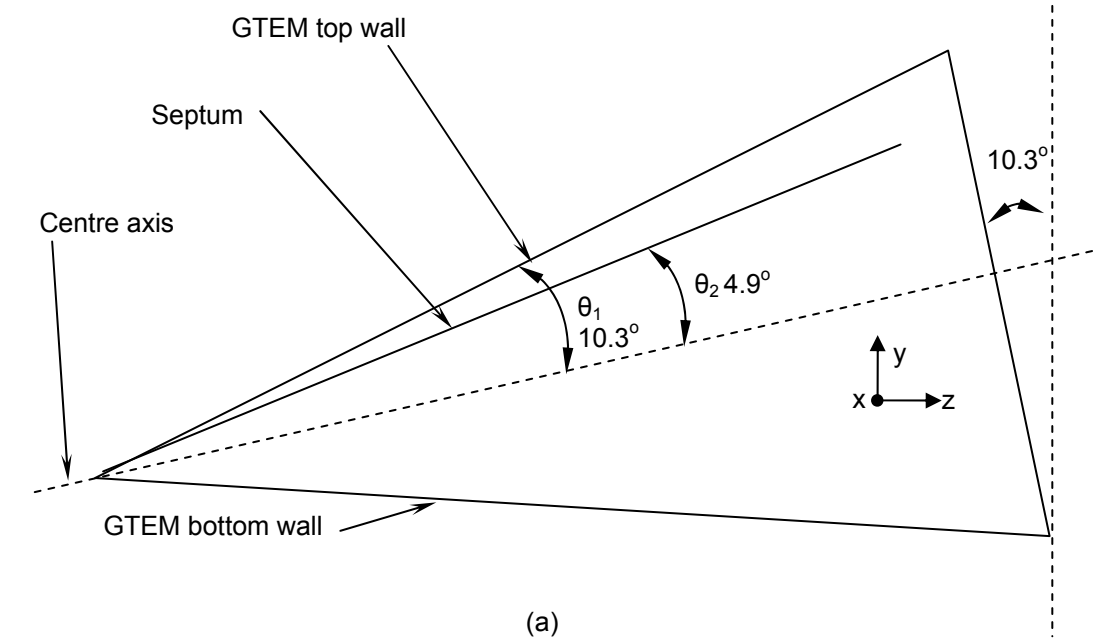

(a)

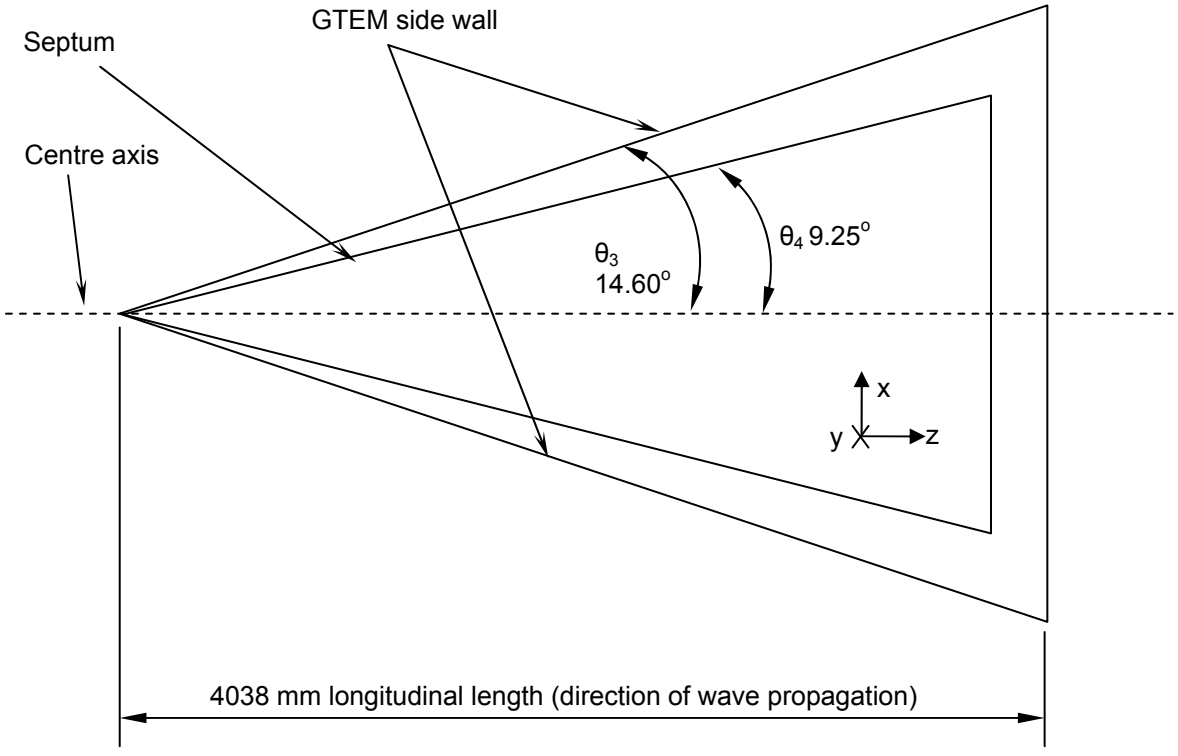

(b)

Figure 3.10 Angle specifications for the GTEM cell according to the manufacturer (ETS) data sheet for (a) side view and (b) top view

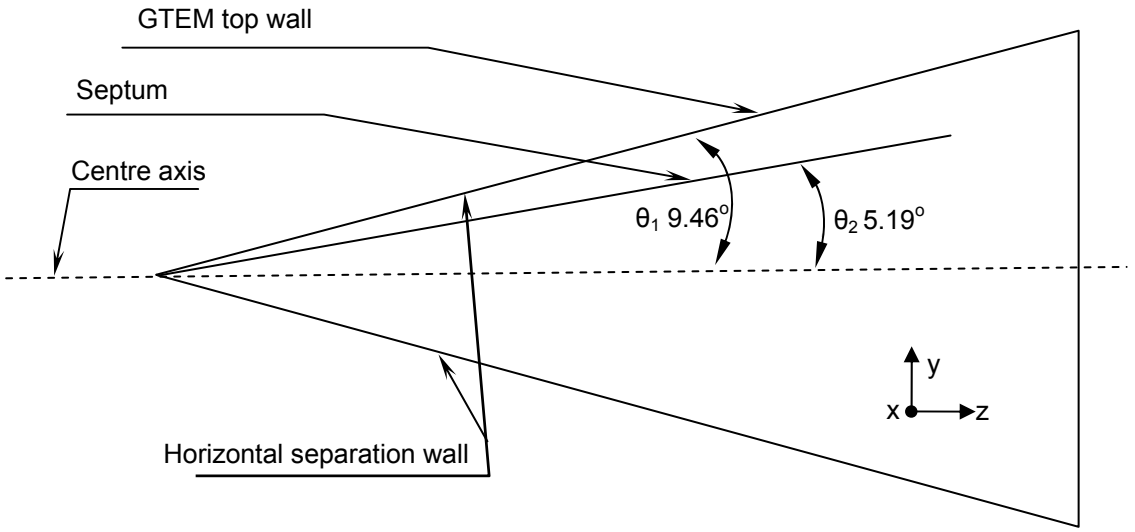

(a)

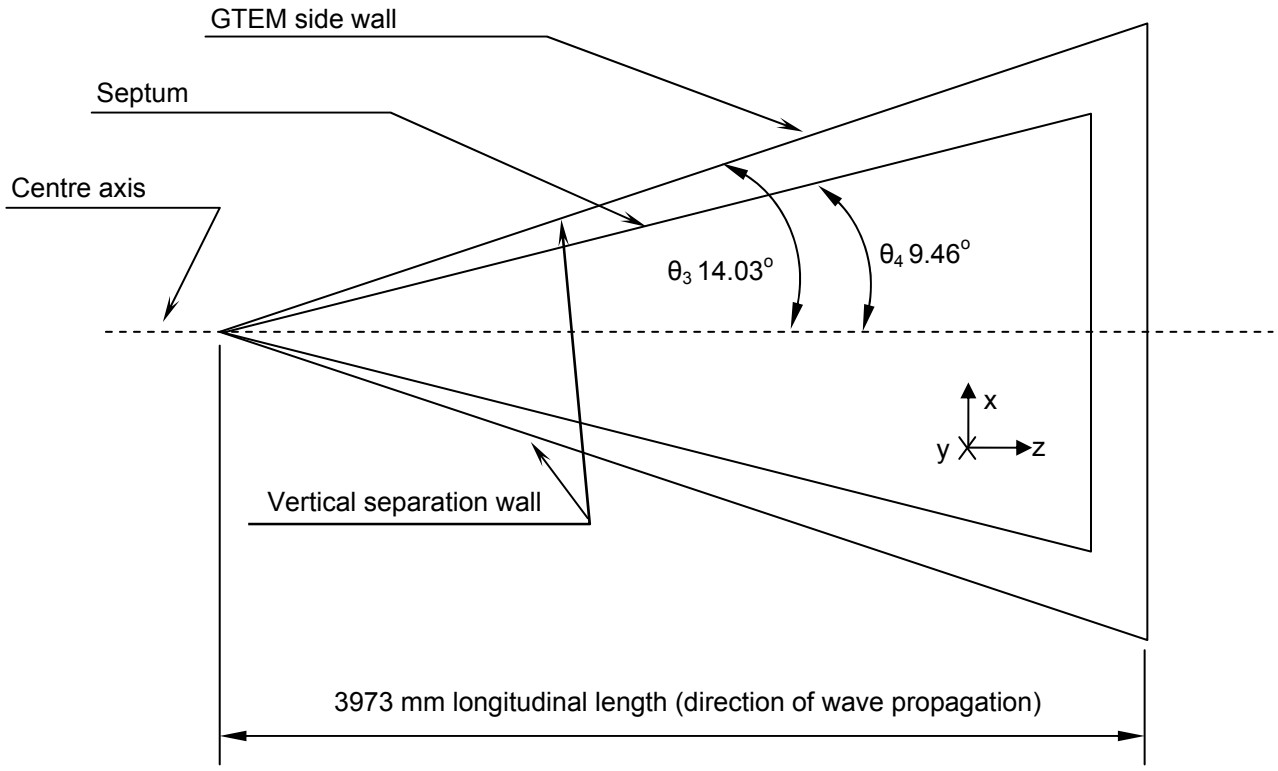

(b)

Figure 3.11 Angle specifications for the GTEM model for (a) side view and (b) top view

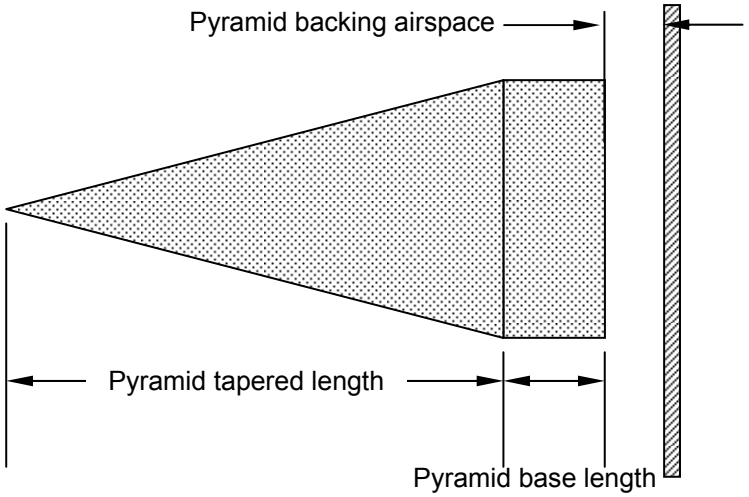

Figure 3.12 Major pyramid absorber geometries

Table 3.1

Geometry differences between the GTEM cell and the GTEM model in comparison

No	Characteristic	GTEM cell	GTEM Model	delta	Unit
1	Resistor quantity	2x16	1x16	-	-
2	Resistor value (per piece)	400	800	0	Ω
3	Horizontal wall separation (side to side) angle	20.60	18.92	1.68	degree
4	Vertical wall separation angle (top-bottom)	29.20	28.06	1.14	degree
5	Separation angle between septum and bottom wall	15.20	14.65	0.55	degree
6	Septum flaring angle	18.50	18.92	0.42	degree
7	Longitudinal length (direction of wave propagation)	4038	3973	65	mm
6	Model length per cell	-	20	-	mm
7	Maximum septum height	90	100	10	mm
9	Pyramid tapered length	430	500	70	mm
10	Pyramid base length	60	60	0	mm
11	Pyramid backing airspace	30	20	10	mm

3.5 The GTEM model error analysis

As previously mentioned, the asymmetric geometry condition of a GTEM cell makes it difficult to model using the Cartesian mesh environment. Square metal blocks were stacked in an appropriate manner to mimic angles that are required for the taper angle in a GTEM cell. By making such an approach, a systematic error known as the stair-casing error is introduced. This error cannot be eliminated but minimization of this error is possible. A way to minimize this error is to reduce mesh size so that the effects of the stair-casing can be significantly reduced. By doing this, the simulation time increases significantly. In this model, the mesh size was chosen to be 20 mm after taking account on its accuracy and simulation time.

The major systemic error due to stair-casing in this model is the ability of the stair-cased meshes to generate the required angles. Wrong angles lead to errors in height to width ratio in the GTEM model. These errors are discussed in the following sections. Another error described as the 'exponential effect in height to width ratio' will also be discussed.

3.5.1 Angle error

In the GTEM cell, there are four major angles involved. These are θ_1=10.3^o, θ_2=4.9^o, θ_3=14.6^o and θ_4= 9.25^o as shown in Figure 3.10. After these angles were formed in the GTEM model, an examination was made to consider the significant of deviations from the actual values. Figure 3.13 (a), (b) and (c) shows the nearest equivalent angles of 14.03^o, 9.46^o and 5.19^o to represent θ_3=14.6^o, θ_1=10.3^o and θ_4= 9.25^o, and θ_2 =4.9^o respectively. It can be seen that the square mesh has prevented the model from being flared according to the correct angle.

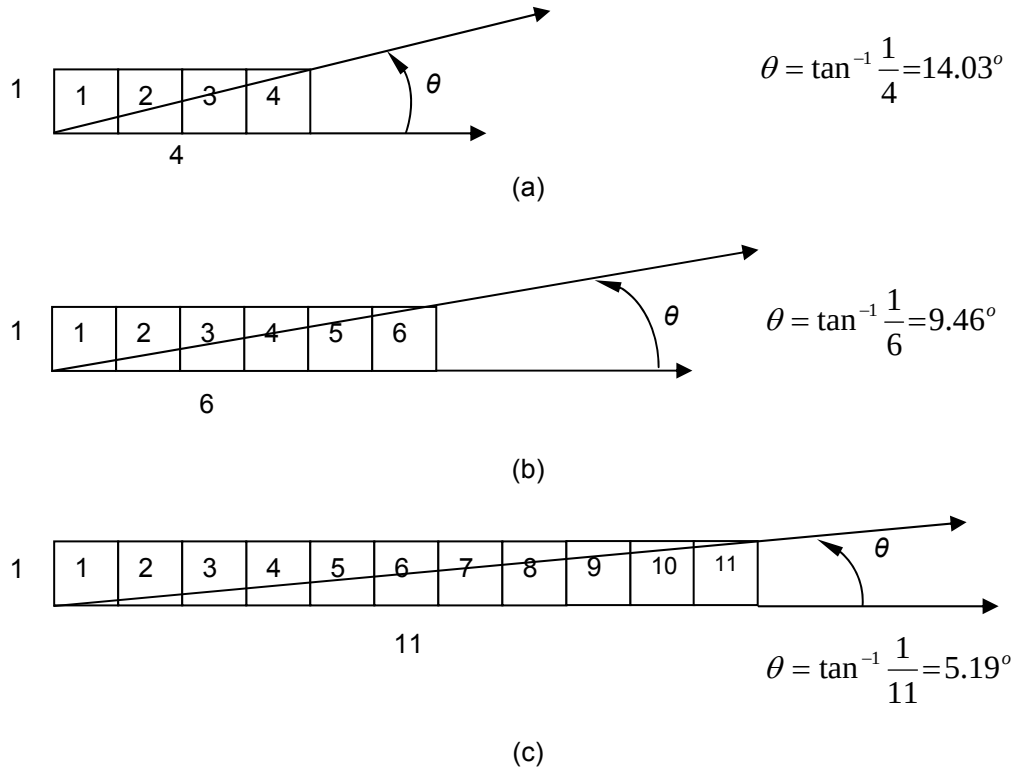

Figure 3.13 Three major angles used to construct the GTEM model using the stair-casing method

In order to get an idea on the severity of this angle error, an error calculation is presented below. The angle errors due to the stair-casing are:

For $\theta_1 = 10.3^o$

Mesh gradient type (b) Figure 3.13:

Error = | 10.3-9.46 | (3.2)

= 0.84^o

For $\theta_2 = 4.9^o$

Mesh gradient type (c) Figure 3.13:

Error = | 4.9-5.19 | (3.3)

= 0.29^o

For $\theta_3 = 14.6^o$

Mesh gradient type (a) Figure 3.13:

Error = | 14.6-14.03 | (3.4)

= 0.57^o

For $\theta_4 = 9.25^o$

Mesh gradient type (b) Figure 3.13:

Error = | 9.25-9.46 | (3.5)

= 0.21^o

It is noted that the approximation to mimic the correct angle with the TLM mesh was reasonable since all four required angles showed a small deviation of less than 1^{o}. These errors distort the characteristic impedance of the cell away from 50 Ω to a value of approximately 46 Ω (see Section 3.6).

3.5.2 Wrong height to width ratio

According to the analytical solution for characteristic impedance of a GTEM by Icheln [9], in order to get 49.01 Ω impedance, the ratio of the height (D) to width (A) ratio of 0.65807 is required. The definition of height (D) and width (A) is shown in Figure 3.14. The equivalent height (D) and width (A) were calculated from the angles obtained from Figure 3.13 of the GTEM model shown in Figure 3.11. The ratio obtained from this calculation based on the GTEM model is 0.665. This comes close compared to the analytical solution provided by Icheln [9]. From this important analysis, a ratio of 0.665 is needed to give acceptable impedance close to 50 Ω. Figure 3.15 shows the resulting height to width ratio due to the stair-case effect. However, the ratio along the length of the GTEM model is not consistently at the correct value as shown by the dashed line in Figure 3.15. The graph in Figure 3.15 shows four different periodic values (ratios). Each period of one particular value is categorized as a segment. Figure 3.16 shows one segment containing four different ratio values.

Along the transmission line of the GTEM model, only part ‘4’ in one segment was in the correct height to width ratio of 0.665 as shown in Figure 3.15. These four different values are mainly caused by the four different geometries that will repeat along the transmission line of the GTEM model to form the walls as shown in Figure 3.17. This is not a solvable problem because it is caused by the systematic error due to the stair- casing. These ratios will produce different characteristic impedances along the transmission line. However, it was found that the three ratios other than the 0.665 later converge exponentially from the apex of the GTEM model towards the far end termination to the correct value. The conclusion drawn from this is that the voltage near the apex will be slightly distorted by the impedance mismatch. The impedance gradually improves as the transmission line progresses towards the termination where the ratio changes to the required value of 0.665. This is proven later in the simulated voltage pulse at the very tip of the apex of the GTEM model (Figure 3.19). The exponential effect associated with the three incorrect ratios is explained further in the next section.

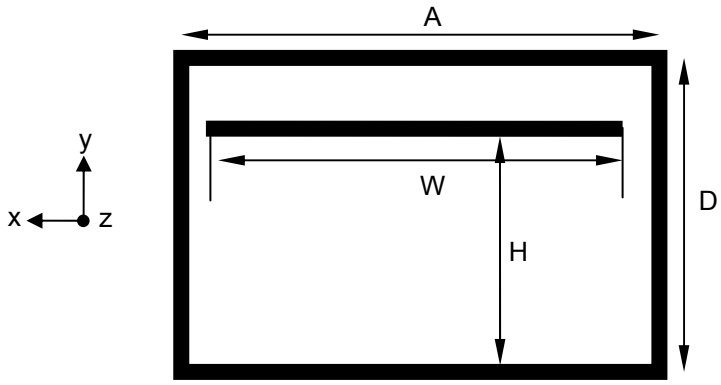

Figure 3.14 Height (D), width (A), septum width (W) and septum height (H) definition of a GTEM cell (cross sectional view)

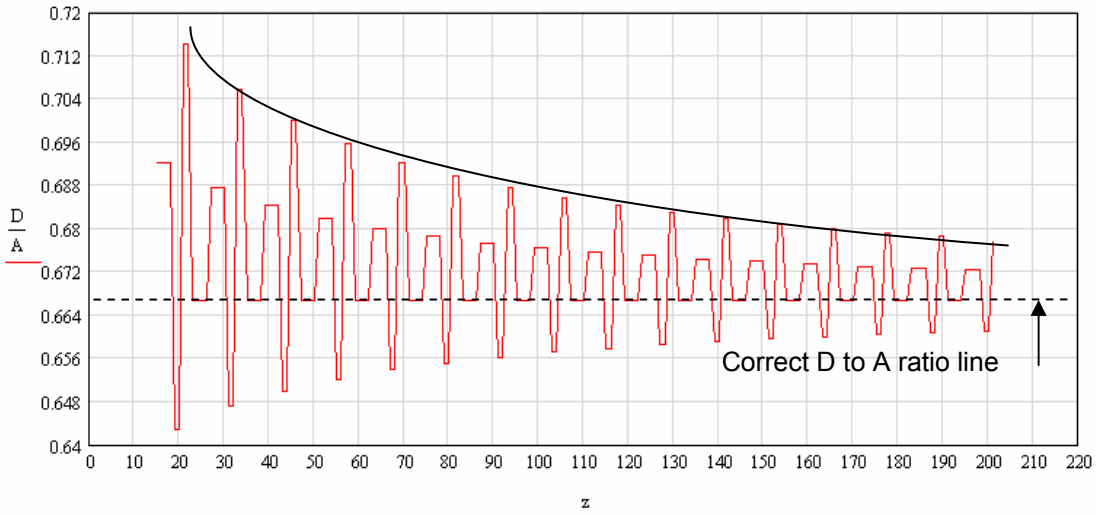

Figure 3.15 The GTEM Model height (D) to width (A) ratio

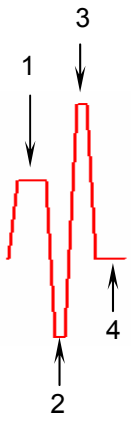

Figure 3.16 A segment containing four different height (D) to width (A) ratios

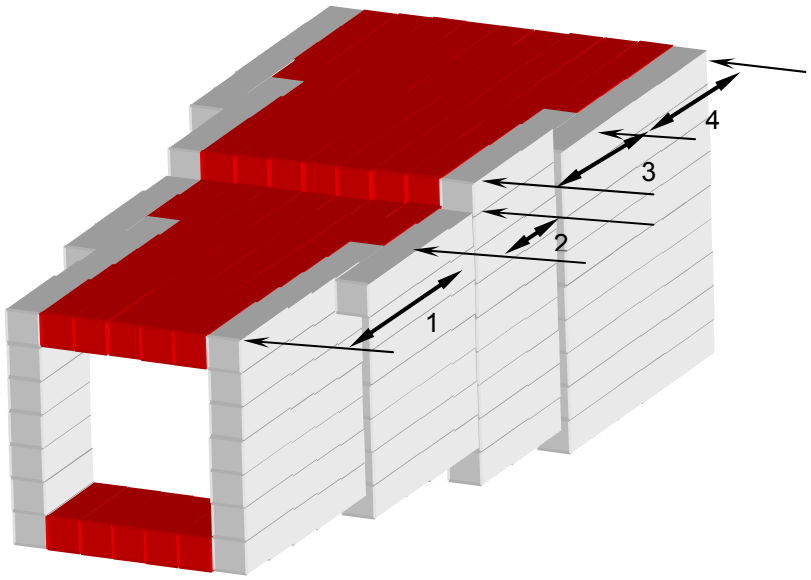

Figure 3.17 Four different repetitive values of the GTEM model geometries

3.5.3 Exponential effect in height to width ratio

This section presents a possible explanation on the exponential decrease of three of the four height to width ratios along the transmission line of the GTEM model. Near the apex of the model, the increase of one cell to form the required length makes a very significant contribution towards the total length of the measured area, whereas towards the far end of the cell, the increase of one cell is not very significant towards the overall length. This is illustrated in Figure 3.18.

In Figure 3.18 (a), the new increment of one cell is significant because the increment contributed 50% towards the new length B which is a 100% increase in comparison to the original length A. However, at the far end of the

GTEM model, shown in Figure 3.18 (b), the new increased one cell only contributed 20% towards the new length B which is a 25% increase compare to original length A. This condition explains the exponential effects in Figure 3.15 and affects the impedance near the apex of the GTEM model. The effect gradually reduces towards the far end of the model.

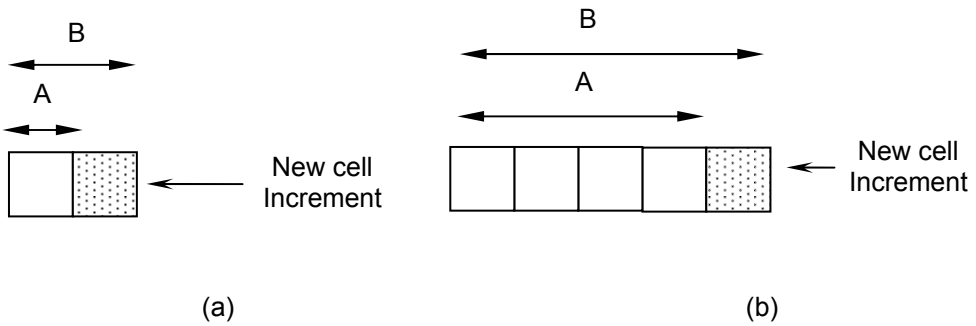

Figure 3.18 The contribution of one cell (shaded) towards the total length B for (a) small value of A and (b) larger value of A. A is the length before the increment

3.6 The GTEM model 50 Ω verification

A model has to be designed to match the characteristic of a real object as near as possible in order to produce reasonable results. This rule applies to the GTEM model as well. Even a complete look-alike model could be useless if the electrical behaviour of model was not as required. Therefore, verifications of a model are crucial before further results are presented.

The completed model of the GTEM cell required further testing and verification to ensure that, the result of the simulation will be accurate and reliable. The GTEM model is not guaranteed to be free from errors judging by

the extensive 20,000 lines of codes. Figure 3.19 shows the initial test run on the model using a pulse wave to test the electrical integrity of the model. The graph shows a mismatch in the transmission line judging from the reflections. Significant reflected voltage is observed when a pulse was sent from the tip of the septum towards the load resistor. The mismatch that occurred at this time, when investigated, was found to be caused by errors in the input file that represent the resistor network. This error was then corrected (Figure 3.21). Figure 3.19 shows the importance of the model verification. Without it, erroneous results will be produced in the form of reflections due to impedance mismatch that will compromise with further simulation results.

The model underwent three verification processes. The first verification process is simple but important in terms of the GTEM model shielding. A signal source is simulated inside the GTEM model while an output power is simulated outside the GTEM model shown in Figure 3.20. This simple simulation makes sure that the signal is contained inside the GTEM model. Should there be any leakage (e.g. due to gaps in model structure), a signal will appear at the output power. When this test was done, no external field outside of the GTEM model was detected. Thus, it can be confirmed that there was no leakage in the GTEM model.

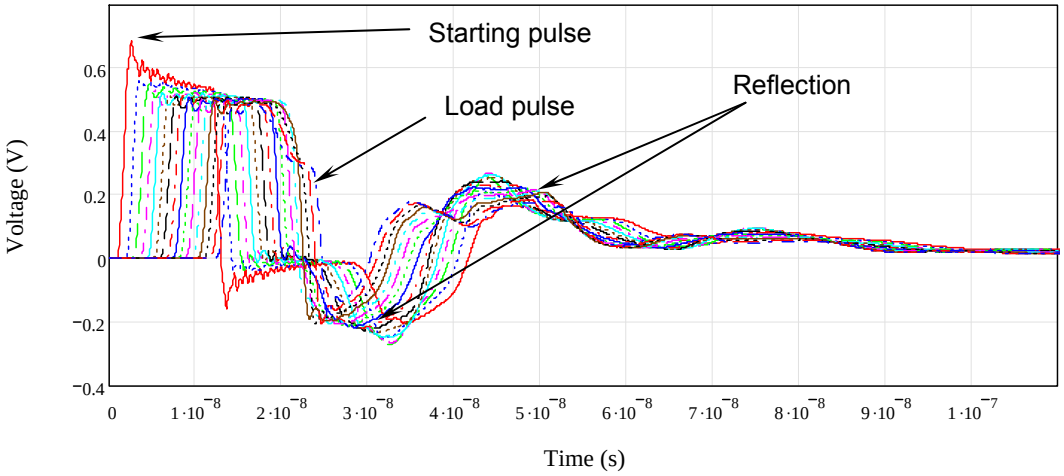

Figure 3.19 Transmission of a pulse in septum. Incorrect data in the transmission line model causes the reflected waves

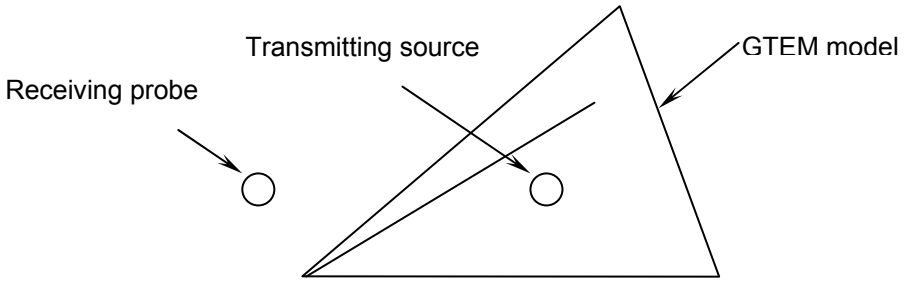

Figure 3.20 The GTEM shielding test

A single short trapezoid pulse was then launched from the apex of the GTEM model towards the end termination. The trapezoid had an amplitude of 1 V, rise time of 1 ns, high time of 10 ns, fall time of 1 ns and low time 1 μs. The voltage between the septum and the floor was simulated at locations along the length of septum to examine the amplitude of the trapezoid signal as it moves along the septum towards the end resistor termination. A faulty

model of the GTEM will cause reflected waves or standing waves pattern as seen earlier in Figure 3.19. After the correction of the problem indicated earlier, the pulse was again examined. The pulse propagation from the near end to the far end in the time domain is shown in Figure 3.21 (a) to (h). The GTEM model met these criteria because: First, from Figure 3.21, a voltage of 0.5 V was propagating along the septum from the near end to the far end, thus it is concluded that the impedance of the GTEM model is approximately matched to the load, the source and the transmission line. Second, a negligible reflected pulse is experienced.

It is expected from the voltage information obtained in the simulation (shown in Figure 3.21) that the impedance of the transmission line in the GTEM model is expected to approximate 50 Ω. To verify this, the third test involves simulating currents along the septum at the voltage probes' locations. This current data was used with the voltage data to calculate the impedance of the GTEM model as the signal propagates along the septum. The impedance corresponding to the locations where the voltages are simulated along the septum is also shown in Figure 3.21 (secondary axis). From this verification test, it is concluded that the GTEM model has a characteristic impedance of 46 Ω approximately.

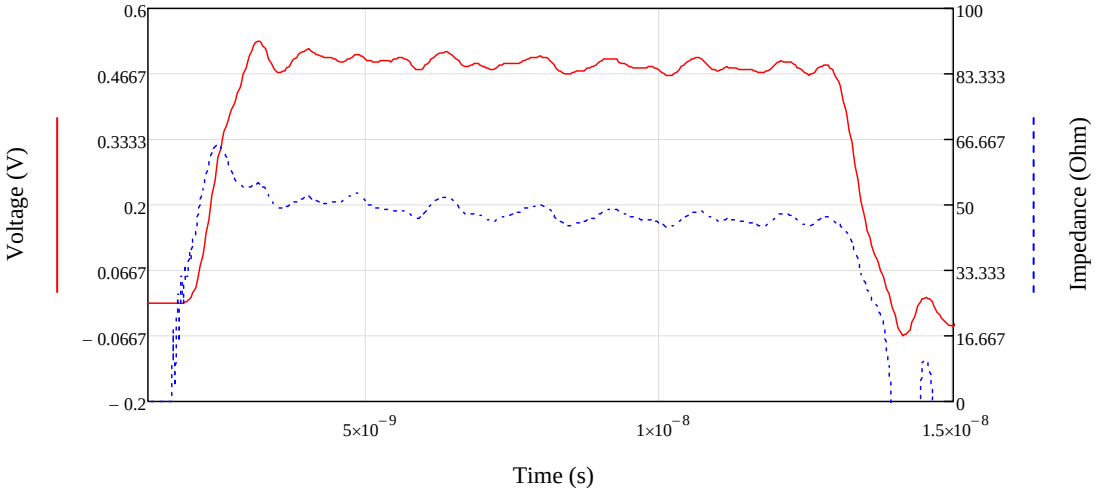
0.6
0.4667
0.3333
0.2
0.0667
– 0.0667
– 0.2
100
83.333
66.667
50
33.333
16.667
0
5×10^−9
1×10^−8
1.5×10^−8
Voltage (V)
Impedance (Ohm)
Time (s)

(a)

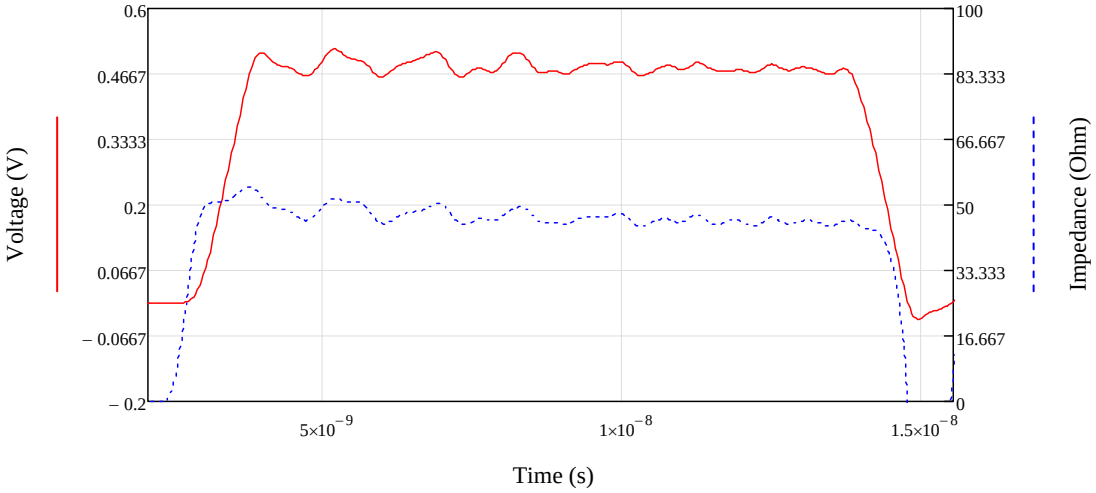
0.6
0.4667
0.3333
0.2
0.0667
– 0.0667
– 0.2
100
83.333
66.667
50
33.333
16.667
0
5×10^−9
1×10^−8
1.5×10^−8
Voltage (V)
Impedance (Ohm)
Time (s)

(b)

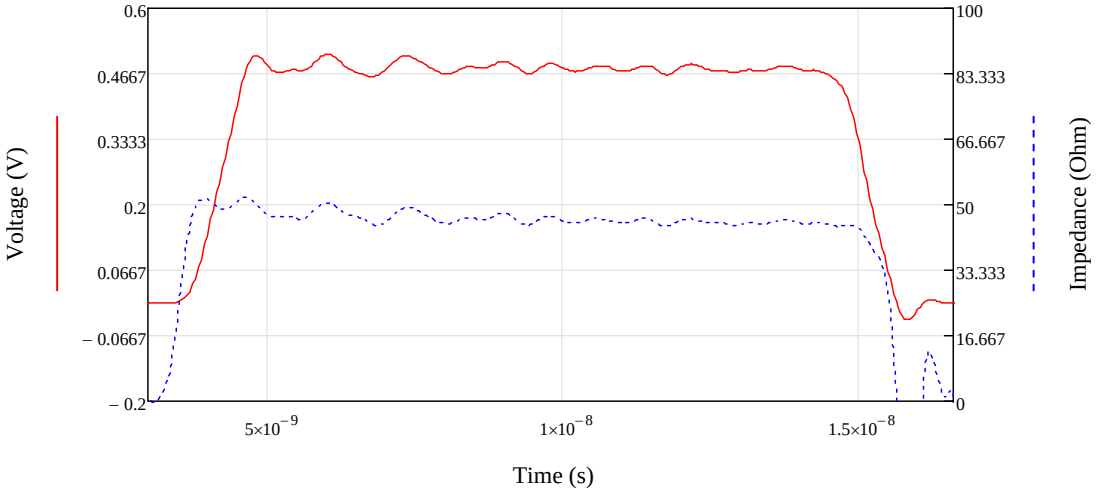
0.6
0.4667
0.3333
0.2
0.0667
– 0.0667
– 0.2
100
83.333
66.667
50
33.333
16.667
0
5×10^−9
1×10^−8
1.5×10^−8
Voltage (V)
Impedance (Ohm)
Time (s)

(c)

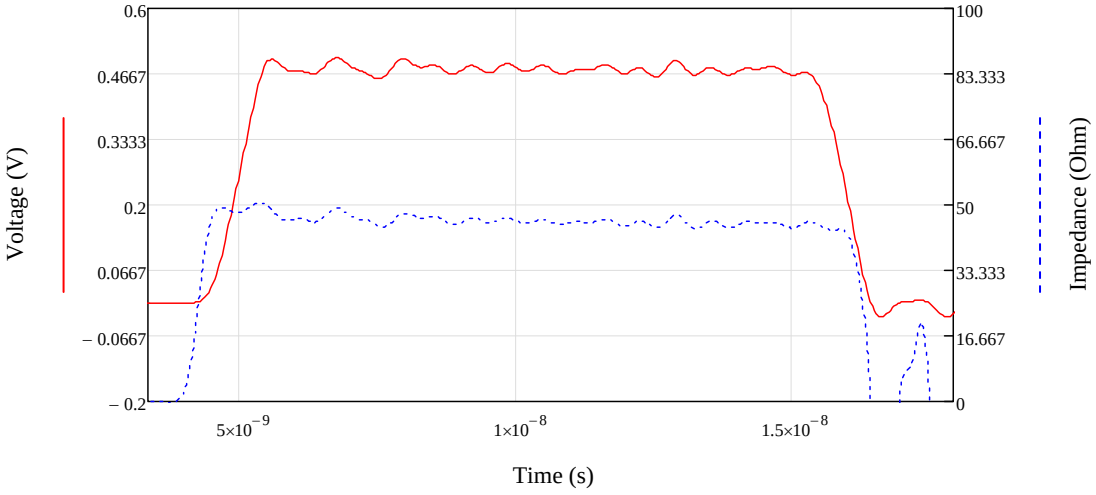
0.6
0.4667
0.3333
0.2
0.0667
– 0.0667
– 0.2
100
83.333
66.667
50
33.333
16.667
0
Voltage (V)
Impedance (Ohm)
5×10^−9
1×10^−8
1.5×10^−8
Time (s)

(d)

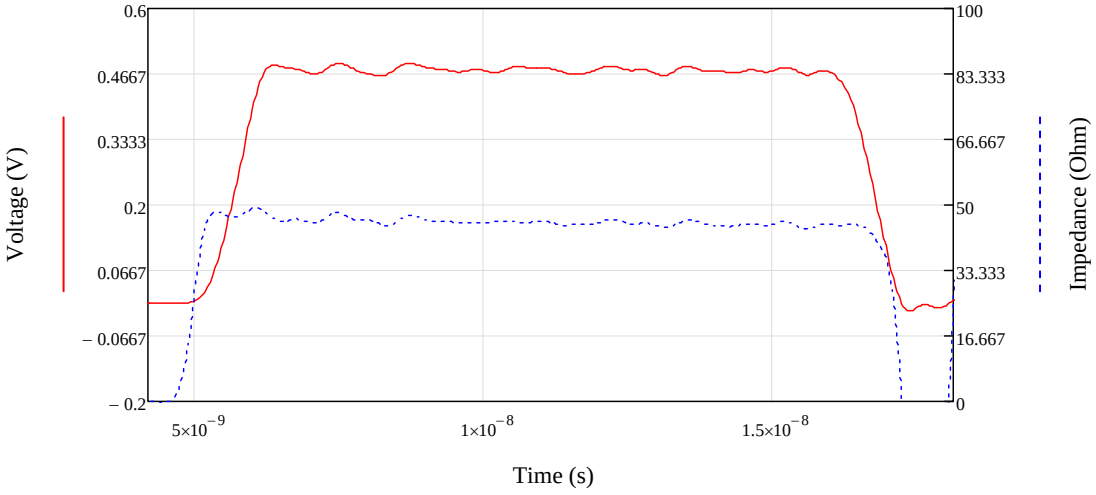
0.6
0.4667
0.3333
0.2
0.0667
– 0.0667
– 0.2
100
83.333
66.667
50
33.333
16.667
0
Voltage (V)
Impedance (Ohm)
5×10^−9
1×10^−8
1.5×10^−8
Time (s)

(e)

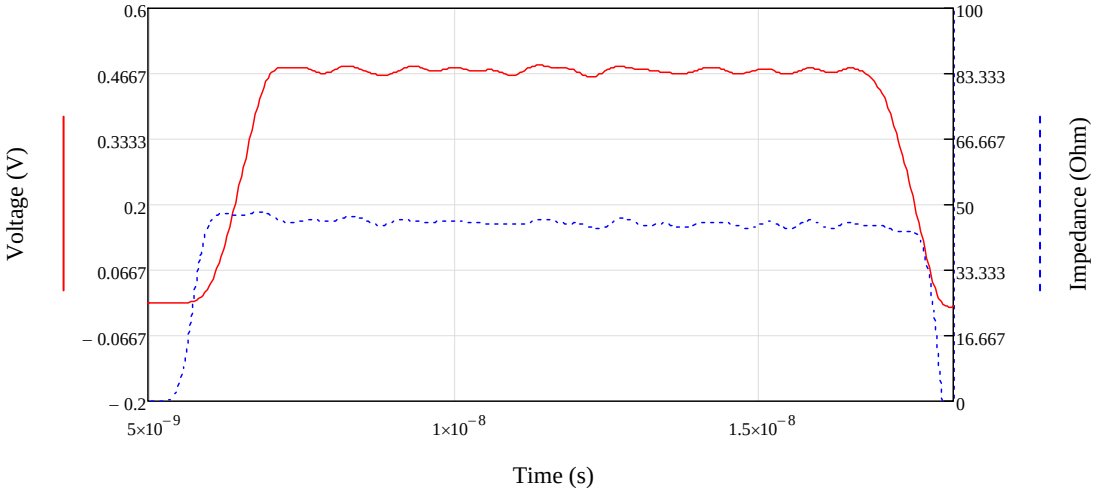
0.6
0.4667
0.3333
0.2
0.0667
– 0.0667
– 0.2
100
83.333
66.667
50
33.333
16.667
0
Voltage (V)
Impedance (Ohm)
5×10^−9
1×10^−8
1.5×10^−8
Time (s)

(f)

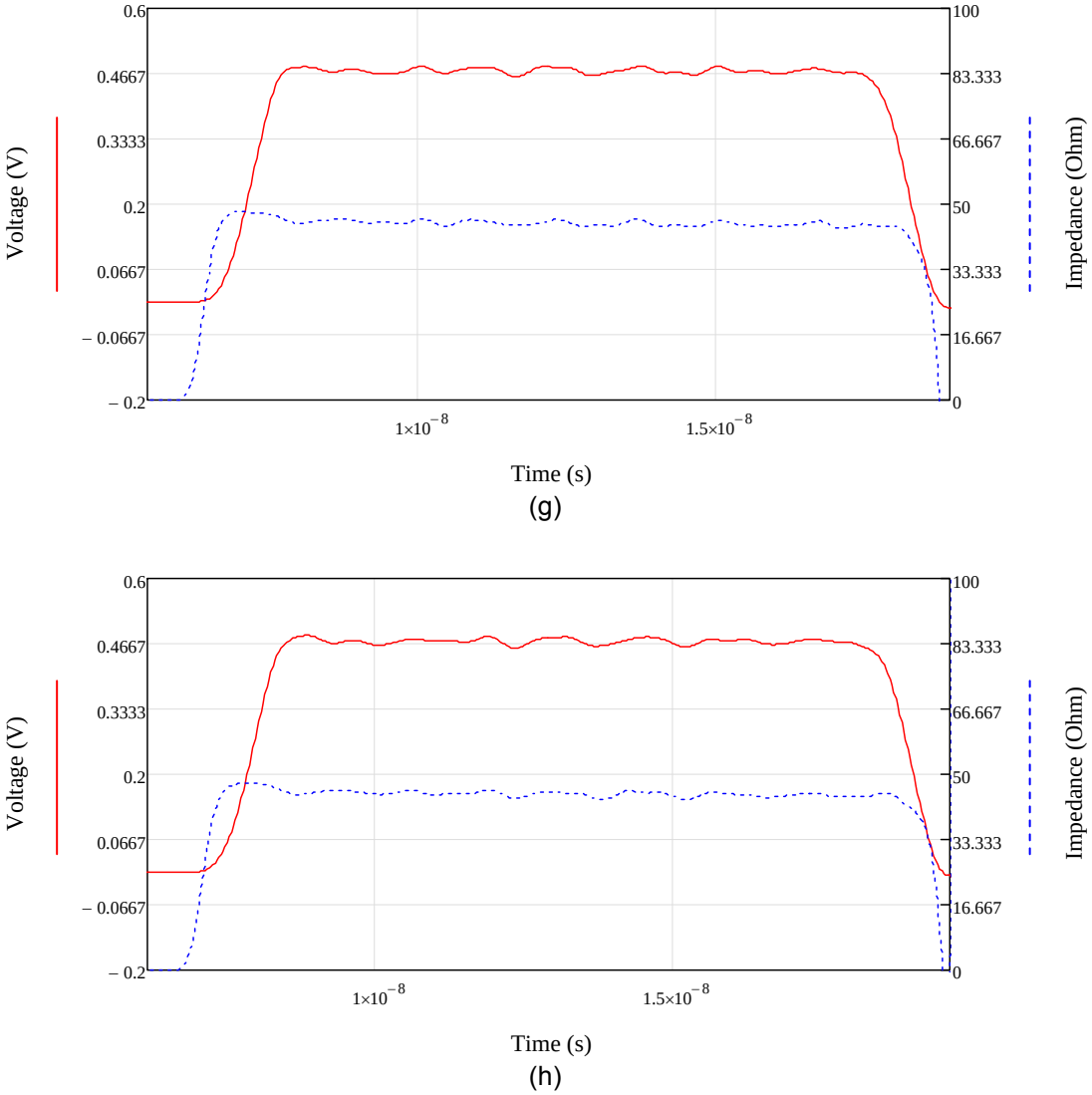

Figure 3.21 Pulse propagation and impedance along the GTEM model transmission line from near end (a) to far end (h)

An experiment was also performed to measure the impedance along the transmission line of the GTEM cell. This was done using a Time-Domain Reflectometer (TDR). The equipment transmitted a pulse and measured the reflected signal to calculate the impedance along the transmission line. This is shown in Figure 3.22. It was clear that the simulated impedance (≈46 Ω) is close but not exactly equal to 50 Ω. The reason for this discrepancy is that a consistent ratio of the height and width cannot be achieved due to the discreet meshing of the model. The obtained ratio is either higher or lower than the correct values due to the stair-casing effect. In Figure 3.22, point ‘a’ defines the starting point in the port of TDR; region ‘b’ is along the cable; point ‘c’ is the starting point of the GTEM cell; region ‘d’ is along the GTEM cell and point ‘e’ is the end termination of the GTEM cell. This measurement confirmed the characteristic impedance of 50 Ω of the real cell.

By completing these three tests, the model has now been verified as fit for purpose and this should give more confidence in the reliability of the following simulations. Further verifications involving comparing results with that obtained from measurements are presented in the following sections.

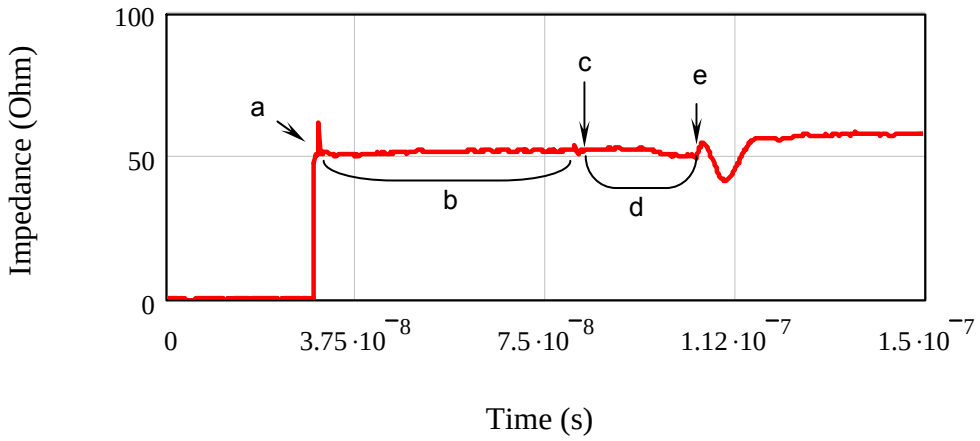

Figure 3.22 Measured impedance using Time-domain-Reflectometer

3.7 Electric and magnetic field distributions

Once the GTEM model had been electrically verified, the model can then be used in the study of the GTEM cell characteristics. In this section, the characteristics of electric and magnetic field distributions were examined. The electric and magnetic field distributions were simulated at the cross section plane of the GTEM model at the usable volume. A useable volume is defined as the volume where the electric field distribution is approximately uniform. The vertical electric field E_y is the dominant electric field component in the GTEM cell. The field distributions of other components i.e. E_x, E_z, H_x, H_y and H_z were also examined.

In normal operation of a GTEM cell, ideally, it is assumed that the TEM wave is the only mode that propagates inside the GTEM cell. This TEM wave is dominated by the E_y and H_x field components. The simulated electric field

components E_x, E_y and E_z at 100 MHz are shown in Figure 3.23 (a) – (c) respectively at the cross section where the septum is 0.75 m from the floor. This field was generated by a 9 V signal at 100 MHz applied at the port of the cell. The vertical electric field E_y shown in Figure 3.23 (b) is the main interest for EMC emission and susceptibility testing. From these Figures, it is concluded that E_x and E_z also contribute to the total field in the GTEM cell. The magnitude of E_x field is less than the magnitude of E_z field. These two components are known as the cross-polar components and they give a useful insight in the actual coupling characteristics inside the GTEM cell.

Printed circuit boards (PCBs) can cause electromagnetic emissions from loops formed by the tracks on the PCB. Therefore, in examining the magnetic dipole moment inferred from emission measurement in the GTEM cell, it would also be valuable to examine the behaviour of the magnetic field inside the GTEM cell. Figure 3.24 (a) – (b) shows the magnetic fields components of H_x, H_y and H_z respectively at 100 MHz at 0.75m septum height. As expected, the contribution of H_x field is larger than H_y and H_z because it is part of the dominant TEM mode. Hence, it is more accurate to refer to the TEM wave as the dominant mode as other modes do also exist in the GTEM cell. The existence of the other modes causes the cross polar coupling of the GTEM cell.

The pattern of the field distribution agrees well with other numerical models reported in [4, 10-18]. A summary drawn from these field plots is that the main coupling in the GTEM cell is contributed by E_y and H_x in the test

volume. However, it is observed that the other field components namely the E_x, E_z, H_x, H_y and H_z have significant impact in the useable test volume too. The power measured at the output port of the GTEM cell could be due to the contribution from one, or more of the field components mentioned, depending on the orientation and emission characteristics of the EUT. The electric field intensity plots in Figure 3.23 and 3.24 suggest that actually the usable volume where by the E_y is uniform is indeed very small. The bigger the volume of the EUT, the more interactions from the unwanted modes will occur. These other modes cause errors in the GTEM cell measurements.

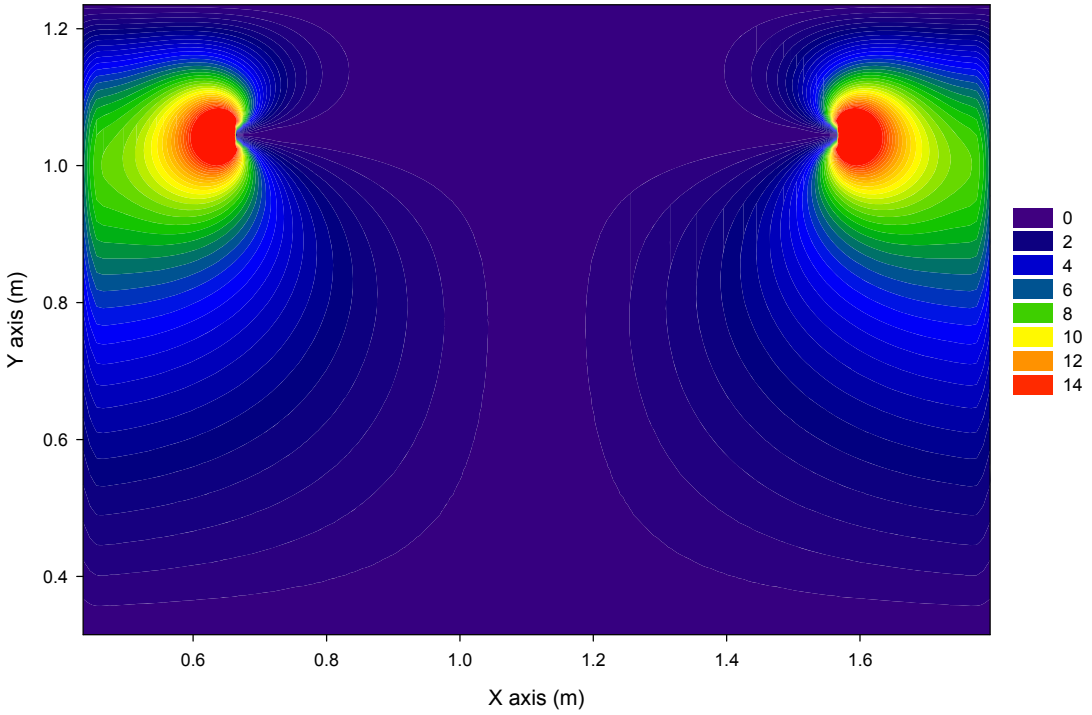
1.2
1.0
0.8
0.6
0.4
Y axis (m)
0.6
0.8
1.0
1.2
1.4
1.6
X axis (m)
0
2
4
6
8
10
12
14

(a)

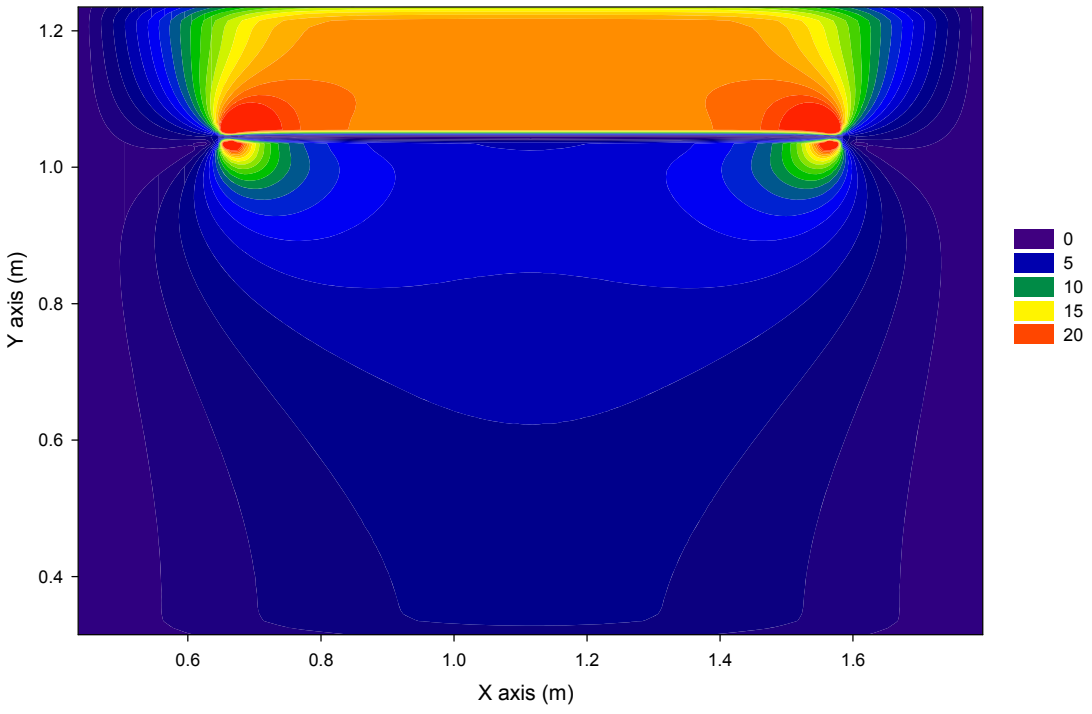
1.2
1.0
0.8
0.6
0.4
Y axis (m)
0.6
0.8
1.0
1.2
1.4
1.6
X axis (m)
0
5
10
15
20

(b)

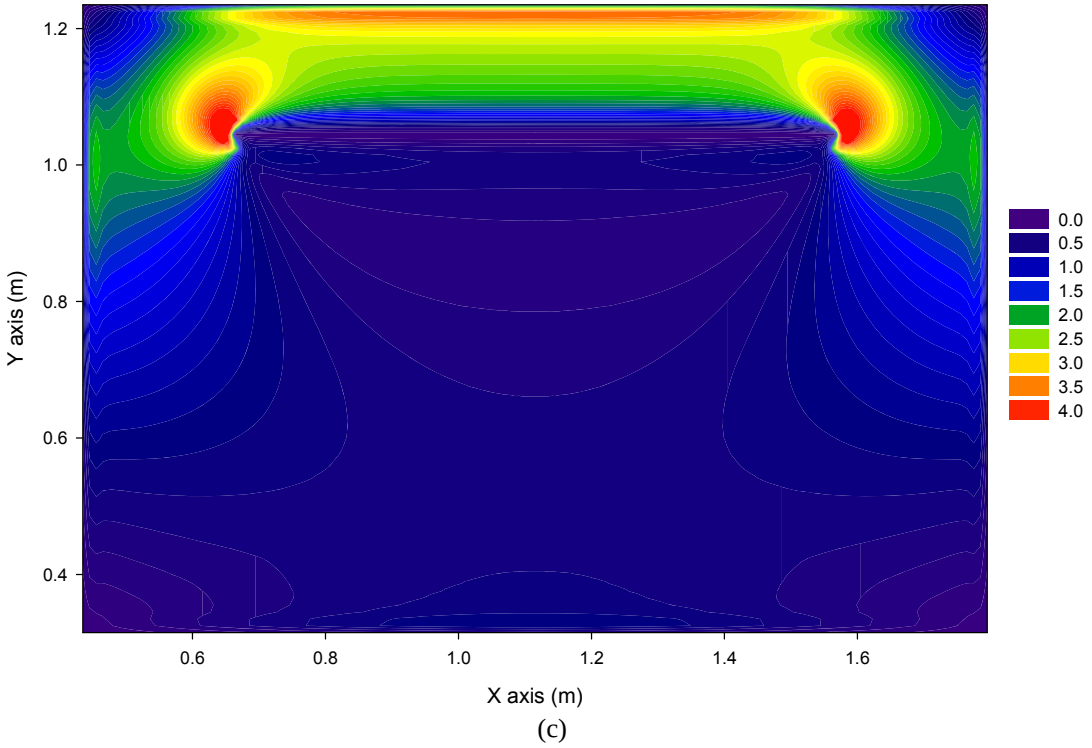

(c)

Figure 3.23 Simulated (a) E_x field (b) E_y field and (c) E_z field distribution for a transversal cross section and at 100 MHz at 0.75 septum height. Legend unit is in V/m

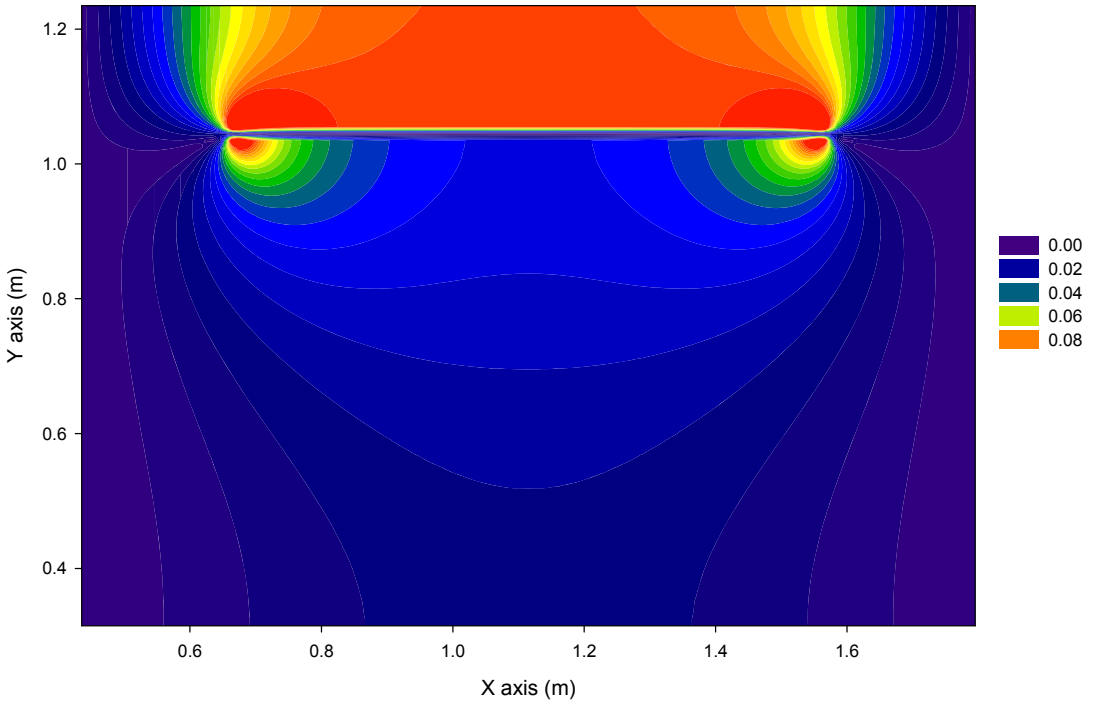
1.2
1.0
0.8
0.6
0.4
Y axis (m)
0.6
0.8
1.0
1.2
1.4
1.6
X axis (m)
0.00
0.02
0.04
0.06
0.08

(a)

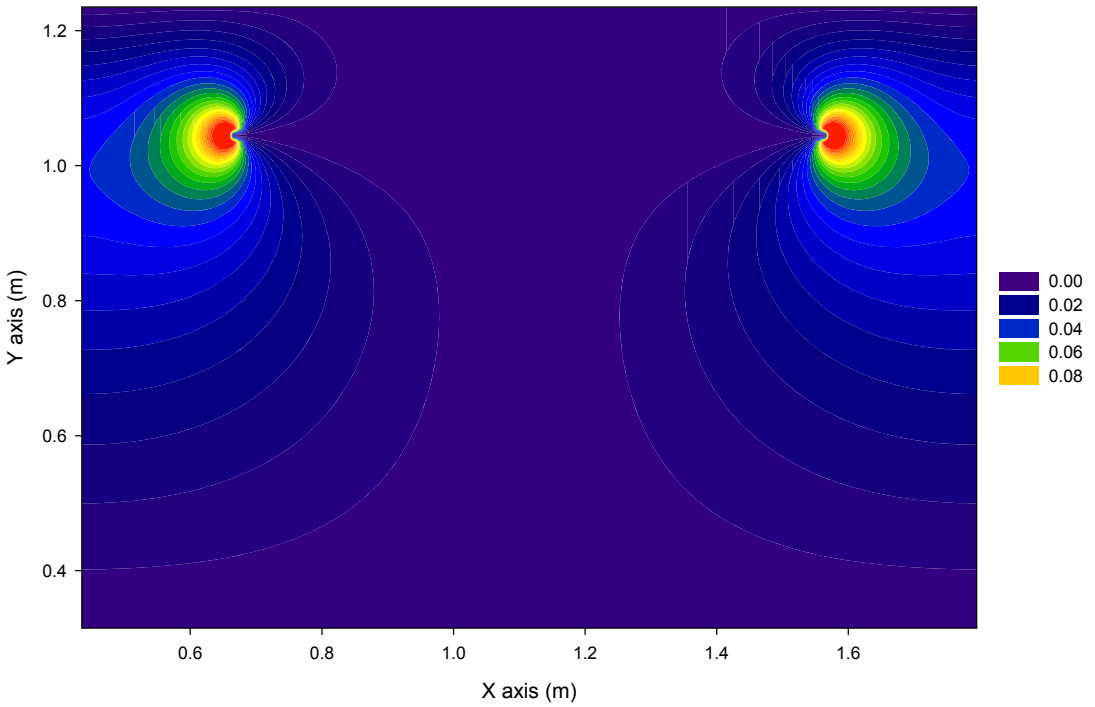
1.2
1.0
0.8
0.6
0.4
Y axis (m)
0.6
0.8
1.0
1.2
1.4
1.6
X axis (m)
0.00
0.02
0.04
0.06
0.08

(b)

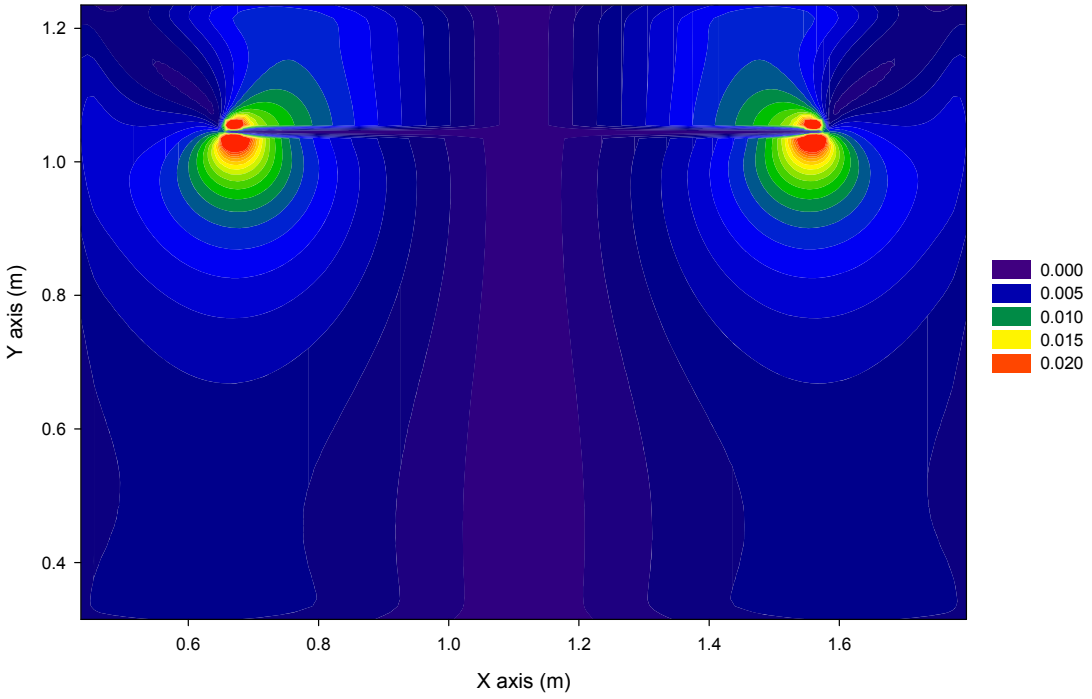

(c)

Figure 3.24 Simulated (a) H_x field (b) H_y field and (c) H_z field output for a transversal cross section and at 100 MHz at 0.75 septum height. Legend unit is in A/m

Since E_y is of primary interest as specified in the standards, this field was further examined in the numerical model as well as in experiments. A direct comparison between the simulation and experiment was made.

In the experimental work, a signal generator (Agilent E8257C) was used to generate the signal for the GTEM cell using the same voltage magnitude as in the TLM model. The TLM model uses an arbitrary signal of 100 MHz and 9 V (peak-to-peak) which is equivalent to 23.06 dBm (calculated) as the input power at the port of the GTEM cell. These values are arbitrarily chosen. A xyz electric field probe (DARE RadiSense Electric Field Probe) was placed at the same height of 0.38 m above the floor as in Figure 3.25. The simulated and measured vertical electric fields at a height of 0.38 m from the floor are shown in Figure 3.26 (a) and (b) respectively. The measured result shows reasonable agreement with the simulation. The small differences are probably due to the presence of the access door and other small features not included in the model.

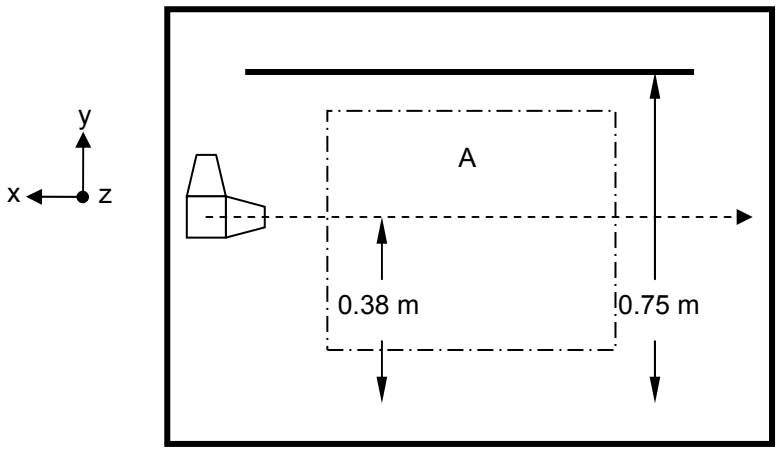

Figure 3.25 Cross sectional view of the GTEM cell. Volume A shows the usable volume of the GTEM cell. Experimental configuration of an electric field probe moving along the dotted line in the x- direction at 0.38 m from the GTEM cell floor at 0.75 m septum height

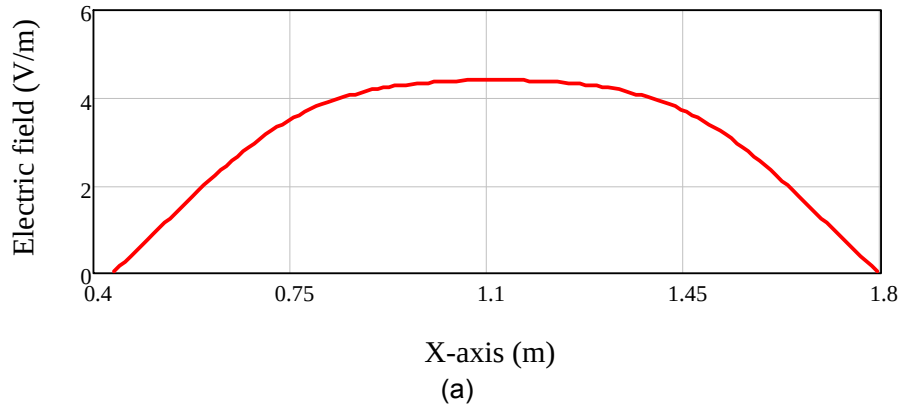

(a)

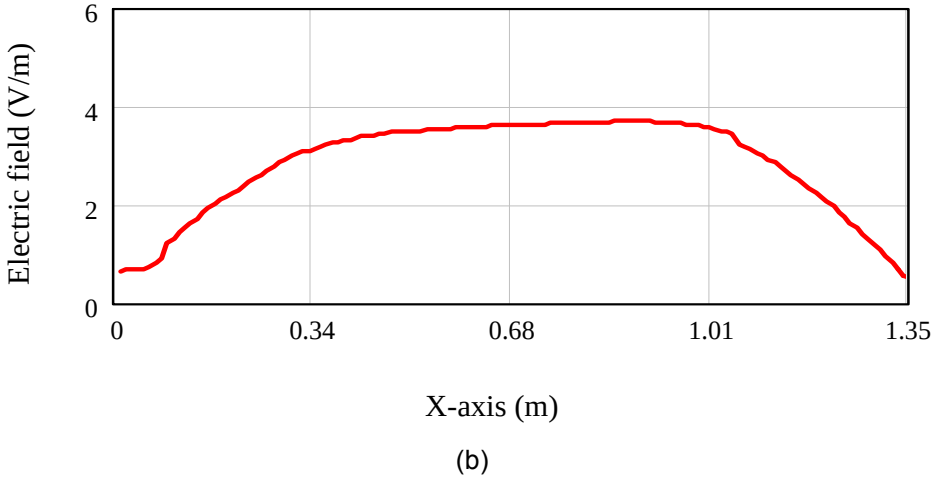

(b)

Figure 3.26 (a) Simulated E_y and (b) measured E_y field output at transversal cross section at 100 MHz at 0.38 m from the floor at a septum height of 0.75 m

3.8 Normalized y-component electric field

According to [19], the algorithm to calculate total radiated power of an EUT requires the primary y component of the TEM mode electric field. Higher order modes do not couple directly into the TEM cell. The e_{oy} is the normalized y component of the electric field of the TEM mode at a particular test location. The term 'normalized' here refers to the electric field generated by 1 W input power. To obtain information on the normalized TEM mode component e_{oy}, further calculations are required.

In the next sub-section, comparisons between various methods to obtain e_{oy} are described. It is important to understand the comparison chart in Figure 3.27 to prevent confusion. First, a comparison between methods to obtain E_y was made between analytical E_y *(ana)*, numerical E_y *(num)* and experimental E_y *(exp)*. The normalized TEM mode component (e_{oy}) can be obtained via two approaches; from experiment and analytically. Both approaches were used to calculate e_{oy} for the numerical model and experiments. This resulted in four different estimates of e_{oy} as shown as in Figure 3.27.

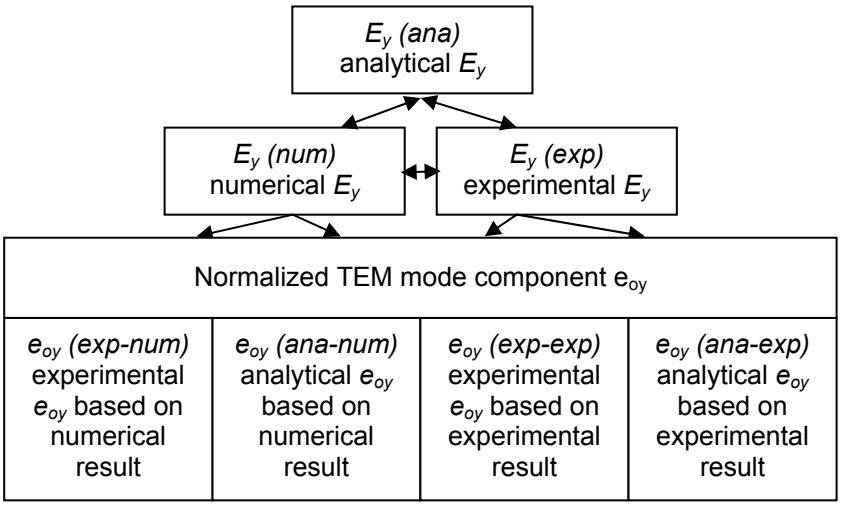

E_y : Vertical electric field

e_{oy} : Normalized TEM mode component

Figure 3.27 Chart showing the notation used for comparison between analytical, numerical and experimental vertical electric field; and different normalized TEM mode components

(A) Analytical E_y (ana)

In TEM propagation, an electric field is established between the septum and the floor when a voltage is applied between the septum and the GTEM cell floor. The generated electric field can be calculated using equation:

$$E_y = \frac{V}{h} \quad \text{V/m} \tag{3.6}$$

where E_y is the electric field in the y direction generated by voltage V across the separation h between the septum and the floor assuming the electric field

is uniform in the GTEM cell. This fact is used by the GTEM cell manufacturer [7] to act as a guide to approximate the y-component electric field from a known input power source. The electric field calculated analytically at 0.38 m (about half of the total septum height of 0.75m) from the cell floor was generated by a 9 V (peak-to-peak) signal at 100 MHz. Hence:

$$Ey_{(ana)} = \frac{3.1815\ \text{Vrms}}{0.7500\,\text{m}} = 4.242\ \text{V/m} \tag{3.7}$$

(B) Numerical E_y (num) and experimental Ey (exp)

From Figure 3.26 (a), the *E_y (num)* electric field at the centre of the cell is 4.22 V/m. Figure 3.26 (b) shows the *E_y (exp)* electric field at the centre of the cell is 3.7 V/m**.**

(C) Experimental e_{oy} (exp-num) based on numerical result

From the numerical data *E_y(num)*, the *e_{oy}(exp-num)* is calculated to simulate the experimental procedure. From numerical model *E_y(num)* is 4.223 V/m

$$Power\ \ input = \frac{Vrms^2}{Z} = \frac{3.1815^2}{46} = 0.2200\,\text{W} \tag{3.8}$$

$$e_{oy}(exp\text{-}num) = \frac{E_y(num)}{\sqrt{Power\,input}} = 9.003\ \sqrt{\Omega}/m \tag{3.9}$$

(D) Analytical e_{oy} (ana-num) based on numerical result

According to Wilson [20], the normalized TEM mode component can be analytically approximated with the equation:

$$e_{oy} = \frac{4}{a}\sqrt{Z}\left[\sum_m \left(\frac{\cosh\left(\frac{m\pi y}{a}\right)}{\sinh\left(\frac{m\pi h}{a}\right)}\cos\left(\frac{m\pi x}{a}\right)\sin\left(\frac{m\pi}{2}\right)J0\left(\frac{m\pi g}{a}\right)\right)\right] \tag{3.10}$$

where:

a is the cell width in metre

Z is the impedance of the cell

h is the septum height in metre

g is the width of the gap between the septum and the side wall in metre

x,y,z is the location of the EUT centre in metre

J0 is the zero-order Bessel function

m is a odd number range variable (1,3..∞)

From the numerical model, *a* = 1.39 m; *Z* = 46 Ω; *h* = 0.75 m; y = 0.38 m; *x* = 0 m; *g* = 0.25 m. Substituting these values into Equation (3.10) resulted in $e_{oy}(cal)$ as 8.838 $\sqrt{\Omega}/m$.

(E) Experimental e_{oy} (exp-exp) based on experimental result

From the experimental data $E_y(exp)$, the $e_{oy}(exp\text{-}exp)$ is calculated using the experimental procedure. From *Ey(exp)* is 3.7 V/m

$$\begin{aligned} Power\ input &= \frac{Vrms^2}{Z} \\ &= \frac{3.1815^2}{50} \\ &= 0.2020\ \text{W} \end{aligned} \tag{3.11}$$

$$\begin{aligned} e_{oy}(exp\text{ - }exp) &= \frac{E_y(exp)}{\sqrt{Power\ input}} \\ &= 9.193\ \sqrt{\Omega}/m \end{aligned} \tag{3.12}$$

(F) Analytical e_{oy} (ana-exp) based on experimental result

From the real GTEM cell structure, *a* = 1.40 m; *Z* = 50 Ω; *h* = 0.75 m; *y* = 0.38 m; *x* = 0 m; *g* = 0.27 m. Substituting these values into (3.10) resulted in $e_{oy}(cal)$ as 9.224 $\sqrt{\Omega}/m$.

The results obtained in the previous sections are summarized in Table 3.2. Reasonable agreement between the analytical E_y, numerical E_y

and experimental E_y is achieved. The normalized TEM mode component can be predicted correctly from this model since the simulated result shows a close agreement with the experiment.

Table 3.2

Summary of y-component E-field and normalized TEM mode component e_{oy}

E_y *(ana)* analytical E_y			
4.242 V/m			
E_y *(num)* numerical E_y		E_y *(exp)* experimental E_y	
4.223 V/m		3.7 V/m.	
Normalized TEM mode component e_{oy} $\sqrt{\Omega}/m$			
e_{oy} *(exp-num)* experimental e_{oy} based on numerical result	e_{oy} *(ana-num)* analytical e_{oy} based on numerical result	e_{oy} *(exp-exp)* experimental e_{oy} based on experimental result	e_{oy} *(ana-exp)* analytical e_{oy} based on experimental result
9.003	8.838	9.193	9.224

3.9 Power Measurement

In this section, the power simulated from the port of the model was compared to the measurement using the GTEM cell. In the experiment, a spectrum analyser was connected to the port of the GTEM cell. A metal box with an aperture (previously described in Chapter 2 Section 2.4) was used as the EUT. The metal box was fed with a -30 dBm signal source at 100 MHz via a fibre optic. Using a similar EUT, a voltage was simulated at the port of the GTEM model when The EUT was excited with a signal with the same voltage and frequency across the aperture. The EUT was arbitrarily orientated.

The voltage simulated at the port of the GTEM model was -65.55 dBm. The measured power at the spectrum analyser is shown in Figure 3.28, which exhibited a power of -68 dBm approximately. Reasonable agreement was achieved between the simulated power of -65.55 dBm and measured power of -68 dBm at 100 MHz.

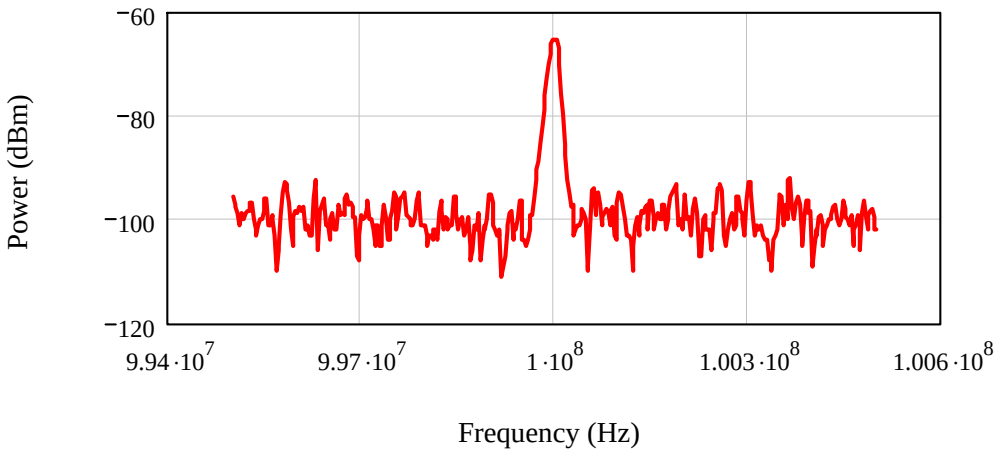

Figure 3.28 Measured power in dBm in the frequency-domain for the first orientation using a spectrum analyser at the port of the GTEM cell

3.10 Conclusion

In this chapter, a reliable TLM model of a GTEM cell that possesses a complex structure is described with details of how the angled structures were constructed using the cubic mesh. It is shown that despite the cubic mesh used to model an angled object which causes the stair-casing errors, the experimental and simulation results are reasonable close. Among the strengths of this model is the ability to include various material properties other than just perfectly conducting metal in shapes and sizes similar to those in actual conditions. In this case, the pyramidal RAM was included in the GTEM model instead of a surface boundary condition. As long as the electromagnetic properties of a material are available, these can be introduced into the TLM model. This feature is valuable in making the model realistic and in achieving very good results even for quantities that are difficult to measure such as phase. In addition, the development of the GTEM model shows the importance of model verification to ensure its reliability and accuracy. This was done by testing the model to produce results that are known beforehand. It is also encouraging that the numerical model gave excellent results compared with measurements thus offering the scope in the future of more testing and compliance certification to be done by simulation.

3.11 References

1. Johns P.B. and Beurle R.L., *"Numerical solution of two-dimensional scattering problems using a transmission-line matrix",* Proc. IEE, 1971, 118(12), p. 1203-1208.

2. Christopoulos C., *"The Transmission-Line Modeling Method: TLM"*, 1995, New Jersey IEEE Press.

3. Paul J., Christopoulos C. and Thomas D.W.P., *"A 3-D Time Domain TLM Electromagnetic Field Solver: regSolve"*, 2000, Nottingham: University of Nottingham.

4. Harrington T.E., Zhong C. and Foegelle M.D. *"GTEM radiated emissions correlation testing and FDTD modeling",* IEEE International Symposium on Electromagnetic Compatibility, Seattle, Washington D.C USA, August 2-6, 1999, p. 770-775.

5. Crawford M.L., *"Generation of Standard EM Fields Using TEM Transmission Cells",* Electromagnetic Compatibility, IEEE Transactions on, 1974, EMC-16(4), p. 189-195.

6. Crawford M.L., Workman J.L. and Thomas C.L., *"Expanding the Bandwidth of TEM Cells for EMC Measurements",* Electromagnetic Compatibility, IEEE Transactions on, 1978, EMC-20(3), p. 368-375.

7. ETS-Lindgren, *"Gigahertz Transverse Electromagnetic cell (GTEM) Model 5400 Series "*, 2005, Cedar Park, TX.

8. Paul J., Christopoulos C. and Thomas D., *"Technical Report 9SRPE040 WP-N2",* University of Nottingham, Nottingham, NG72RD, United Kingdom, May 2001.

9. Icheln C., *"The construction and application of a GTEM cell"*, Master Thesis, Faculty of Electrical Engineering, 1995, Technical University of Hamburg-Harburg.

10. Ishigami S., Harima K. and Yamanaka Y. *"Estimation of E-field distribution in a loaded GTEM cell",* IEEE International Symposium on Electromagnetic Compatibility, Montreal, Canada, August 13-17, 2001, p. 129-134.

11. De Leo R., Rozzi T., Svara C. and Zappelli L., *"Rigorous analysis of the GTEM cell",* IEEE Transactions on Microwave Theory and Techniques, 1991, 39(3), p. 488-500.

12. Harrington T.E. *"GTEM fields FDTD modeling",* IEEE International Symposium on Electromagnetic Compatibility, Austin, Texas USA, August 18-22, 1997, p. 614-619.

13. Hansen D., Ristau D., Radasky W.A. and Smith K.S. *"Sources of problems in the GTEM field structure and recommended solutions",* International Symposium on Electromagnetic Compatibility, Santa Clara, California USA, August 19-23, 1996, p. 48-51.

14. Hansen D., Ristau D., Spaeth T., Radasky W.A., and Smith K.S. *"Expansions on the GTEM field structure problem",* IEEE International Symposium on Electromagnetic Compatibility, Atlanta, USA, August 14-18, 1995, p. 538-542.

15. De Leo R. and Schiavoni A., *"FDTD evaluation of scattering by metallic objects in GTEM cells",* Science, Measurement and Technology, IEE Proceedings-, 1994, 141(4), p. 287-292.

16. Radasky W.A., Smith K.S., Hansen D. and Ristau D. *"Calculations and measurements of fast EM pulses in the GTEM cell",* International Symposium on Electromagnetic Compatibility, 1996, Santa Clara, California USA, August 19-23, 1996, p. 52-57.

17. Pierantoni L., Rozzi T., De Leo R. and Zappelli L. *"Numerical modelling of diffraction by objects in GTEM cell",* Second International Conference on Computation in Electromagnetics, 1994, p. 351-354.

18. Malaric K., Sarolic A., Roje V., Bartolic J., and Modlic B. *"Measured distribution of electric field in GTEM-cell",* IEEE International Symposium on Electromagnetic Compatibility, Montreal, Canada, August 13-17, 2001, p. 139-141 vol.1.

19. 61000-4-20, *"Electromagnetic Compatibility (EMC) – Part 4: Testing and measurement techniques. Section 20: Emission and immunity testing in transverse electromagnetic (TEM) waveguides",* International Electrotechnical Commission, Geneva, Switzerland, 2003.

20. Wilson P., *"On correlating TEM cell and OATS emission measurements",* IEEE Transactions on Electromagnetic Compatibility, 1995, 37(1), p. 1-16.

Chapter 4

The Effect of Phase Differences

4.0 Introduction

A substantial amount of work has been done to better understand the behaviour of the GTEM cell. Examples are the analytical or numerical field modelling of a GTEM cell [1], [2] and [3], cable positioning [4], number of orientations [5], [6] and [7], correlation algorithms [7] and [8], and uncertainty budgets [9] and [10]. Chapter 1 has described that by using a GTEM cell, the important measurement of phase is lost because a second port is not available. To deal with this, the IEC 61000-4-20 [11] assumes that there is no phase difference between dipole moments if the EUT size is small as

compared to the wavelength. Many of these investigations do not discuss the reliability of this assumption. Turnbull and Marvin [12] have introduced an analytical technique in the situation where the dipole moments are not in phase but no actual phase measurement was performed using a GTEM cell.

Dipole moments are considered in phase when an EUT is electrically small but there is evidence that this assumption does not hold in practical cases [7]. This is apparent with current equipment that operates beyond the GHz range and thus becomes electrically large. Early work to investigate the existence of a phase difference between the dipole moments was presented in Chapter 1. This work has shown evidence that phase differences between the dipole moments do exist and in fact, are quite significant.

In this chapter, the effect on the voltage received at a GTEM output port when a phase difference between dipole moments exists is presented. The magnitude of the power measured at the GTEM output port was observed when the phase between antennas is varied from -180^{o} to 170^{o}. It is commonly assumed that the phase difference between dipole moments does not contribute to power magnitude measured at the GTEM output port and the results from the work presented here disprove this assumption. Experimental results presented later in the chapter show significant changes in the measured power magnitude when the phase was altered. Simulations using TLM were done to support these experimental results and the variations in power magnitude agree with experiments. SuperNEC^{TM} was used to produce

the radiation patterns for several phase differences which were later used to explain phase effects.

The term 'vertical electric field' of the GTEM cell refers to the dominant y-axis field component of the GTEM cell. The weaker coupling components are the longitudinal z and horizontal x components.

4.1 Two monopoles used as emitters

An EUT consisting two equal monopole antennas mounted parallel to each other on top of a brass metal box was used in this study. The monopoles are 19 cm in length and are separated by 24 cm from each other because the two holes with 24 cm separation were previously drilled on the metal box. Both the monopole antennas mounted on top of the metal box are fed separately using two independent signal generators, but the phase difference between the two sinusoid signals from the generators is locked and does not drift over time. This EUT has been introduced earlier in Chapter 2 in Figure 2.17. This EUT is suitable for the study of phase in GTEM cell measurements because the fields produced by these two monopoles affect each other since both monopoles are in the same polarization.

For the first EUT orientation according to the IEC 61000-4-20, the phase between the two monopoles was changed from -180^{o} to $+170^{o}$ in 10^{o} steps. The voltages generated at the port of the GTEM cell were measured for

each phase angle. The EUT was then sequentially rotated to the second and third orientations according to IEC 61000-4-20 and the procedure mentioned above was repeated. The experiments were performed at the frequencies of 200 MHz, 1,000 MHz and 2,000 MHz to accommodate both low and high frequencies.

The use of experimental results alone is not enough to fully study the behaviour of the EUT due to phase differences. Simulations were performed using TLM (using the model described in Chapter 3) to support these experiments. In the simulations, the output of the GTEM model is simulated at phase differences of 0^o, 50^o, 140^o and 180^o. The simulations were only performed for a few points due to the long simulation times but these chosen phase angles are adequate to produce useful results should the effect of phase differences between the monopole antennas become significant. The same procedure applies to the second and third orientations. These results are presented in Section 4.2.

4.2 The effect of phase differences on the received power

In this section, the effect of phase differences on the received power is presented. The simulation and experimental results for the power received at 200 MHz in dBm from three orientations are shown in Figure 4.1. The simulation results are close to the experimental results with both showing the

same general pattern. This provides confidence in the reliability and accuracy of the GTEM TLM model as well as the measurements. The simulated effects of phase difference at the frequencies of 1,000 MHz and 2,000 MHz are shown in Figure 4.2 and 4.3 respectively. The experimental procedures were not performed at the frequencies of 1,000 MHz and 2,000 MHz because the fibre optic spherical dipole antenna built earlier in this work (described in Chapter 2) was made with an LED transceiver which limits the usable frequency to 200 MHz. Hence, reliable measurements could not be performed above this frequency limit.

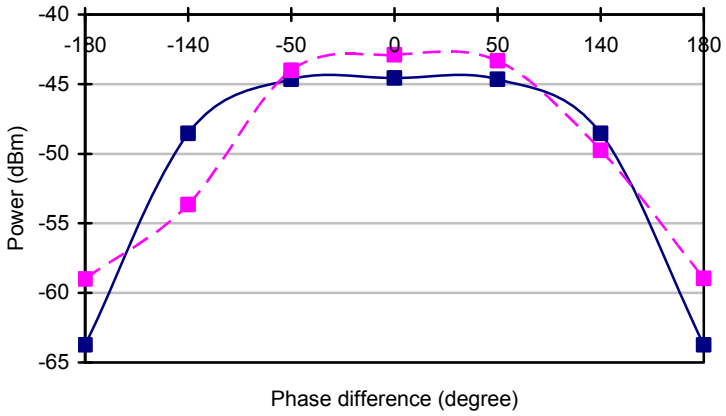

(a)

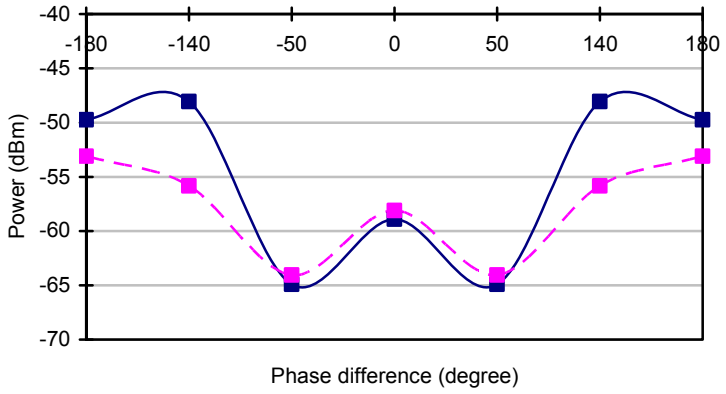

(b)

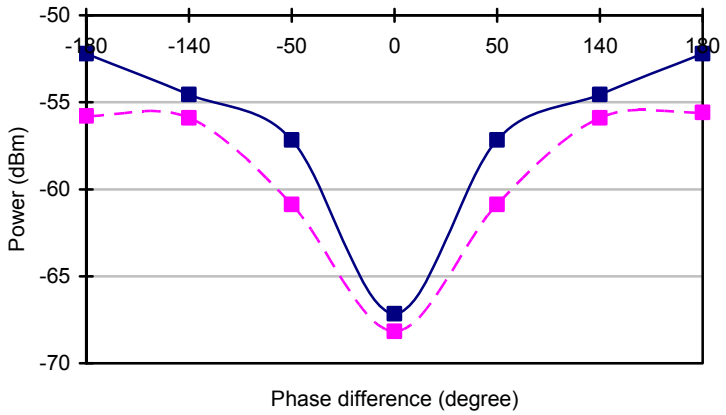

(c)

Figure 4.1 Received power in dBm at the GTEM port due to phase change for (a) orientation 1, (b) orientation 2 and (c) orientation 3 at 200 MHz. Solid line corresponds to simulated results and the dashed line correspond to experimental results

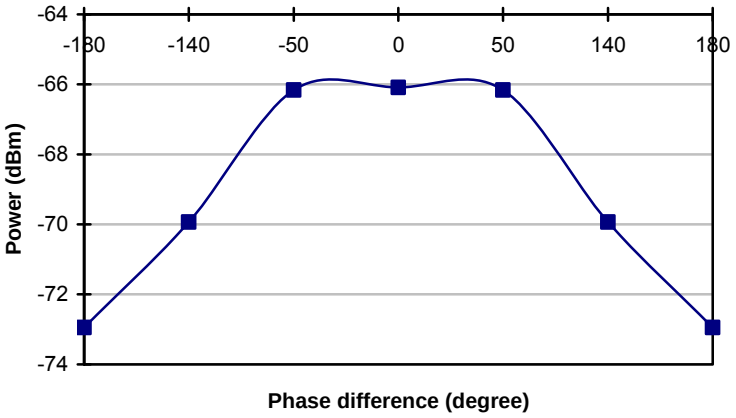

(a)

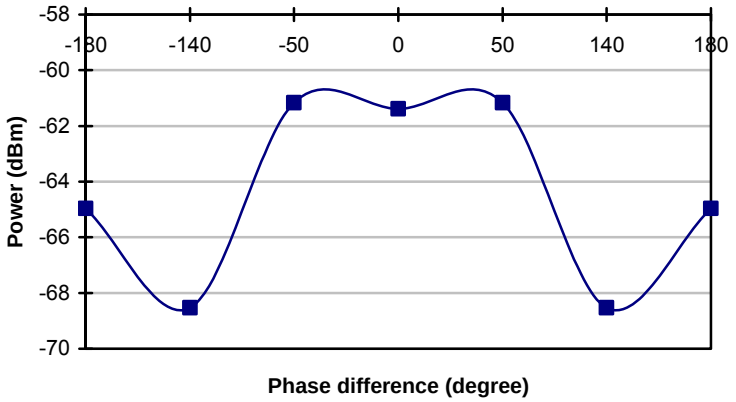

(b)

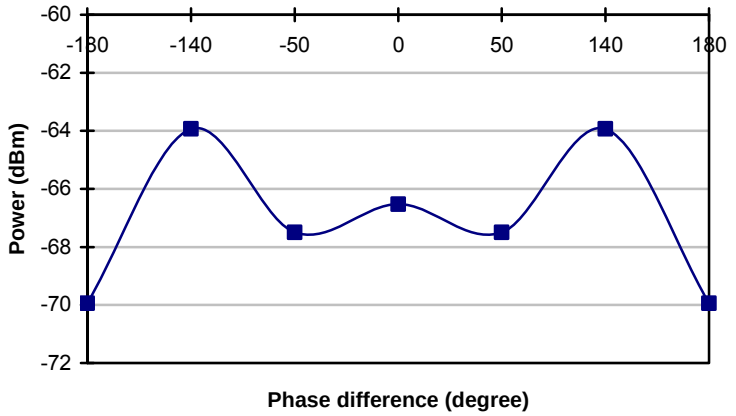

(c)

Figure 4.2 Received power in dBm at the GTEM port due to phase change for (a) orientation 1, (b) orientation 2 and (c) orientation 3 at 1,000 MHz

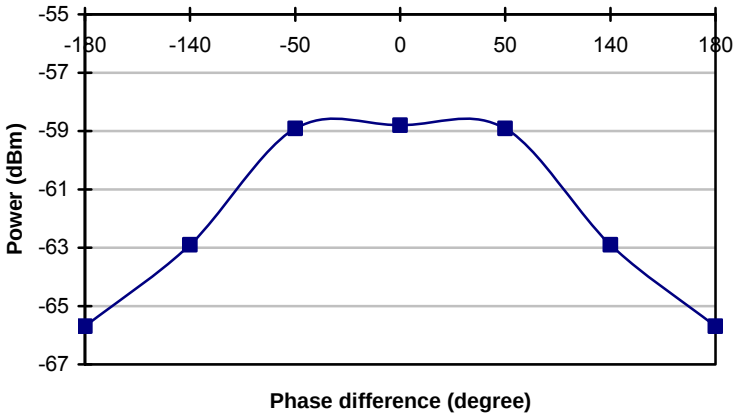

(a)

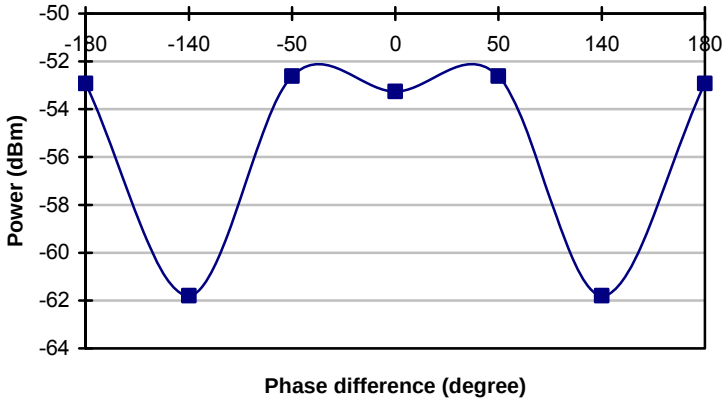

(b)

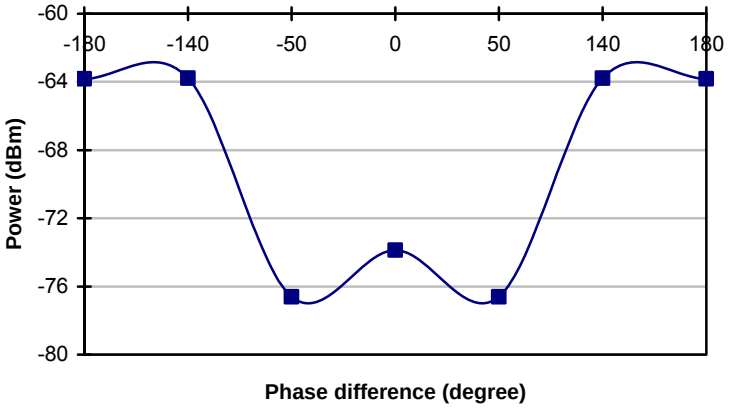

(c)

Figure 4.3 Received power in dBm at the GTEM port due to phase change for (a) orientation 1, (b) orientation 2 and (c) orientation 3 at 2,000 MHz

4.2.1 The total power radiated according to the IEC 61000-4-20

The total power radiated by the EUT in the GTEM cell measurement is obtained from the three orientation-three voltage method according to the IEC 61000-4-20. From the voltages measured at the GTEM port, the total power radiated by the EUT, P_o can be calculated by:

$$P_o = \frac{\eta_o}{3 \cdot \pi} \cdot \frac{k_o^2}{e_{oy}^2 \, Z_c} \cdot S^2 \ \text{W} \tag{4.1}$$

where,

$$S = \sqrt{V_{p1}^2 + V_{p2}^2 + V_{p3}^2} \tag{4.2}$$

$k_o = \frac{2\pi}{\lambda}$ is the wave number (4.3)

$\eta_o = \sqrt{\frac{\mu_o}{\varepsilon_o}}$ is the free space wave impedance (377 Ω) (4.4)

where V_{p1}, V_{p2} and V_{p3} are the RMS voltages measured from the three EUT orientations, S is the root-sum-square of the three measured RMS voltages, Z_c is the characteristic impedance of the GTEM cell which is 46 Ω in the case of this model (Chapter 3), e_{oy} is the field factor which is the normalized y-component of the electric field of the TEM mode at the EUT location.

The resulting total radiated power for the three orientations due to the particular phase points is shown in Figure 4.4 for 200 MHz, 1,000 MHz and 2,000 MHz respectively.

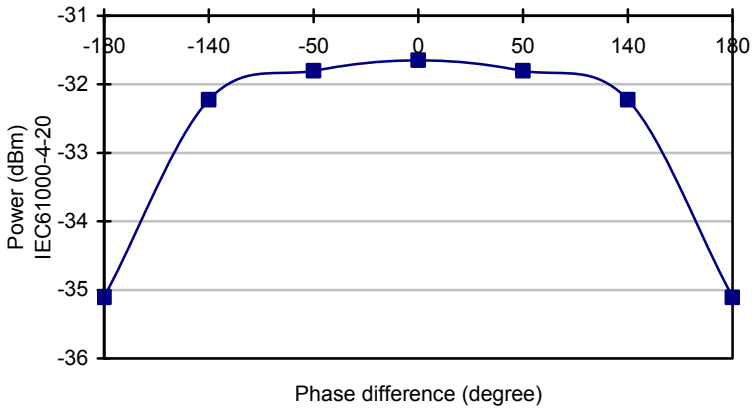

(a)

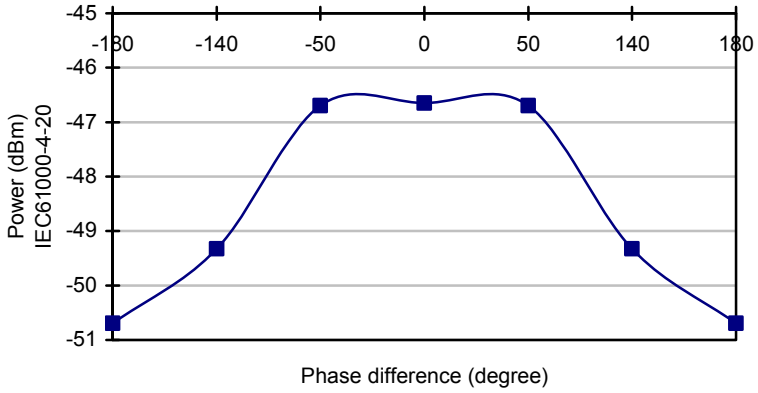

(b)

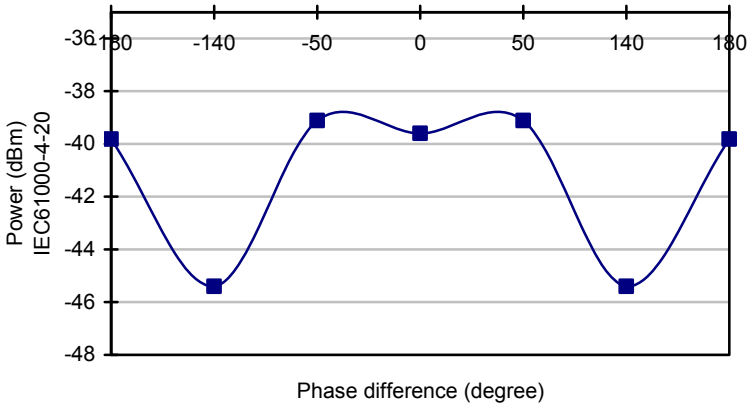

(c)

Figure 4.4 Total radiated power for (a) 200 MHz (b) 1,000 MHz and (c) 2,000 MHz according to the IEC 61000-4-20

4.2.2 The maximum electric field E_{max}; a correlation to OATS

The total radiated power obtained from Section 4.2.1 can be used to correlate to OATS maximum electric field (E_{max}) measurements. The algorithm for performing the correlation can be found in [11]. In the calculation, the height of the EUT from the ground plane is specified as 0.8 m, the distance between the EUT and the antenna is 3 m and the antenna height scan is from 1-4 m. These values are in accordance to CISPR 22 [13].

The results of the correlation are shown in Figure 4.5 for electric field in horizontal polarization and Figure 4.6 for electric field in vertical polarization. Each graph represents the electric field in a particular polarization for a single frequency at four different heights (1m, 2m, 3m and 4m), representing the height scan. As per definition in [11], E_{max} is the maximum electric field obtained during the scan from 1-4 m, which in this case is shown by the line marked with '♦'.

When the calculated values of the total radiated power in free space are correlated to OATS, the effect due to the phase also appears in OATS correlation results. Thus, when an inaccuracy is present in the early stage of a measurement, all subsequent calculations or correlations will be subject to the same inaccuracies.

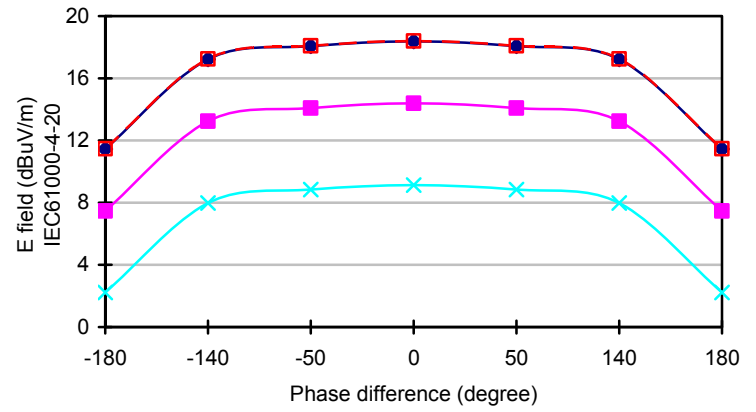

(a)

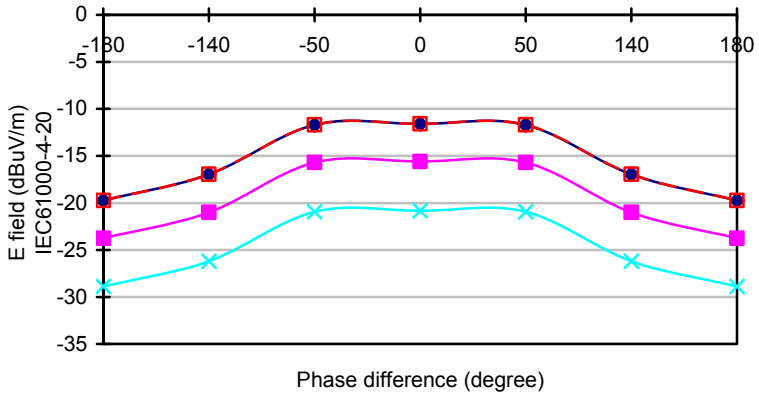

(b)

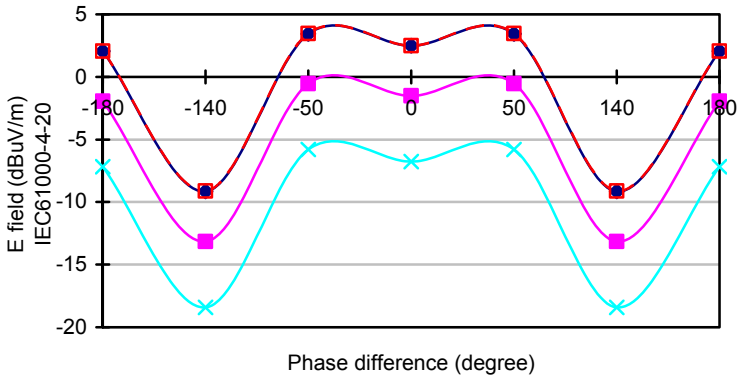

(c)

Legend: ♦ 1 m; □ 2 m; ■ 3 m; × 4 m

Figure 4.5 Horizontal electric field for four different antenna heights (1-4m) for (a) 200 MHz (b) 1,000 MHz and (c) 2,000 MHz according to IEC 61000-4-20

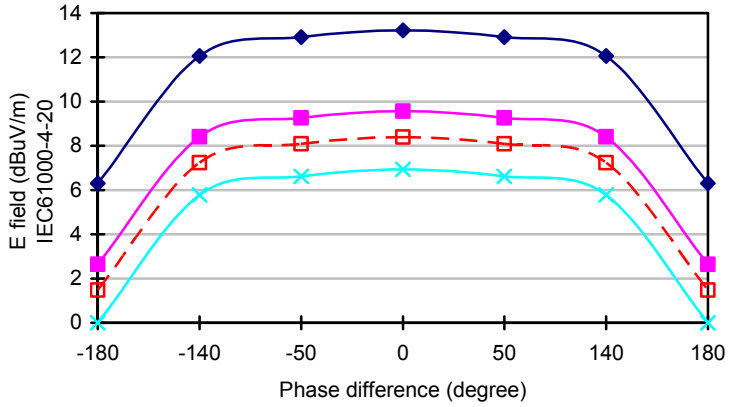

(a)

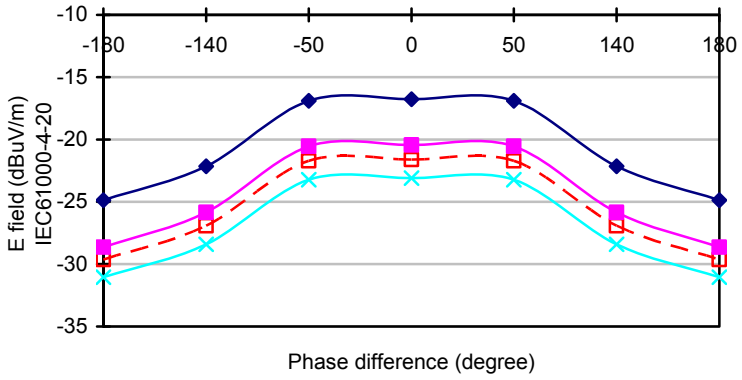

(b)

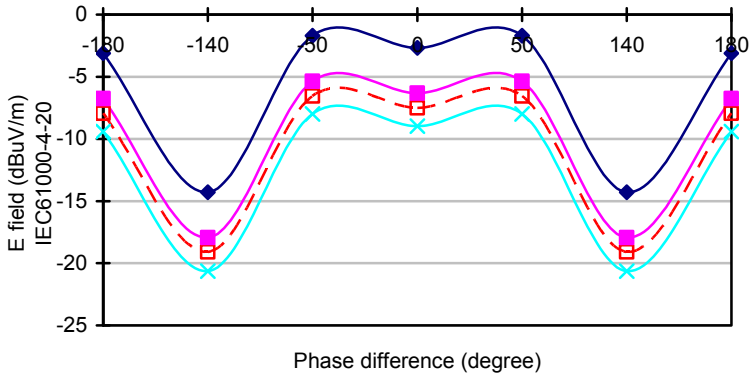

(c)

Legend: ♦ 1 m; □ 2 m; ■ 3 m; × 4 m

Figure 4.6 Vertical electric field for four different antenna heights (1-4m) for (a) 200 MHz (b) 1,000 MHz and (c) 2,000 MHz according to IEC 61000-4-20

4.2.3 The comparison with free space total power

The total radiated power from the three orientations due to the particular phase points for 200 MHz, 1,000 MHz and 2,000 MHz (Figure 4.4) are compared with the total power radiated in free space. In the simulation, the EUT is modelled in free space and the total power radiated by the EUT is obtained. The total radiated power simulated in free space for the frequencies 200 MHz, 1,000 MHz and 2,000 MHz are plotted in Figure 4.7 in dashed line in comparison with the total radiated powers calculated using the IEC 61000-4-20 which appear in secondary axis in solid line. The error increases as the frequency goes higher. Due to the lack of suitable experimental facility, it was not possible to confirm directly experimentally the results obtained from simulation that the total radiated power is constant. However, it was confirmed experimentally that the input power fed into the EUT remained constant.

In the next section, the changes in the total power radiated by the EUT due to phase differences are analyzed and possible explanations are suggested.

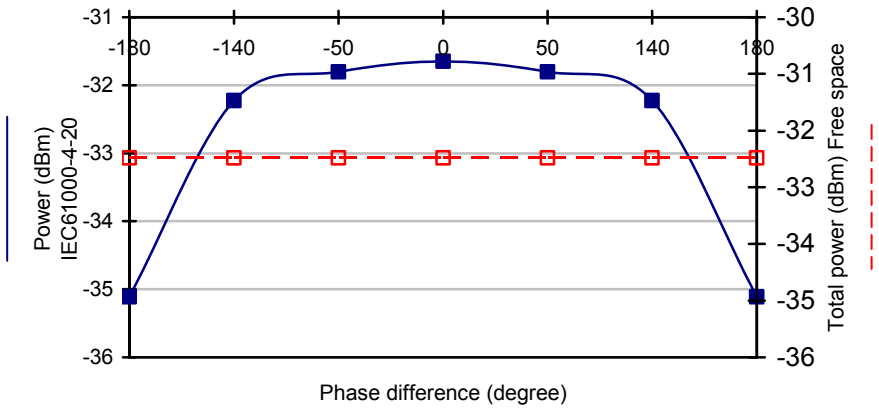

(a)

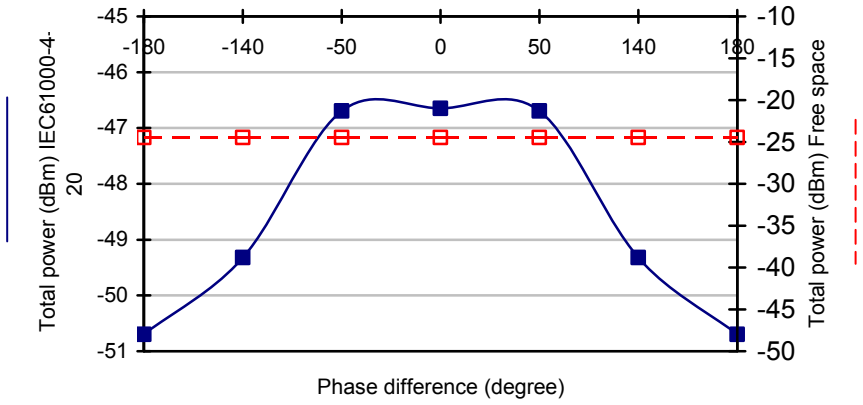

(b)

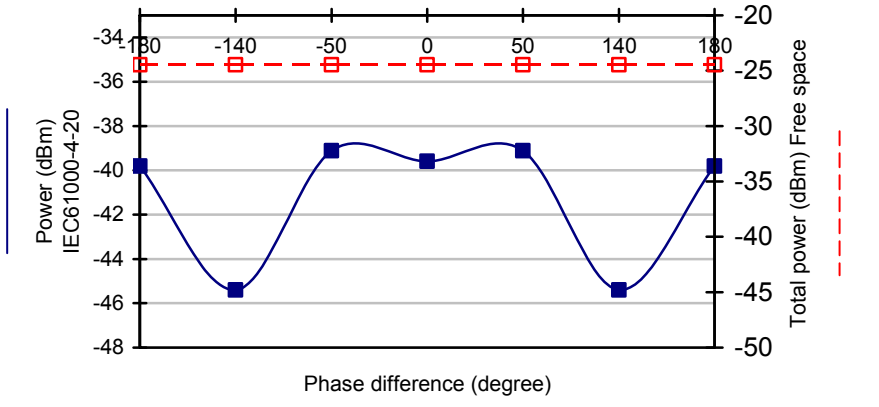

(c)

Figure 4.7 Total radiated power for (a) 200 MHz (b) 1,000 MHz and (c) 2,000 MHz for both the IEC and free space

4.3 The changes in radiation pattern due to phase differences

In order to investigate the reasons behind the effect of phase differences in the total radiated power calculated using [11] in the GTEM cell, the radiation patterns of the EUT for several phase differences were obtained from simulation. The TLM solver is unsuitable for simulating far field emission pattern due to the required large mesh size. Free trial SuperNEC^{TM} simulation software was used to perform this work. In SuperNEC^{TM}, the excitation voltage for one of the monopoles was kept constant throughout the whole simulation while the phase of the excitation voltage for the second monopole was changed.

The radiation patterns for the phase differences of 0^o, 90^o and 180^o in the xy plane at 200 MHz are initially examined and are illustrated in Figure 4.8. Initial examination shows changes of the radiation patterns as the phase difference between the monopoles was altered from 0^o to 180^o. These changes hold possible explanations for the phase difference effect on the measured power and are discussed in detail in the following sections.

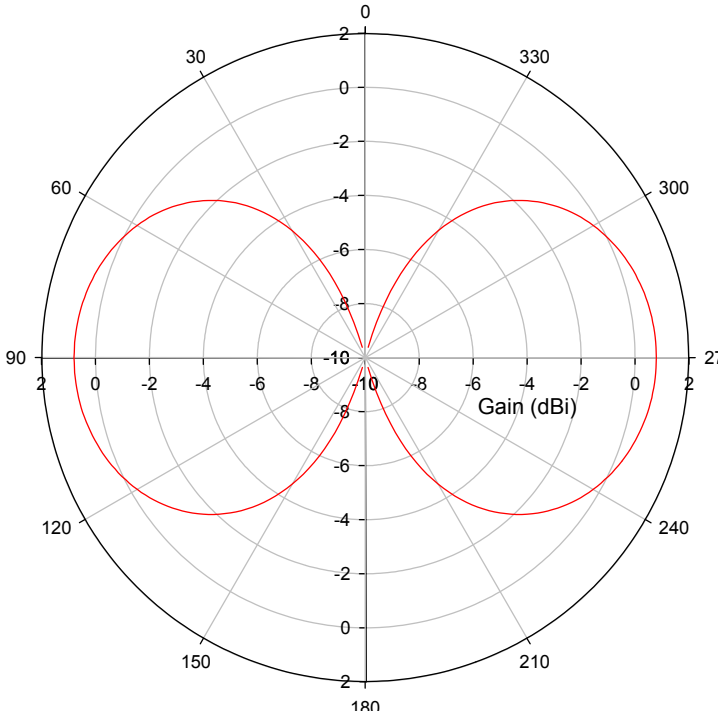
0
30
330
60
300
90
120
240
150
210
180
Gain (dBi)

(a)

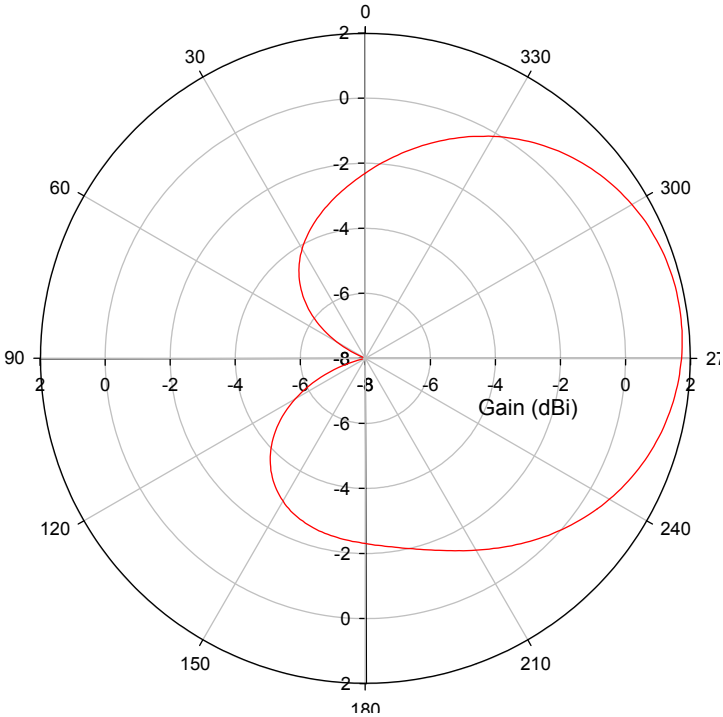
0
30
330
60
300
90
120
240
150
210
180
Gain (dBi)

(b)

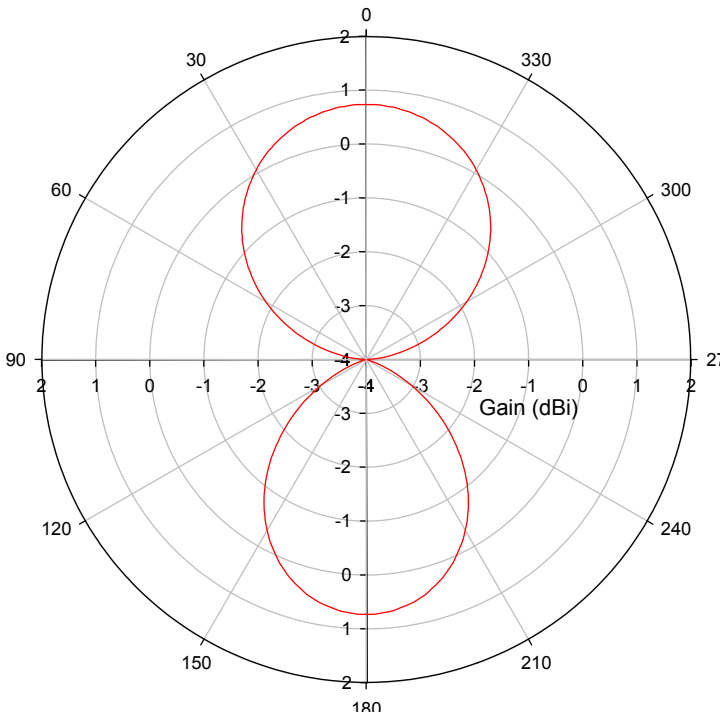

(c)

Figure 4.8 The radiation pattern of the two monopoles with a phase difference of (a) 0^{o}, (b) 90^{o} and (c) 180^{o} for the xy plane at 200 MHz

4.4 An explanation of phase effects

This section presents possible explanations for the behaviour of the simulated voltages in the GTEM model due to the phase difference between the excitation voltages for the two monopoles on the EUT. The simulated powers for all three orientations are presented together for comparison in Figure 4.9 for 200 MHz. It is difficult to explore by analytical methods the coupling of the EUT to the GTEM cell. Instead, an explanation of the coupling is sought from the simulated radiation pattern.

The power measured from a GTEM cell depends on the coupling between the EUT and the GTEM cell. Ideally, a GTEM cell operates in TEM mode where only the vertical y electric field of a GTEM cell will strongly couple into the TEM mode of the GTEM cell. This is known as the co-polar coupling. However, the horizontal x and longitudinal z components also couple into the TEM mode but fairly weakly compared to the vertical y component. This is known as the cross-polar coupling. All power measured from a GTEM output port is a sum of all the three components.

The dominant and minor electric field components for a monopole are shown in Figure 4.10. When the dipole is placed vertically inside the GTEM cell, the dominant electric field lines align with the vertical y direction inside the GTEM cell. This condition generates the highest voltage across the GTEM port. Thus, the amount of vertical y electrical field generated by an EUT dominates the coupling inside the GTEM cell. The longitudinal z has the second best coupling and the horizontal x field has the worst coupling inside the GTEM cell. This is summarized in Figure 4.11.

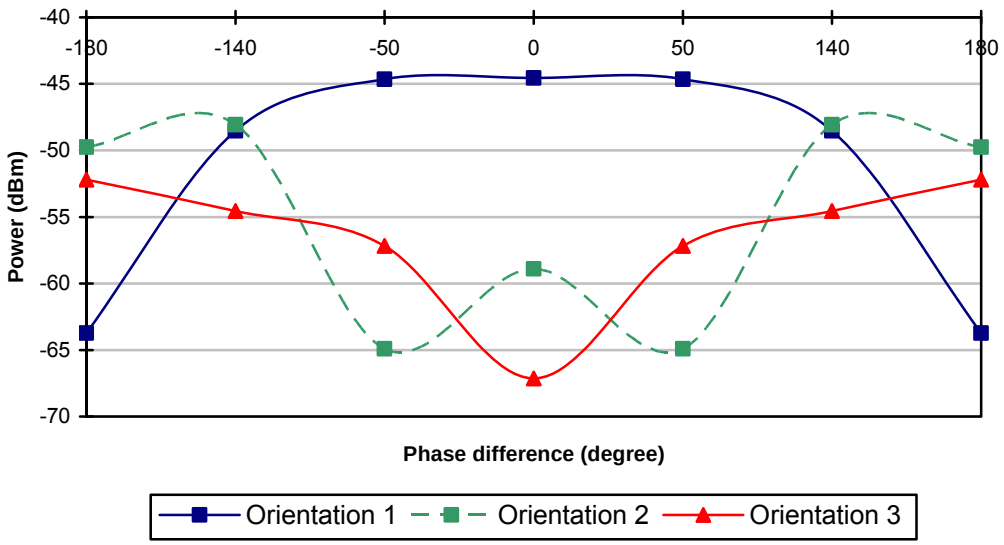

Figure 4.9 The simulated powers at the GTEM model port obtained from three orientations for two monopole EUT configuration at 200 MHz

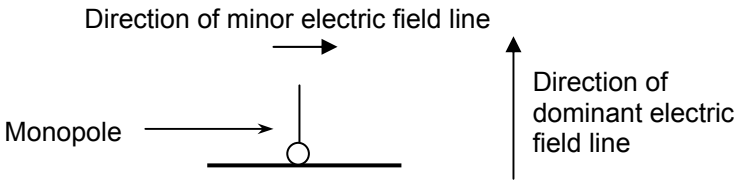

Figure 4.10 Direction of dominant and minor electric field components existing around a monopole antenna

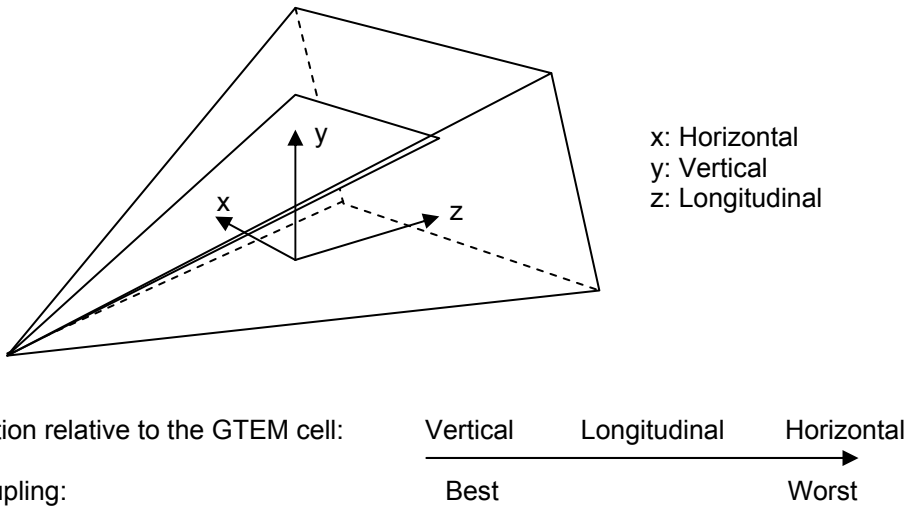

Figure 4.11 The ranking for electric field coupling mechanism of a GTEM cell

In the first orientation of the EUT, at the phase difference of 0^o, the radiation pattern at 200 MHz (Figure 4.12 (a)) shows a uniform ring shaped pattern. This phase angle results in the highest voltage output in the simulation because the dominant electric field component is aligned with the y axis in respect to the GTEM cell. As the phase angle was changed from 0^o to 180^o, the radiation pattern changed to a new shape shown in Figure 4.12 (b). During the transition from 0^o to 180^o, the radiation lobe at one side decreased as shown in Figure 4.13 and this decreases the vertical y electric field intensity. When the phase angle reaches 180^o, it was observed that the direction of the dominant electric field has changed. This happened because the radiation pattern was also changed due to the phase difference of 180^o. The main lobes at 180^o are now directed vertically as shown in Figure 4.12 (b) as opposed to the main lobes at 0^o which were directed horizontally. This changed the electric field line of the EUT radiation pattern to the horizontal x position of the GTEM cell. This alignment of electric field line in the horizontal x position results in the cross-polar coupling giving a low voltage and explains the behaviour of the voltage drop in Figure 4.1 (a) as the phase moves from 0^o to 180^o. Figure 4.14 summarizes the transition of radiation pattern from 0^o to 180^o at orientation one.

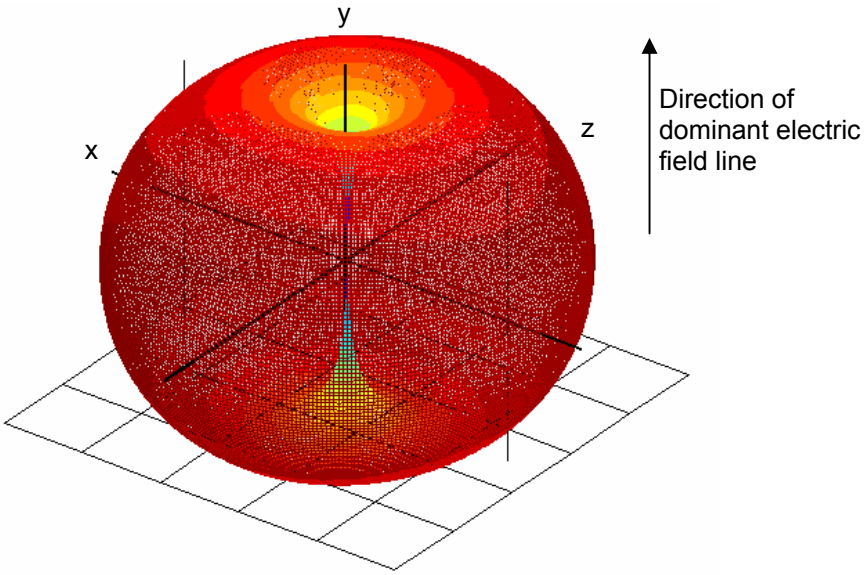

(a)

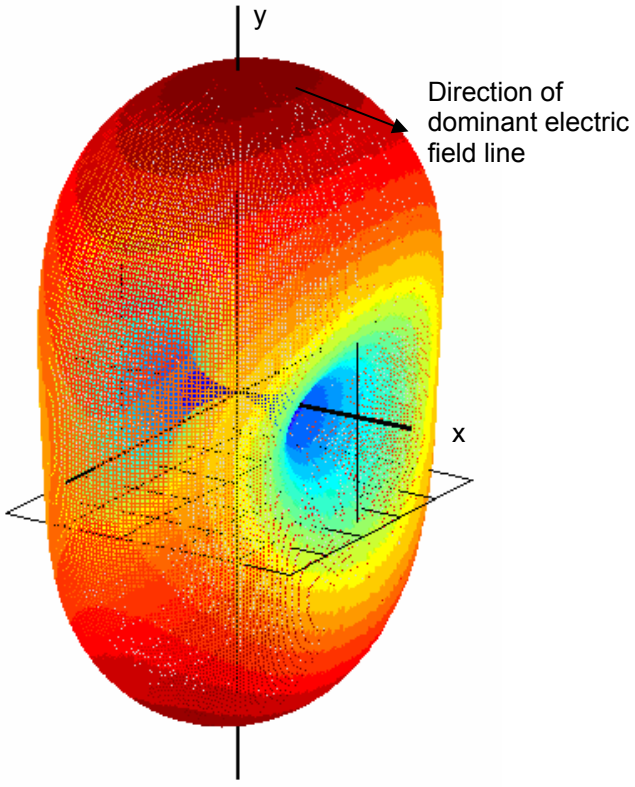

(b)

Figure 4.12 3D Radiation pattern for (a) 0^{o} and (b) 180^{o} phase difference at 200 MHz

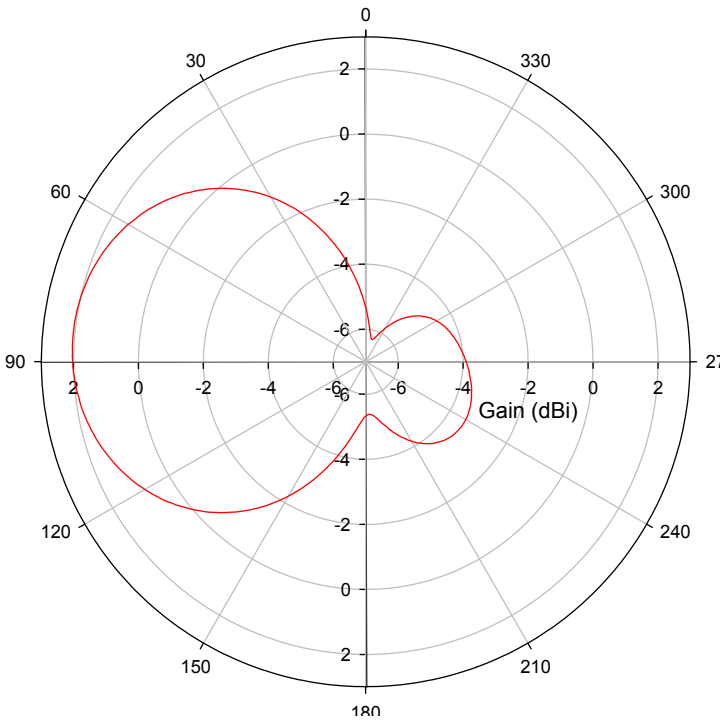

Figure 4.13 2D Radiation pattern at 60^{o} phase difference at 200 MHz

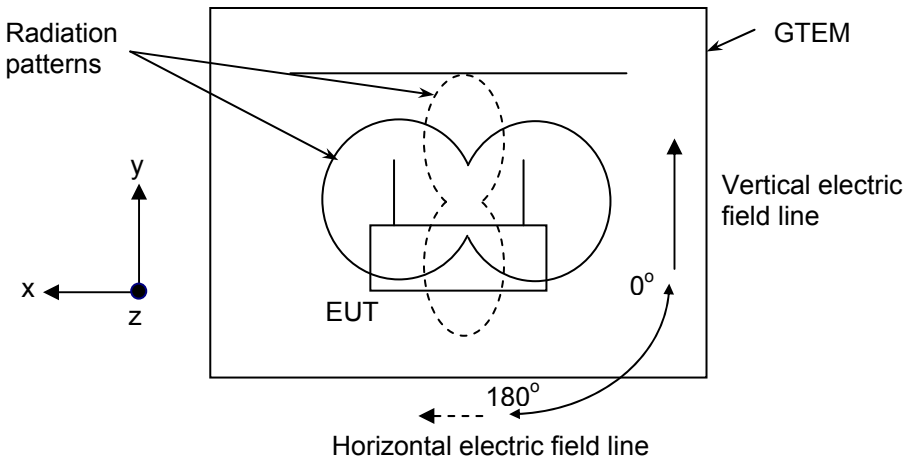

Figure 4.14 Radiation pattern change from 0^{o} to 180^{o} at orientation one

In the second orientation of the EUT, the maximum simulated power is received at the phase angle of 180^{o}. This is because at the angle of 180^{o}, the dominant electric field generated by the antenna radiation pattern shown in Figure 4.12 (b) is aligned with the y direction in the GTEM cell, thus resulting in the highest voltage for that particular phase angle. However, the worse coupling does not occur at 0^{o} in this case. Again, the answer is found in the radiation pattern characteristics at this particular angle.

In this orientation, phase difference at 50^{o} exhibits the lowest simulated power. During the 0^{o} to 50^{o} phase transition, the radiation pattern changes and this decreases the electric field intensity at the right lobes as shown in Figure 4.15 (looking at the xy plane). As the phase angle continues to increase towards the 180^{o} e.g. at 70^{o} the left lobe (looking at the xy plane) in Figure 4.16 (b) begins to increase in magnitude and also most importantly, the dominant electric field is changing from the longitudinal z towards the vertical y direction of the GTEM cell, thus increasing its coupling into the GTEM cell. Figure 4.17 summarizes the transition of the radiation pattern from 0^{o} to 180^{o} at orientation two of the EUT.

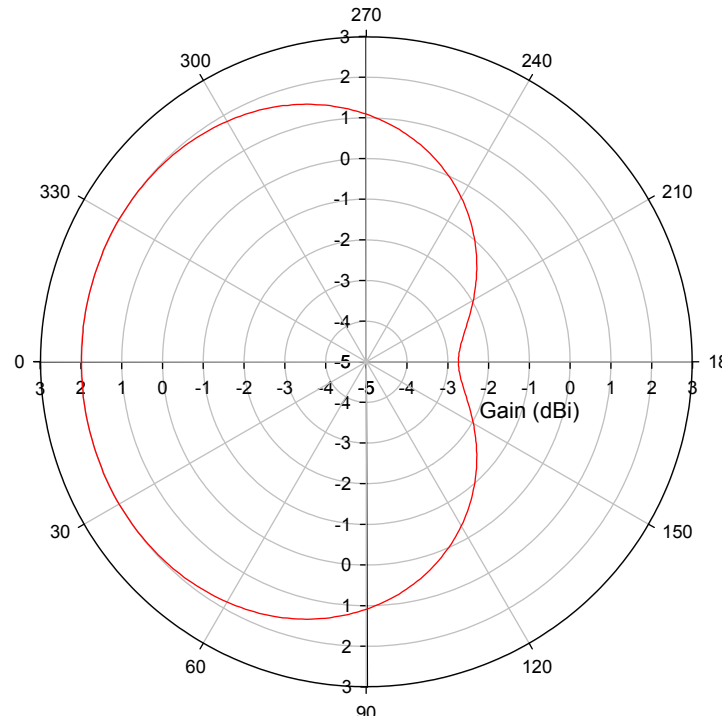

(a)

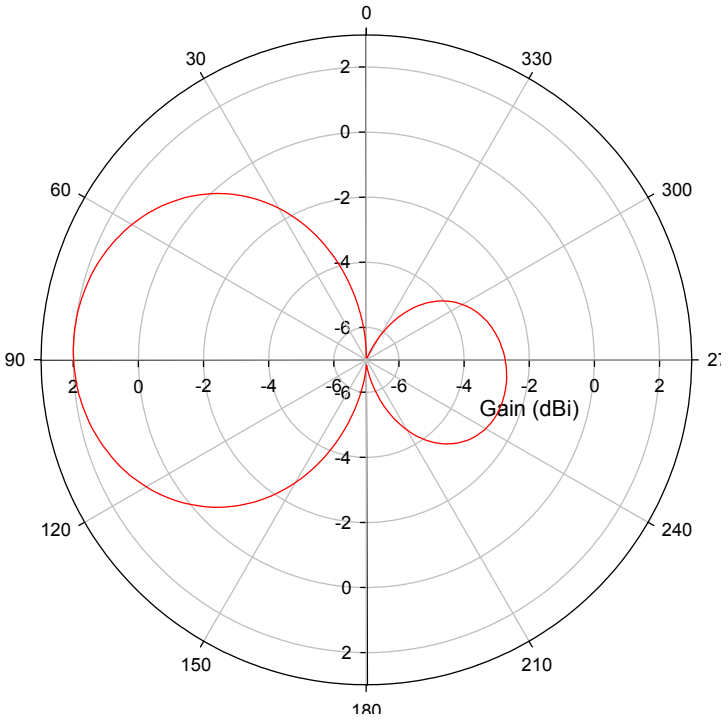

(b)

Figure 4.15 2D Radiation pattern at 50° phase difference looking at the (a) xz and (b) xy plane

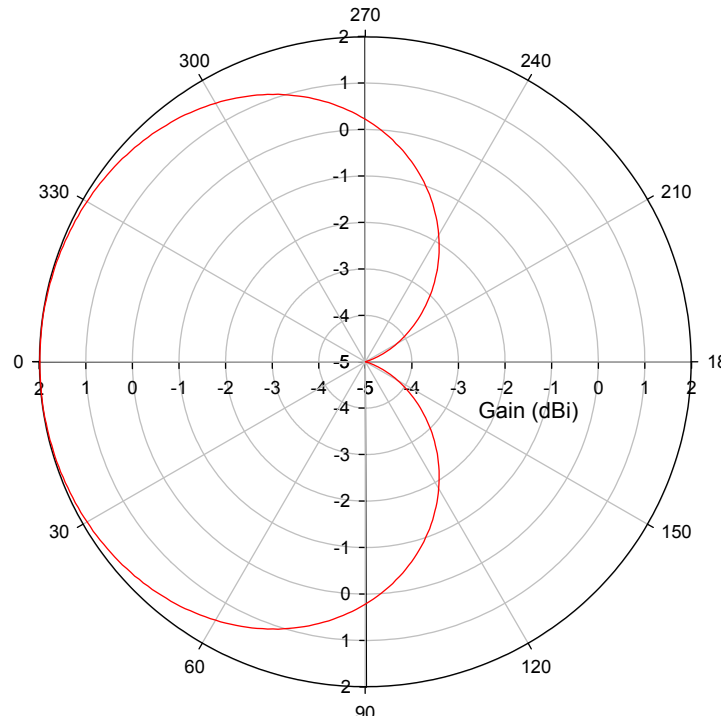

(a)

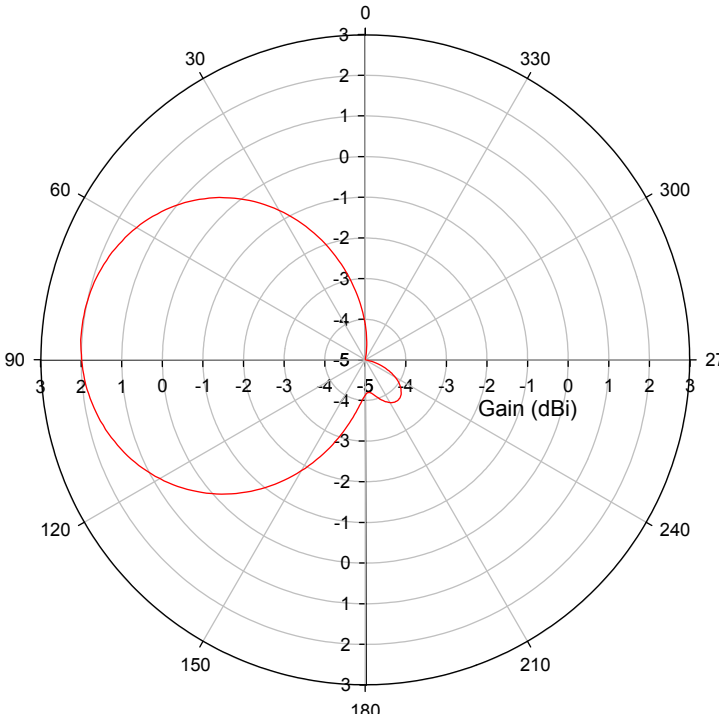

(b)

Figure 4.16 2D Radiation pattern at 70^{o} phase difference looking at the (a) xz and (b) xy plane

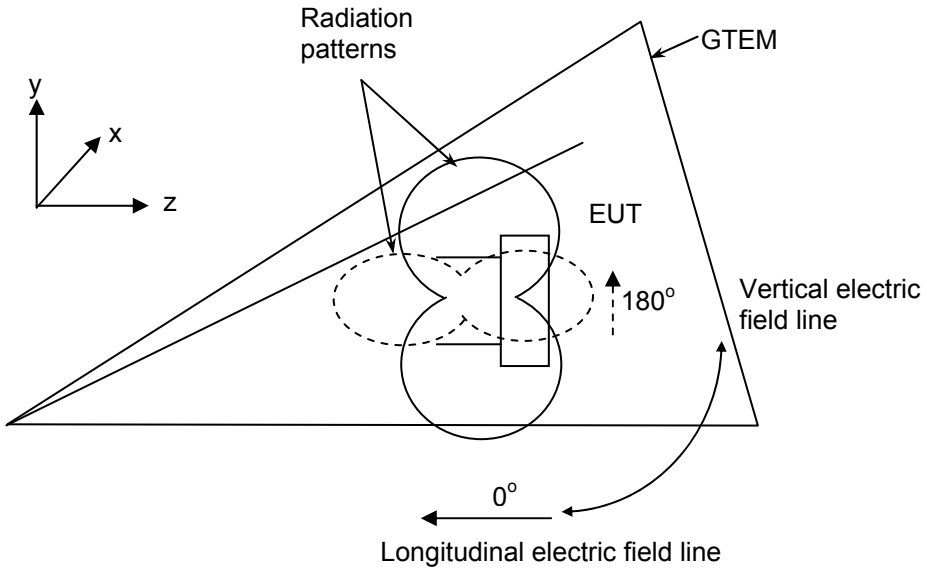

Figure 4.17 Radiation pattern change from 0° to 180° at orientation two

The phenomena observed at the first and second orientations apply also to the third orientation of the EUT. From the 0° to 180° transition, the dominant electric field direction changes from horizontal x to longitudinal z direction of the GTEM cell, thus increasing the voltage at the GTEM output port. The small increase of voltage during the 0° to 180° transition is because the dominant electric field at 0° and at 180° is in the cross-polar direction. Figure 4.18 summarizes the change of radiation pattern from 0° to 180° for orientation three of the EUT. The changes in radiation pattern as phase changes and the subsequent changes in coupling to the GTEM cell, explain the observed changes in power obtained at the port of the GTEM cell.

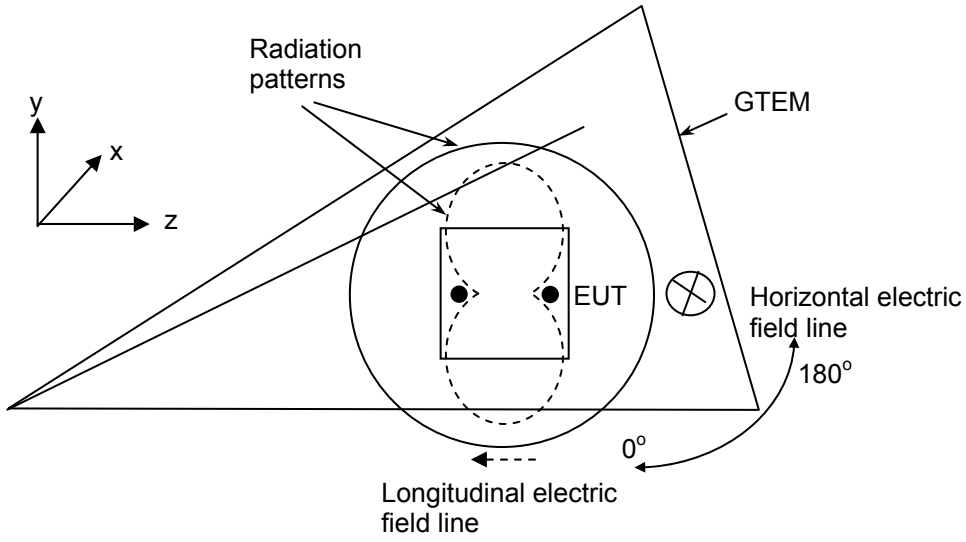

Figure 4.18 Radiation pattern change from 0^o to 180^o at orientation three

4.5 Error bounds analysis

An uncertainty budget in GTEM measurements has been documented in [9]. Many uncertainties in GTEM cell measurements are less complicated to characterize as compared to the phase. From the results shown in Section 4.2, it is evident that the phase difference may not be ignored and an uncertainty due to phase must be included. The work presented here has produced information that can be useful in calculating an overall uncertainty budget in the GTEM measurements.

The uncertainty due to the phase difference between dipole moments for measurement in the GTEM cell for the EUT consisting of two monopole antennas on top of a metal box is shown in Figure 4.19. Uncertainties are

obtained by calculating the deviation between the maximum and minimum values from the total radiated power shown previously in Figure 4.4. A simple three orientation method of the EUT considered here according to [11] would have a 3.461 dB uncertainty between the maximum and minimum of the total power radiated at a low frequency such as 200 MHz. Although this value is still within the normally accepted EMC error margin of ± 6 dB tolerance, it is important to emphasize that the error still exists. It is shown in Figure 4.19 that as the frequency goes higher up to the Gigahertz region, the errors exceed the ± 6 dB. These values can be used in future calculations of the GTEM measurement uncertainty budget.

To further support this theory, the investigation of the phase effects was broadened to other types of EUT in terms of the number, type and position of radiators. As these investigations are quite lengthy, the results are presented in figures in Appendix C.

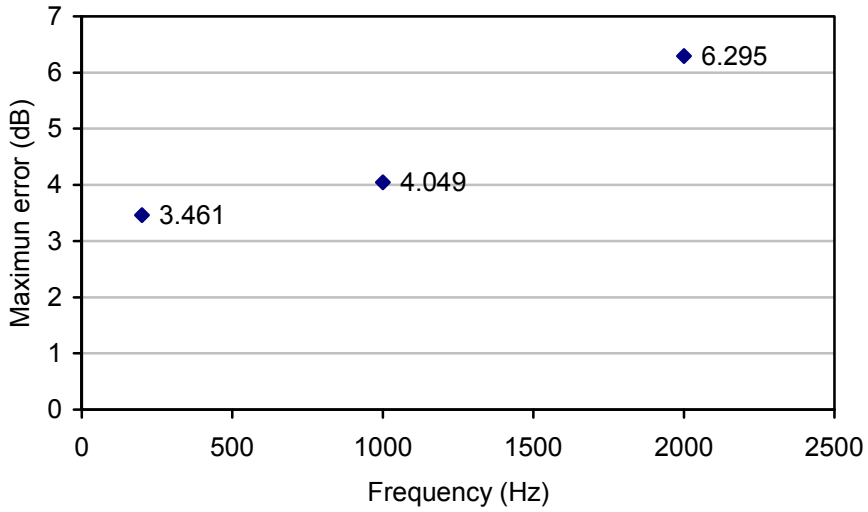

Figure 4.19 Maximum error in dB for the deviation between the maximum and the minimum of the total power radiated due to phase for three different frequencies

4.6 Conclusion

The work done in this chapter stressed the importance of the GTEM TLM numerical model. This model again provides very important insights in the study of the impact of phase difference between dipole moments. This model not only helps to better describe the behaviour of the GTEM cell, but also helps to describe the radiation behaviour of the EUT due to phase differences.

Based on the results obtained, the phase difference between dipole moments cannot be ignored. The results show radiation pattern changes when the phase between the signals feeding the monopoles was altered. The phase difference between these two signals could lead to different radiation patterns. In the case of two parallel monopoles, a significant change of radiation pattern is experienced. The change of radiation pattern subsequently affects how the emission of an EUT is coupled into a GTEM cell.

An interesting aspect of this investigation is the field polarization produced by the radiators in an EUT relative to the GTEM field components. This applies to electric or magnetic fields. This is crucial for a GTEM cell testing since the change of the alignment of the electric and magnetic field relative to the dominant field inside the GTEM cell affects the measured emission level of the EUT at certain orientations. This is the reason for the observed power peaks at different frequencies in all the three orientations.

In this work, a practical construction of a EUT comprised of two parallel monopoles was investigated. Simulations and experimental measurements were also performed for other EUT constructions in the effort to characterize the emission of EUTs due to phase difference between the dipole moments in a broader range of configurations. The same phase effect is observed for these EUTs. These results are presented in Appendix C.

An analytical approach to characterize the behaviour of an EUT due to phase differences between dipoles is not a straight forward task. In this work, it is shown that, the behaviour of the EUT is predictable from the knowledge of the electric or magnetic field alignment relative to the dominant field inside the GTEM cell. This can be established from the radiation pattern.

After showing the importance of phase in GTEM cell measurements, a method to measure the phase of an EUT using the GTEM cell is presented in next chapter and the impact of this measurement is presented.

4.7 References

1. Ishigami S., Harima K. and Yamanaka Y. *"Estimation of E-field distribution in a loaded GTEM cell",* IEEE International Symposium on Electromagnetic Compatibility, Montreal, Canada, August 13-17, 2001, p. 129-134.

2. De Leo R., Rozzi T., Svara C. and Zappelli L., *"Rigorous analysis of the GTEM cell",* IEEE Transactions on Microwave Theory and Techniques, 1991, 39(3), p. 488-500.

3. Harrington T.E. *"GTEM fields FDTD modeling",* IEEE International Symposium on Electromagnetic Compatibility, Austin, Texas USA, August 18-22, 1997, p. 614-619.

4. Goodwin S. and Marvin A.C., *"An analysis of the effects of cable layout on cable to antenna coupling inside a screened room",* IEEE Transactions on Electromagnetic Compatibility, 1991, 33(3), p. 163-171.

5. Osburn J.D. and Bronaugh E.L. *"Advances in GTEM to OATS correlation models",* IEEE International Symposium on Electromagnetic Compatibility, Dallas, August 9-13, 1993, p. 95-98.

6. Carbonini L. *"A new procedure for evaluating radiated emissions from wideband TEM cell measurements",* International conference Electromagnetic Advanced Applications, Torino, 1995, p. 133-136.

7. Ae-Kyoung L. *"An algorithm for an advanced GTEM to ground plane correlation of radiated emission test",* IEEE International Symposium on Electromagnetic Compatibility, Santa Clara, California, August 19-23, 1996, p. 58-62.

8. Wilson P., *"On correlating TEM cell and OATS emission measurements",* IEEE Transactions on Electromagnetic Compatibility, 1995, 37(1), p. 1-16.

9. Nothofer A., Bozec D., Marvin A., Alexander M., and McCormack L., *"The Use of GTEM Cells for EMC Measurements"*. Measurement Good Practice Guide No.65, 2003, UK: National Physical Laboratory, York EMC Services Ltd.

10. Harrington T.E. and Bronaugh E.L. *"EUT directivity and other uncertainty considerations for GHz-range use of TEM waveguides",* IEEE International Symposium on Electromagnetic Compatibility, Montreal, Canada, August 13-17, 2001, p. 117-122.

11. 61000-4-20, *"Electromagnetic Compatibility (EMC) – Part 4: Testing and measurement techniques. Section 20: Emission and immunity testing in transverse electromagnetic (TEM) waveguides",* International Electrotechnical Commission, Geneva, Switzerland, 2003.

12. Turnbull L. and Marvin A.C., *"A treatment of the phase properties of GTEM to open-area test-site correlation techniques",* IEEE Transactions on Electromagnetic Compatibility, 1998, 40(1), p. 62-69.

13. CISPR22, *" Information technology equipment - Radio disturbance characteristics - Limits and methods of measurements",* Third Edition 1997-11.

Chapter 5

The Phase Measurement Method

5.0 Introduction

Initially, TEM cells were used to measure emissions from EUTs. Due to frequency limitations of TEM cells, the GTEM cell was invented to accommodate higher frequencies. However, a GTEM cell has only one port and with this restriction, phase measurement on the dipole moments is difficult to obtain due to the lack of a second port acting as a phase reference.

In this chapter a solution is proposed to solve this problem based on the NBS Technical Note 1059 [1]. The importance of this method described in [1] is that not only the power measured from an EUT is taken into account, but

also the phase. This led to the question if the method can be used in a GTEM cell. The technique described in [1] uses a TEM cell for measuring the magnitudes and phases of EUT emissions simultaneously since a TEM has two ports which enable a straightforward phase measurement.

The following section describes the measurement procedure using a GTEM cell to obtain phase information. The result is then used to investigate the effects of phase difference between dipole moments of an EUT on the total radiated power from the EUT. The reliability of this method in real practical measurement environments was also investigated.

5.1 The phase measurement method

In the phase measurement, two signals from an EUT are required. The first signal is where the emission from the EUT is measured in magnitude and phase while the second signal is used only as the phase reference signal to the first signal. The phase measurement in a TEM cell involves a phase comparison of the signals measured between the first and second port. This measurement procedure requires careful handling. Among the errors that could result from this measurement in a TEM cell are: (1) the error due to the unequal lengths of the two cables, which are not well calibrated and (2) the error due to the phase shifts introduced by the amplifier and the hybrid junction. The method proposed here using the GTEM cell aims to eliminate

these problems. To perform the phase measurement using a GTEM cell, a two-port bidirectional network analyser is necessary. A typical bidirectional two-port network analyser has a phase measurement function. The network analyser displays the phase difference between two signals as well as their magnitudes.

In a TEM cell measurement according to [1], an arbitrary orientation of an EUT is selected as the first orientation as shown in Figure 5.1(a). The EUT is then rotated 45^{o} from the first orientation around the z axis (Figure 5.1(b)) for the first measurement and then another 90^{o} around the z axis (Figure 5.1(c)) for the second measurement. Magnitude measurements of P1 and P2 for the first orientation and P3 and P4 for the second orientation can be obtained simultaneously in the TEM cell as shown in Figure 5.1. Similarly, the phase information is extracted from the signal pairs in each orientation.

To perform the phase measurement in a GTEM cell where only one port is available, additional rotations are needed. This is an 180^{o} rotation at the y axis to mimic the second port in a TEM cell. A simple diagram showing the idea of 180^{o} rotation is shown in Figure 5.2. The 180^{o} rotation actually performs the job of getting the required information i.e. phase and magnitude for the second required direction (that is the P2 or P4). The 180^{o} rotation in relation to the GTEM geometry is shown in Figure 5.3. In all, 12 orientations are required for performing the phase measurement in a GTEM cell as opposed to the six orientations in a TEM cell.

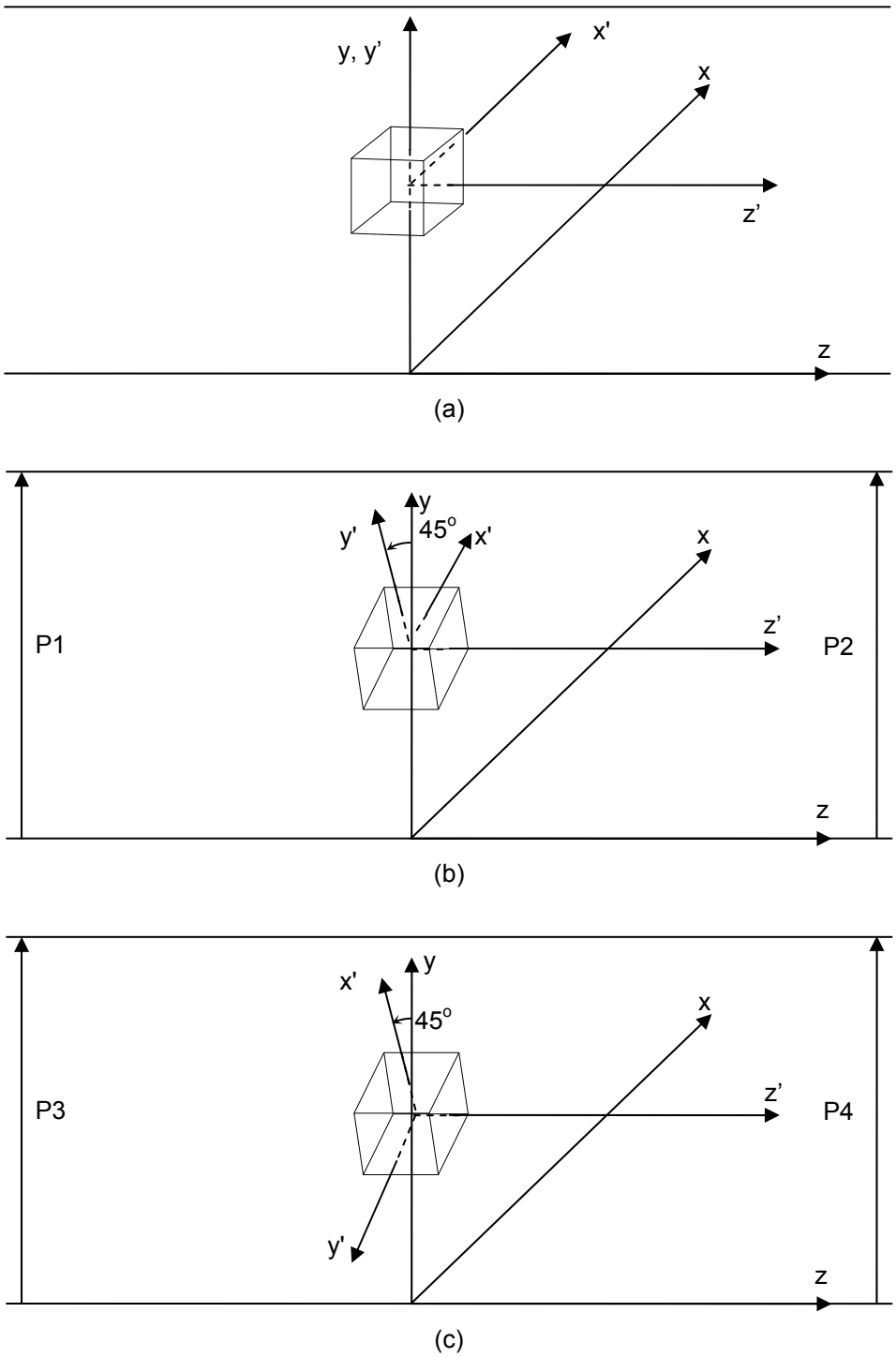

Figure 5.1 Two EUT orientations in the TEM cell for first orientation. Adapted from [2]. (a) is the first orientation. First measurement of P1 and P2 are taken when the EUT is rotated 45° (a) from the first orientation. Second measurement of P3 and P4 are taken when the EUT is rotated 90° (b) from the first orientation

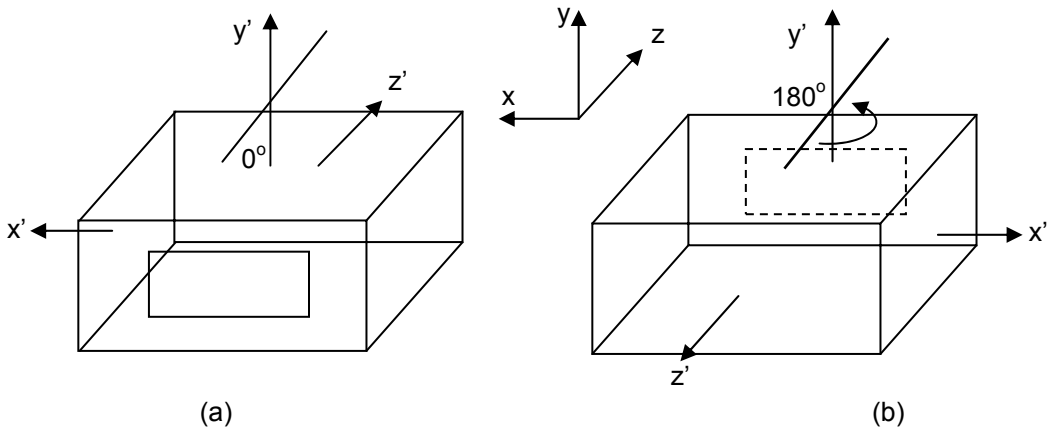

Figure 5.2 An arbitrary EUT orientation at 0^{o} at (a) and turned 180^{o} at (b). Primed axes are EUT's axes while the GTEM axes are non prime

To measure phase, a phase reference signal from the EUT, which is fixed and independent of the EUT orientations, was obtained. In this case, the signal that feeds the EUT is coupled out to the network analyser via a directional coupler to act as the reference signal. By doing this, the phase is locked to a reference and thus, the phase information can then be recovered. The flow of the phase measurement using the network analyser is shown in Figure 5.4.

Simulations to support the 180^{o} rotation of the EUT were first done to establish the efficacy and validity of this method. This is presented in the following section.

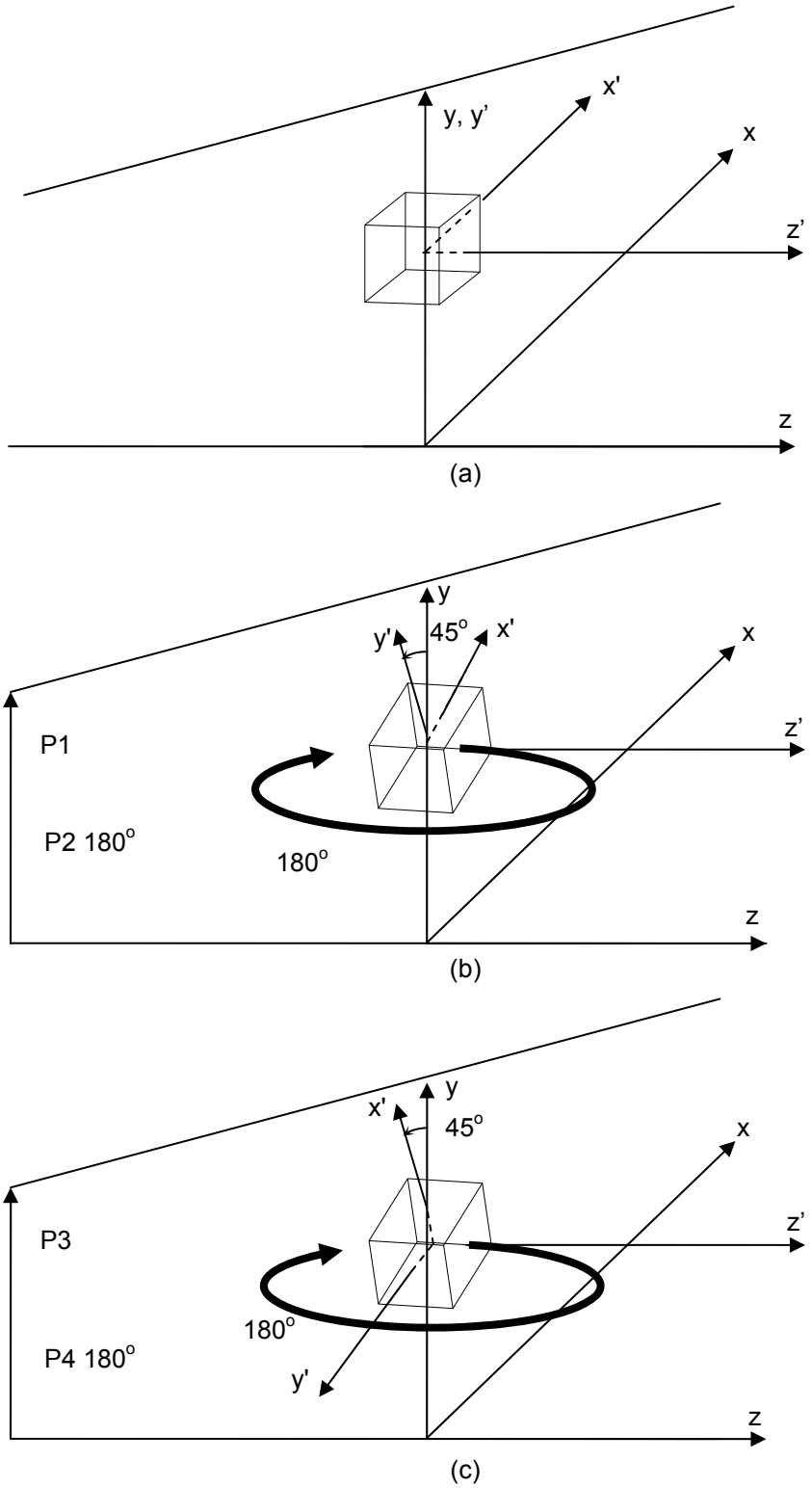

Figure 5.3 The equivalent EUT orientations in the GTEM cell measurement with (b) P2 and (c) P4 measured after the EUT is rotated 180°

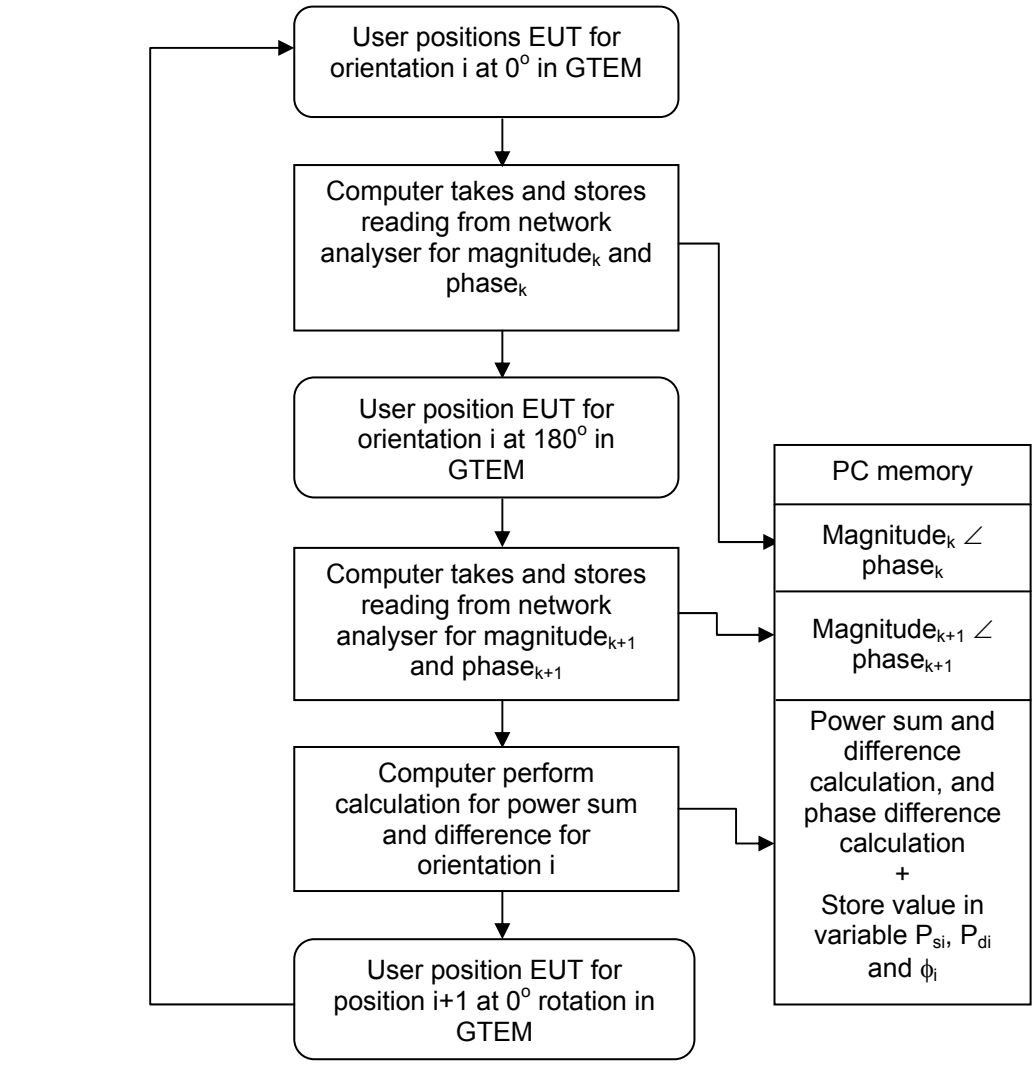

Legend

i	-	1..6
k	-	1..12
P_{si}	-	Power sum i
P_{di}	-	Power difference i

User task

Computer task

Figure 5.4 Flow diagram of GTEM phase measurement

5.2 Verification of the 180^o rotation of the EUT

To verify the symmetrical property of a GTEM cell, the simulated voltages of a magnetic loop using the GTEM model were compared with the TEM model. The purpose of this study is to investigate the credibility of a GTEM cell mimicking the two ports system in a TEM cell by exploiting the symmetrical property of a GTEM cell. In the TEM model, the voltages can be simulated at both ports as shown in Figure 5.5 (a). However, two separate simulations were required for the GTEM model. The first is when the magnetic loop was at 0^o and the second is after the magnetic loop was rotated 180^o around the vertical axis of the EUT centre point. By doing this, two voltage readings were obtained showing the phase behaviour of these two orientations as shown in Figure 5.6 (a). The magnetic loop was chosen as the EUT in this case because it is an asymmetric radiator in one of its plane; hence, it affects the phase received at the ports of the TEM and GTEM models. The results shown in Figure 5.5 (b) and 5.6 (b) conclude that the phase difference between the signals received at both ports in the TEM model agreed reasonably with the phase difference between the signals received at the port of the GTEM model when the EUT orientations are at 0^o and 180^o. The phase difference is approximately 60^o. This result supports the hypothesis mentioned in Section 5.1 that a phase measurement method based on 180^o rotation of an EUT at the vertical axis of the GTEM is feasible.

The measurement method is put to test in a practical experiment described in the following section.

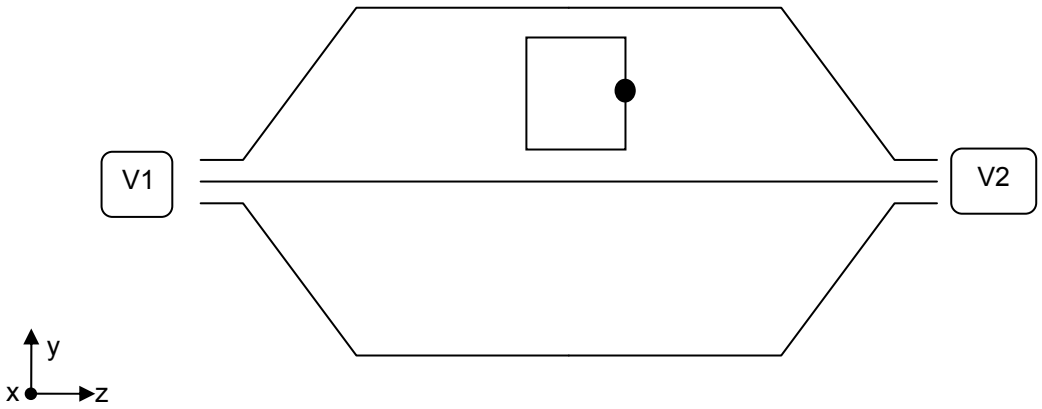

(a)

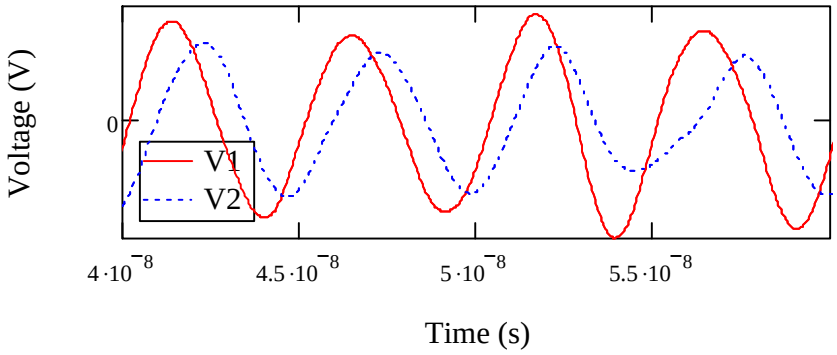

(b)

Figure 5.5 Comparison of phase difference between voltages received at the two ports of the TEM model. (a) The simulation setup and (b) the simulation result

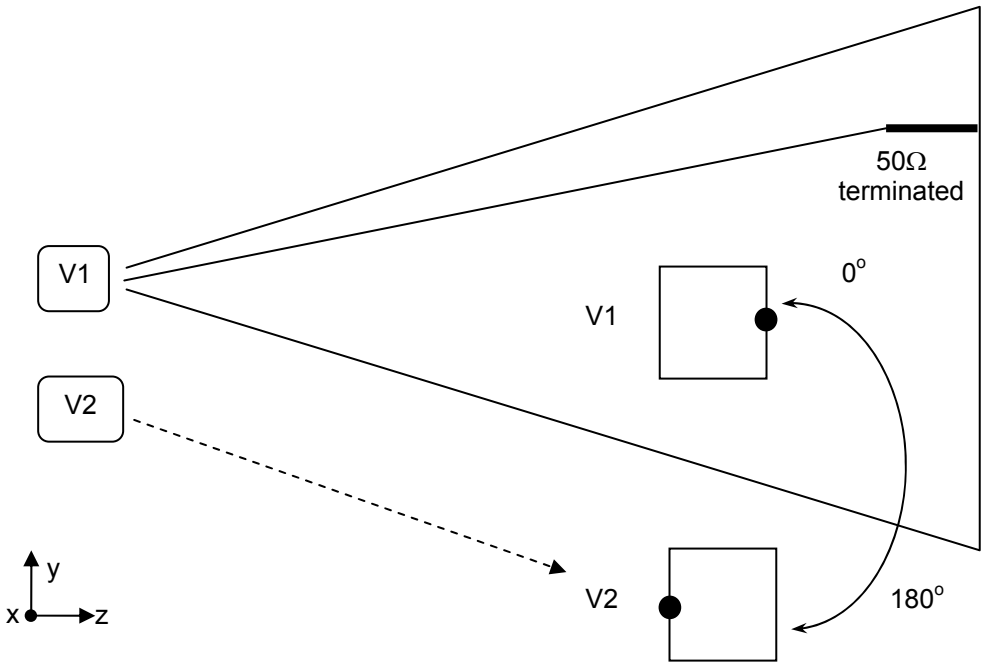

(a)

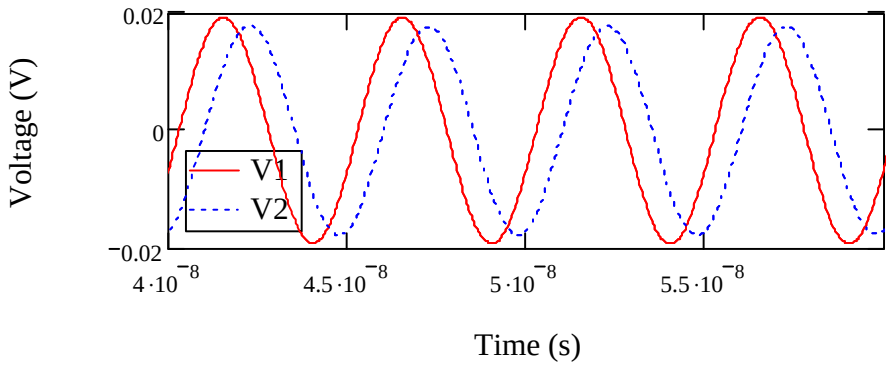

(b)

Figure 5.6 Comparison of phase difference between voltages received at the port of the GTEM model. (a) The simulation setup (two separate simulations) and (b) the simulation result

5.3 The Dummy EUT Setup Concept

The first experiment is important to confirm that the proposed method works with the network analyser. First, the EUT is represented by a signal generator. This signal generator was used to act as the radiating EUT at a particular orientation. Second, a second signal generator is used to act as a reference signal obtained from the same EUT. The intention here is to mimic the phase measurement in the GTEM cell where the first signal generator acted as the received signal from the output port of the GTEM cell while the second signal generator acted as the reference signal obtained from the EUT. The experimental setup is shown in Figure 5.7. Both outputs of the signal generators were fed into the network analyser capable of measuring phase difference. A computer was used to control all the instruments via available remote control interface such as General Purpose Interface Bus (GPIB). In order for this setup to work properly, both signal generators must have their clocks locked. This can be done easily as typical signal generators have input or output ports for an external 10MHz clock signal. This connection disables one of the internal clocks of one of the signal generators and thus provides a constant relative phase between the two signal generators to avoid phase drift.

The first reading is taken when both signal generators are switched on. The result is shown in Figure 5.8. Next, using the phase offset function in the signal generator, the signal generator acting as the EUT was set to a phase

offset of ϕ degrees. As this was performed, the phase shown in the network analyser would change to a new phase reading (second reading). The phase difference (readings from network analyser) between the first and second reading was found to be ϕ degrees and agreed with the value set in the signal generator.

To gain better confidence in the reliability of this measurement, both outputs from the signal generators were coupled to an oscilloscope using two directional couplers as shown in Figure 5.9 and the result is shown in Figure 5.10. The phase difference obtained from the oscilloscope agreed with result from the network analyser and the phase offset set in the signal generator. These two experiments support the phase measurement using the proposed method and a practical measurement involving the GTEM cell and an EUT can now be performed.

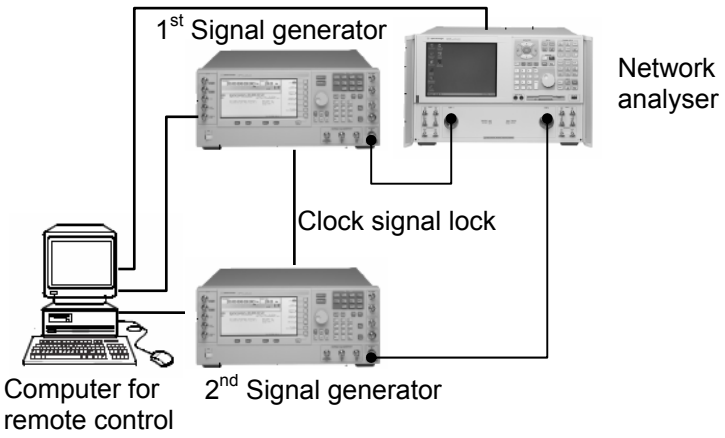

Figure 5.7 Two signal generators were used to verify algorithm. One acted as the EUT and the other acted as the reference signal. Both signal generators are clock locked to produce constant phase difference

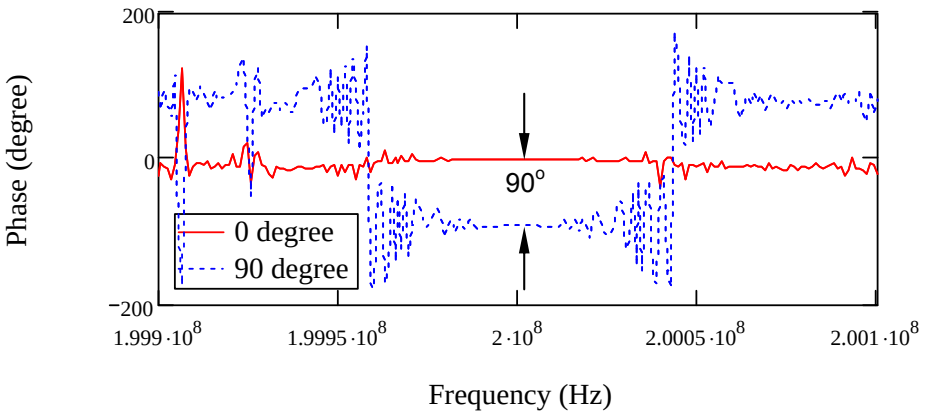

Figure 5.8 Phase measurement using (a) Network analyser

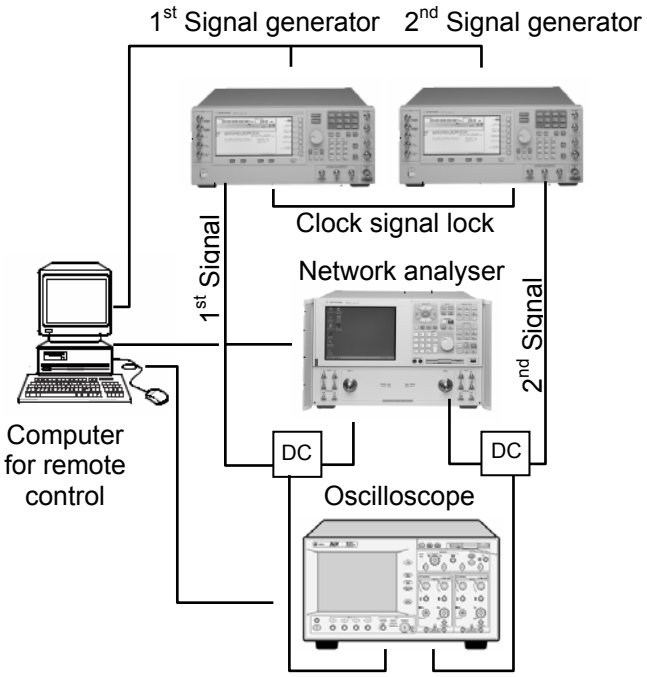

Figure 5.9 A redundant verification using an oscilloscope. Phase difference measured using the network analyser should agree with that obtained using oscilloscope

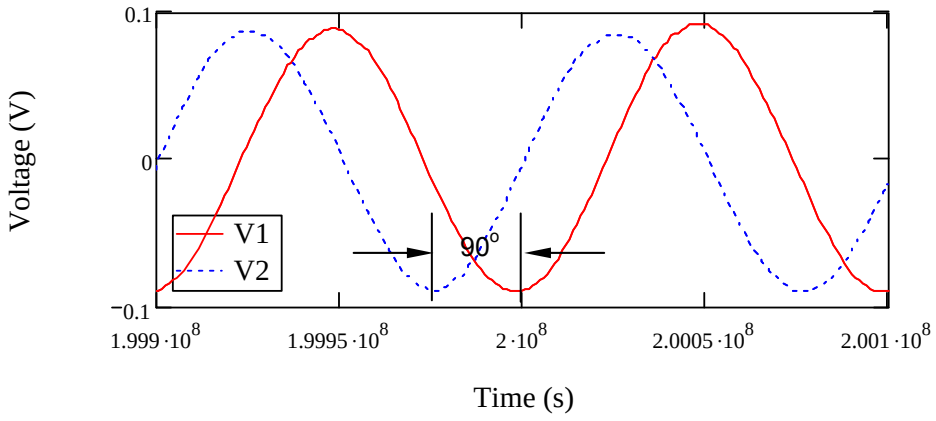

Figure 5.10 Phase measurement using (a) Network analyser and (b) oscilloscope. Both agree each other at 90°

5.4 The practical experiment setup

In this section, a practical experiment setup as shown in Figure 5.11 was put under test. In this experiment, a real phase measurement from an EUT is performed. This EUT is a metal box with an aperture and a signal source was excited across the aperture of the box. The signal from the signal generator supplying the voltage to the EUT was coupled to the first port of the network analyser acting as the reference signal using a directional coupler. The second port of the network analyser was connected to the output port of the GTEM cell where the emission from the EUT inside the GTEM was measured. The first phase reading at the network analyser corresponds to the phase of the radiated signal at the first orientation. The EUT was then placed in a different orientation. The second phase reading corresponded to the phase of the radiated signal at the second orientation. The difference between these two phases is equivalent to the phase difference between these two orientations.

In order to increase the dynamic range of this test system by 30dB, a few modifications were done to the external front-panel jumper cable of the network analyser. These changes enable the user to customize the PNA to make different types of measurements. The front panel jumpers are shown in Figure 5.12 (a) and (b) for port 1 and port 2 of the network analyser respectively. The PNA has four built in receivers with two at each measuring port. Each receiver is linked to the external input/output port via front panel

coaxial cables and through an internal RF switch. The RF switch introduces a switching loss and by bypassing the RF switch, additional 30 dB dynamic range was obtained. To perform the bypass, the following configuration was done. First, the two short coaxial cables connecting the 'CPLR ARM' to 'RCVR A IN' and the 'SOURCE OUT' to 'RCVR R1' IN were removed. The disconnected ports were terminated using 50 Ω SMA terminations to prevent reflection which could damage the internal signal generator. The 'RCVR A IN' port would now act as the first receiver and was coupled to the signal which phase is to be measured. The 'RCVR R1 IN' port is the second receiver and was coupled to the reference signal. It is important to note here that, the input power into these ports of the PNA should be below the maximum input power that the network analyser can handle. This prevents damage.

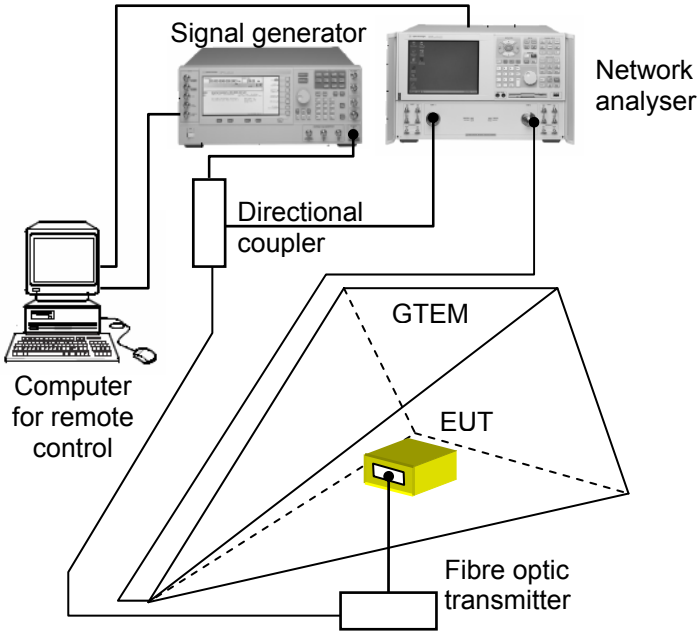

Figure 5.11 Experiment setup to measure the phase difference between two different EUT orientations

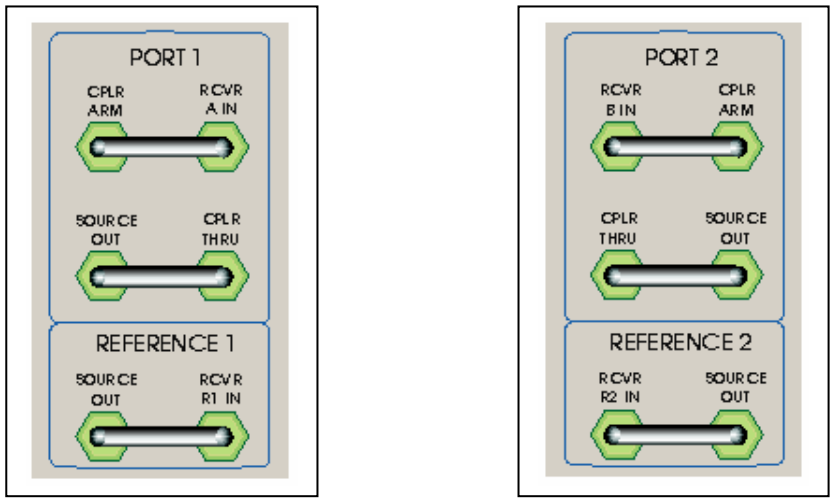

(a)

(c)

Figure 5.12 (a) Front panel jumpers for port 1 and port 2 and (b) the completed cable connection

5.5 The methodology verification

To make sure that this method works as expected, three verification tests were done. These verifications were performed experimentally and were then confirmed by simulations. These are explained in detail in the following sections.

5.5.1 Verification of the phase measurement technique

The intention of this work is to verify the phase measurement technique mentioned Section 5.4. Phase measurement was performed using the GTEM cell according to the proposed technique and the results were compared to the simulations using the GTEM model mentioned in Chapter 3. In this verification, three different EUT orientations were considered. These three orientations are shown in Figure 5.13 and are according to the EUT orientations for radiated emission testing inside a GTEM cell, set by the IEC 61000-4-20 [2]. The EUT used in this work is the metal box with an aperture with the excitation signal fed via the fibre optic cable.

The simulated voltage results for the three different orientations shown in Figure 5.13 are shown in Figure 5.14. These simulated voltage results were then compared by overlapping each signal as shown in Figure 5.15. Any phase difference $\Delta\phi$ can then be observed. The third orientation shown in

Figure 5.14 (c) resulted in noise because the emission from the third orientation does not couple well with the field inside the GTEM model. Since the third position resulted in noise, only the first and second orientations are used in the comparison with the actual phase measurement using the GTEM cell.

In the phase measurement, the experimental set up described in Section 5.4 was performed. The measured phase at the first orientation was ϕ_{exp1}. By rotating the EUT to the second orientation, the measured phase at the second orientation ϕ_{exp2} was obtained. The phase difference between these two orientations can then be obtained by subtracting ϕ_{exp2} from ϕ_{exp1}. The same applies for the third EUT orientation.

From the simulation result, the phase difference ($\Delta\phi$) between first and second orientation can be observed in Figure 5.15 and is approximately 155^{o}. This result is shown in Figure 5.16. In the experimental measurement, the measured phase for the first orientation is 7^{o} and at the second orientation is 173^{o}. With these two values, the phase difference between the first and second orientation is 166^{o}. Apart from the error of 9^{o} between the measurement and the simulation, this result has produced confidence in the phase measurement techniques mentioned in Section 5.4 thus, could be performed reliably.

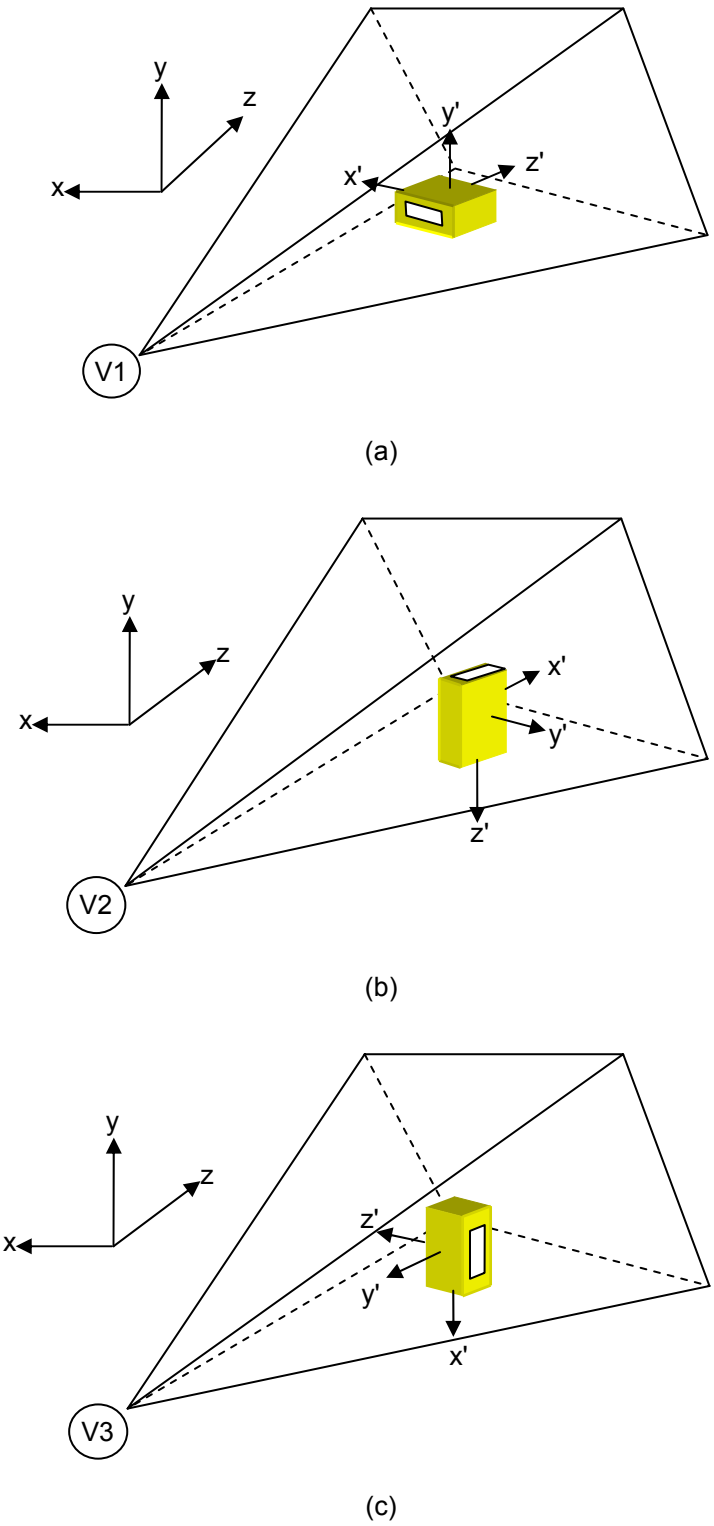

Figure 5.13 EUT in the (a) first, (b) second and (c) third orientation

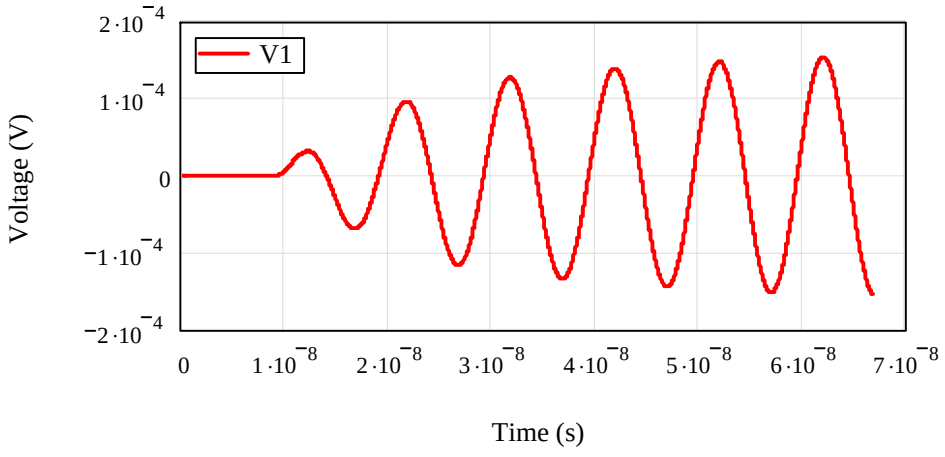

(a)

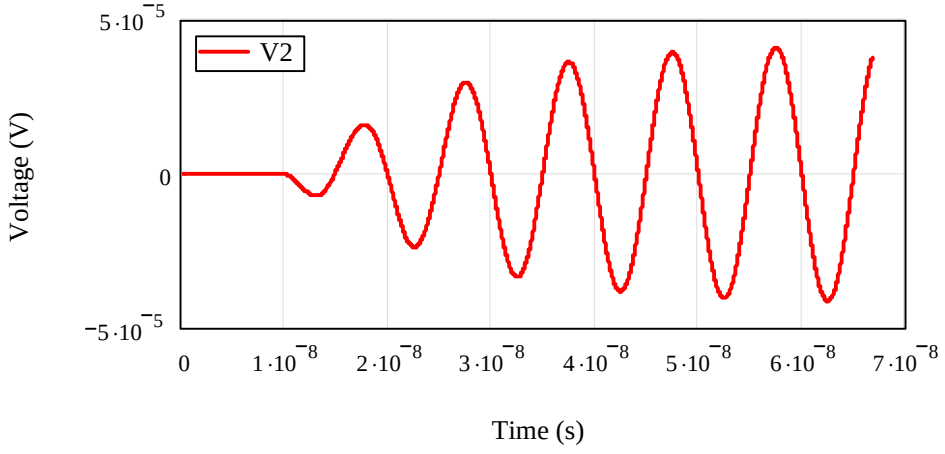

(b)

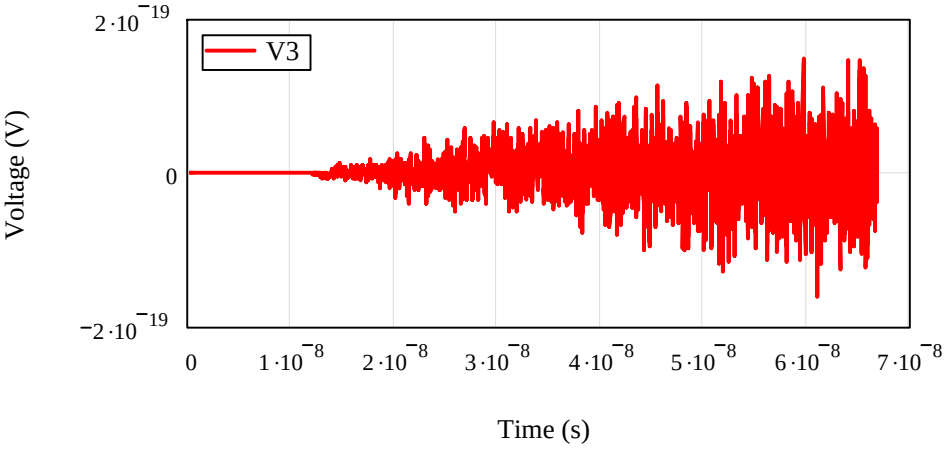

(c)

Figure 5.14 Simulated time-domain voltage (a) V1 for the first orientation, (b) V2 for the second orientation and (c) V3 for the third orientation. These voltages have relative phase information between each other

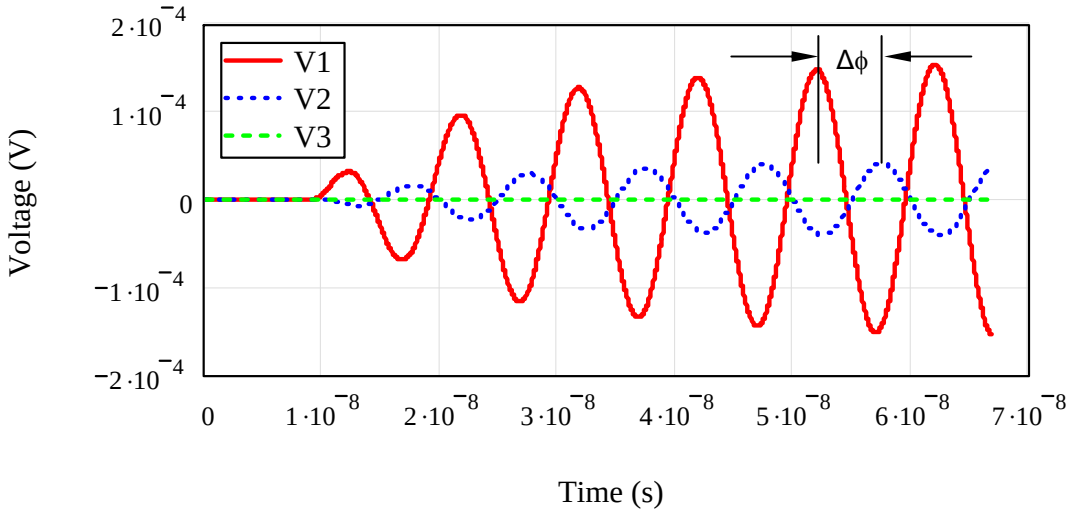

Figure 5.15 Overlapping three voltages to calculate the phase difference between three signals. Note that voltage V3 is barely visible due its very low magnitude compared to V1 and V2

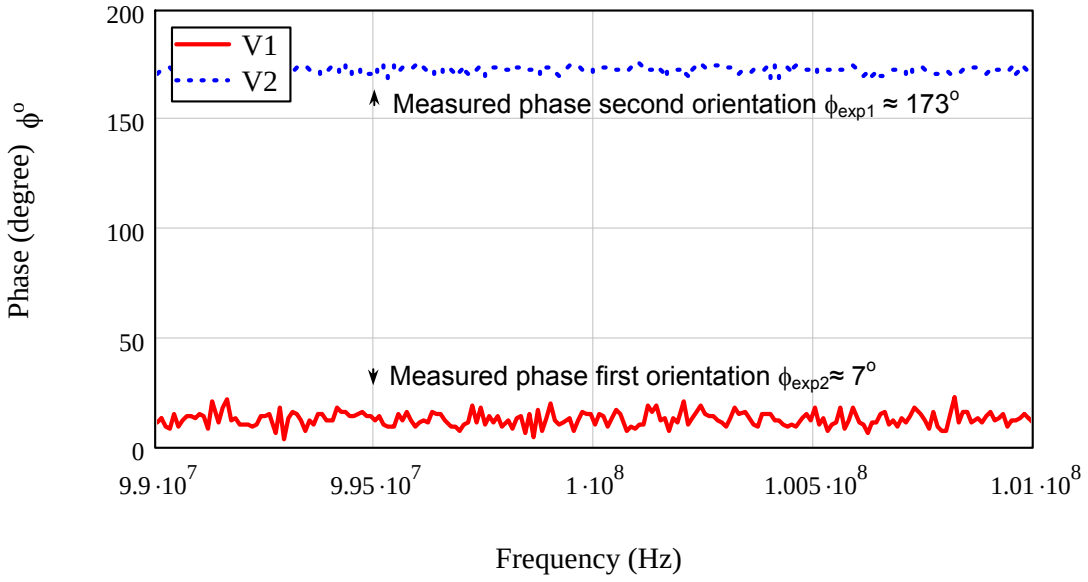

Figure 5.16 Phase property of the signals measured at two different orientations

5.5.2 An experimental verification according to NBS

Since there was no TEM cell available at the time that this work was done, a straight forward comparison between the results obtained in the GTEM and TEM cell could not be done. However, a sample experimental result using the phase method in a TEM cell has been done and it is available in [1]. By comparing the radiation pattern of the EUT obtained from the GTEM cell with the results available in [1], a good assessment of the reliability of the phase measurement method using the GTEM cell can be made.

According to [1], an EUT is represented by a spherical dipole radiator with a radius of 5 cm. This EUT is fed at the poles and held together by a dielectric disc to form a 3 mm gap between the two hemispheres. The signal to the spherical dipole is fed via a fibre optic link so there is no interference arising from a cable. This EUT is similar to the constructed spherical dipole radiator mentioned in Chapter 2 (Section 2.3). With this EUT, the procedure is then tested using the GTEM cell. The measured magnitudes and phases for all orientations are shown in Table 5.1. They cannot be compared directly with the result in [1] because, the power input into the EUT in [1] is not known. However, the result in Table 5.1 can be used to calculate the far field radiation pattern in free space which can be compared with the result in [1]. Since both the EUT used in [1] and in this work are a spherical dipole radiator, the resulting radiation pattern calculated from the GTEM cell result should be a doughnut shaped and the shape should also match reasonably with that in [1].

The far field radiation pattern radiated in free space as a function of θ can be calculated using Equation (5.1) and the total radiated power is calculated using Equation (5.2).

Table 5.1 The measured magnitudes and phases from the GTEM cell

Orientations	Rotations (degree)	0^o (magnitude∠phase)	180^o (magnitude∠phase)
1	45^o	-44.1∠-29	-40.7∠-72
	90^o	-43.4∠-29	-42.4∠-65
2	45^o	-45.3∠-33	-39.9∠-56
	90^o	-44.0∠-31	-41.8∠-46
3	45^o	-44.0∠-65	-41.0∠-71
	90^o	-60.0∠-21	-53.0∠-45

$$
\begin{aligned}
P(\theta,\phi) = \frac{15\pi}{r^2\lambda^2}\Big[&\left(M_{ex}{}^2 + k^2 M_{mx}{}^2\right)\cdot\left(\cos^2\theta\cdot\cos^2\phi+\sin^2\phi\right)+\ldots\\
&\left(M_{ey}{}^2 + k^2 M_{my}{}^2\right)\cdot\left(\cos^2\theta\cdot\sin^2\phi+\cos^2\phi\right)+\left(M_{ez}{}^2 + k^2 M_{mz}{}^2\right)\cdot\sin^2\theta-\ldots\\
&2\left\{M_{ex}M_{ey}\cdot\cos\left(\theta_e^{1'}\right)+k^2 M_{mx}M_{my}\cdot\cos\left(\theta_m^{1'}\right)\right\}\sin^2\theta\cdot\sin\phi+\cos\phi-\ldots\\
&2\left\{M_{ey}M_{ez}\cdot\cos\left(\theta_e^{2'}\right)+k^2 M_{my}M_{mz}\cdot\cos\left(\theta_m^{2'}\right)\right\}\sin\theta\cdot\cos\theta+\sin\phi-\ldots\\
&2\left\{M_{ez}M_{ex}\cdot\cos\left(\theta_e^{3'}\right)+k^2 M_{mz}M_{mx}\cdot\cos\left(\theta_m^{3'}\right)\right\}\sin\theta\cdot\cos\theta+\cos\phi+\ldots\\
&2k\left\{M_{ex}M_{my}\cdot\sin\left(\xi_{ex,my}\right)-M_{ey}M_{mx}\cdot\sin\left(\xi_{ey,mx}\right)\right\}\cdot\cos\theta+\ldots\\
&2k\left\{M_{ey}M_{mz}\cdot\sin\left(\xi_{ey,mz}\right)-M_{ez}M_{my}\cdot\sin\left(\xi_{ez,my}\right)\right\}\cdot\sin\theta\cdot\cos\phi+\ldots\\
&2k\left\{M_{ez}M_{mx}\cdot\sin\left(\xi_{ez,mx}\right)-M_{ex}M_{mz}\cdot\sin\left(\xi_{ex,mz}\right)\right\}\cdot\sin\theta\cdot\sin\phi\Big]
\end{aligned}
\tag{5.1}
$$

$$
\begin{aligned}
P_{total} &= \frac{40\cdot\pi^2}{\lambda^2}\cdot\left[M_{ex}{}^2 + M_{ey}{}^2 + M_{ez}{}^2 + k^2\left(M_{mx}{}^2 + M_{my}{}^2 + M_{mz}{}^2\right)\right]\\
&= 2.23\times10^{-7}\ \text{W}\\
&= -36.50\ \text{dBm}
\end{aligned}
\tag{5.2}
$$

Where

$$r = 0.30\ \text{m} \tag{5.3}$$

$$\lambda = C \big/ 100M \quad \text{m} \tag{5.4}$$

$$M_{ex} = 2.64\times10^{-5},\ M_{ey} = 4.55\times10^{-5} \text{ and } M_{ez} = 2.87\times10^{-5} \tag{5.5}$$

$$M_{mx} = 6.97\times10^{-6},\ M_{my} = 1.48\times10^{-5} \text{ and } M_{mz} = 8.59\times10^{-6} \tag{5.6}$$

$$\theta_e^{1'} = -83.96^o,\ \theta_e^{2'} = 83.06^o \text{ and } \theta_e^{3'} = 24.88^o \tag{5.7}$$

$$\theta_m^{1'} = 28.45^o,\ \theta_m^{2'} = 47.12^o \text{ and } \theta_m^{3'} = -67.26^o \tag{5.8}$$

$$\xi_{ex,my} = -132.64^o,\ \xi_{ey,mx} = -42.51^o \text{ and } \xi_{ey,mz} = -195.80^o \tag{5.9}$$

$$\xi_{ez,my} = -145.98^o,\ \xi_{ez,mx} = -184.84^o \text{ and } \xi_{ex,mz} = -142.45^o \tag{5.10}$$

The procedure to calculate the unknowns (Equations 5.5 - 5.10) in Equation (5.1) and (5.2) is included in Appendix D. The calculated radiation pattern of the EUT is plotted and shown in Figure 5.17. The radiation pattern of the EUT in [1] is also shown in Figure 5.18 for comparison.

From this comparison, small discrepancies are observed. The result obtained from the GTEM experiment does not show an exact match to the result from NBS. However, the result shows a doughnut shaped radiation pattern as one would expect from a spherical dipole antenna. It is believed that the discrepancies were caused by the corrupted phase information when the EUT is not rotated around its centre. This means that the actual phase difference between the first orientation and the orientation after 180^o rotation may have changed during repositioning. In other words, the new position of the EUT has deviated to a new centre as shown in Figure 5.19. This can be

corrected by using a high precision turntable. At the time of this experiment, no such turn table is available and rotation of the EUT is done using marking on a platform. A suitable EUT manipulator is proposed and is described in Appendix E.

Since the EUT is spherical, it is housed inside a foam structure (octagonal object) to ease positioning (shown in Chapter 2, Figure 2.8). Due to imperfect machining of the foam structure, the actual centre of the hole that houses the spherical dipole is not exactly centred as shown in Figure 5.20 (a). This leads to small errors because the rotation centre of the foam structure may not coincide with the electrical centre of the EUT. Another error arising from this imperfection is that the sides are not perfectly shaped to give an exact angle as shown in Figure 5.20 (b). This is derived from the result that the dipole orientation, ϕ is actually $\approx 60^{o}$ (shown in Equation (D.53a) in Appendix D) instead of 45^{o} as stated in [1].

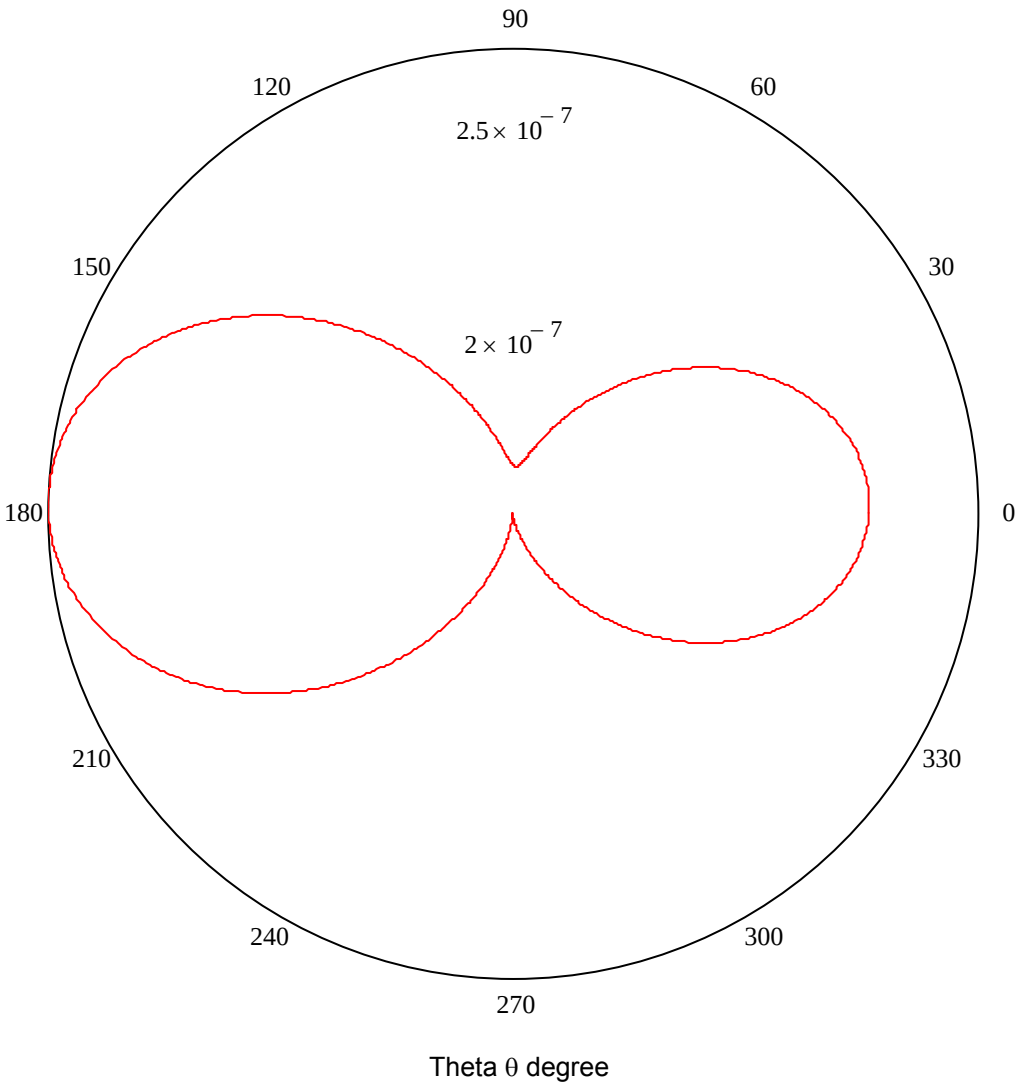

Figure.5.17 Calculated power pattern (W) in free space in the ϕ plane showing the main lobe of the spherical dipole radiator used in the GTEM cell experiment

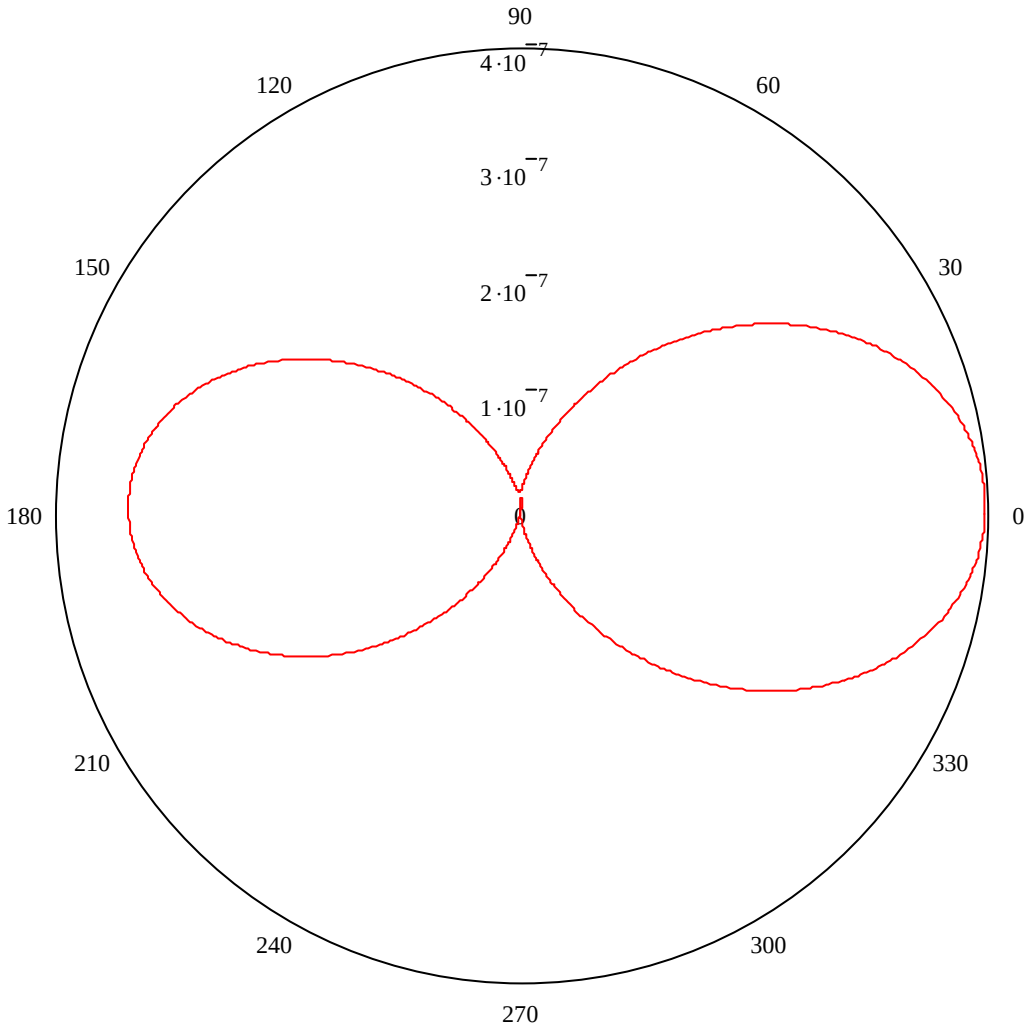

Figure.5.18 Calculated power pattern (W) in free space in the ϕ plane showing the main lobe of the spherical dipole radiator used in TEM cell experiment adapted from [1]

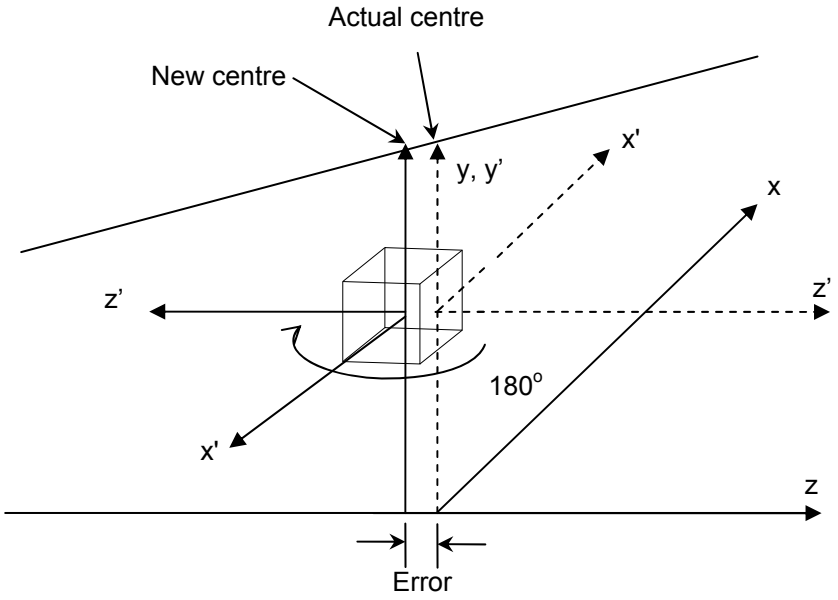

Figure 5.19 Deviation from the actual centre of the EUT after an 180° rotation at the y axis

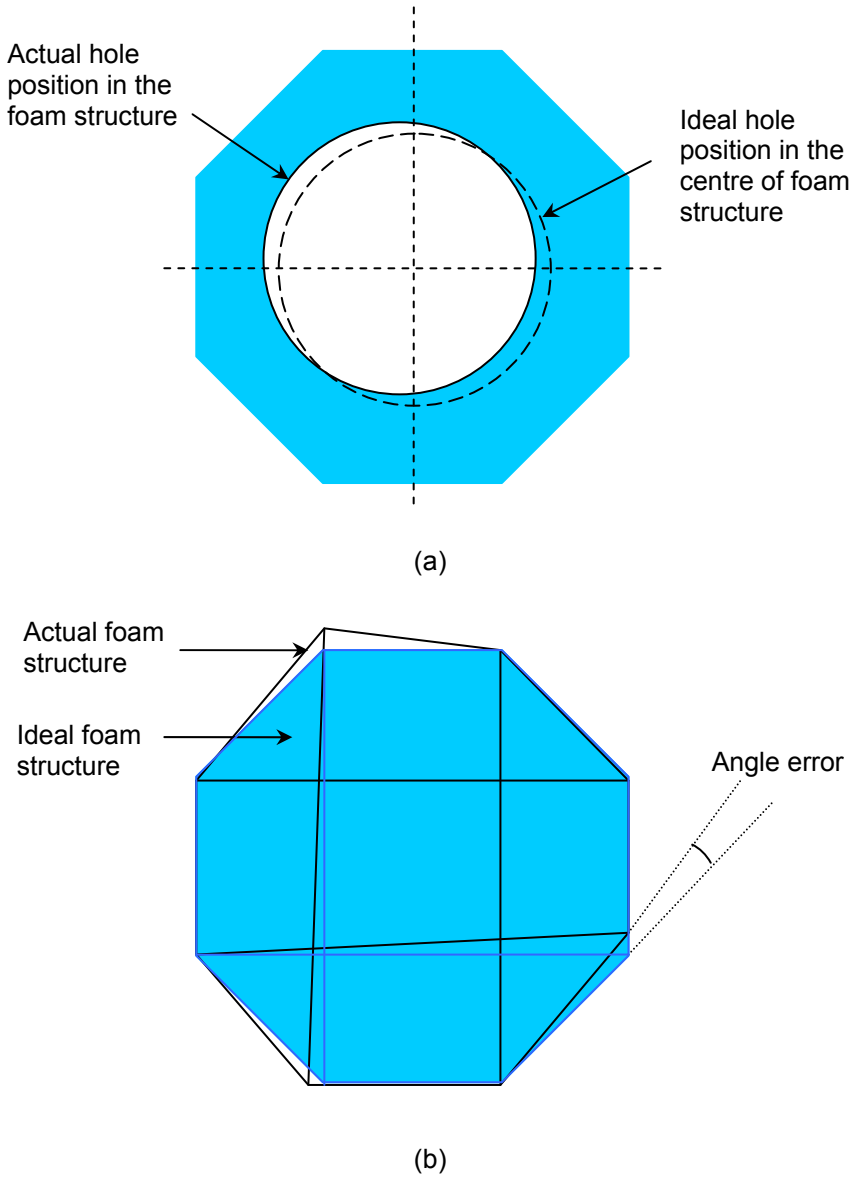

Figure 5.20 Imperfection in machining the foam structure resulting in (a) deviated actual hole position and (b) angle error at the sides of the foam structure

5.5.3 An experimental verification according to the IEC 61000-4-20

To further investigate the level of accuracy in performing phase measurements in the GTEM cell, a comparison is made between the result obtained in Section 5.5.2 and a measurement performed according to the IEC 61000-4-20 (three orientation method). The same EUT was used in the measurement and the three voltage readings were obtained from the three orientations. The total radiated power is calculated by:

$$P_{total} = \frac{\eta_o}{3 \cdot \pi} \cdot \frac{{k_o}^2}{{e_{oy}}^2 \cdot Z_c} \cdot S^2 \tag{5.11}$$

where

$$\eta_o = 377\,\Omega \tag{5.12}$$

$$k_o = \frac{2\pi}{\lambda} \tag{5.13}$$

$$\lambda = \frac{c}{200 \times 10^6} \tag{5.14}$$

$$e_{oy} = 9.06 \tag{5.15}$$

$$Z_c = 50\Omega \tag{5.16}$$

$$S = \sqrt{{V_1}^2 + {V_2}^2 + {V_3}^2} \tag{5.17}$$

where V_1, V_2 and V_3 are the voltages of the three orientations obtained from the power (P_1, P_2 and P_3 in dBm) using the spectrum analyser. The measured power P_1, P_2 and P_3 were:

$$P_1 = -42.9 \text{ dBm} \tag{5.18a}$$

$$P_2 = -52.0 \text{ dBm} \tag{5.18b}$$

$$P_3 = -42.2 \text{ dBm} \tag{5.18c}$$

After the conversion from dBm to Volts using Z = 50 Ω, the total power radiated can be calculated by:

$$\begin{aligned} P_{total} &= \frac{\eta_o}{3 \cdot \pi} \cdot \frac{k_o{}^2}{e_{oy}{}^2 \cdot Z_c} \cdot S^2 \\ &= 1.01 \times 10^{-6} \quad \text{W} \\ &\approx -29.96 \quad \text{dBm} \end{aligned} \tag{5.19}$$

This result (Equation 5.19) differs by about 6 dB from the result obtained from the measurement that includes phase (Equation 5.2). This is rather significant and to justify this error, a TLM simulation was performed as described in the following section.

5.5.4 Verification using the TLM simulation

A simulation using the TLM method was performed as the third verification test. A spherical antenna was modelled and was fed in the centre with the same power and frequency as in the experiments in Section 5.5.3. The total radiated power of the EUT was simulated using the software using function “powerOutputTest”. The resulting instantaneous power is shown in

Figure 5.21. The total radiated power of the EUT is calculated (Equation 5.20) by taking the average of the power shown in Figure 5.21.

$$\begin{aligned} P_{total} &= \frac{2.95\times10^{-7} - \left(7.73\times10^{-9}\right)}{2} \\ &= 1.51\times10^{-7} \quad \text{W} \\ &\approx -38.20 \quad \text{dBm} \end{aligned} \tag{5.20}$$

The simulated total radiated power is -38.20 dBm (Equation 5.20) while the total radiated power obtained from the measurement using the GTEM cell that involves phase is -36.50 dBm (Equation 5.2). Apart from a small discrepancy of 1.7 dB, the results agree reasonably well. From this verification process, it is concluded that the phase measurement method that is described in this chapter is reasonably accurate despite some errors that occurred during the measurement. These errors could be further reduced by using a more accurate mechanical manipulator.

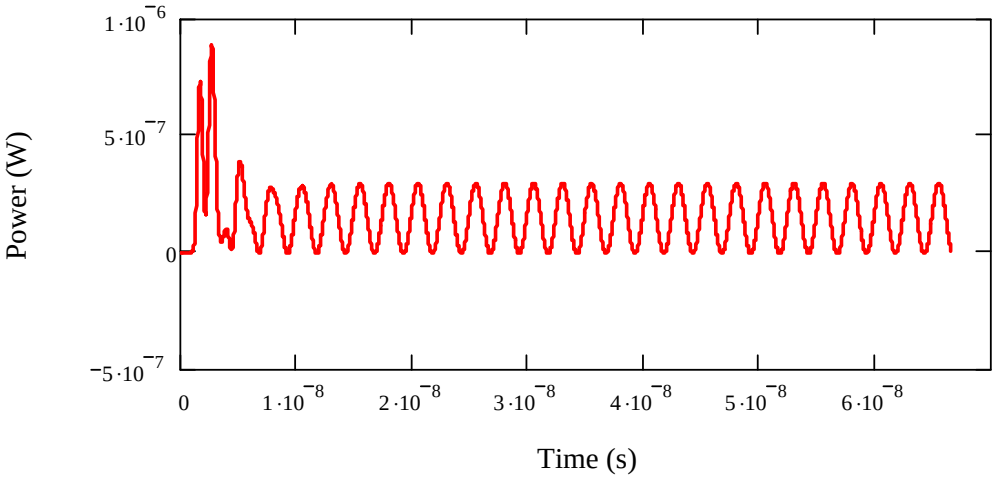

Figure 5.21 The simulated instantaneous power of the dipole antenna

5.6 The impact of phase measurement on the total radiated power

In the last section, a total radiated power measurement using the GTEM cell that includes the phase measurement was introduced. In this section, the significance of the inclusion of the phase is discussed. Three different methods of obtaining the total power radiated from a EUT were outlined. The first is the measurement using the GTEM cell that includes the phase. The second method is the measurement according to the industry standard IEC 61000-4-20 [2]. The third method is a numerical simulation using a TLM model. The same EUT is used in all three methods. The EUT is represented in software in the simulations. All results are shown in Table 5.2.

From the measurement that involves the phase [1], the calculated total power radiated is -36.50 dBm. Using the method in [2], the calculated total power radiated is -29.97 dBm. In the simulation, the total power radiated is given as -38.20 dBm. It is noticeable that the measurement taken using the GTEM cell that involves the phase measurement produced a very close result when compared to the result obtained by simulation. The result obtained from the measurement according to [2] differs by about 8.23 dB from the simulation.

Only a simple antenna system, which is a dipole antenna, is used in this work. This result shows that a large error can occur even for a single radiator. For several dipole moments, larger errors would be expected. It is reasonable to expect that by excluding phase, errors will increase for an EUT

with many dipole moments. It is concluded that, by taking the phase into account, errors in measurements can be reduced.

Table 5.2

Comparison of total power radiated between three different methods

No	Method	Total power radiated (dBm)	Absolute difference against TLM simulation results (|dB|)
1	GTEM + phase	-36.50	1.70
2	GTEM + IEC 61000-4-20	-29.97	8.23
3	TLM simulation	-38.20	

5.7 Conclusions

It is demonstrated in this chapter that phase measurements can be done in a GTEM cell. On first examination, the experimental setup mentioned in Section 5.4 may not seem practical for phase measurements because electronic equipment do not have an easily accessible reference signal. To make the measurements practical for normal electric appliances, a small antenna receiver circuit mounted on the turn-table inside a GTEM cell can be added. This setup keeps the reference phase signal constant as the EUT is rotated and no physical attachment is necessary. This circuit could change the received electrical signal to optical signal and transmit it to an external fibre optic receiver. This circuit should be designed to cause minimum distortion to the primary vertical field in the usable volume. Outside of the GTEM cell, the optical signal could be easily converted to electrical signal and then connected to the network analyser. A low noise amplifier could be added

in case the signal is too weak. As an alternative, it is strongly suggested to use the method mentioned in Section 5.4 because it adds +30dB broadband dynamic range while a normal amplifier can only add about +20dB narrowband. This cuts the cost of an additional amplifier to do this measurement. In addition, the worry of phase shifts in some amplifiers is eliminated.

This chapter has introduced a phase measurement technique using a GTEM cell which has not been attempted before. The method proved to be accurate and reliable given that the result from the numerical model agreed very well with those obtained from the experiment. This work is very useful because it opens the way of examining the assumption inherent in current practice that all dipole moments are in phase. In addition, future work in the characterization of emissions in GTEM cells could be more accurate if phase change is taken into account.

5.8 References

1. Ma M.T. and Koepke G. *"A method to quantify the radiation characteristics of an unknown interference source",* NBS Tech. Note 1059, United States Department of Commerce, National Bureau of Standards, October 1982.

2. 61000-4-20, *"Electromagnetic Compatibility (EMC) – Part 4: Testing and measurement techniques. Section 20: Emission and immunity testing in transverse electromagnetic (TEM) waveguides",* International Electrotechnical Commission, Geneva, Switzerland, 2003.

Chapter 6

Discussion and Conclusions

6.0 Summary of the work

Conclusions were presented at the end of each chapter in this Thesis summarizing important points in each chapter. In this last chapter, the main points arising from these conclusions are brought together and discussed.

In Chapter 1, the methods of performing tests using a GTEM cell were reviewed. Most of the existing methods using a GTEM do not include phase measurement because it cannot be easily done because a GTEM cell has only one port. Many of these methods require several EUT orientations. The IEC 61000-4-20 adopted a technique whereby only three orientations are

required to obtain the total power radiated by an EUT. Two major assumptions were made. First, an EUT is electrically small; that is less than 0.1 times the wavelength. Second, there is only one dominant radiator and there is no phase difference between dipole moments coming from a single dominant dipole radiator.

A GTEM model presented in Chapter 3 is used in various studies throughout the entire thesis. It has proven to be an invaluable tool in characterizing the emission measurements in a GTEM cell as well as characterizing the behaviour of a GTEM cell. Some GTEM cell parameters are difficult to study experimentally. The phase measurement technique is one of them. However, it is easily investigated using the TLM simulations. The GTEM model presented in Chapter 3 is one of the early models developed using TLM. The model's success is due to the inclusion of realistic pyramidal RAM that has dielectric properties similar to actual RAM. In the development of the model, some extensive verification processes to make sure that the model is working correctly were presented. Comparisons between values obtained from experiment and from simulated results show that the model works well.

All the EUTs used in this work are described in Chapter 2. By knowing the electrical behaviour of these EUTs, measurement or simulation results can be interpreted more easily. Various types of EUT such as electric radiator, magnetic radiator or a combination of both were considered in this Thesis.

This is important to ensure the practicality of the work described in this Thesis.

It is shown in Chapter 4 that the impact of phase on the power magnitude received at the GTEM output port is significant even from a simple radiator such as a dipole antenna. Various types of radiator systems such as the combinations of magnetic and electric radiator are considered in the study of phase impact and it is found that the measured power magnitudes for all of the EUTs are influence by phase differences. Possible explanations for the nature of coupling mechanisms in the GTEM cell as a function of phase are presented. It is found that the phase difference between two radiators on the same EUT changes the overall radiation pattern of the EUT. When this happens, the directions of the major electric or magnetic field components will change. This directly affects coupling inside a GTEM cell. This study has given some insight into possible errors due to phase that can be included in an uncertainty budget in future GTEM emission testing. The errors due to the phase mentioned in the Thesis indicate potential or possible discrepancies that may occur under worst case conditions.

In Chapter 5, an experimental technique to measure the phase difference between dipole moments in a GTEM cell is presented. This is done in an effort to show that phase measurement can be made in a GTEM. It is shown that the GTEM and TEM are similar electrically thus by rotating an EUT through 180^{o} on the y axis, measurements that mimic the measurements

taken on the second port of a TEM cell can be done. Good results are obtained by comparing to the results from a TEM cell.

6.1 Future work

This Thesis provides some insights on the behaviour and the performance of a GTEM cell. This work will lead to many other further investigations in the future. The accomplishment of a complete TLM model of a GTEM results in a tool that can be used to improve the architecture of a GTEM cell by GTEM cell manufacturers. This model has been properly constructed and verified to prove its reliability. Therefore, this model is good to study other GTEM characteristics such as the determination of a proper resistor network at the termination of the septum by determining the current distribution on the septum. This is normally very difficult to accomplish experimentally using test and trial. Pyramidal sizes, shapes and placement architecture can also be investigated using this model in order to provide better and effective loading for higher frequencies. Another investigation is the behaviour of cables placed inside a GTEM cell and their impact.

The Thesis has presented the potential problem that may arise if phase information is ignored. This investigation may be used to improve the existing standards' algorithm such as the IEC 61000-4-20 for better accuracy. In addition, a new experimental method may be developed to measure or

somehow obtain preliminary phase information from an EUT before an emission test to warn the test engineers of the potential errors that might arise during testing.

A new method of emission testing using a GTEM cell that involves phase information as outlined in the Thesis can be improved and then realized commercially. This includes the development of software and an EUT positioner automation system to improve accuracy. It is hoped that the phase difference between the dipole moments of an EUT can be integrated into the measurement procedures in a future standard in the hope of achieving a better accuracy in EMC testing.

Appendix

A Development of fibre optic spherical dipole radiator

Figure A.1 shows the PCB layout of the optical fibre receiver. Figure A.2 has similar function as in Figure A.1 with the difference that the PCB in Figure A.1 has to be designed to fit into a spherical brass ball whereas the PCB in Figure A.2 was fitted into the metal box. The optical fibre transmitter is shown in Figure A.3. The schematic diagrams of the receiver and transmitter are shown in Figure A.4 and Figure A.5 respectively. The components used in both schematics are outlined in Table A.1 and A.2.

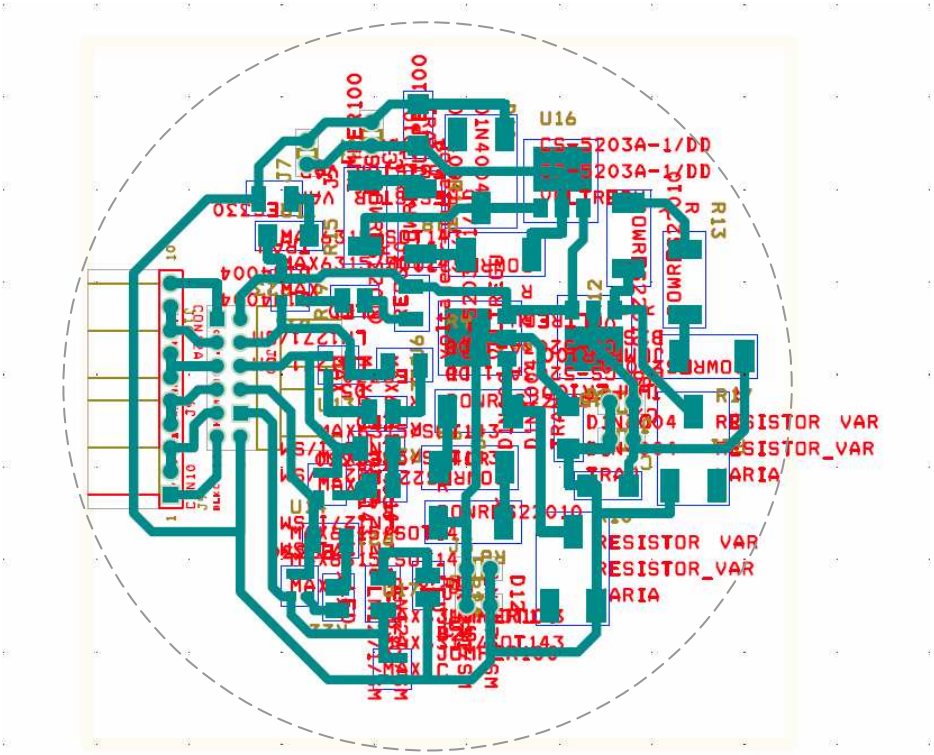

Figure A.1 Printed circuit board footprints for the spherical dipole radiator

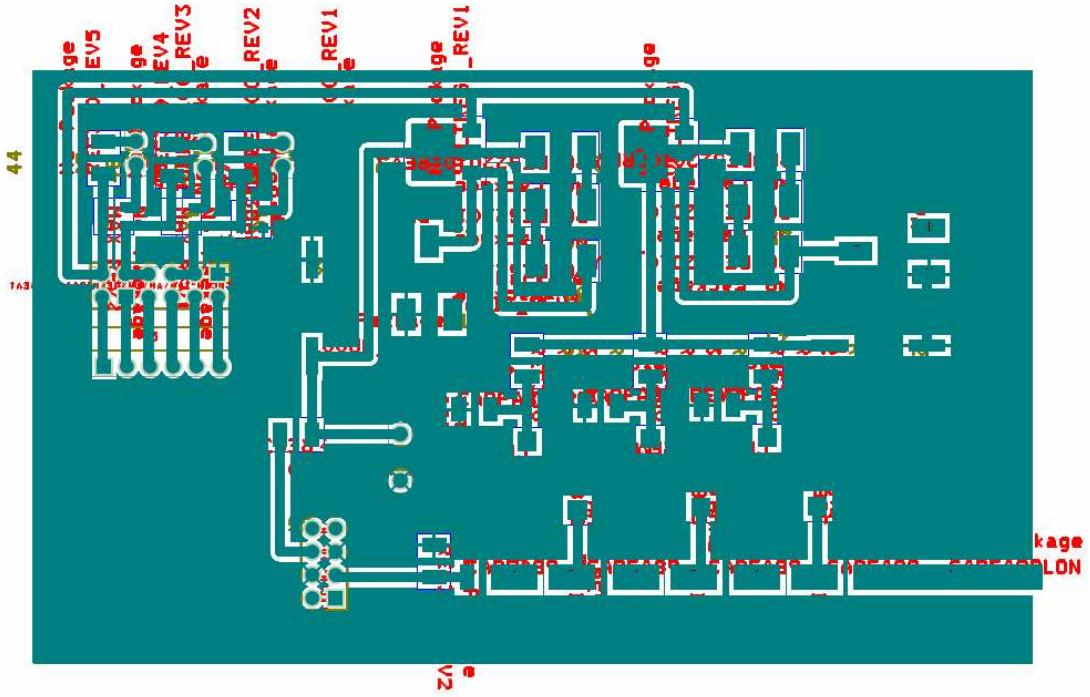

Figure A.2 Printed circuit board footprints for the metal box radiator

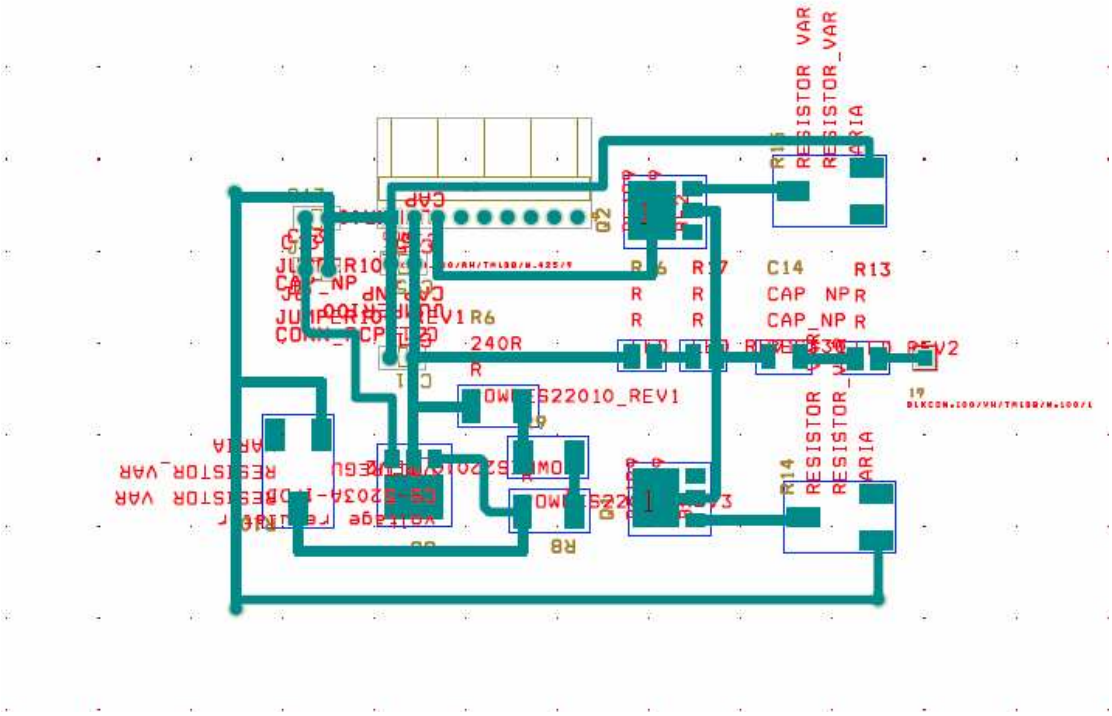

Figure A.3 Printed circuit board footprints for the radio to fibre optic driver unit

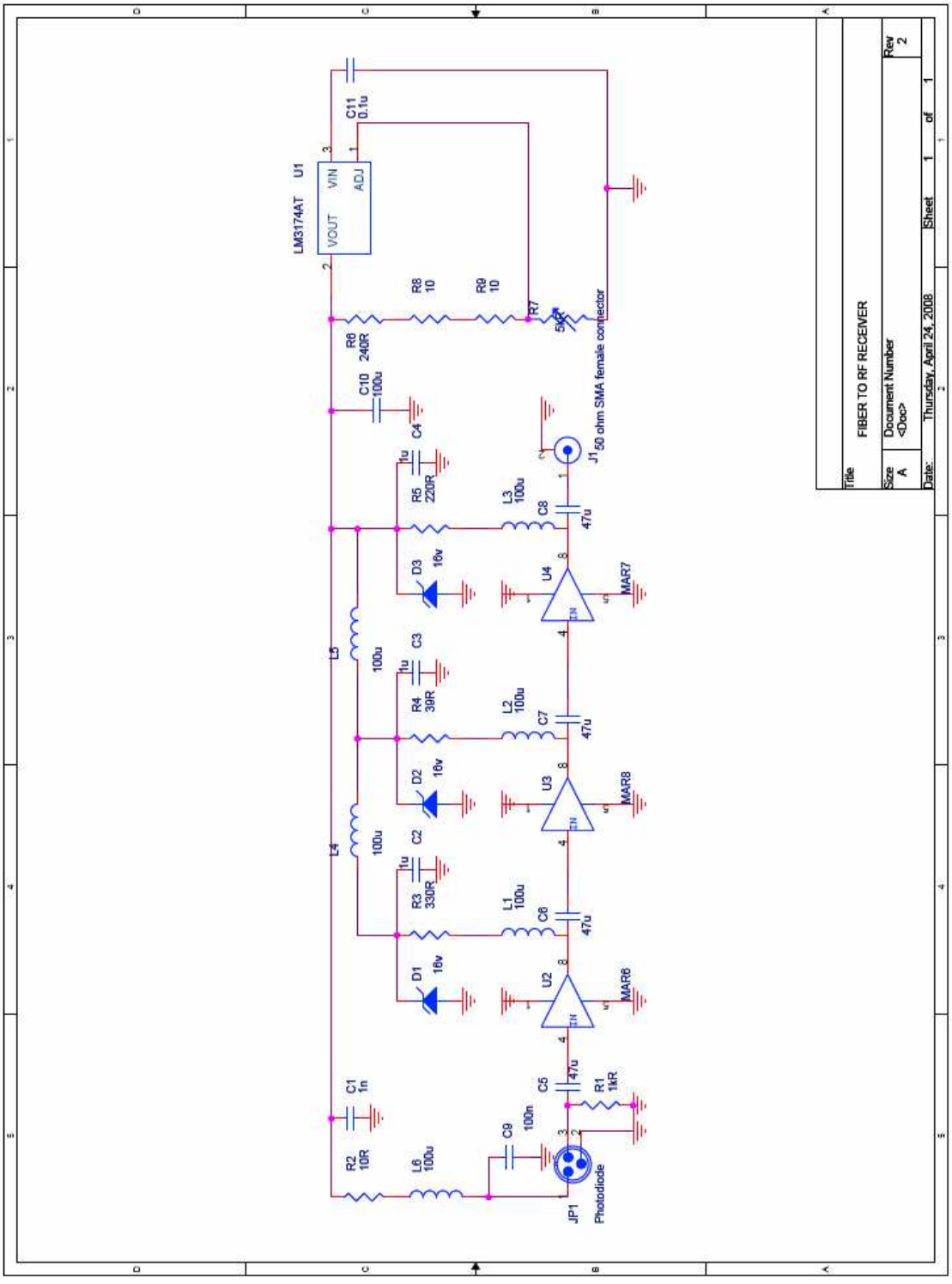

Figure A.4 Schematic for the spherical dipole radiator and metal box radiator

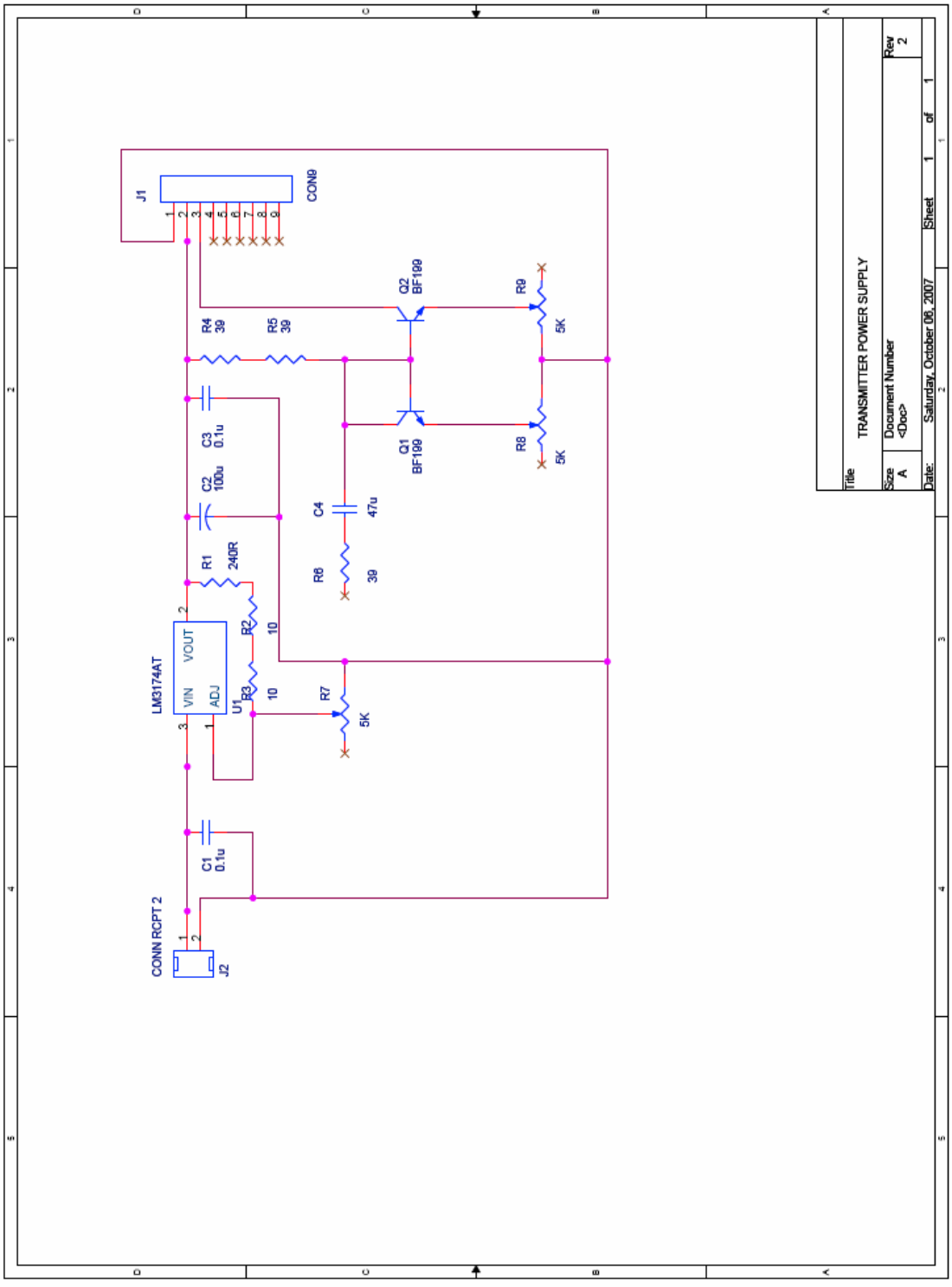

Figure A.5 Schematic for the radio to fibre optic driver unit

Table A.1 List of components used in fibre optic receiver circuit

Component	Value	Part number	Available from	Manufacturer	Description
C1	1nF	B37872K5102K60	FA757561	Epcos	Capacitor, 1206
C2.C3,C4	1uF	B37872K9105K62	FA757550	Epcos	Capacitor, 1206
C5,C6,C7,C8	47uF	12065C473KAT2A	FA 499377	Avx	Capacitor, 1206,
C9 C11	100nF	12065C104KAT00J	FA499389	Avx	Capacitor, 1206
C10	100uF	100 vfc 5c1	FA3679788	Panasonic	Capacitor, case g
R1	1KΩ	RC-01-1K-5P5.	512734	Phycomp	Resistor, 1206
R2 R8,R9	10Ω	232271161109	FA 9240284	Phycomp	Resistor, 1206
R3	330Ω	RC-02H-330R-1P5.	FA 513313	Phycomp	Resistor, 1206
R4	39Ω	RC-02H-39R-1P5.	FA 3600956	Phycomp	Resistor, 1206
R5	220Ω	RC-02H-220R-1P5.	FA513120	Phycomp	Resistor, 0805
R6	240Ω	232276260221	FA9235930	Phycomp	Resistor, 2512
R7	5KΩ	3386G-1-502	FA 658662	Bourns	Variable resistor
D1,D2,D3	16V	BZX84-B16.	FA3163118	Nxp	Diode, zener
J1	9 ways	M20-9770906	RS472922	Harwin	2.54mm (.100") PITCH
J2	2 ways	M20-9770206	RS472922	Harwin	2.54mm (.100") PITCH
U1	-	LM317AEMP	FA 4125435	National semiconductor	Voltage regulator type:Positive Adjustable
U2	20	MAR6sm	-	Minicircuit	Surface mount Monolithic amplifier
U3	12.5	MAR8sm	-	Minicircuit	Surface mount Monolithic amplifier
U4	22.5	MAR7sm	-	Minicircuit	Surface mount Monolithic amplifier
L1,L2,L3,L4,L5,L6	100u	ADCH-80A	-	Minicircuit	RF choke
Photodiode	-	HFBR-2416Z	FA1173150	Avago technologies	Receiver, fibre optic

Table A.2 List of components used in fibre optic transmitter circuit

Component	Value	Part number	Available from	Manufacturer	Description
C1,C3	0.1 uF	12065C104KAT00J	FA499389	Avx	Capacitor, 1206
C2	100uF	100 vfc 5c1	FA3679788	Panasonic	Capacitor, case g
R1	240Ω	232276260221	FA9235930	Phycomp	Resistor, 2512
R2,R3	10Ω	232271161109	FA 9240284	Phycomp	Resistor, 1206
R4,R5,R6	39Ω	RC-02H-39R-1P5.	FA 3600956	Phycomp	Resistor, 1206
R7,R8,R9	5KΩ POT	3386G-1-502	FA 658662	Bourns	Variable resistor
Q1,Q2	NPN	BFG 198/199	RS1003101	NXP	Transistor
J1	9 ways	M20-9770906	RS472922	Harwin	2.54mm (.100") PITCH
J2	2 ways	M20-9770206	RS472922	Harwin	2.54mm (.100") PITCH
U1	-	LM317AEMP	FA 4125435	National semiconductor	Voltage regulator type: Positive Adjustable
CON9	-	HFBR-2416Z	FA1173150	Avago technologies	125Mhz analogue receiver

B The field distributions inside the GTEM cell due to loading

In this Section, the three major components of the electric field distribution, E_x, E_y and E_z are investigated under unloaded and loaded conditions. Grounding of the loaded EUT is also studied. The E_y electric field is of prime interest in this study since it is the major electric field in a GTEM cell. The electric field distributions, E_x, E_y and E_z when there is no load inside the GTEM were shown previously in Figure 3.23 in Chapter 3. An EUT consisting of a rectangular metal brass box is then loaded into the useable volume of the GTEM and the electric field distribution is then investigated. The results are shown in Figure B.1. It is observed that the electric field distribution does not change significantly as compared to the condition when the GTEM is not loaded. With the same EUT still loaded inside the GTEM, this time, a connection is established between the EUT metallic body and the GTEM body. The resulting electric field distribution is seen in Figure B.2. The electric field distribution is now slightly altered as compared to the two earlier conditions. The ground connection of the EUT has established a new potential distribution between the metal brass box and the septum and this alters the electric field distribution inside the GTEM for all E_x, E_y and E_z.

The same explanation applies to the magnetic field H_x. The magnetic field distributions, H_x, when there is no load inside the GTEM were shown previously in Figure 3.24 in Chapter 3. Figure B.3 shows the H_x distributions of the GTEM cell when the same loading conditions are applied.

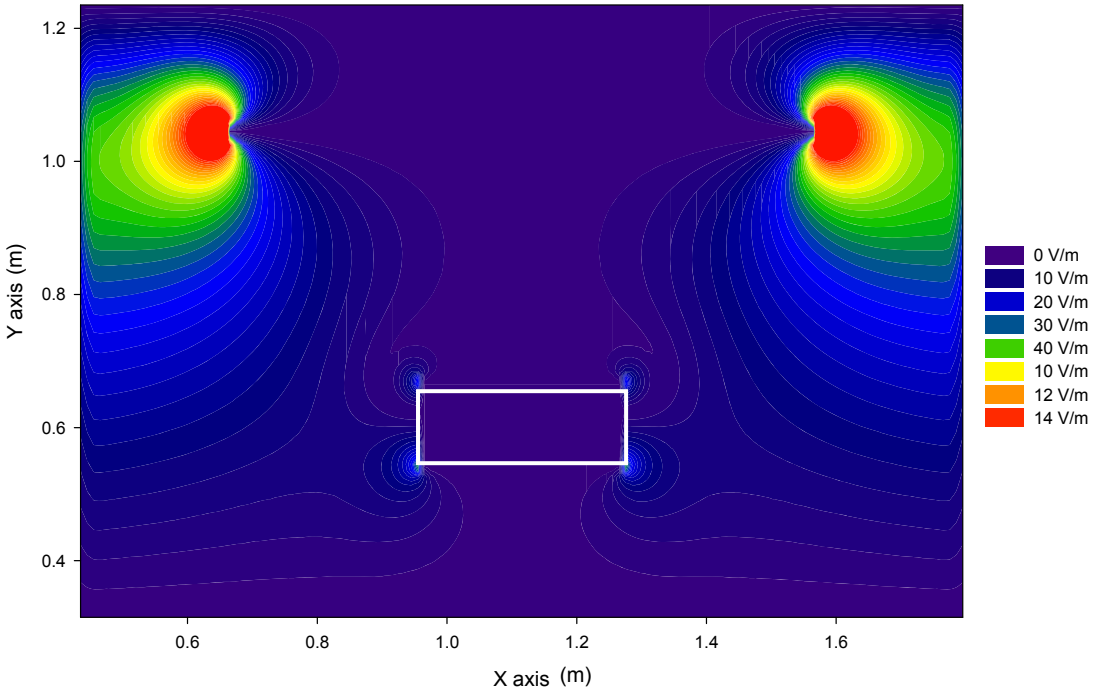
1.2
1.0
0.8
0.6
0.4
Y axis (m)
0.6
0.8
1.0
1.2
1.4
1.6
X axis (m)
0 V/m
10 V/m
20 V/m
30 V/m
40 V/m
10 V/m
12 V/m
14 V/m

(a)

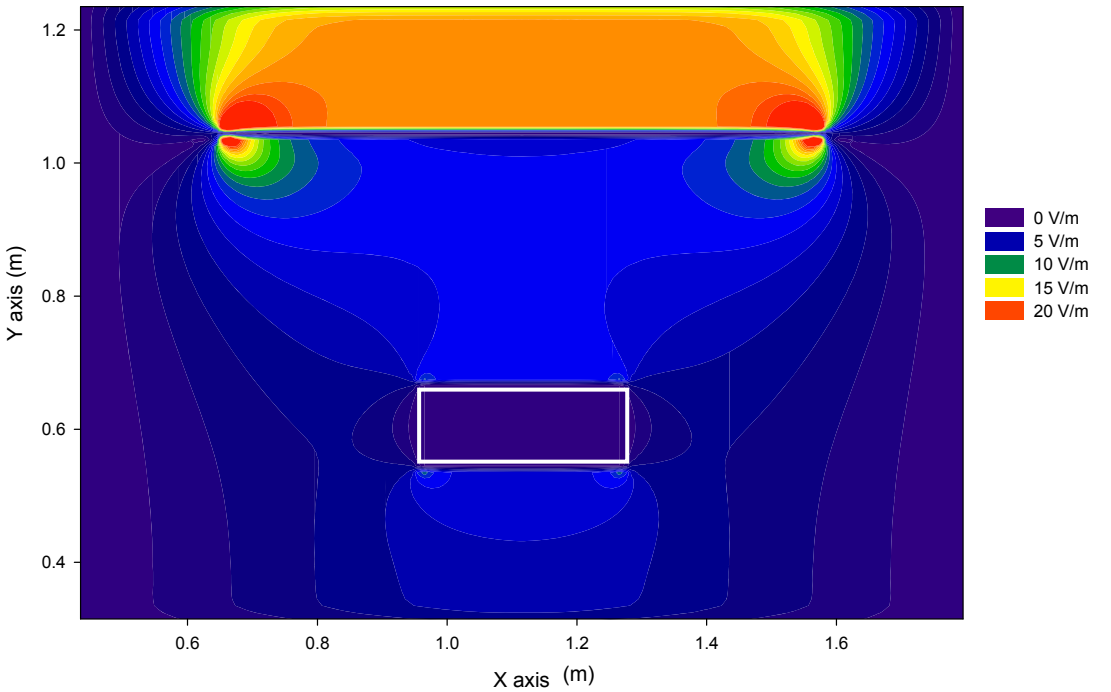
1.2
1.0
0.8
0.6
0.4
Y axis (m)
0.6
0.8
1.0
1.2
1.4
1.6
X axis (m)
0 V/m
5 V/m
10 V/m
15 V/m
20 V/m

(b)

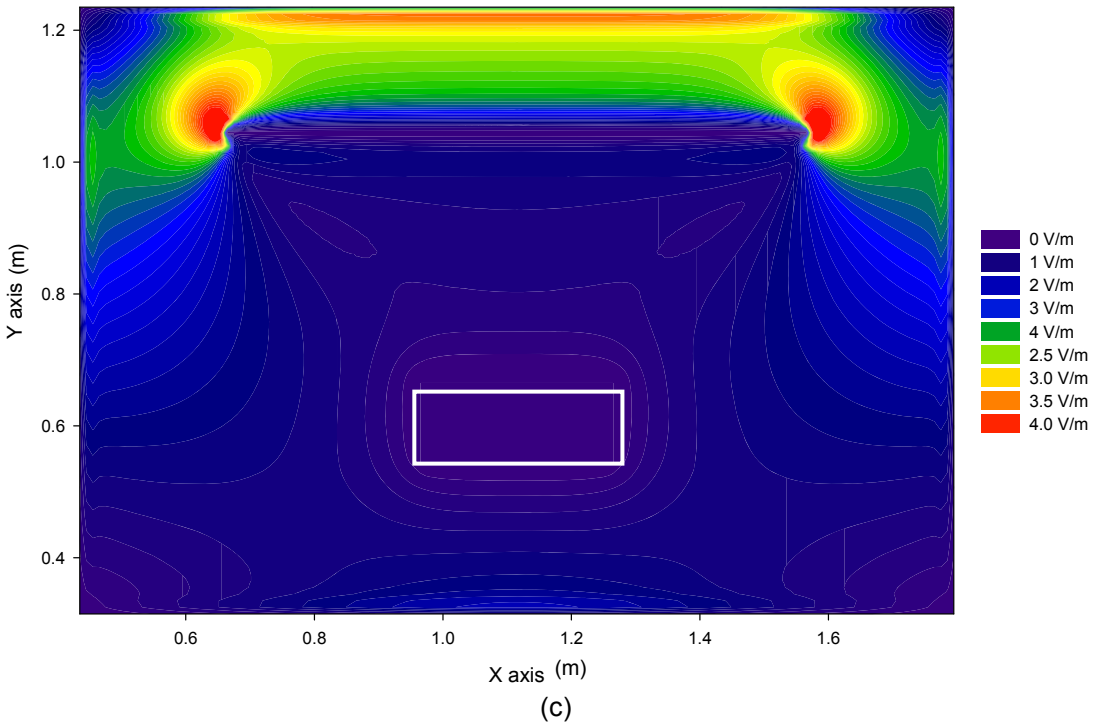

(c)

Figure B.1 Electric field distributions for E_x, E_y and E_z (a)-(c) for loaded without grounding. Numbers in the Figure indicate the electric field in V/m at particular points. EUT location is highlighted by the white rectangular box

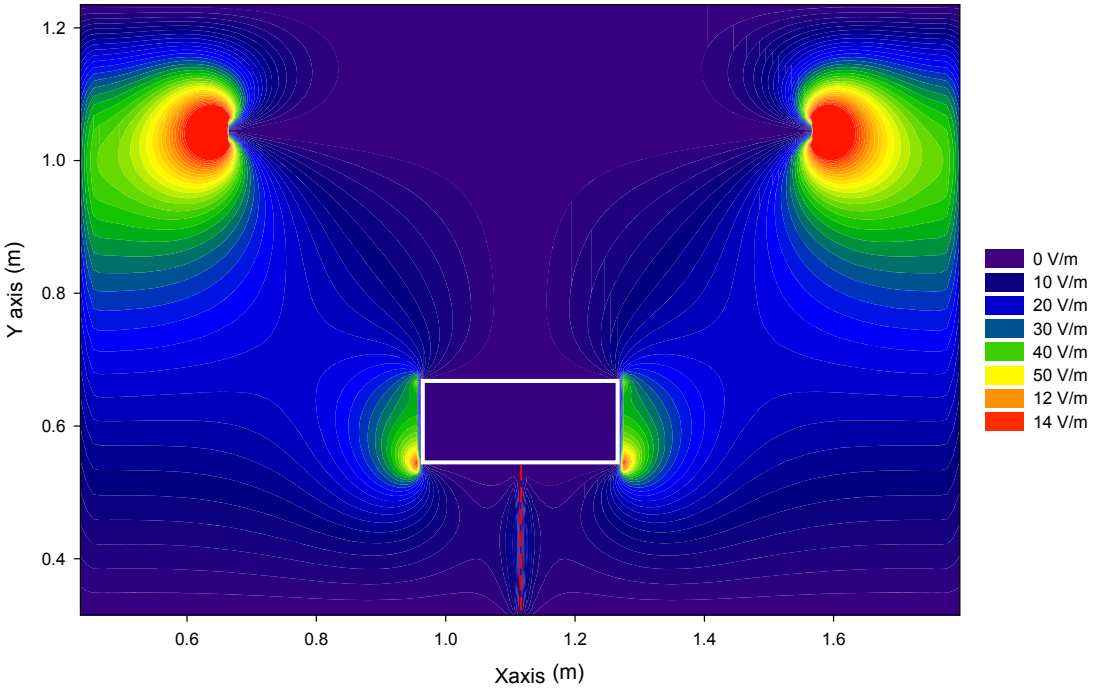
1.2
1.0
0.8
0.6
0.4
Y axis (m)
0.6
0.8
1.0
1.2
1.4
1.6
Xaxis (m)
0 V/m
10 V/m
20 V/m
30 V/m
40 V/m
50 V/m
12 V/m
14 V/m

(a)

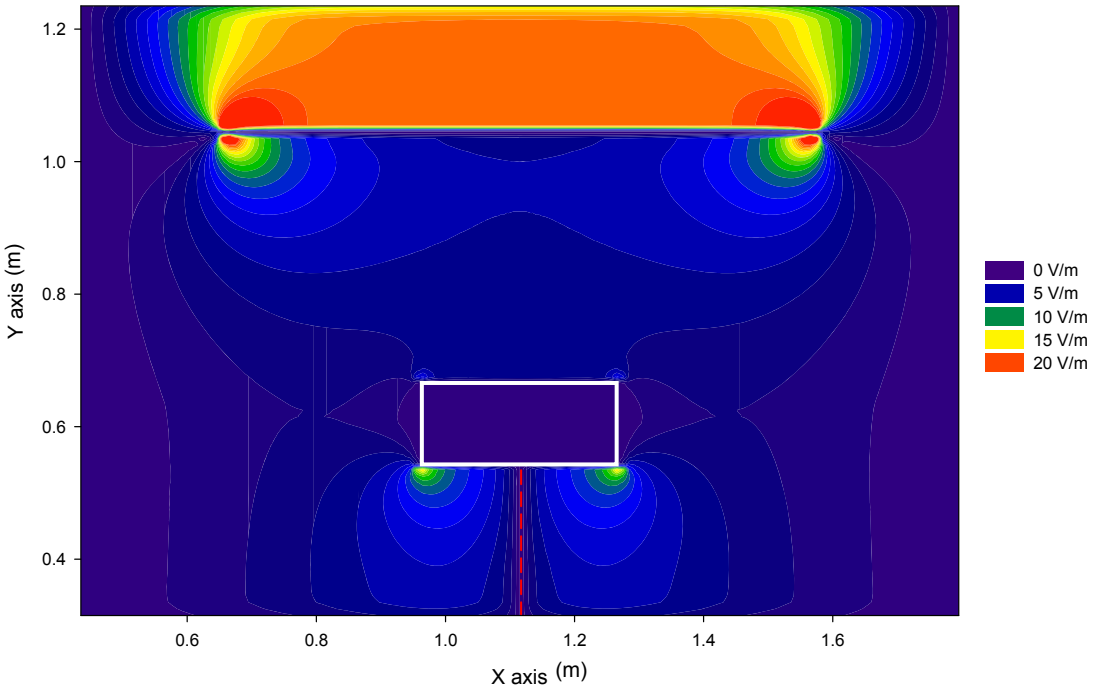
1.2
1.0
0.8
0.6
0.4
Y axis (m)
0.6
0.8
1.0
1.2
1.4
1.6
X axis (m)
0 V/m
5 V/m
10 V/m
15 V/m
20 V/m

(b)

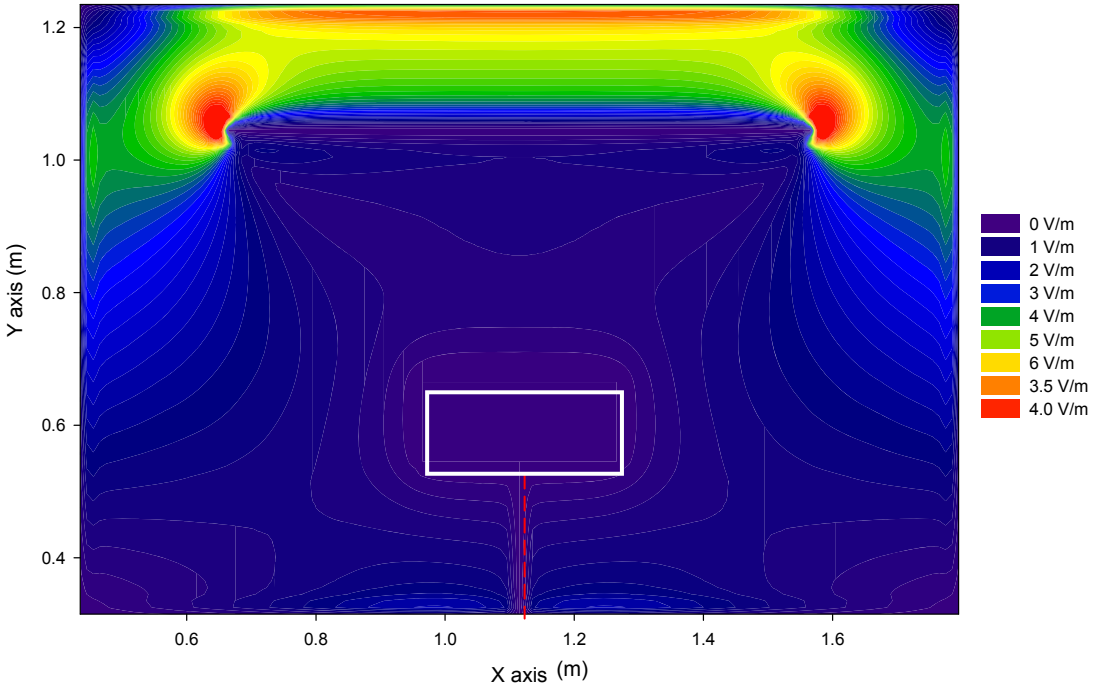

(c)

Figure B.2 Electric field distributions for E_x, E_y and E_z (a)-(c) for loaded with grounding. Numbers in the Figure indicate the electric field in V/m at particular points. EUT location is highlighted by the white rectangular box and the grounding cable is shown by the dotted red line

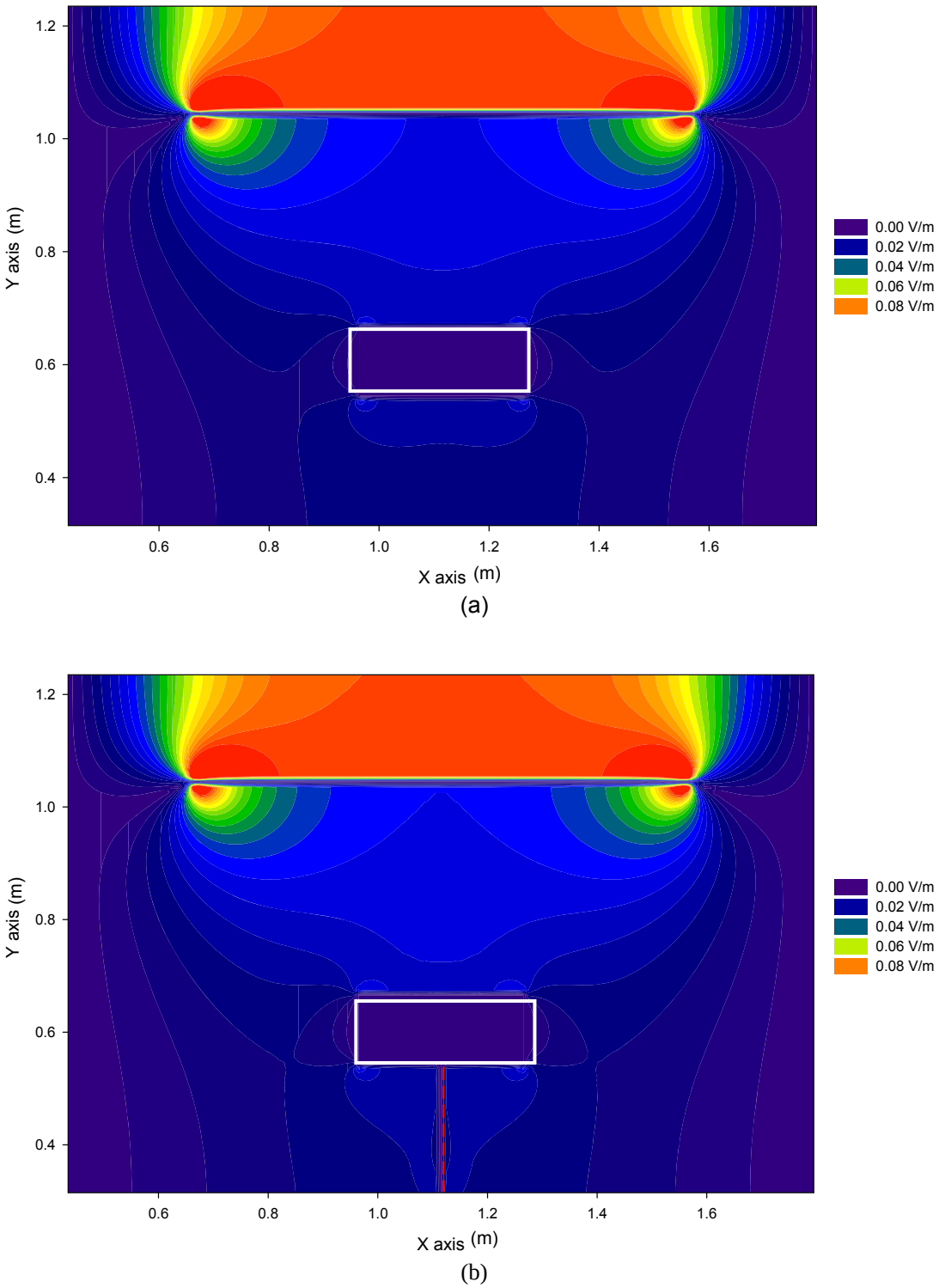

Figure B.3 Horizontal magnetic field distributions, H_x, for (a) loaded and (b) loaded and grounded. EUT location is highlighted by the rectangular box and the grounding cable is shown by the dotted red line

C Further presentation of the impact of total power radiated as a function of phase by other EUTs Using IEC 61000-4-20

This Section presents the continuation of the study of the total power radiated by other EUTs using the correlation algorithm according to IEC 61000-4-20. The purpose is to extend the discussion on the error due to phase difference for other types of EUTs. These include investigations of the effects of electric and magnetic behaviour, number of radiators and the orientation of the radiators. The considered EUTs are (1) a metal box with a slot and a raised lid, (2) a metal box with slots on its two sides and (3) a metal box with three orthogonal monopoles. Due to the significant amount of time required to produce these results in simulations, only experimental work is done for the first two EUTs. The last EUT test cannot be performed experimentally because a third signal generator to excite the third monopole at the time of this writing is not available. Thus, only simulations are performed on this EUT.

C.1 Metal box with a slot and a raised lid (Measurement only)

The construction of this EUT shown in Figure C.1 has been described in Chapter 2 under Section 2.7. Figure C.2 shows the power measured at the GTEM cell output port for three different orientations when the phase between the two radiators is altered. Using the correlation algorithm in IEC 61000-4-20, the total power radiated is calculated shown in Figure C.3. The frequency of this test is at 200 MHz. From this EUT, an uncertainty of 3.44 dB is observed due to the phase effect.

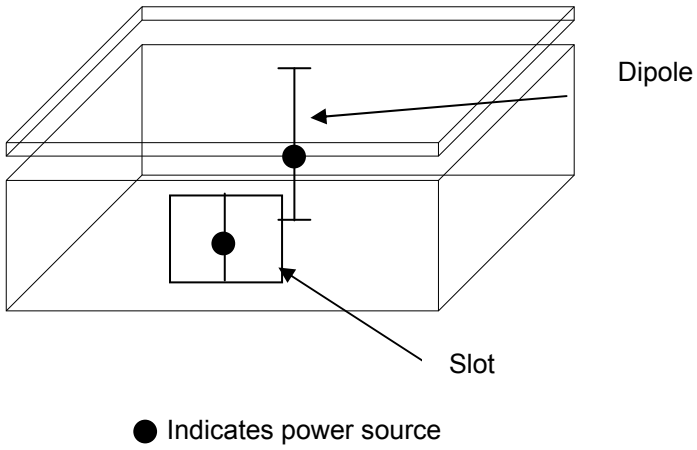

Figure C.1 Metal box with slot and raised lid

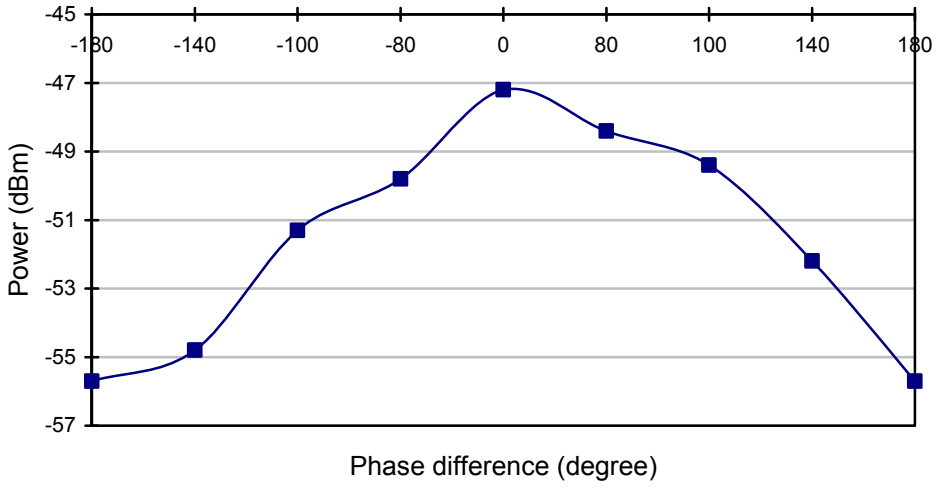
-45
-47
-49
-51
-53
-55
-57
Power (dBm)
-180
-140
-100
-80
0
80
100
140
180
Phase difference (degree)

(a)

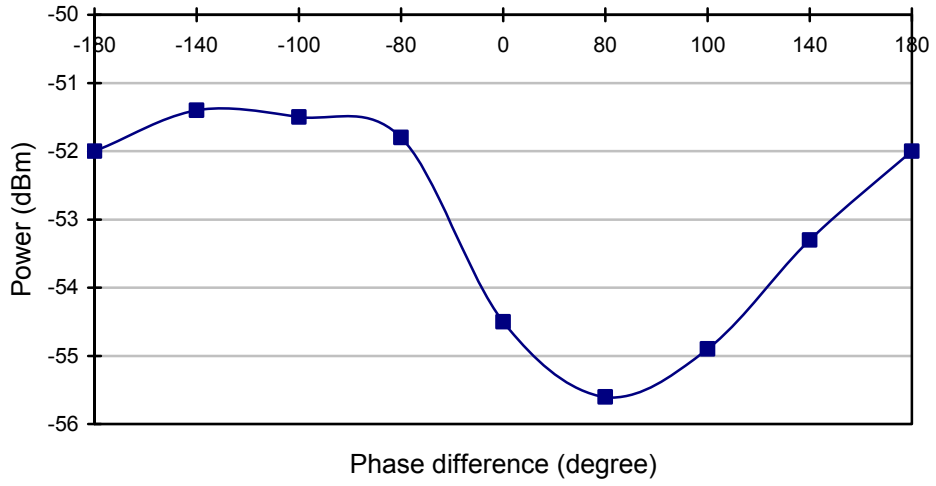
-50
-51
-52
-53
-54
-55
-56
Power (dBm)
-180
-140
-100
-80
0
80
100
140
180
Phase difference (degree)

(b)

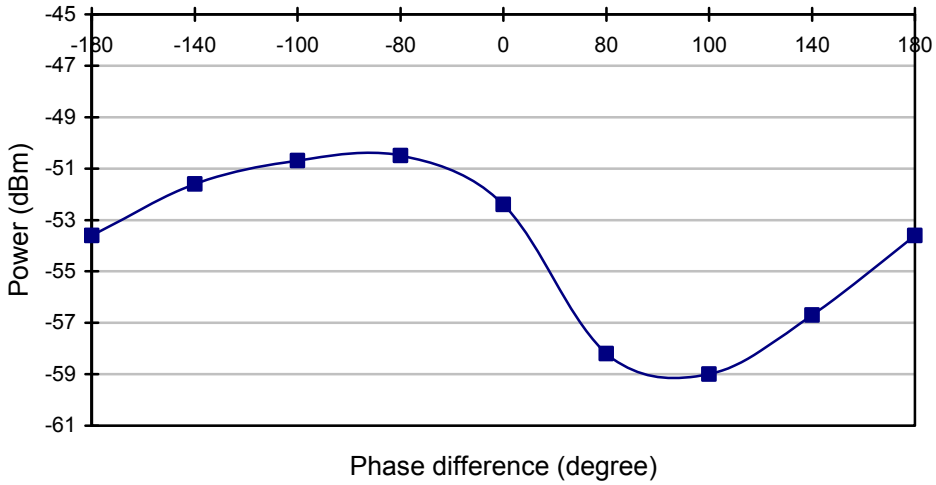

(c)

Figure C.2 Received power at orientation (a) one, (b) two and (c) three

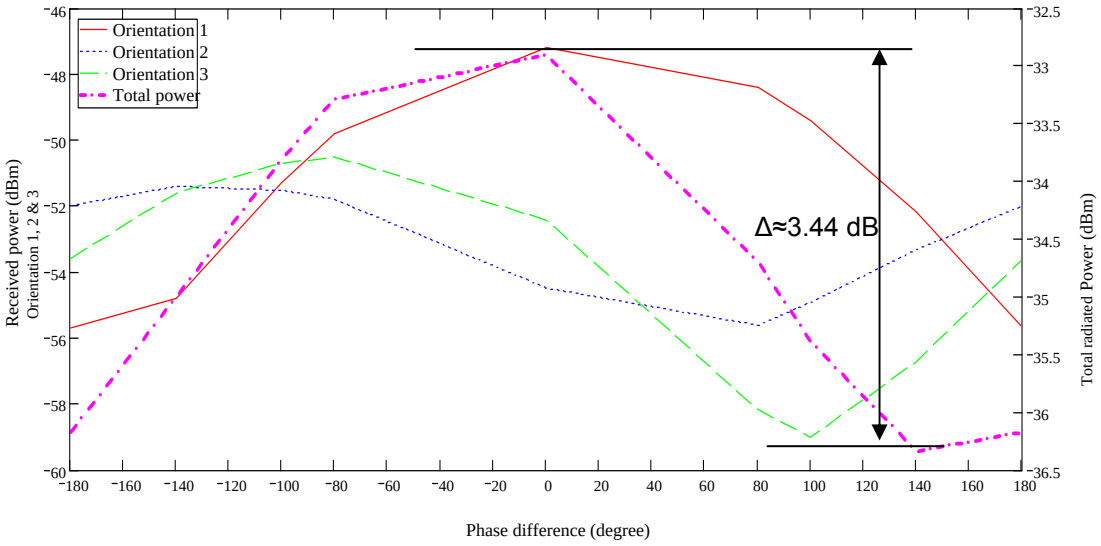

Figure C.3 Total radiated power of the EUT according to IEC 61000-4-20

C.2 Metal box with slots on two sides (Measurement only)

The construction of this EUT shown in Figure C.4 has been described in Chapter 2 under Section 2.8. Figure C.5 shows the power measured at the GTEM cell output port for three different orientations when the phase between the two radiators is altered. Using the correlation algorithm in IEC 61000-4-20, the total power radiated is calculated shown in Figure C.6. The frequency of this test is at 200 MHz. From this EUT, an uncertainty of 4.50 dB is observed due to the phase effect.

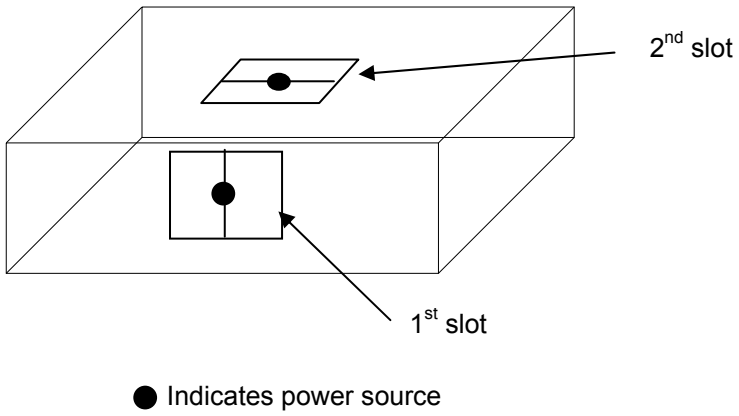

Figure C.4 Metal box with slot on two sides at 200 MHz

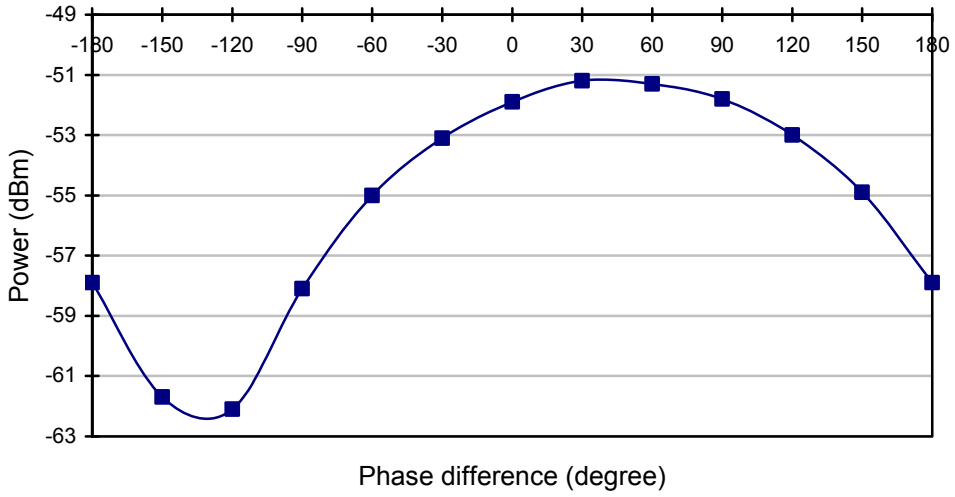
-49
-51
-53
-55
-57
-59
-61
-63
-180 -150 -120 -90 -60 -30 0 30 60 90 120 150 180
Power (dBm)
Phase difference (degree)

(a)

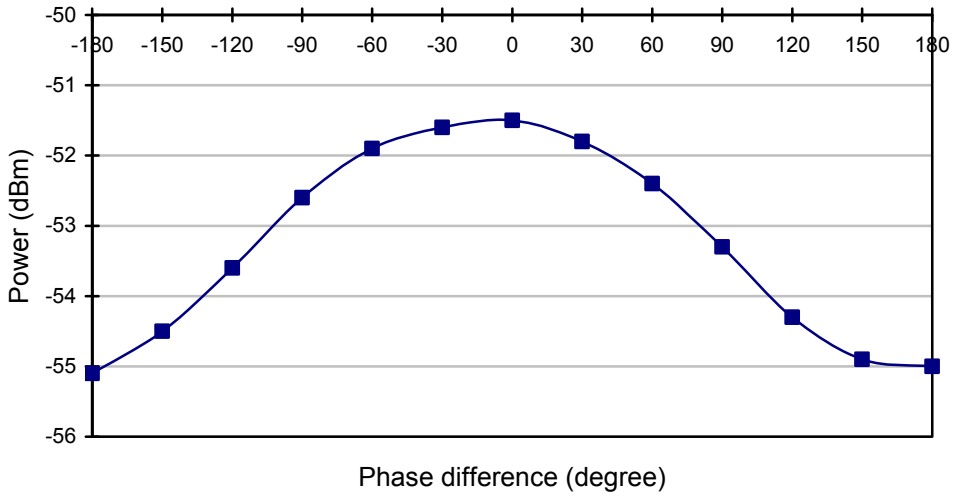
-50
-51
-52
-53
-54
-55
-56
-180 -150 -120 -90 -60 -30 0 30 60 90 120 150 180
Power (dBm)
Phase difference (degree)

(b)

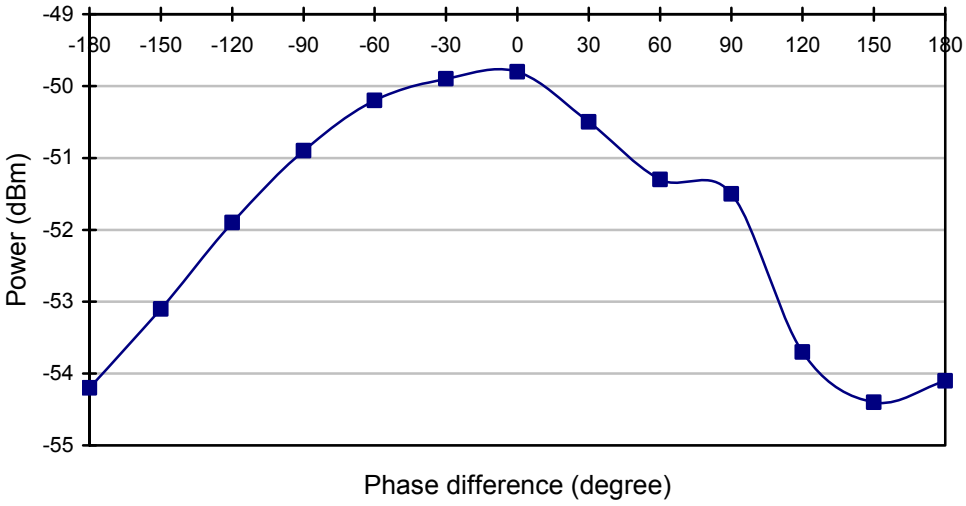

(c)

Figure C.5 Received power at orientation (a) one, (b) two and (c) three

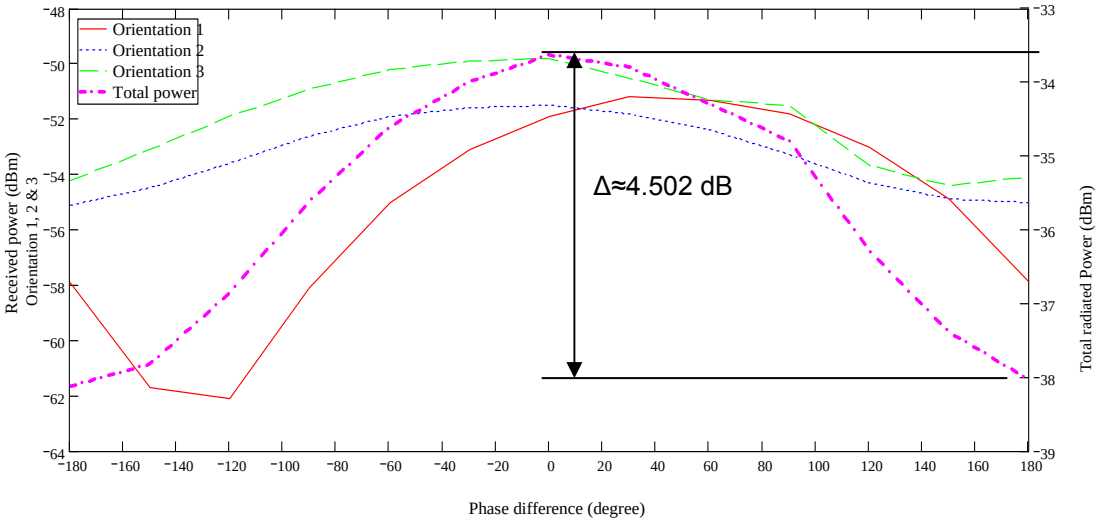

Figure C.6 Total radiated power of the EUT according to IEC 61000-4-20

C.3 Three Orthogonal monopoles (Simulation only)

The construction of this EUT shown in Figure C.7 has been described in Chapter 2 under Section 2.9. Since this EUT involves three radiators, 3D graphs are plotted to show the phase relationship between these radiators. Figure C.8-C.10 shows the power measured at the GTEM cell output port for three different orientations when the phase between the two radiators is altered. Using the correlation algorithm in IEC 61000-4-20, the total power radiated is calculated shown in Figure C.11. The frequency of this test is at 200 MHz. From this EUT, an uncertainty of 3.954 dB is observed due to the phase effect.

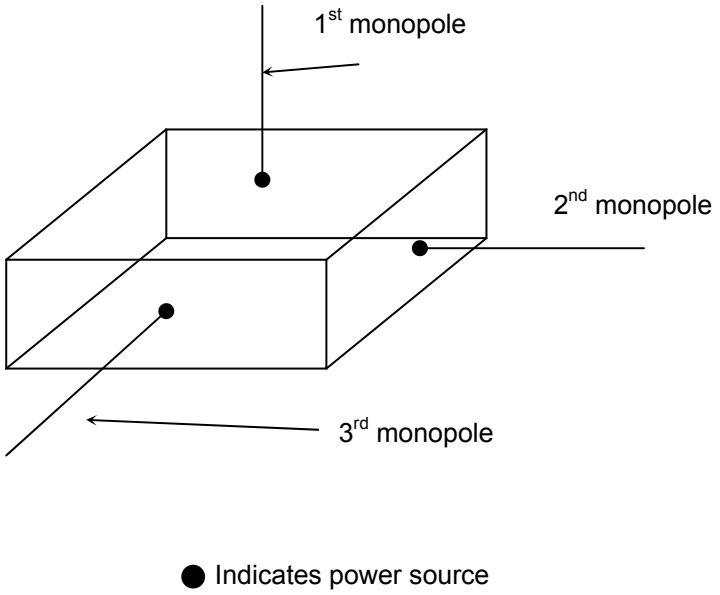

Figure C.7 Three Orthogonal monopoles at 200 MHz

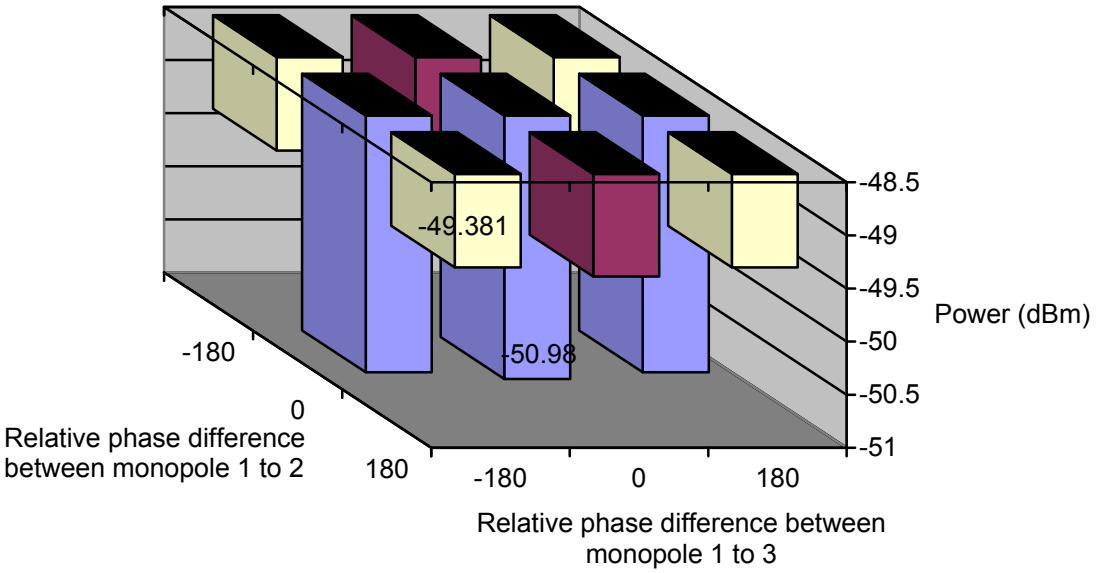

(a)

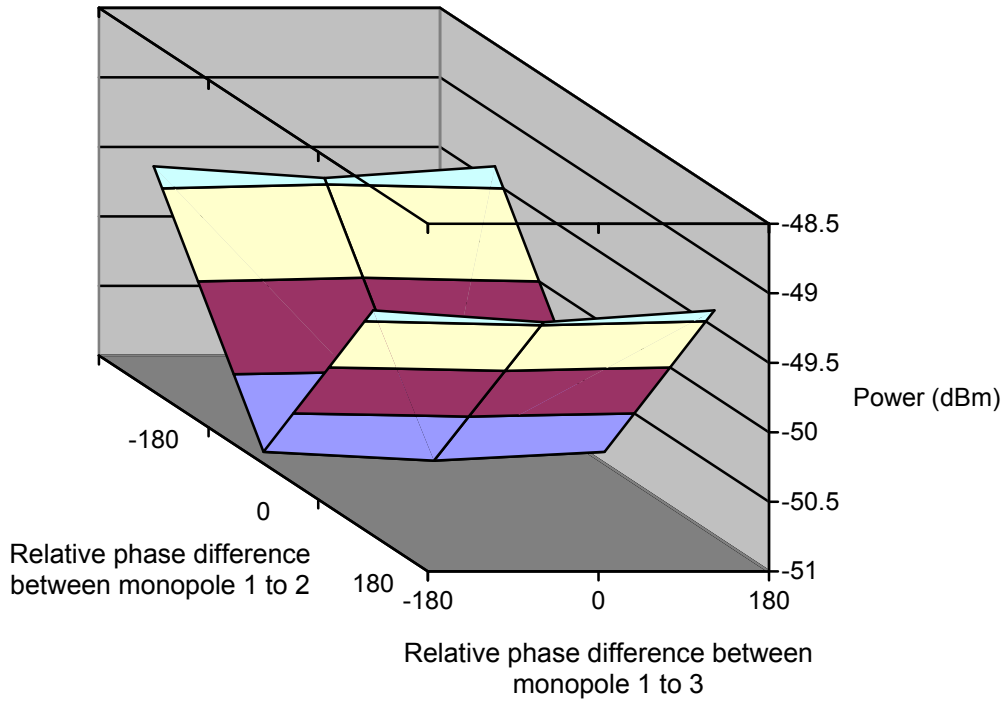

(b)

Figure C.8 Received power at orientation one for (a) bar graph and (b) surface plot

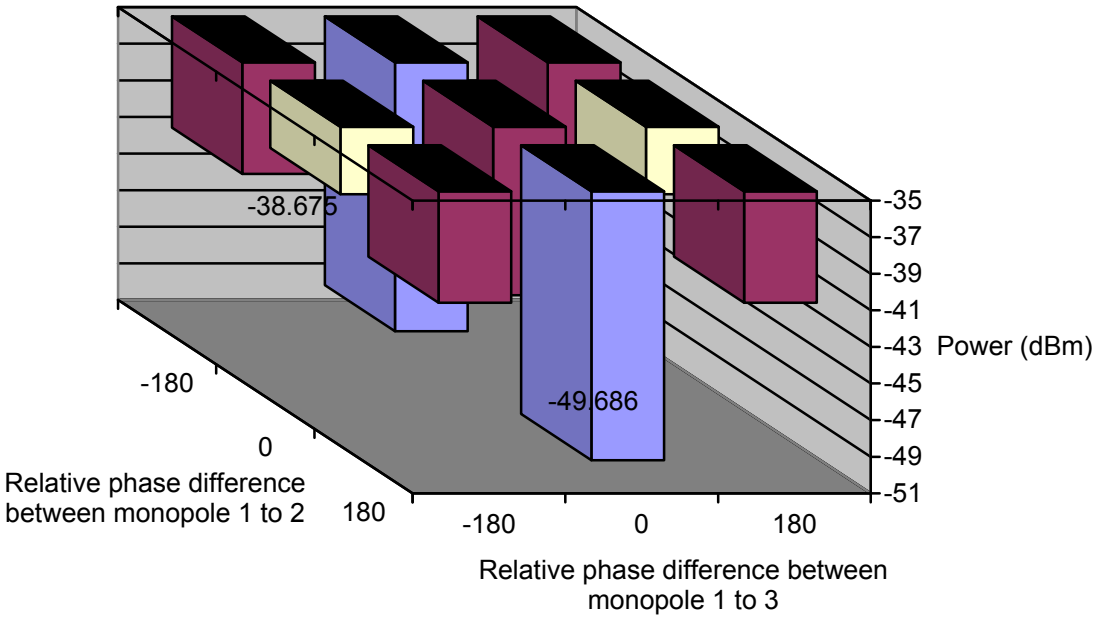

(a)

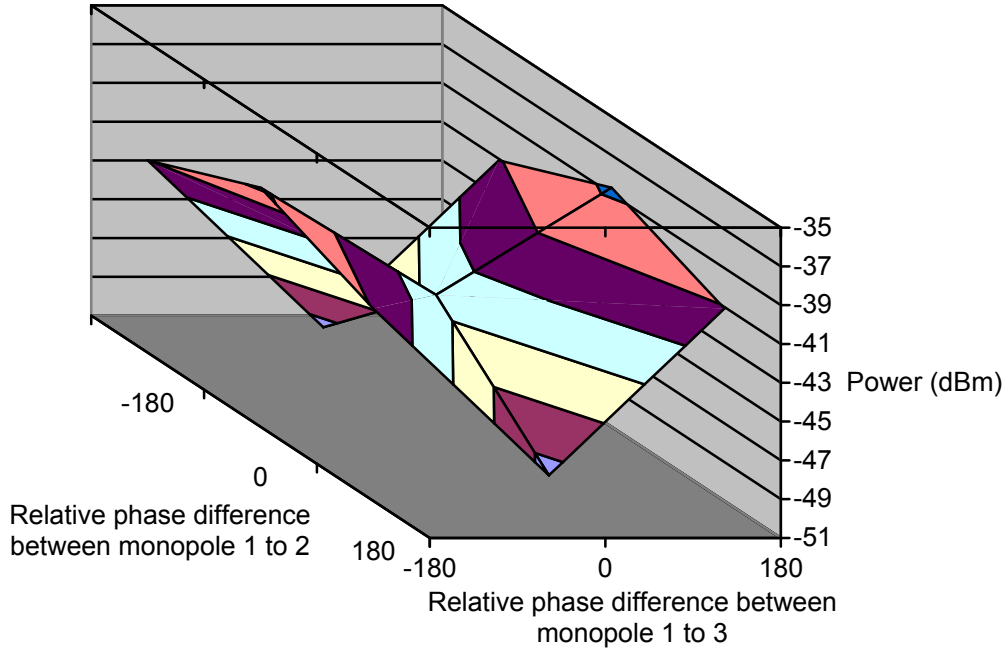

(b)

Figure C.9 Received power at orientation two for (a) bar graph and (b) surface plot

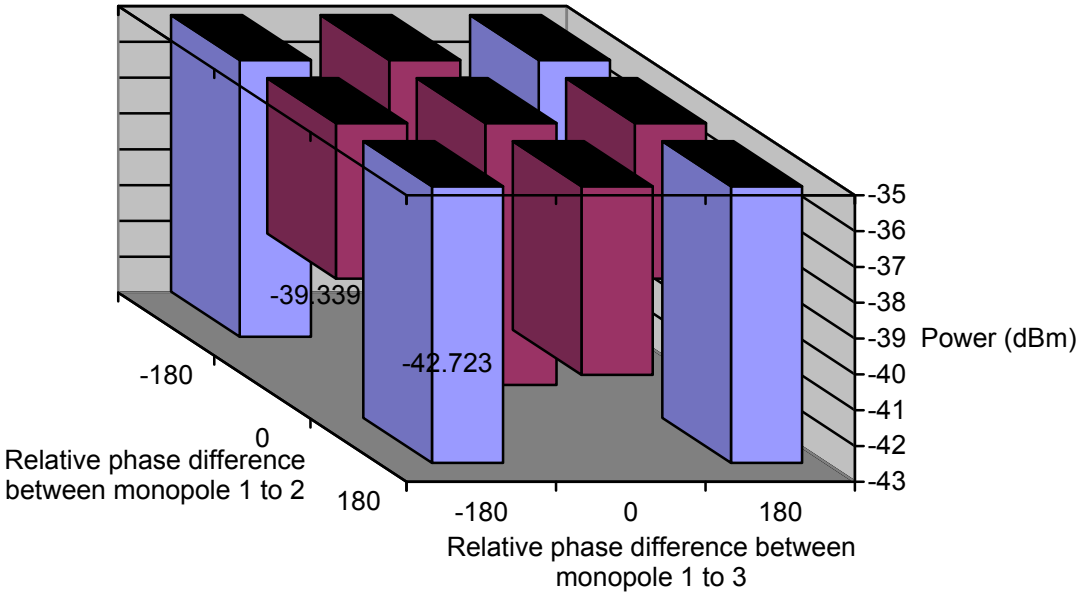

(a)

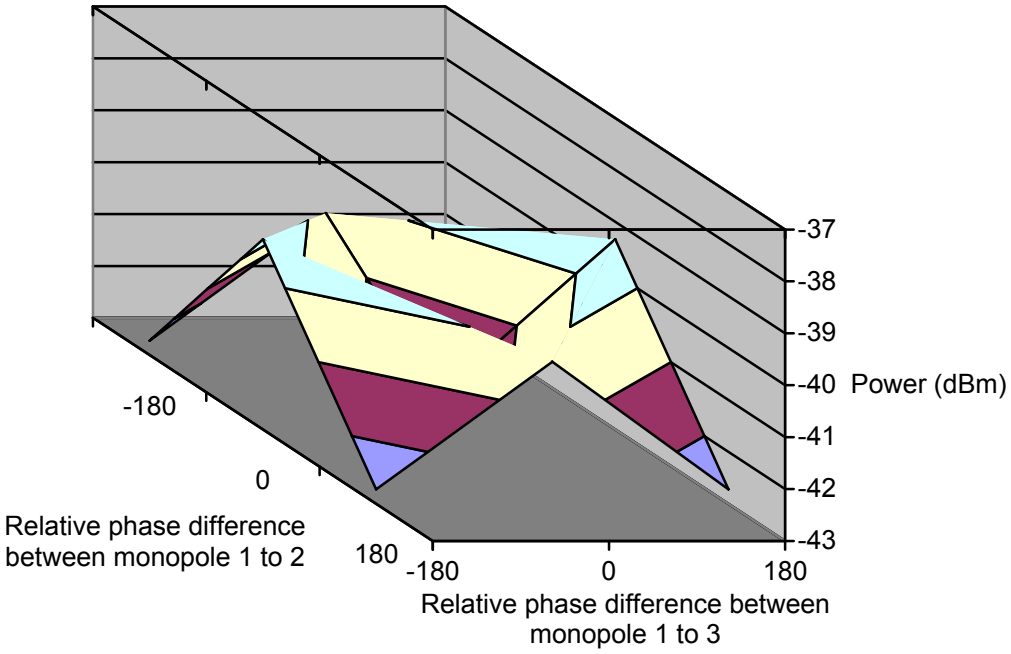

(b)

Figure C.10 Received power at orientation three for (a) bar graph and (b) surface plot

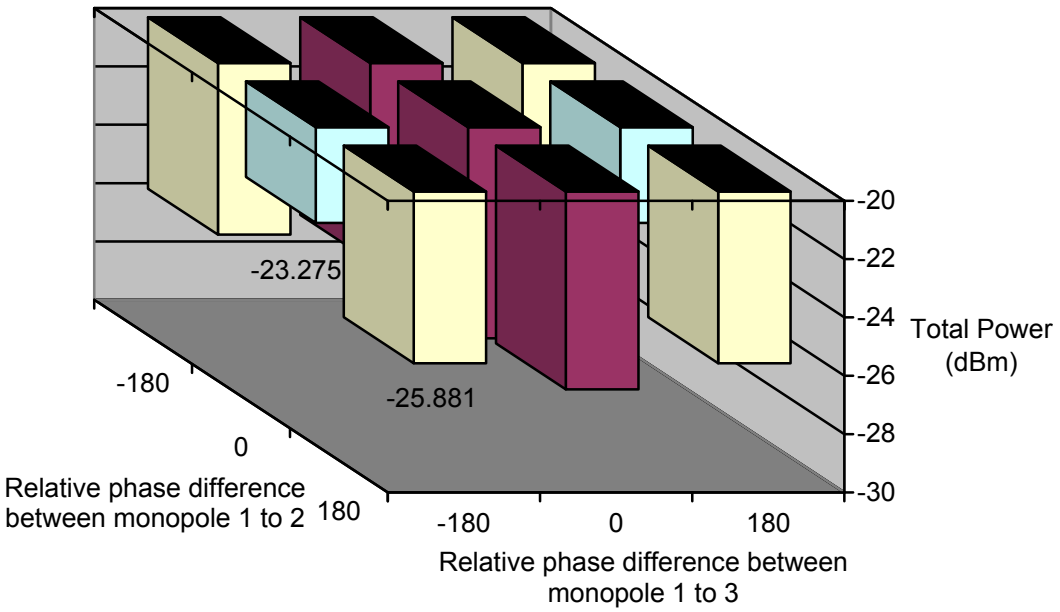

(a)

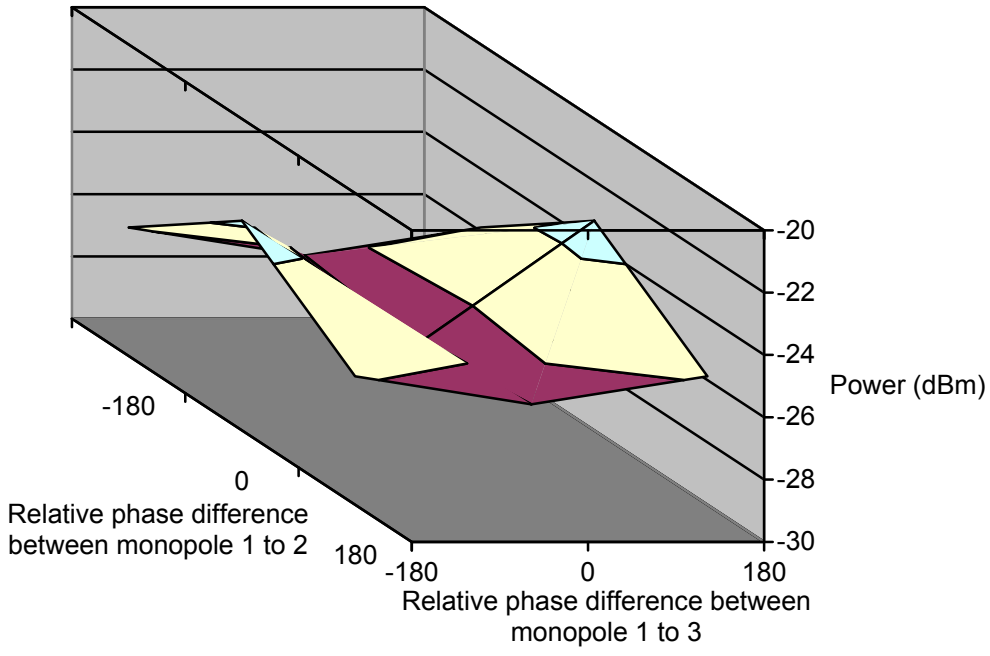

(b)

Figure C.11 Total radiated power of the EUT according to IEC 61000-4-20 for (a) bar graph and (b) surface plot

C.4 Summary of total power radiated uncertainty

The summary of total power radiated uncertainty due to phase for four EUTs are shown in Table C.1. It is important to perform this investigation on other EUTs because the error due to phase difference may not be well supported if only one type of EUT is tested. By providing more results especially on other types of EUTs, it can be now concluded that the error due to the phase difference between dipole moments is present and not only for the two monopoles EUT but also on other more practical EUTs with different types of radiators, construction details and orientations.

Table C.1

Summary of total power radiated discrepancy due to phase for four EUTs

No	EUT	Radiator quantity	Type of radiators	Uncertainty (dB)
1	Two parallel monopoles on top of a metal box	2	Electric	3.461
2	Metal box with slot and raised lid	2	Electric and magnetic	3.440
3	Metal box with slot on two sides	2	magnetic	4.500
4	Three Orthogonal monopoles	3	Electric	3.954

D Calculation of total power radiated and radiation pattern according to NBS Technical Note 1059

This Section presents the procedure for calculating the total radiated power from an EUT using the GTEM cell which involves the phase according to NBS technical note 1059. In this case, a spherical dipole radiator was used as the EUT for the measurements.

As outlined in Chapter 5, the six orientations are required to obtain the phase information in a TEM cell. To perform the same measurement using a GTEM cell, an additional 180° rotation is required for each orientation. $P_{i,0^o}$ is the magnitude $M_{i,0^o}$ and phase $\phi_{i,0^o}$ measured when the EUT is at 0° and $P_{i,180^o}$ is the magnitude $M_{i,180^o}$ and phase $\phi_{i,180^o}$ measured when the EUT is at 180° for orientations $i=1...6$ shown in equation (D.4a and D.4b)

$$P_{i,0^o}=M_{i,0^o}\angle\phi_{i,0^o} \quad \text{(D.4a)}$$

$$P_{i,180^o}=M_{i,180^o}\angle\phi_{i,180^o} \quad \text{(D.4b)}$$

The measured magnitudes and their phases are shown in equations (D.4c to D.4n)

$$P_{1,0^o}=-44.1\angle-29^o \quad \text{(D.4c)}$$

$$P_{1,180^o}=-40.7\angle-72^o \quad \text{(D.4d)}$$

$$P_{2,0^o}=-43.4\angle-29^o \quad \text{(D.4e)}$$

$$P_{2,180^o} = -42.4\angle -65^o \quad \text{(D.4f)}$$

$$P_{3,0^o} = -45.3\angle -33^o \quad \text{(D.4g)}$$

$$P_{3,180^o} = -39.9\angle -56^o \quad \text{(D.4h)}$$

$$P_{4,0^o} = -44.0\angle -31^o \quad \text{(D.4i)}$$

$$P_{4,180^o} = -41.8\angle -46^o \quad \text{(D.4j)}$$

$$P_{5,0^o} = -44.0\angle -65^o \quad \text{(D.4k)}$$

$$P_{5,180^o} = -41.0\angle -71^o \quad \text{(D.4l)}$$

$$P_{6,0^o} = -60.0\angle -21^o \quad \text{(D.4m)}$$

$$P_{6,180^o} = -53.0\angle -45^o \quad \text{(D.4n)}$$

The magnitudes of $P_i\,(i = 1...6)$ which are in dBm are converted to W in the process as required in the algorithm. New values of $P_i\,(i = 1...6)$ (in dBm) are defined with prime as $P_i^{'}\,(i = 1...6)$ (in W) where $P_{i,0^o}^{'}$ is the magnitude $M_{i,0^o}^{'}$ and phase $\phi_{i,0^o}$ measured when the EUT is at 0^o and $P_{i,180^o}^{'}$ is the magnitude $M_{i,180^o}^{'}$ and phase $\phi_{i,180^o}$ measured when the EUT is at 180^o. This is shown in equations (D.5a to D.5b).

$$P_{i,0^o}^{'} = \left(10^{\frac{P_{i,0^o}}{10}} \cdot 0.001\right)\angle M_{i,0^o} \quad \text{(D.5a)}$$

$$P'_{i,180^o} = \left(10^{\frac{P_{i,180^o}}{10}} \cdot 0.001 \right) \angle M_{i,180^o} \quad \text{(D.5b)}$$

The sums of power $S_i(i = 1...6)$ measured from the GTEM cell are the sums of $P'_{i,0^o}$ and $P'_{i,180^o}$ for each value of i.

$$S_1 = P'_{1,0^o} + P'_{1,180^o} \quad \text{(D.6a)}$$

$$S_2 = P'_{2,0^o} + P'_{2,180^o} \quad \text{(D.6b)}$$

$$S_3 = P'_{3,0^o} + P'_{3,180^o} \quad \text{(D.6c)}$$

$$S_4 = P'_{4,0^o} + P'_{4,180^o} \quad \text{(D.6d)}$$

$$S_5 = P'_{5,0^o} + P'_{5,180^o} \quad \text{(D.6e)}$$

$$S_6 = P'_{6,0^o} + P'_{6,180^o} \quad \text{(D.6f)}$$

The differences of power $D_i(i = 1...6)$ measured from the GTEM cell are the differences of $P'_{i,0^o}$ and $P'_{i,180^o}$ for each value of i.

$$D_1 = P'_{1,0^o} - P'_{1,180^o} \quad \text{(D.7a)}$$

$$D_2 = P'_{2,0^o} - P'_{2,180^o} \quad \text{(D.7b)}$$

$$D_3 = P'_{3,0^o} - P'_{3,180^o} \quad \text{(D.7c)}$$

$$D_4 = P'_{4,0^o} - P'_{4,180^o} \quad \text{(D.7d)}$$

$$D_5 = P'_{5,0^o} - P'_{5,180^o} \quad \text{(D.7e)}$$

$$D_6 = P'_{6,0^o} - P'_{6,180^o} \quad \text{(D.7f)}$$

The phase difference $\phi_i^{'}$ between the sum $S_i(i=1...6)$ and difference $D_i(i=1...6)$ for each value of i can be obtained by equation (D.8a).

$$\phi_i^{'} = \angle(S_i - D_i) \quad \text{(D.8a)}$$

$$\phi_1^{'} = -141.75^o \quad \text{(D.8b)}$$

$$\phi_2^{'} = -141.75^o \quad \text{(D.8c)}$$

$$\phi_3^{'} = -166.19^o \quad \text{(D.8d)}$$

$$\phi_4^{'} = -153.91^o \quad \text{(D.8e)}$$

$$\phi_5^{'} = -172.03^o \quad \text{(D.8f)}$$

$$\phi_6^{'} = -170.41^o \quad \text{(D.8g)}$$

The electric dipole moments M_{ex}, M_{ey} and M_{ez} can be calculated by:

$$\begin{pmatrix} M_{ex}{}^2 \\ M_{ey}{}^2 \\ M_{ez}{}^2 \end{pmatrix} = \frac{C \cdot S_i}{2 \cdot (p^2 + q^2)} \quad \text{(D.9)}$$

$$M_{ex} = 2.64 \times 10^{-5} \quad \text{(D.10a)}$$

$$M_{ey} = 4.55 \times 10^{-5} \quad \text{(D.10b)}$$

$$M_{ez} = 2.87 \times 10^{-5} \quad \text{(D.10c)}$$

The magnetic dipole moments M_{mx}, M_{my} and M_{mz} can be calculated by:

$$\begin{pmatrix} M_{mx}{}^2 \\ M_{my}{}^2 \\ M_{mz}{}^2 \end{pmatrix} = \frac{C \cdot D_i}{2 \cdot k^2 \left(p^2 + q^2\right)} \tag{D.11}$$

$$M_{mx} = 6.97 \times 10^{-6} \tag{D.12a}$$

$$M_{my} = 1.48 \times 10^{-5} \tag{D.12b}$$

$$M_{mz} = 8.59 \times 10^{-6} \tag{D.12c}$$

where

$$C = \begin{pmatrix} 1 & 1 & -1 & -1 & 1 & 1 \\ 1 & 1 & 1 & 1 & -1 & -1 \\ -1 & -1 & 1 & 1 & 1 & 1 \end{pmatrix} \tag{D.13}$$

$$S_i = \begin{pmatrix} S_1 \\ S_2 \\ S_3 \\ S_4 \\ S_5 \\ S_6 \end{pmatrix} \tag{D.14a}$$

$$D_i = \begin{pmatrix} D_1 \\ D_2 \\ D_3 \\ D_4 \\ D_5 \\ D_6 \end{pmatrix} \tag{D.14b}$$

Once the electric and magnetic dipole moments are obtained, the phase relationship θ_e between electric dipole moments can be calculated. θ_e^1 is the

phase relationship between M_{ex} and M_{ey} ; θ_e^2 is the phase relationship between M_{ey} and M_{ez} ; and θ_e^3 is the phase relationship between M_{ez} and M_{ex} .

$$\theta_e^1 = \cos^{-1}\left(\frac{S_1 - S_2 + f\left(S_3 + S_4 - S_5 - S_6\right)}{2\cdot\left(q^2 - p^2\right)\cdot M_{ex}\cdot M_{ey}}\right) \quad \text{(D.15a)}$$

$$\theta_e^1 = 83.96^o$$

$$\theta_e^2 = \cos^{-1}\left(\frac{S_3 - S_4 + f\left(-S_1 - S_2 + S_5\right) + S_6}{2\cdot\left(q^2 - p^2\right)\cdot M_{ey}\cdot M_{ez}}\right) \quad \text{(D.15b)}$$

$$\theta_e^2 = 83.06^o$$

$$\theta_e^3 = \cos^{-1}\left(\frac{S_5 - S_6 + f\left(S_1 + S_2 - S_3 - S_4\right)}{2\cdot\left(q^2 - p^2\right)\cdot M_{ez}\cdot M_{ex}}\right) \quad \text{(D.15c)}$$

$$\theta_e^3 = 24.88^o$$

θ_m^1 is the phase relationship between M_{mx} and M_{my} ; θ_m^2 is the phase relationship between M_{my} and M_{mz} ; and θ_m^3 is the phase relationship between M_{mz} and M_{mx} .

$$\theta_m^1 = \cos^{-1}\left(\frac{-D_1 + D_2 + f\left(D_3 + D_4 - D_5 - D_6\right)}{2\cdot k^2\cdot\left(q^2 - p^2\right)\cdot M_{mx}\cdot M_{my}}\right) \quad \text{(D.16a)}$$

$$\theta_m^1 = 112.73^o$$

$$\theta_m^2 = \cos^{-1}\left(\frac{-D_3 + D_4 + f\left(-D_1 - D_2 + D_5 + D_6\right)}{2\cdot k^2\cdot\left(q^2 - p^2\right)\cdot M_{my}\cdot M_{mz}}\right) \quad \text{(D.16b)}$$

$$\theta_m^2 = 120.52^o$$

$$\theta_m^3 = \cos^{-1}\left(\frac{-D_5 + D_6 + f\left(D_1 + D_2 - D_3 - D_4\right)}{2 \cdot k^2\left(q^2 - p^2\right) \cdot M_{mz} \cdot M_{mx}}\right) \quad \text{(D.16c)}$$

$$\theta_m^3 = 146.25^o$$

In order to satisfy the requirement of the phase relationships between dipole moments to be

$$\theta_e^1 + \theta_e^2 + \theta_e^3 = 0 \quad \text{(D.17a)}$$

$$\theta_m^1 + \theta_m^2 + \theta_m^3 = 0 \quad \text{(D.17b)}$$

the values of θ_e^1, θ_e^2 and θ_e^3 were adjusted to new values (with prime) as

$$\theta_e^{1'} = -\theta_e^1 \quad \text{(D.18a)}$$

$$\theta_e^{2'} = \theta_e^2 \quad \text{(D.18b)}$$

$$\theta_e^{3'} = \theta_e^3 \quad \text{(D.18c)}$$

so that:

$$\theta_e^{1'} + \theta_e^{2'} + \theta_e^{3'} = 23.97^o \quad \text{(D.19)}$$

It is noticed that the result of equation (D.19) is not exactly 0^o as required by equation (D.17a) due to errors in measurement. For the magnetic moments, equation (D.17b) is not used because the EUT is known to be purely electric which would result in insensible value. The new values of the electric dipole

moments phase relationship can be used to calculate the phase relationship of the magnetic dipole moments. The phase relationships of the magnetic dipole moments can be calculated by

$$\theta_m^1 = \sin^{-1}\left(\frac{M_{1,2}}{N_{1,2}}\right)$$
$$\theta_m^1 = 28.45^o \; or \; 180 - 28.45^o \tag{D.20}$$

where

$$M_{1,2} = 2\cdot\left(M_{mx}{}^2 - M_{my}{}^2\right)\cdot M_{ex}\cdot M_{ey}\cdot\sin\left(\theta_e^{1'}\right) + \left(M_{ex}{}^2 - M_{ey}{}^2\right)\cdot\ldots \\ \left(M_{mx}{}^2 - M_{my}{}^2\right)\cdot\tan\left(\phi_1^{'} - \phi_2^{'}\right) \tag{D.21a}$$

$$N_{1,2} = -2\cdot\left(M_{ex}{}^2 - M_{ey}{}^2\right)\cdot M_{mx}\cdot M_{my} + 4\left(M_{ex}\right)\cdot M_{ey}\cdot M_{mx}\cdot M_{my}\cdot\ldots \\ \tan\left(\phi_1^{'} - \phi_2^{'}\right)\cdot\sin\left(\theta_e^{1'}\right) \tag{D.21b}$$

$$\theta_m^2 = \sin^{-1}\left(\frac{M_{3,4}}{N_{3,4}}\right)$$

$$\theta_m^2 = -47.12^o \; or \; 180 + 47.12^o \tag{D.22}$$

where

$$M_{3,4} = 2\cdot\left(M_{my}{}^2 - M_{mz}{}^2\right)\cdot M_{ey}\cdot M_{ez}\cdot\sin\left(\theta_e^{2'}\right) + \left(M_{ey}{}^2 - M_{ez}{}^2\right)\cdot\ldots \\ \left(M_{my}{}^2 - M_{mz}{}^2\right)\cdot\tan\left(\phi_3^{'} - \phi_4^{'}\right) \tag{D.23a}$$

$$N_{3,4} = -2\cdot\left(M_{ey}{}^2 - M_{ez}{}^2\right)\cdot M_{my}\cdot M_{mz} + 4\left(M_{ey}\right)\cdot M_{ez}\cdot M_{my}\cdot M_{mz}\cdot\ldots \\ \tan\left(\phi_3^{'} - \phi_4^{'}\right)\cdot\sin\left(\theta_e^{2'}\right) \tag{D.23b}$$

And,

$$\theta_m^3 = \sin^{-1}\left(\frac{M_{5,6}}{N_{5,6}}\right)$$

$$\theta_m^2 = -67.26^o \; or \; 180 + 67.26^o \tag{D.24}$$

where

$$M_{5,6} = 2\cdot\left(M_{mz}{}^2 - M_{mx}{}^2\right)\cdot M_{ez}\cdot M_{ex}\cdot\sin\left(\theta_e^{3'}\right) + \left(M_{ez}{}^2 - M_{ex}{}^2\right)\cdot\ldots \\ \left(M_{mz}{}^2 - M_{mx}{}^2\right)\cdot\tan\left(\phi_5^{'} - \phi_6^{'}\right) \tag{D.25a}$$

$$N_{5,6} = -2\cdot\left(M_{ez}{}^2 - M_{ex}{}^2\right)\cdot M_{mz}\cdot M_{mx} + 4\left(M_{ez}\right)\cdot M_{ex}\cdot M_{mz}\cdot M_{mx}\cdot\ldots \\ \tan\left(\phi_5^{'} - \phi_6^{'}\right)\cdot\sin\left(\theta_e^{3'}\right) \tag{D.25b}$$

From equation (D.20),(D.22) and (D.24), the values of θ_m^1, θ_m^2 and θ_m^3 were adjusted to new values (with prime) as

$$\theta_m^{1'} = 28.45^o \tag{D.26a}$$

$$\theta_m^{2'} = 47.12^o \tag{D.26b}$$

$$\theta_m^{3'} = -67.26^o \tag{D.26c}$$

so that

$$\theta_m^{1'} + \theta_m^{2'} + \theta_m^{3'} = -8.30^o \tag{D.27}$$

It is noticed that the result of equation (D.27) is not exactly 0^o as required by equation (D.17b) since the EUT is more electric than magnetic. Considering the value in equation (D.27) reasonably agrees to that equation (D.17b), the phase relationship ξ, between the electric dipole moments ψ_e and the magnetic dipole moments ψ_m are calculated in the following.

For

$$\xi_{ex,my} = \psi_{ex} - \psi_{my} = \frac{\psi_{1,0} + \psi_{2,0}}{2} \tag{D.28}$$

$$\xi_{ex,my} = -132.64^{o} \tag{D.29}$$

where

$$\psi_{1,0} = \phi_1^{'} + \alpha_{1,0} - \beta_{1,0} \tag{D.30a}$$

$$\psi_{2,0} = \phi_2^{'} + \alpha_{2,0} - \beta_{2,0} \tag{D.30b}$$

and

$$\alpha_{1,0} = \tan^{-1}\left(\frac{q \cdot M_{ey} \cdot \sin\left(\theta_e^{1'}\right)}{p \cdot M_{ex} + q \cdot M_{ey} \cdot \cos\left(\theta_e^{1'}\right)}\right) \tag{D.31a}$$

$$\alpha_{2,0} = \tan^{-1}\left(\frac{-p \cdot M_{ey} \cdot \sin\left(\theta_e^{1'}\right)}{q \cdot M_{ex} + p \cdot M_{ey} \cdot \cos\left(\theta_e^{1'}\right)}\right) \tag{D.31b}$$

$$\beta_{1,0} = \tan^{-1}\left(\frac{q \cdot M_{mx} \cdot \cos\left(\theta_m^{1'}\right) - p \cdot M_{my}}{q \cdot M_{mx} \cdot \sin\left(\theta_m^{1'}\right)}\right) \tag{D.31c}$$

$$\beta_{2,0} = \tan^{-1}\left(\frac{-p \cdot M_{mx} \cdot \cos\left(\theta_m^{1'}\right) - q \cdot M_{my}}{-p \cdot M_{mx} \cdot \sin\left(\theta_m^{1'}\right)}\right) \tag{D.31d}$$

For

$$\xi_{ey,mx} = \psi_{ey} - \psi_{mx} = \frac{\psi_{1,1} + \psi_{2,1}}{2} \tag{D.32}$$

$$\xi_{ey,mx} = -42.51^{o} \tag{D.33}$$

where

$$\psi_{1,1} = \phi_1^{'} + \alpha_{1,1} - \beta_{1,1} \tag{D.34a}$$

$$\psi_{2,1} = \phi_2^{'} + \alpha_{2,1} - \beta_{2,1} \tag{D.34b}$$

and

$$\alpha_{1,1} = \tan^{-1}\left(\frac{-p \cdot M_{ex} \cdot \sin\left(\theta_e^{1'}\right)}{p \cdot M_{ex} \cdot \cos\left(\theta_e^{1'}\right) + q \cdot M_{ey}}\right) \tag{D.35a}$$

$$\alpha_{2,1} = \tan^{-1}\left(\frac{-q \cdot M_{ex} \cdot \sin\left(\theta_e^{1'}\right)}{q \cdot M_{ex} \cdot \cos\left(\theta_e^{1'}\right) + p \cdot M_{ey}}\right) \tag{D.35b}$$

$$\beta_{1,1} = \tan^{-1}\left(\frac{q \cdot M_{mx} - p \cdot M_{my} \cdot \cos\left(\theta_m^{1'}\right)}{p \cdot M_{my} \cdot \sin\left(\theta_m^{1'}\right)}\right) \tag{D.35c}$$

$$\beta_{2,1} = \tan^{-1}\left(\frac{-p \cdot M_{mx} - q \cdot M_{my} \cdot \cos\left(\theta_m^{1'}\right)}{q \cdot M_{my} \cdot \sin\left(\theta_m^{1'}\right)}\right) \tag{D.35d}$$

For

$$\begin{aligned}\xi_{ey,mz} &= \psi_{ey} - \psi_{mz} \\ &= \frac{\psi_{3,0} + \psi_{4,0}}{2}\end{aligned} \tag{D.36}$$

$$\xi_{ey,mz} = -195.80^{o} \tag{D.37}$$

where

$$\psi_{3,0} = \phi_3^{'} + \alpha_{3,0} - \beta_{4,0} \tag{D.38a}$$

$$\psi_{4,0} = \phi_4^{'} + \alpha_{4,0} - \beta_{4,0} \tag{D.38b}$$

and

$$\alpha_{3,0} = \tan^{-1}\left(\frac{-q \cdot M_{ez} \cdot \sin\left(\theta_e^{2'}\right)}{p \cdot M_{ey} + q \cdot M_{ez} \cdot \cos\left(\theta_e^{2'}\right)} \right) \tag{D.39a}$$

$$\alpha_{4,0} = \tan^{-1}\left(\frac{-p \cdot M_{ez} \cdot \sin\left(\theta_e^{2'}\right)}{q \cdot M_{ey} - p \cdot M_{ez} \cdot \cos\left(\theta_e^{2'}\right)} \right) \tag{D.39b}$$

$$\beta_{3,0} = \tan^{-1}\left(\frac{q \cdot M_{my} \cdot \cos\left(\theta_m^{2'}\right) - p \cdot M_{mz}}{p \cdot M_{my} \cdot \sin\left(\theta_m^{2'}\right)} \right) \tag{D.39c}$$

$$\beta_{4,0} = \tan^{-1}\left(\frac{-p \cdot M_{my} \cdot \cos\left(\theta_m^{2'}\right) - q \cdot M_{mz}}{-p \cdot M_{my} \cdot \sin\left(\theta_m^{2'}\right)} \right) \tag{D.39d}$$

For

$$\begin{aligned} \xi_{ez,my} &= \psi_{ez} - \psi_{my} \\ &= \frac{\psi_{3,1} + \psi_{4,1}}{2} \end{aligned} \tag{D.40}$$

$$\xi_{ez,my} = -145.98^{o} \tag{D.41}$$

where

$$\psi_{3,1} = \phi_3^{'} + \alpha_{3,1} - \beta_{4,1} \tag{D.42a}$$

$$\psi_{4,1} = \phi_4^{'} + \alpha_{4,1} - \beta_{4,1} \tag{D.42b}$$

and

$$\alpha_{3,1} = \tan^{-1}\left(\frac{-p \cdot M_{ey} \cdot \sin\left(\theta_e^{2'}\right)}{p \cdot M_{ey} \cdot \cos\left(\theta_e^{2'}\right) + q \cdot M_{ez}} \right) \tag{D.43a}$$

$$\alpha_{4,1} = \tan^{-1}\left(\frac{-q \cdot M_{ey} \cdot \sin\left(\theta_e^{2'}\right)}{q \cdot M_{ey} \cdot \cos\left(\theta_e^{2'}\right) - p \cdot M_{ez}} \right) \tag{D.43b}$$

$$\beta_{3,1} = \tan^{-1}\left(\frac{q \cdot M_{my} - p \cdot M_{mz} \cdot \cos\left(\theta_m^{2'}\right)}{p \cdot M_{mz} \cdot \sin\left(\theta_m^{2'}\right)}\right) \quad \text{(D.43c)}$$

$$\beta_{4,1} = \tan^{-1}\left(\frac{-p \cdot M_{my} - q \cdot M_{mz} \cdot \cos\left(\theta_m^{2'}\right)}{q \cdot M_{mz} \cdot \sin\left(\theta_m^{2'}\right)}\right) \quad \text{(D.43d)}$$

For

$$\begin{aligned}\xi_{ez,mx} &= \psi_{ez} - \psi_{mx} \\ &= \frac{\psi_{5,0} + \psi_{6,0}}{2}\end{aligned} \quad \text{(D.44)}$$

$$\xi_{ez,mx} = -184.84^{o} \quad \text{(D.45)}$$

where

$$\psi_{5,0} = \phi_5^{'} + \alpha_{5,0} - \beta_{5,0} \quad \text{(D.46a)}$$

$$\psi_{6,0} = \phi_6^{'} + \alpha_{6,0} - \beta_{6,0} \quad \text{(D.46b)}$$

and

$$\alpha_{5,0} = \tan^{-1}\left(\frac{q \cdot M_{ex} \cdot \sin\left(\theta_e^{3'}\right)}{p \cdot M_{ez} + q \cdot M_{ex} \cdot \cos\left(\theta_e^{3'}\right)}\right) \quad \text{(D.47a)}$$

$$\alpha_{6,0} = \tan^{-1}\left(\frac{-p \cdot M_{ex} \cdot \sin\left(\theta_e^{3'}\right)}{q \cdot M_{ez} - p \cdot M_{ex} \cdot \cos\left(\theta_e^{3'}\right)}\right) \quad \text{(D.47b)}$$

$$\beta_{5,0} = \tan^{-1}\left(\frac{q \cdot M_{mz} \cdot \cos\left(\theta_m^{3'}\right) - p \cdot M_{mx}}{q \cdot M_{mz} \cdot \sin\left(\theta_m^{3'}\right)}\right) \quad \text{(D.47c)}$$

$$\beta_{6,0} = \tan^{-1}\left(\frac{-p \cdot M_{mz} \cdot \cos\left(\theta_m^{3'}\right) - q \cdot M_{mx}}{-p \cdot M_{mz} \cdot \sin\left(\theta_m^{3'}\right)}\right) \quad \text{(D.47d)}$$

For

$$\begin{aligned}\xi_{ex,mz} &= \psi_{ex} - \psi_{mz} \\ &= \frac{\psi_{5,1} + \psi_{6,1}}{2}\end{aligned} \tag{D.48}$$

$$\xi_{ex,mz} = -142.45^{o} \tag{D.49}$$

where

$$\psi_{5,1} = \phi_5^{'} + \alpha_{5,1} - \beta_{5,1} \tag{D.50a}$$

$$\psi_{6,1} = \phi_6^{'} + \alpha_{6,1} - \beta_{6,1} \tag{D.50b}$$

and

$$\alpha_{5,1} = \tan^{-1}\left(\frac{-p \cdot M_{ez} \cdot \sin\left(\theta_e^{3'}\right)}{p \cdot M_{ez} \cdot \cos\left(\theta_e^{3'}\right) + q \cdot M_{ex}}\right) \tag{D.51a}$$

$$\alpha_{6,1} = \tan^{-1}\left(\frac{-q \cdot M_{ez} \cdot \sin\left(\theta_e^{3'}\right)}{q \cdot M_{ez} \cdot \cos\left(\theta_e^{3'}\right) - p \cdot M_{ex}}\right) \tag{D.51b}$$

$$\beta_{5,1} = \tan^{-1}\left(\frac{q \cdot M_{mz} - p \cdot M_{mx} \cdot \cos\left(\theta_m^{3'}\right)}{p \cdot M_{mx} \cdot \sin\left(\theta_m^{3'}\right)}\right) \tag{D.51c}$$

$$\beta_{6,1} = \tan^{-1}\left(\frac{-p \cdot M_{mz} - q \cdot M_{mx} \cdot \cos\left(\theta_m^{3'}\right)}{q \cdot M_{mx} \cdot \sin\left(\theta_m^{3'}\right)}\right) \tag{D.51d}$$

The electric dipole strength is calculated by

$$\begin{aligned}M_{er} &= \sqrt{{M_{ex}}^2 + {M_{ey}}^2 + {M_{ez}}^2} \\ &= 5.99 \times 10^{-5} \text{ Amp/m}\end{aligned} \tag{D.52a}$$

The magnetic dipole strength is calculated by

$$M_{mr} = \sqrt{M_{mx}{}^2 + M_{my}{}^2 + M_{mz}{}^2} = 1.84\times10^{-5}\ \text{Amp/m}^2 \quad \text{(D.52b)}$$

The electric dipole orientation is calculated by

$$\phi_e = \tan^{-1}\left(\frac{M_{ey}}{M_{ex}}\right) = 59.83^o \quad \text{(D.53a)}$$

$$\theta_e = \cos^{-1}\left(\frac{M_{ez}}{M_{er}}\right) = 61.34^o \quad \text{(D.53b)}$$

The magnetic dipole orientation is calculated by

$$\phi_m = \tan^{-1}\left(\frac{M_{my}}{M_{mx}}\right) = 64.75^o \quad \text{(D.54a)}$$

$$\theta_m = \cos^{-1}\left(\frac{M_{mz}}{M_{mr}}\right) = 62.26^o \quad \text{(D.54b)}$$

The total radiated power is then calculated as follow:

$$P_{total} = \frac{40\cdot\pi^2}{\lambda^2}\cdot\left[M_{ex}{}^2 + M_{ey}{}^2 + M_{ez}{}^2 + k^2\left(M_{mx}{}^2 + M_{my}{}^2 + M_{mz}{}^2\right)\right]$$
$$= 2.23\times10^{-7}\ \text{W} = -36.50\,\text{dBm} \quad \text{(D.55)}$$

E.1 Suggested manipulator to aid phase measurement system

To complete the phase measurement experimental setup using a GTEM cell, an EUT manipulator was proposed. An EUT manipulator is an important tool in the GTEM EMC testing because as it ensures that an EUT is rotated correctly into the orientations especially for the measurement that requires many EUT orientations. It also improves repeatability. In the phase measurement experimental setup, an EUT manipulator eases the job of turning the EUT from 0^o to 180^o while maintaining the centre point of the EUT.

The proposed manipulator is a modification of currently available manipulator in the market such as [1]. The manipulator is shown in Figure E.1. It integrates the 3 axis orthogonal positioner in [2] into the turntable mentioned in [1]. By doing so, it meets all requirements to position an EUT to any orientation.

A feature of this manipulator is the ability to rotate the EUT accurately around the centre of the EUT (by adjusting Part A), so that the turning axis is at the centre point of the EUT. This manipulator keeps the centre point of EUT unchanged no matter how it is rotated. It can also accommodate the type of EUT orientations produced by Wilson [3], Ma [4] and other orientation types which are required by other GTEM measurement techniques. This manipulator can be automated in future by pneumatic or string-pulley actuation system.

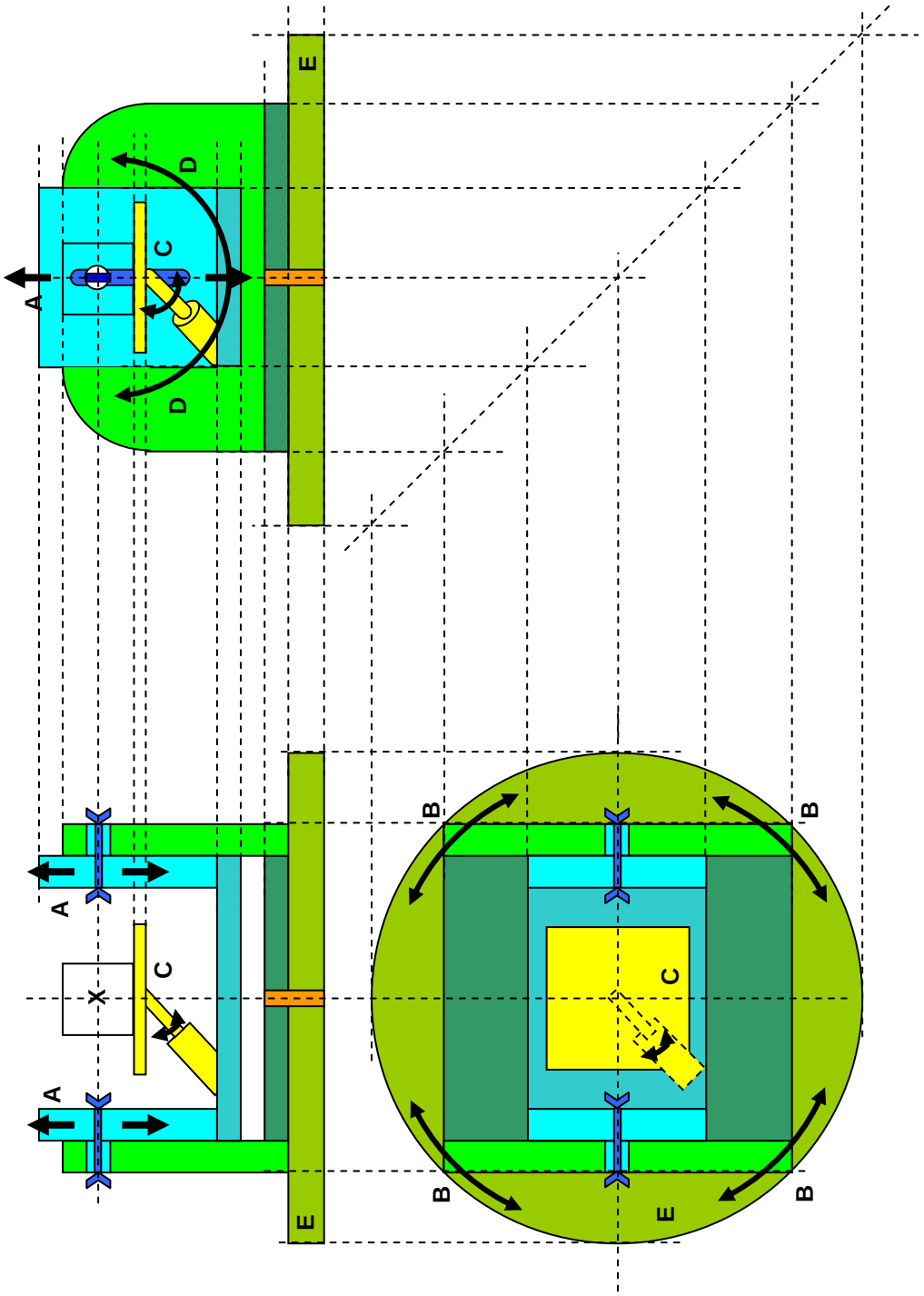

A: Vertical height adjustment to centre EUT **B**: Vertical rotation (NBS) i.e.: [0^{o}] and [180^{o}]

C: Orthogonal rotation (Wilson) [xx' yy' zz'], [xy' yz' zx'] and [xz' yx' zy']

D: Horizontal rotation (NBS) i.e.: [45^{o}] and [90^{o}] **E**: Static plate **X**: EUT centre point

Figure E.1 A proposed EUT manipulator for phase measurement using a GTEM cell and other type of orientations

E.2 References

1. ETS-Lindgren, *"Gigahertz Transverse Electromagnetic cell (GTEM) Model 5400 Series "*, 2005, Cedar Park, TX.

2. 61000-4-20, *"Electromagnetic Compatibility (EMC) – Part 4: Testing and measurement techniques. Section 20: Emission and immunity testing in transverse electromagnetic (TEM) waveguides",* International Electrotechnical Commission, Geneva, Switzerland, 2003.

3. Wilson P., *"On correlating TEM cell and OATS emission measurements",* IEEE Transactions on Electromagnetic Compatibility, 1995, 37(1), p. 1-16.

4. Ma M.T. and Koepke G., *"A method to quantify the radiation characteristics of an unknown interference source",* NBS Tech. Note 1059, Oct. 1982.

End of Thesis